PEGylated micelles for diagnostic and therapy against solid tumors

Stéphane Hoang

THESE DE DOCTORAT

NNT : 2023UPASF063

PEGylated micelles for diagnosis and therapy against solid tumors

Micelles PEGylées pour le diagnostic et la thérapie de tumeurs solides.

Thèse de doctorat de l'Université Paris-Saclay et de l'Université Charles

École doctorale n° 571 : Sciences chimique : molécules, matériaux, instrumentation et biosystèmes (2MIB)
Spécialité de doctorat : Chimie
Graduate School : Chimie. Référent : Faculté des sciences d'Orsay

Thèse préparée dans l'unité de recherche **Médicaments et Technologies pour la Santé** (Université Paris-Saclay, CEA, INRAE) et le **Département de Systèmes Polymères et Supramoléculaires** (Université Charles, ICM) sous la direction de **Edmond GRAVEL**, chercheur, la co-direction de **Martin HRUBÝ**, Professeur des Universités.

Thèse soutenue à Paris-Saclay, le 13 Octobre 2023, par

Stéphane HOANG

Composition du Jury

Membres du jury avec voix délibérative

Simona MURA Professeur des Universités, Université Paris-Saclay	Présidente
Alberto BIANCO Directeur de recherche CNRS, Université de Strasbourg	Rapporteur & Examinateur
Céline FROCHOT Directrice de recherche CNRS, Université de Lorraine	Rapporteur & Examinateur
Jan SEDLACEK Professeur des Universités, Université Charles	Examinateur

Charles University

Faculty of Science

Study programme: Macromolecular Chemistry

CHARLES
UNIVERSITY

MSc. Stéphane Hoang

PEGylated micelles for diagnostic and therapy against solid tumors

PEGylované micely pro diagnostiku a terapii solidních nádorů

Doctoral thesis

Supervisor:

Prof. Martin Hrubý

co-supervisor:

Dr Edmond Gravel

Prague, 01.08.2023

Acknowledgment

First, I would like to thank the jury members for accepting to judge my PhD thesis.

I would like to thank Frédéric TARAN, head of the *Service de Chimie Bioorganique et de Marquage*, who allowed me to do my PhD in his laboratory. I would also like to thank Eric DORIS, head of the Tritium team, for welcoming me in his team.

I would like to express my gratitude to both my supervisors Edmond GRAVEL and Martin HRUBÝ, who allowed me to do this cotutelle PhD in very good conditions. During these three years, I got to know two amazing people, profesionally and personally. Thank you for your time, especially for the correction of my PhD thesis.

I would like to thank all the members of the SCBM laboratory, including the analysis team and the adminitrative hub, who contributed to these three great years.

Special thanks to my colleague claire, to the fake red-head who has borderline jokes (but we still like you), to my personal timekeeper who made sure I was aware of coming after 9 am (almost) everyday and to Mister Richaaard aka le bgdu86.

I would also like to thank the people from the Institute of Macromolecular Chemistry, and especially the people from the Department of Supramolecular Polymer Systems. Thank you Petr STEPANEK and Jiri PANEK for your kindness and time when I was in Prague. I really enjoyed discussing with you both, especially in french with Petr.

I would like to thank the post-docs and PhD students with whom I spent a lot of times (in bars). My special thanks to Miro and Martina with whom I have my best memories from my time in Prague.

And finally, I would like to thank my parents who always supported me throughout the PhD thesis.

Table of contents

Abbreviations list

ABC	Accelerated Blood Clearance
BFc	Benzoylferrocene
CMC	Critical Micellar Concentration
Cp	Cyclopentadiene
CTC	Charge transfer complex
CTTS	Charge transfer to solvent
DLS	Dynamic Light Scattering
DBFc	Dibenzoylferrocene
DFO	Deferoxamine
DFP	Deferiprone
DiD	1,1′-dioctadecyl-3,3,3′,3′- tetramethylindodicarbocyanine, 4-chlorobenzenesulfonate salt
DLL4	Delta-Like Ligand 4
DMA	2,3-dimethylmaleic anhydride
DMSO	Dimethylsulfoxide
DPBF	1,2-diphenylisobenzofuran
EDC.HCl	*N*-ethyl-*N*′-(3-dimethylaminopropyl) carbodiimide hydrochloride
EGF	Epidermal Growth Factor
EPR	Enhanced Permeability and Retention
Fc	Ferrocene
FDA	Food and Drug Administration
FGF	Fibroblast Growth Factor
GOs	Graphene Oxides
HIF-1	Hypoxia-Inducible Factor 1
IC	Internal Conversion
ISC	Intersystem Crossing
LCST	Lower Critical Solution Temperature
LED	Light Emitting Diode
LSPR	Localized Surface Plasmon Resonance

MeOH	Methanol
MLCT	Metal to ligand charge transfer
NHS	*N*-hydroxysuccinimide
NIR	Near-infrared
NR	Nile Red
PAMAM	Poly(amidoamine)
PCDA	10,12-pentacosadiynoic acid
PCL	Poly(ε-caprolactone)
PDT	Photodynamic Therapy
PEG	Poly(ethylene glycol)
PEO	Poly(ethylene oxide)
PET	Positron Emission Tomography
PLA	Poly(lactic acid)
POxs	Poly(2-oxazoline)s
PPO	Poly(propylene oxide)
PS	Photosensitizer
PTT	Photothermal Therapy
PVP	Poly(*N*-vinyl-2-pyrrolidone)
ROS	Reactive Oxygen Species
TFA	Trifluoroacetic acid
TFAA	Trifluoroacetic anhydride
TfR	Transferring Receptor
THF	Tetrahydrofuran
TPBC	*meso*-Tetraphenylbacteriochlorin
TPC	*meso*-Tetraphenylchlorin
TPP	*meso*-Tetraphenylporphyrin
US	Ultrasound
VEGF	Vascular Endothelial Growth Factor
VPF	Vascular Permeability Factor
VR	Vibrational relaxation
XPS	X-ray Photoelectron Spectroscopy

GENERAL INTRODUCTION

1. Nanosystems in medicine

1.1. Nanomedicine

1.1.1. Definition

Nanomedicine can be defined as the use of nanoobjects to perform diagnosis, therapy or regenerative medical tasks. Nanoobjects, in general, are designated as materials that have at least one of their three dimensions in the nanoscale (from 1 to 100 nm), and nanoparticles, in particular, are materials that have all three dimensions in the nanoscale. Nanoparticles possess physicochemical characteristics such as thermal, magnetic, optical and catalytic properties that drastically differ from their conventional bulk material.[1] As a consequence, these novel properties led to the development of innovative drug systems, based on the improvement of conventional medicine. In cell-based therapeutics, conventional medicine's main drawback is the lack of specificity which leads to harmful effects on healthy cells. As a result, nanomedicine aims at progressing toward more specific and targeted treatments for the purpose of limiting side effects and increasing the potency of the treatment.[2,3] Indeed, nanoparticles can be tuned at different levels, mainly their shape, size, surface, shell, and core, to fit the requirements for a given application. Such versatility opens a new world of possibilities in medicine in terms of strategy, development and innovation in the treatment of various diseases.

1.1.2. Historical background

The concept of using nanoobjects for medical purposes itself was foreshadowed in the 1950s by Richard Phillips Feynman who mentioned the potential use of nanoscale machines for medicine. However, his words went mostly unnoticed and it was only in the 1980s, when progress in nanotechnology allowed the direct visualization and manipulation of objects at a nanometric scale, that Feynman was recognized as one of the pioneers. Following the development of technologies such as transmission electron microscopy (TEM), atomic force microscope (AFM), and scanning tunneling microscope (STM), a whole new scientific discipline specific to the nanoworld opened up, including nanomedicine.

[1] N. Joudeh and D. Linke, Journal of Nanobiotechnology, 2022, https://doi.org/10.1186/s12951-022-01477-8.
[2] M. Rasool et al., Bioengineered, 2022, https://doi.org/10.1080/21655979.2021.2012907.
[3] R. M. Samarasinghe et al., International Journal of Molecular and Cellular Medicine, 2012, https://www.ncbi.nlm.nih.gov/pmc/articles/PMC3920502/

The first Food and Drug Authority (FDA)-approved nanomedicine (Doxil® in 1995) consisted of doxorubicin, a chemotherapeutic drug, encapsulated into liposomes.[4] This first nanoformulation led later on to similar liposomal assemblies that are Caelyx® (1996) and Myocet® (2000) for the treatment of diseases such as leukemia, breast and ovarian cancers. More recently, NBTXR3, developed by Nanobiotix and approved in 2019, is a nanodrug made of hafnium oxide nanoparticles activated by external X-ray to induce cell death.[5] Similarly, NH TherAguix developed AguIX®, a gadolinium-based nanoparticle, which is currently in 5 clinical trials. All these nanomadicines are spherical particles with diameters below 100 nm, great in vivo stability and either active or passive targeting properties.

1.2. Physical features of nanoparticles

1.2.1. Size

The small size of nanoparticles is responsible for their unique properties. Indeed, in the case of gold, the bulk material is mostly inert, however, once turned into nanoparticles, the material exhibits incredible behavior such as high catalytic activity and therapeutic properties that are non-existant in the raw material. The size of nanoparticles also greatly dictates the way they interact with their environment. In a biological medium, particle size plays an important role in the cellular internalization process.[6] Indeed, particles of diameters below 100 nm will tend to be internalized via caveolae-mediated endocytosis whereas particles above 100 nm will be more inclined to undergo clathrin-mediated endocytosis or macropinocytosis (**Fig. 1**). In the tumor microenvironment, defective blood vessels have permeable endothelium with pores as large as several hundred nanometers. Thus, smaller nanoparticles extravasate into the tumor much more efficiently than larger ones. In addition, studies showed that among liposomes with a diameter between 40-700 nm, the ones with a size ranging from 50 to 150 nm had the best blood circulation time and the best accumulation in the tumor.

[4] N.D. James et al., Clinical Oncology, 1994, https://doi.org/10.1016/S0936-6555(05)80269-9.
[5] A. Darmon et al., Cancer Cell International, 2022), https://doi.org/10.1186/s12935-022-02615-w.
[6] S. Mazumdar et al., Acta Pharmaceutica Sinica B, 2021, https://doi.org/10.1016/j.apsb.2021.02.019.

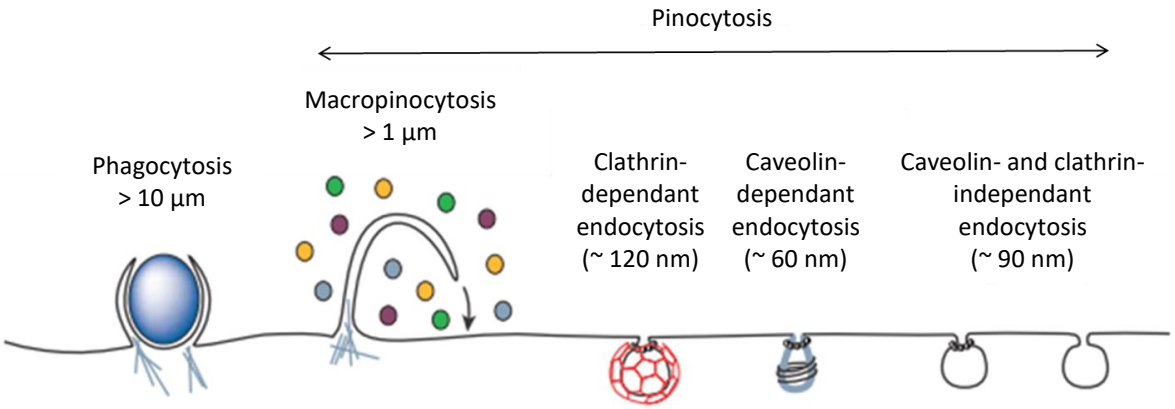

Fig. 1: Different internalization pathways according to the particle's size.

On the other hand, liposomes larger than 200 nm displayed very poor extravasation and therefore, less activity than their smaller counterparts.[7] It was also shown that nanoparticles of hydrodynamic radius ranging from 4 to 8 nm, corresponding to serum protein size, have much lower nonspecific bindings at their surface due to low contact points from the protein-nanoparticles to bind to each other.[8]

1.2.2. Shape

Although size is the main factor in particle behavior, the shape is not to be overlooked. Nanoparticles come in various geometries: spheres, wires, tubes, stars, rings, cones, cylinders, ellipsoids and more. For a given material, one can have multiple shapes for specific properties and applications.[9,10] Spherical gold nanoparticles are widely used in cancer therapy for their redox catalytic[11] property or drug delivery.[12] For example, CNM-Au8, a gold formulation for the treatment of neurodegenerative diseases, was approved by the FDA in 2019. Nanorod-shaped gold nanoparticles are also widely studied. Gold nanorods are pseudo-one-dimensional nanoparticles the length of which can be finely tuned to modulate localized longitudinal

[7] A. Nagayasu et al., Advanced Drug Delivery Reviews, 1999, https://doi.org/10.1016/S0169-409X(99)00041-1.
[8] S. Nie, Nanomedicine, 2010, https://doi.org/10.2217/nnm.10.23.
[9] R. Toy et al., Nanomedicine, 2014, https://doi.org/10.2217/nnm.13.191.
[10] P. Lagarrigue et al., Pharmaceutics, 2022, https://doi.org/10.3390/pharmaceutics15010032.
[11] Yongle Du et al., Bioconjugate Chemistry, 2018, https://doi.org/10.1021/acs.bioconjchem.7b00756.
[12] G. J. Hutchings and J. K. Edwards, Frontiers of Nanoscience, 2012, https://doi.org/10.1016/B978-0-08-096357-0.00001-7.

surface plasmon resonance absorption band to the desired wavelength for the targeted application (e.g. photodynamic therapy).

Shape also matters for lipidic nanoparticles such as micelles. Spherical micelles are the most comon, however, worm-like micelles, also called filomicelles, show different behaviours in cancer treatment regarding their blood circulation time, their phagocytosis rate and target selectivity due to their elongated shape. For instance, it was shown that long filomicelles from block copolymers have a 10-fold longer blood circulation half-life than their spherical counterpart but a lesser accumulation by passive diffusion in the tumor tissue.[13] Hence, shape plays a major role in the behaviour of nanoparticles and has to be considered to best suit the target application.

1.2.3. Surface area to volume ratio

A key feature that results from the size and shape of the particle is the surface area to volume (S/v) ratio. As the volume of a particle decreases, its S/v ratio increases exponentially resulting in an increase of the fraction of surface atoms f.[14] The latter is defined as the ratio between the total number of surface atoms and the total number of atoms in the nanoparticle. For small nanoparticles (< 20 nm) and considering that the atoms are perfectly spherical, f can be approximated as being ~ 1/d, with d the diameter of the nanoparticle in nm. For instance, a 20 nm spherical gold nanoparticle has about 5% of its atoms at the surface, whereas a 2 nm particle has 50% of its atoms at the surface.[15] In other words, the lower the volume, the more atoms are located at the particle's surface. This results in an enhancement of the reactivity, as more reactive sites are readily available. This property is highly exploited in catalysis when using metal-based nanocatalysts such as palladium or ruthenium metals.[16,17] In biological environment, a high surface area to volume ratio can promote interactions between the nanoparticle and the surface of biological entities leading to undesired effects, loss of specificity or lower blood circulation time. To limit the destabilization interactions with the medium, nanoparticles assemble into spheres to increase their stability. Indeed, among all

[13] Y. Geng et al., Nature Nanotechnology, 2007, https://doi.org/10.1038/nnano.2007.70.
[14] P. N. Navya and H. K. Daima, Nano Convergence, 2016, https://doi.org/10.1186/s40580-016-0064-z.
[15] S. Nanda and K. K. Nanda, Journal of Chemical Education 2021, https://doi.org/10.1021/acs.jchemed.0c01247.
[16] X. Cai et al., Frontiers in Chemistry, 2019, https://doi.org/10.3389/fchem.2019.00042.
[17] I. Favier et al., Comptes Rendus Chimie, 2009, https://doi.org/10.1016/j.crci.2008.10.017.

shapes and for a given volume, spheres have the lowest S/v ratio, resulting in the least surface tension. From a biological perspective, the surface area to volume ratio is determinant of the nanoparticle's reactiveness and thus, its stability in biological systems.

1.2.4. Surface charge

The immune system is one actor of the capture and elimination of nanoparticles. Some serum proteins, known as opsonines, can adsorb at the surface of the nanoparticles, promoting their aggregation and clearance.[18] This phenomenon is called opsonization. The nonspecific adsorption of proteins makes the nanoparticles more visible to phagocytic cells, causing them to be detected and phagocytosed by a receptor-mediated mechanism. Opsonization is heavily dependent on the particles' surface chemistry. Charged particles are much more prone to opsonization. Indeed, negatively and positively charged nanoparticles can more easily interact with proteins by electrostatic interactions. As most blood plasma proteins and cell surfaces possess overwhelmingly negative charge, negatively charged nanoparticles show lower cellular uptake, and thus higher circulation time in constrast with positively charged nanoparticles that are easily detected and eliminated by phagocytes (**Fig. 2**).[19] In comparison, neutral particles display much lower opsonization and clearance due to the presence of unreactive and bulky groups (polymers) at their surface.[20] Typical polymers used in neutral nanoparticles are polysaccharides and poly(ethylene) oxide. Their high hydrophilicity increases the solubility of the nanoparticles and their flexibility, size and neutrality greatly reduce the interactions with foreign agents. This type of polymer provides stealth property to nanoparticles that can escape from the immune system and, as a consequence, have increased blood circulation time and biodistribution along with lower clearance, allowing them to reach the tumor site more efficiently.

[18] F. Alexis et al., Molecular Pharmaceutics, 2008, https://doi.org/10.1021/mp800051m.
[19] H. -X. Wang et al., Nano Today, 2016, https://doi.org/10.1016/j.nantod.2016.04.008.
[20] Q. Yang and S. K. Lai, Wiley Interdisciplinary Reviews: Nanomedicine and Nanobiotechnology, 2015, https://doi.org/10.1002/wnan.1339.

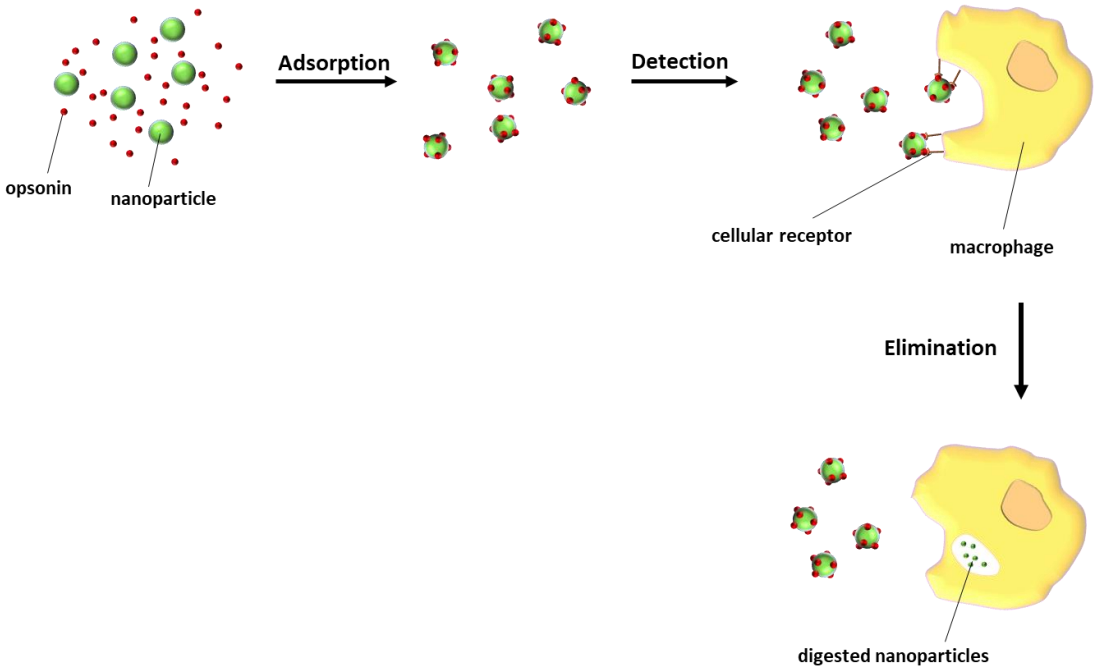

Fig. 2: Opsonization process of nanoparticles.

1.3. Solid tumor tissue

1.3.1. Angiogenesis

In healthy or diseased tissues, blood vessels grow continuously from the existing vasculature. This natural biological process is called angiogenesis and involves the migration, growth, and differentiation of endothelial cells (**Fig. 3**).[21,22] Angiogenesis is crucial as the newly formed blood vessels, or capillaries, are responsible for transporting nutrients and oxygen to the tissues. This phenomenon takes place in various biological processes such as reproduction, embryonic development, or wound healing. The main mechanism involved in angiogenesis is known as sprouting. Tissues in need of oxygen, also known as hypoxic tissues, overexpress hypoxia-inducible factor 1 (HIF-1) which is a major regulator of oxygen homeostasis within cells. As a transcription factor, HIF-1 activates various genes involved in the homeostasis of oxygen, leading to the release of pro-angiogenic factors such as epidermal growth factor (EGF), fibroblast growth factor (FGF) and most importantly, vascular endothelial growth factor (VEGF).

[21] L. Treps and J. Gavard, Médecine/Sciences, 2015, https://doi.org/10.1051/medsci/20153111013.
[22] M. Papetti and I. M. Herman, American Journal of Physiology-Cell Physiology, 2002, https://doi.org/10.1152/ajpcell.00389.2001.

By releasing VEGF, a gradient of concentration is detected by nearby existing vessels, triggering the migration and differentiation of endothelial cells called tip cells (**Fig. 3A**). These tip cells are guided by the gradient of VEGF due to their overexpression of the VEGF receptor, VEGF-R2, allowing the capillaries to grow toward the hypoxic signal (**Fig. 3B**). As the tip cells migrate, the interaction of VEGF-R2 and VEGF induces the production of the delta-like ligand 4 (DLL4) protein, ligand of Notch receptor. DLL4 and Notch being located at the surface of the cells, the interaction only occurs when two cells are in direct contact. Therefore, the expression of DLL4 from the tip cells activates the Notch receptors of neighboring cells only. The activation of Notch receptors results in the decrease of VEGF-R2 expression while increasing VEGF-R1 (**Fig. 4**). The latter does not promote migration, making the affected cells, called stalk cells, only proliferating behind the tip cells (**Fig. 3C**). This process ensures the proper growth of the capillary in the right direction. When two different tip cells converge into one another, a single blood vessel is formed by anastomosis. This newly formed vessel guarantees the transport of oxygen to the hypoxic tissue. Once sufficient oxygen is provided, the VEGF level turns back to normal and the neovessel is stabilized by maturation via the recruitment of pericytic cells (**Fig. 3D**). However, in the case of a tumor, the different steps of the angiogenesis are highly altered such as an abnormally high amount of tip cells engaged, the participation of non-endothelial cells in the growth of new vessels, the unstable nature of the latter and the dysregulation of secreted factors favoring the sprouting of new vessels.

1.3.2. Tumor: angiogenesis and micro-environment

The tumor is defined as the uncontrolled and aberrant proliferation of cells in a heterogenous environment called tumor stroma. Tumor cells, like other cells, need oxygen and nutrients to grow and therefore share similar mechanisms regarding their development. Tumor cells use angiogenesis to supply the large amounts of oxygen and nutrients required to support their exceptional proliferation rate. Indeed, as the tumor tissue grows, less and less oxygen is transported to the tumor by diffusion. As a consequence, the center of the tumor is mainly constituted of necrotic tissue and a gradient of oxygen is observed from the anoxic center to

the hypoxic periphery.[23] This poor oxygen supply results in the activation of angiogenesis. As in normal tissues, tumoral angiogenesis heavily relies on the expression of VEGF to recruit new

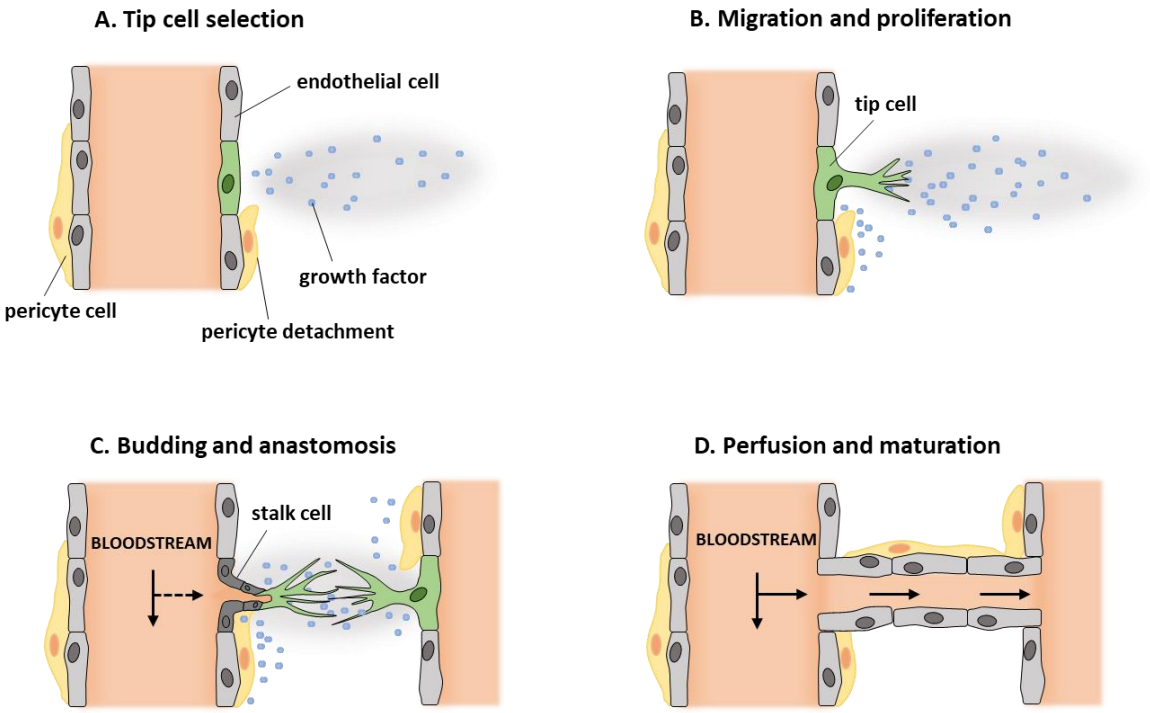

Fig. 3: Main steps of angiogenesis for the creation of a new blood vessel.

vessels and provide sufficient oxygen for the growing tissue. The rapid proliferation of the tumor cells requires abundant and constant oxygen supply, leading to the recruitment of more vessels which is mediated by the increased release of growth factors such as VEGF. For these reasons, the expression of VEGF in tumor tissues is much higher than in healthy tissues. As a consequence, tumor vascularization is disorganized, the vessels are uneven and randomly branched, resulting in irregular blood flow throughout the tumor.[24] Besides VEGF, other secreted proteins also participate in the vascularization of the tumor, such as fibroblast growth factor (FGF).

[23] R. H. Thomlinson and L. H. Gray, British Journal of Cancer, 1955, https://doi.org/10.1038/bjc.1955.55.
[24] P. Carmeliet and R. K. Jain, Nature, 2000, https://doi.org/10.1038/35025220.

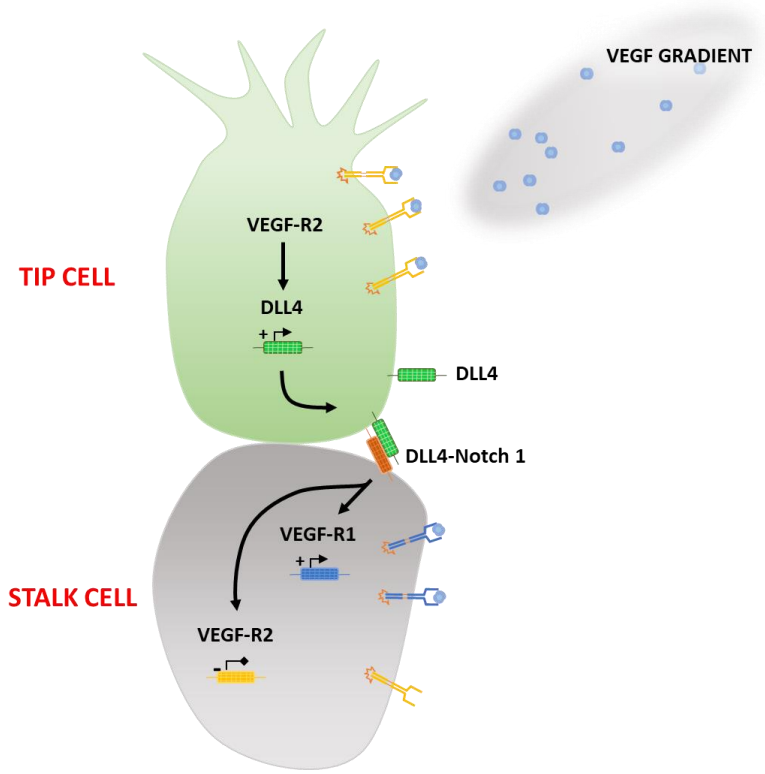

Fig. 4: Interaction between the tip cell and stalk cells induced by a gradient of VEGF.

While VEGF initiates angiogenesis, FGF likely maintains the process all along. Indeed, it was shown that both VEGF and FGF cooperate to increase cell proliferation.[22] Apart from being a protein that stimulates endothelial cells, VEGF, also known as vascular permeability factor (VPF), increases the permeability of nearby blood vessels. VEGF is the most potent factor that induces vasodilatation of existing vessels. As a result, blood pressure is lower in the affected vessels that, in addition, are more permeable. The newly and rapidly formed vessels, or neovessels, constitute an immature network of vessels featuring leaky membranes that allow the extravasation of various exogenous compounds as well as the infiltration of neoplastic cells resulting in metastatic tumors (**Fig. 5**). The leakiness is introduced by nanosized pores along the neovessels, varying from a dozen to a few hundred nanometers.[25] Besides these pores, the interendothelial junctions are widely opened and the vessels' walls are discontinuous with, in

[25] T. Stylianopoulos and R. K. Jain, Proceedings of the National Academy of Sciences, 2013, https://doi.org/10.1073/pnas.1318415110.

some cases, the absence of a basement membrane.[26] Furthermore, another specificity of the tumor environment is the defective lymphatic system, leading to the failure of lymphatic drainage, thus raising the interstitial fluid tension. This results in the retention of molecules inside the tumor tissue. These features combined with vasodilatation are highly exploited in chemotherapeutic strategies using nanoparticles. The leaky structure provides much greater access to the tumor tissue as opposed to healthy tissues, enabling better targeting of nanomedicines.

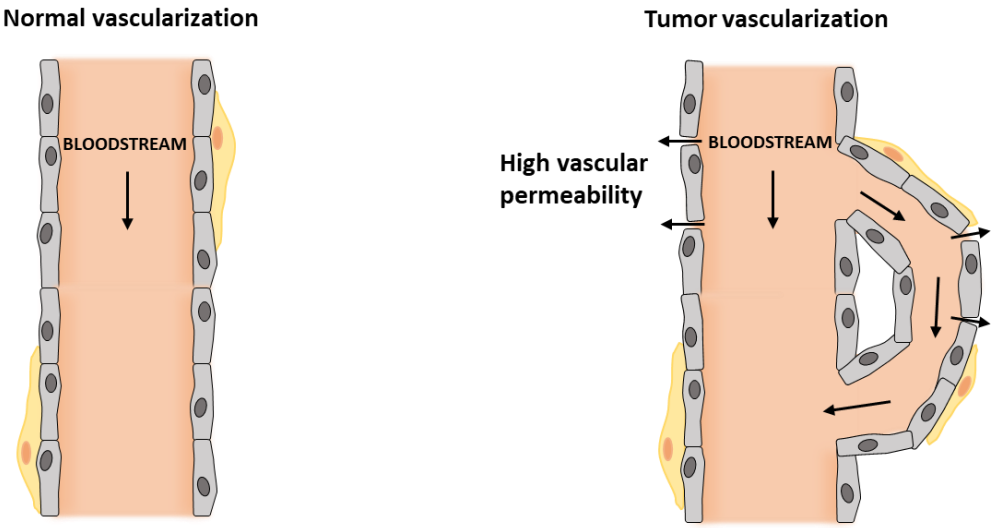

Fig. 5: Comparison between blood vessels in normal (left) and tumor (right) tissues.

1.3.3. Vectorization: passive and active targeting

The concept of being able to vectorize, guide, or target more specifically an area was theoretically introduced by Paul Ehrlich in early 1900s, where he mentioned the "magic bullet", describing an ideal toxic drug that would only react with the target. The specific action of the drug with solely the target would greatly reduce side effects. This concept, named vectorization, has emerged with the rise of nanomedicine and has supported novel strategies regarding the design, conceptualization, and application of new drug systems. The specific

[26] H. Hashizume et al., The American Journal of Pathology, 2000, https://doi.org/10.1016/S0002-9440(10)650067.

delivery of nanodrugs to the desired site of action can be achieved by passive and/or active targeting.

Passive targeting, as the name suggests, relies solely on the passive diffusion of the drug from the blood flow to reach the neoplastic tissue. In leaky and dilated vessels, nanoparticles can extravasate from the bloodstream to the tumor tissue more easily due to weaker endothelial barriers (**Fig. 6**). The longer the nanoparticles are circulating in the bloodstream, the more they accumulate inside the tumor, owing to the fact that their clearance is low enough to do so. This principle was first described in 1986 by Matsumura and Maeda when they showed in tumor-bearing mice that their polymer conjugated to the anticancer protein neocarzinostatin had better accumulation in the tumor than the protein itself.[27] The main explanation was that neocarzinostatin, being a relatively low molecular weight protein (12 kDa) below the renal threshold (40 kDa) underwent urinary elimination as opposed to the polymer-protein drug conjugate of high molecular weight (> 40 kDa) which, as a nanoparticle, circulated longer and accumulated into the tumor. Later on, this effect was coined as the enhanced permeability and retention (EPR) effect. The name comes from the combination of a hypervascularized environment and defective vessels of increased permeability with an impaired lymphatic system that makes the particles stagnate in the tumor (retention effect).

[27] Y. Matsumura and H. Maeda, Cancer Research, 1986, https://aacrjournals.org/cancerres/article/46/12_Part_1/6387/490212/A-New-Concept-for-Macromolecular-Therapeutics-in

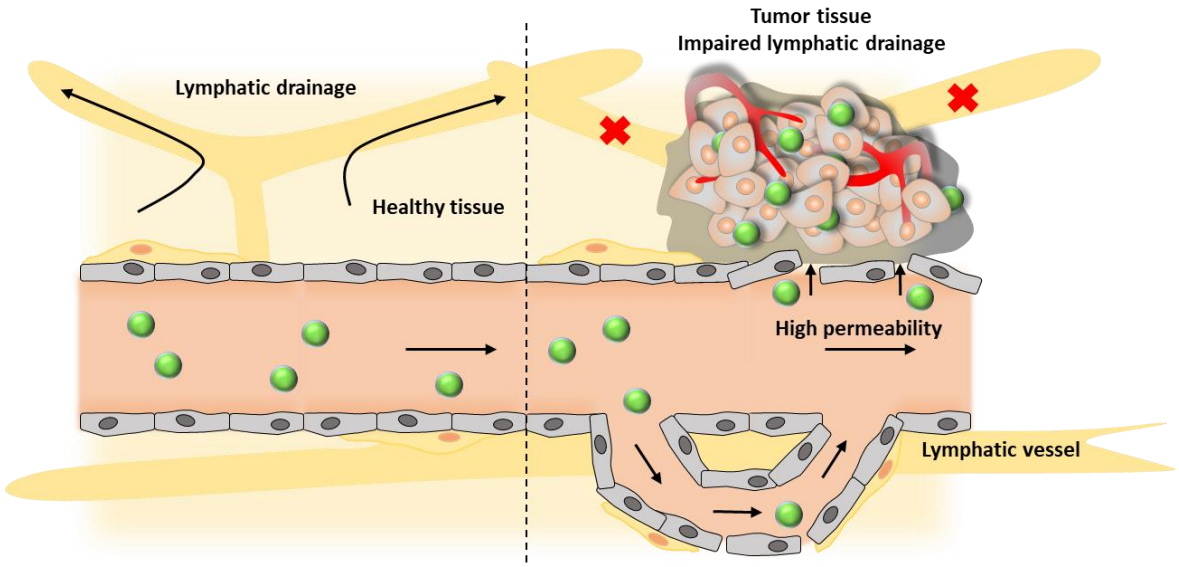

Fig. 6: Vascularization of healthy (left) and tumor (right) tissues showing the EPR effect.

Since then, various nanodrugs were designed, using liposome-based vectors in which anticancer molecules are encapsulated such as Doxil®. These nanocarrier-drug systems are based on the combination of a vector, the nanoparticle that is in direct interaction with the environment, and the drug, most of the time located inside the vector and safe from the external medium. However, as Maeda and Matsumura observed, passive targeting is only efficient if the nanoparticles can circulate long enough to accumulate in the tumor over time. As mentioned earlier, the main reasons of the low accumulation of nanoparticles by passive diffusion are the hepatic and renal elimination pathways. To circumvent these issues, the formulation of nanovectors improved over the last decades, and more advanced nanocarriers were developed. It's well-known that charged particles tend to interact more than their neutral counterparts due to electrostatic interactions.

In this regard, nanoparticles coated with nonionic chains such as poly(ethylene glycol) (PEG),[28] polysaccharides,[29] or poly(2-oxazoline)s[30] were built. Their common properties are their high hydrophilicity enhancing the solubility of the nanoparticles, and their long and dense polymer

[28] S. Chen et al., Nanomedicine: Nanotechnology, Biology and Medicine, 2016, https://doi.org/10.1016/j.nano.2015.10.020.
[29] T. G. Barclay et al., Carbohydrate Polymers, 2019, https://doi.org/10.1016/j.carbpol.2019.05.067.
[30] T. X. Viegas et al., Bioconjugate Chemistry, 2011, https://doi.org/10.1021/bc200049d.

chains that create a corona at the surface of the particles, acting as a shield that greatly reduces the adsorption of serum proteins. This strategy of making the nanoparticles stealthy is called antifouling, and PEGylation (i.e. the use of PEG as a coating agent) is the most common method. Although PEG is generally considered as a nonimmunogenic and nonantigenic material, its overuse in detergents and clinical trials stimulate anti-PEG antibodies leading to an immunological response. This phenomenon, called accelerated blood clearance (ABC), is recognized and proved to decrease the therapeutic efficacy of PEG-based drugs.[31] Reducing the nanoparticle surface interactions also impacts nanoparticle-cell interactions involved in cellular uptake, for instance. Indeed, it was shown that PEGylated liposomes and non-PEGylated liposomes displayed different accumulation behaviour in tumor cells, as non-PEGylated liposomes were found in larger amounts in tumor cells.[32] The EPR effect only permits the nanoparticles to accumulate in the tumor tissue and does not promote the cellular uptake. Indeed, the high interstitial fluid tension makes the motion much more difficult for nanoparticles. In addition, the EPR effect and its characteristics greatly vary from one patient to another and from one tumor to another, even within the same tumor type.[33] Therefore, passive diffusion is sometimes not sufficient and modifications introducing targeting properties are necessary to achieve a better therapeutic effect.

Active targeting relies on the conjugation of targeting groups at the surface of the nanoparticles (**Fig. 7**). These groups are most commonly small molecules, antibodies and peptides.[34] The goal of such modification is to selectively aim for upregulated proteins or receptors, specifically overexpressed by the targeted cancer cells. Typically, various drugs are designed to inhibit growth factors such as VEGF and FGF responsible for tumor proliferation. In other cases, internalization receptors are targeted. Nanoparticles containing the ligand bind to the corresponding receptor prior to internalization and the cytotoxic drug is released. These approaches reduce off-target drug delivery and improve selective cellular uptake at the same time. Indeed, a recent study compared the efficacy of docetaxel loaded in polymeric nanoparticles, with and without GE11 peptide at the surface to specifically target the epidermal

[31] A. M S. Abu Lila et al., Journal of Controlled Release, 2013, https://doi.org/10.1016/j.jconrel.2013.07.026.
[32] S. S. Nunes et al., Pharmaceutics, 2022, https://doi.org/10.3390/pharmaceutics14020272.
[33] H. Maeda and M. Khatami, Clinical and Translational Medicine, 2018, https://doi.org/10.1186/s40169-018-0185-6.
[34] A. F. Sikorski et al., International Journal of Nanomedicine, 2015, https://doi.org/10.2147/IJN.S74514.

growth factor protein which is overexpressed in many cancers.[35] The biological assays were performed in vitro using MCF-7 and MDA-MB-231 cancer cell lines. In both cases, the targeted nanoparticles displayed much higher potency with IC_{50} of 5.1 ng/mL and 173.5 ng/mL for MDA-MBB-231 and MCF-7 respectively against 30.1 ng/mL and 886.2 ng/mL for the non-targeted nanoparticles.

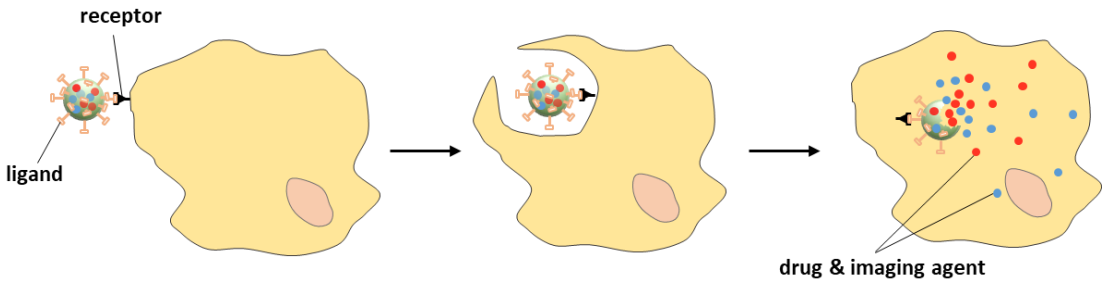

Fig. 7: Principle of active targeting based on ligand-receptor interaction for the release of drugs and imaging agents.

Another example is the targeting of transferrin, which is a glycoprotein used for the transport of iron from the extracellular space to the intracellular medium via interaction with the transferrin receptor 1 (TfR1). As tumor cells grow rapidly, apart from oxygen and nutrients, iron is also a crucial component for the proper functioning of cells. Adriamycin, an anticancer drug, was successfully conjugated to transferrin in order to target the overexpressed TfR1.[36] Passive targeting is a prerequisite for active targeting as the latter requires direct contact of the ligand with the targeted receptor. Active targeting provides new opportunities and possibilities for cancer treatment. The choice of the targeting group is critical for the behavior and efficacy of the administrated nanoparticles.

Combining passive and active targeting, various types of nanoparticles in the last decades were designed, synthesized and tested from in vitro cell cultures to clinical studies.

[35] T. D. Clemons et al., Langmuir, 2018, https://doi.org/10.1021/acs.langmuir.8b02946.
[36] J. Munns et al., BJU International, 1998, https://doi.org/10.1046/j.1464-410X.1998.00736.x.

2. Nanoparticles for cancer treatment

2.1. Metal-based nanoparticles

Metal-based nanoparticles have unique properties that are not found in the corresponding bulk metal. These characteristics come from the small size and high surface area to volume ratio of nanoparticles which drastically alter the physicochemical properties of the material. Metal-based nanoparticles are divided into two categories: metal and metal oxide nanoparticles. The latter can be prepared by treating the bulk metal in basic aqueous solution.[37,38] The most common metals are iron, copper, gold, silver or zinc. Metal-based nanoparticles find use in various applications against cancer such as phototherapy, hyperthermia, drug delivery and imaging. A major difference against organic nanoparticles, besides their chemical constitution, is that metal-based nanoparticles also benefit from the metallic properties that organic nanoparticles such as liposomes or micelles do not possess. The intrinsic properties of metals have opened alternative methods for cancer treatment. For example, the magnetic property of magnetite Fe_3O_4 is exploited to induce hyperthermia under strong magnetic field but it can also be used as a contrasting agent in magnetic resonance imaging (MRI).[39] Another great example is the use of the optical properties of gold nanoparticles. These particles present strong light absorption depending on their size and shape. They can be photo-excited by visible, near infrared or X-ray illumination, leading to different mechanisms of action.[40,41]

2.1.1. Gold nanoparticles

Gold nanoparticles were first synthesized by Turkevich et al. in 1951 by reducing hydrogen tetrachloroaurate ($HAuCl_4$) with sodium citrate.[42] However, this approach yielded polydisperse spherical gold nanoparticles. Over the course of time, the method was improved by Frens in 1973 to obtain smaller and less polydisperse nanoparticles, ranging from 10 to 20 nm. A major problem remained, the synthesized nanoparticles were aggregating during the process,

[37] M. Kundu et al., Journal of Cluster Science, 2016, https://doi.org/10.1007/s10876-016-1140-6.
[38] V. Srivastava et al., Ceramics International, 2013, https://doi.org/10.1016/j.ceramint.2013.04.110.
[39] C. -H. Lu and J. -K. Hsiao, Tzu Chi Medical Journal, 2023, https://doi.org/10.4103/tcmj.tcmj_65_22.
[40] Y. Chen et al., International Journal of Nanomedicine, 2020, https://doi.org/10.2147/IJN.S272902.
[41] R. S. Riley and E. S. Day, WIREs Nanomedicine and Nanobiotechnology, 2017, https://doi.org/10.1002/wnan.1449.
[42] J. Turkevich et al., Discussions of the Faraday Society, 1951, https://doi.org/10.1039/df9511100055.

resulting in low colloidal stability. The utilization of surfactants such as Tween 20 improved the process, but it was still not efficient enough.

Only until 1994, Brust et al. developed a method of synthesizing hydrophobic nanoparticles of 1–3 nm using alkanethiols as stabilizing agents.[43] This method gained major interest as it was reproducible, reliable, very simple to implement, and yielded stable colloids. This high colloidal stability comes from the fact that thiols bind strongly to gold and the resulting gold nanoparticles are more stable and less likely to aggregate. Spherical gold nanoparticles show low toxicity and excellent biocompatibility, which make them very promising for nanomedicine. They have been used in photothermal therapy (PTT) and photodynamic therapy (PDT). Photothermal therapy is the process in which the illumination of a nanoparticle induces heat due to the rapid electron excitation-relaxation process within the particle. In the case of gold nanoparticles, light-induced excitation of the localized surface plasmon resonance (LSPR) generates heat around the particle, increasing the temperature of the surrounding tissue which can lead to cell death.[41] In the case of photodynamic therapy, gold nanoparticles are used as vectors and not as the active center. A photosensitizer is incorporated either as a conjugate at the surface or entrapped in the antifouling shell. Under illumination, the photosensitizer is excited and able to generate singlet oxygen that can oxidize biomacromolecules leading to cell death. In a recent study, Stuchinskaya et al. reported that zinc phthalocyanine (photosensitizer) combined with antibody-targeted gold nanoparticles showed increased phototoxicity compared to the non-targeted system that displayed minimal effect.[44] Mixed systems combining PTT and PDT, respectively provided by the gold nanoparticle and photosensitizer, are also developed. However, using spherical gold nanoparticles is not optimal as their surface plasmon resonance absorption band is located around 520 nm, which is not suitable for in vivo experiments. The invention of gold nanorods allowed us to circumvent that problem. Indeed, gold nanorods have the ability to be finely tuned and have their surface plasmon resonance absorption band changed with respect to their size. Therefore, nanorods absorbing in near-infrared (700–1200 nm) were successfully synthesized and combined with photosensitizers to induce dual cytotoxic effects as recently reported by Gong et al.[45] Indeed, indocyanine green

[43] M. Brust et al., Journal of the Chemical Society, Chemical Communications, 1994, https://doi.org/10.1039/C39940000801.
[44] T. Stuchinskaya et al., Photochemical & Photobiological Sciences, 2011, https://doi.org/10.1039/c1pp05014a.
[45] B. Gong et al., Journal of Nanobiotechnology, 2021, https://doi.org/10.1186/s12951-020-00754-8.

(λ_{abs} = 805 nm) could be conjugated to gold nanorods (LSPR = 790 nm) for an enhanced effect by PTT and PDT under illumination at 808 nm. Gold nanoparticles also exist as nanocage and nanoshell, making them extremely versatile for applications in sensing, radiotherapy and imaging.

2.1.2. Iron oxides nanoparticles

Iron oxides are another class of highly studied metal nanoparticles. They occur naturally and can be found under numerous compositions: magnetite (Fe_3O_4), hematite (α-Fe_2O_3), and maghemite (γ-Fe_2O_3 and β-Fe_2O_3). Iron oxide nanoparticles are biocompatible, have low toxicity, can be easily functionalized, and can be magnetic. Several iron oxide drugs were FDA-approved, such as Resovist® and Feridex I.V®, both used for the detection of liver tumors.[39] Iron oxide nanoparticles cannot be used as such and require a hydrophilic surface coating for biomedical applications. In the examples of Resovist and Feridex, carboxydextran and dextran are respectively used as hydrosoluble shells. In the medical field, iron oxides are mainly used in MRI as contrasting agents.[46] However, they also find their use in cancer treatment, as PTT or PDT agents, just like gold nanoparticles.[47,48] However, the particularity of iron as opposed to gold is that it can be magnetic, offering new properties. Magnetic iron oxide nanoparticles made of magnetite and maghemite are developed in cancer treatment (hematite is non-magnetic). Under a strong external alternative magnetic field (AMF), the magnetic particles can be directed to the tumor through the capillaries surrounding the tumor site, assisting passive targeting. This method of targeting is called magnetic targeting and was first studied using magnetic microspheres and nanocrystals with doxorubicin administered to rats.[49] Then, experiments in different tumor models were performed on rabbits and mice by different groups.[50,51,52] These studies showed that magnetic targeting helps in targeting the tumor tissue and thus allows lowering the amount of drug administrated. Magnetic iron oxide nanoparticles,

[46] H. Wu et al., Acta Biomaterialia, 2011, https://doi.org/10.1016/j.actbio.2011.05.031.
[47] M. Salimi et al., Nanomaterials, 2020, https://doi.org/10.3390/nano10112310.
[48] A. B. Seabra, Metal Nanoparticles in Pharma, 2017, https://doi.org/10.1007/978-3-319-63790-7_1.
[49] K. J. Widder et al., Experimental Biology and Medicine, 1978, https://doi.org/10.3181/00379727-158-40158.
[50] E. Huenges et al., Journal of Drug Targeting, 2003, https://doi.org/10.1080/1061186031000150791.
[51] C. Alexiou et al., Cancer Research, 2000, https://aacrjournals.org/cancerres/article/46/12_Part_1/6387/490212/A-New-Concept-for-Macromolecular-Therapeutics-in
[52] A. S. Lübbe et al., Cancer Research 56, 1996, https://aacrjournals.org/cancerres/article/56/20/4694/502651/Preclinical-Experiences-with-Magnetic-Drug?searchresult=1

as well as gold nanoparticles, can induce hyperthermia leading to cell death.[53] Hyperthermia is the process in which the nanoparticles generate heat under external stimulus which raises the local temperature. There are two types of hyperthermia: by light illumination, also called photothermal therapy, and by applying a low frequency alternating magnetic field, called magnetic hyperthermia. Instead of exciting electrons through the absorption of photons, the magnetic field changes the orientation of the magnetic moment of the nanoparticles. Then, different relaxation mechanisms lead to the release of heat from the nanoparticles (**Fig. 8**).[54] The increased temperature reaches between 40 to 46 °C, enough to induce tissue necrosis. This method is considered as noninvasive compared to conventional treatments.

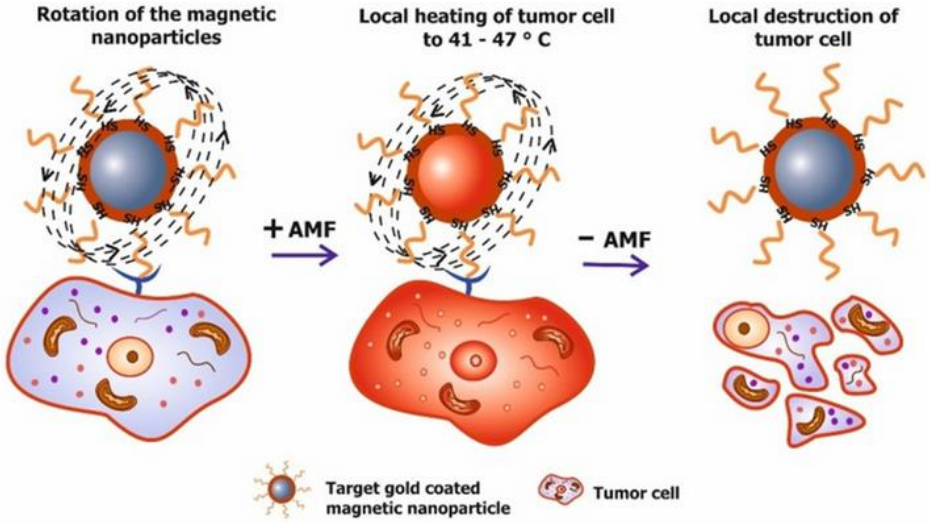

Fig. 8: Main steps of magnetic hyperthermia under AMF.

Gold and iron oxide nanoparticles are probably the most studied metal nanoparticles, from a historical point of view, but also from the current amount of approved drugs based on these two metals. In the meantime, another family of inorganic nanoparticles emerged, namely carbon nanoparticles with the discovery of fullerenes (1985), carbon nanotubes (1991) and graphene (2004).

[53] T. J. Gutiérrez and V. A. Alvarez, Handbook of Nanomaterials for Industrial Applications, 2018, https://doi.org/10.1016/B978-0-12-813351-4.00032-8.
[54] A. E. Deatsch and B. A. Evans, Journal of Magnetism and Magnetic Materials, 2014, https://doi.org/10.1016/j.jmmm.2013.11.006.

2.2. Carbon-based nanomaterials

Carbon is the only known atom capable of creating macrostructures, called allotropes, only by itself. The ability to link multiple identical atoms in a row is called catenation, and this property is the most predominant with carbon atoms. Thanks to this unique characteristic, infinite structures like graphite, a stacking of graphene sheets, exist. On the opposite, finite structures such as fullerene or carbon nanotubes are also stable and find their applications in several fields, including nanomedicine (**Fig. 9**). Carbon nanotubes and graphene are often miscalled nanoparticles, but in fact, they are nanomaterials, which is different due to the fact that at least one of their dimension is well above 100 nm. Their length largely bypasses the limit of the 100

Fig. 9: Different carbon nanomaterials: graphene (left), carbon nanotube (middle) and fullerene (right).

nm that would define a nanoparticle, however, one of their other dimension is below 100 nm, making them nanomaterials. While not strictly considered as nanoparticles, they are heavily studied and used in cancer treatment so their cases will be briefly discussed.

2.2.1. Fullerenes

Fullerene is described as a hollow, or cage, sphere made of sp^2 carbons where electrons are delocalized all around the surface of the sphere via the π-bonds. The most stable and abundant fullerene is C_{60}. Made of 60 carbon atoms, it is not soluble in water and therefore relies on surface functionalization for medical applications, just like metal particles. However, the effect of surface derivatization is much more impacting on the physicochemical properties of the C_{60}. Indeed, in fullerenes, the reactive sites are the π-bonds and the only way of introducing groups is to reduce the double bonds by addition reactions. The main consequence is changes in the

shape of the particle, which can impact the biological properties from one fullerene to another. Therefore, only a few groups are grafted onto the surface.[55] The high chemical stability, small size (ca. 0.5–1 nm),[56] cage shape, and high possibilities of functionalization make fullerenes interesting for drug delivery.[57] Fullerenes are also known to be potent antioxidants, able to scavenge free radicals.[58] The 30 π-bonds of C_{60} are electron deficient due to massive delocalization, making them reactive to electron-rich entities such as free radicals. Fullerenes can thus be used as antioxidants against free radicals for cancer treatment.

2.2.1. Carbon nanotubes

Carbon nanotubes are hollow cylinders made of sp2-hybridized carbon atoms, allowing the delocalization of electrons at their surface. They can also be seen as rolled-up sheets of graphene. Carbon nanotubes can be described by two dimensions: one corresponds to the diameter, and the other to the length. They are either single-walled or multi-walled. Their aspect ratio (l/d) is high, providing much greater specific surface area than fullerenes. This results in the possibility of conjugating multiple groups at the surface, such as hydrophilic, targeting, and reactive moieties, opening a wide range of possible chemical modifications.[59,60] Another important feature of carbon nanotubes is their long hollow shape, granting them high free volume for increased drug loading. Yang et al. developed a dual drug delivery system based on multi-walled nanotubes with cisplatin encapsulated inside while doxorubicin was loaded at the surface for a synergistic effect.[61] In other studies, Pt-based compounds were successfully conjugated on nanotubes. These compounds are known to interact with DNA by chelation as showed Dhar and coworkers.[62] Magnetic iron oxide nanoparticles were also loaded onto multi-walled carbon nanotubes on which was added doxorubicin. The assembly could be used as an imaging tool as well as therapeutic agent.[63] One strategy to treat cancer is to target

[55] L. L. Dugan et al., Proceedings of the National Academy of Sciences, 1997, https://doi.org/10.1073/pnas.94.17.9434.
[56] A. Goel et al., Carbon, 2004, https://doi.org/10.1016/j.carbon.2004.03.022.
[57] S. Yamago et al., Chemistry & Biology, 1995, 10.1016/1074-5521(95)90219-8.
[58] A. Dellinger et al., Nanomedicine, 2013, https://doi.org/10.2217/nnm.13.99.
[59] K. H. Son et al., International Journal of Nanomedicine, 2016, https://doi.org/10.2147/IJN.S112660.
[60] L. Tang et al., Journal of Nanobiotechnology, 2021, https://doi.org/10.1186/s12951-021-01174-y.
[61] T. Yang et al., Journal of Materials Science: Materials in Medicine, 2017, https://doi.org/10.1007/s10856-017-5920-9.
[62] S. Dhar et al., Journal of the American Chemical Society, 2008, https://doi.org/10.1021/ja803036e.
[63] H. Wu et al., Acta Biomaterialia, 2011, https://doi.org/10.1016/j.actbio.2011.05.031.

enzymes responsible for DNA replication. By inhibiting these proteins, cells replication is stopped leading to apoptosis. Topoisomerases I and II are well-known enzymes and their inhibition has been the subject of many studies aiming at slowing down cancer growth. Commonly used topoisomerase inhibitors are camptothecin and irinotecan. Tian et al. showed that encapsulation of camptothecin in multi-walled carbon nanotubes coated with Pluronic P123, a triblock copolymer, displayed enhanced tumoral activity compared to free camptothecin.[64] Carbon nanotubes, thanks to their high aspect ratio, can bear multiple functional groups at once, such as targeting ligands, anticancer drugs, antifouling shell, and other reactive moieties.

2.2.3. Graphene

Graphene is a single layer of sp^2-chained carbon atoms and the stacking of multiple graphene sheets is called graphite. Pure graphene has very limited applications in nanomedicine. Nearly all nanoparticle formulations make use of spherical shapes due to their higher stability, isotropic properties, and the possibility of drug encapsulation. However, graphene is very different due to its elongated planar shape that provides a strong π-stacking effect used to non-covalently load aromatic drugs such as doxorubicin onto the surface.[65] Another intrinsic property of graphene is its sharp shape making it easier to damage cells membrane.[66,67] Graphene derivatives were developed to provide more interesting properties, namely graphene oxides and graphene quantum dots. Graphene oxides are graphenes with high content of oxygen at the surface by introducing hydrophilic groups such as carboxylic acids, hydroxyls, and ethers. Introducing such groups increases the water solubility and the possibility of further functionalization. Gong et al. developed fluorinated graphene oxides with high NIR absorption for doxorubicin delivery on HeLa and A549 cells.[68] However, GOs tend to aggregate in high concentrations of salt and proteins such as in serum and culture cell medium[69,70] and their high toxicity in high dose limits their in vivo applications.[71] Graphene quantum dots were developed

[64] Z. Tian et al., Journal of Nanoscience and Nanotechnology, 2011, https://doi.org/10.1166/jnn.2011.3100.
[65] L. Zhang et al., Small, 2010, https://doi.org/10.1002/smll.200901680.
[66] S. Pandit et al., Advanced Materials Interfaces, 2018, https://doi.org/10.1002/admi.201701331.
[67] Y. Li et al., Proceedings of the National Academy of Sciences, 2013, https://doi.org/10.1073/pnas.1222276110.
[68] B. Gong et al., Journal of Nanobiotechnology, 2021, https://doi.org/10.1186/s12951-020-00754-8.
[69] Z. Liu et al., Journal of the American Chemical Society, 2008, https://doi.org/10.1021/ja803688x.
[70] E. Song et al., ACS Applied Materials & Interfaces, 2014, https://doi.org/10.1021/am502423r.
[71] K. Wang et al., Nanoscale Research Letters, 2010, https://doi.org/10.1007/s11671-010-9751-6.

mostly as an improvement over graphene oxides. They are much smaller and fall into the range of nanoparticles as they are pseudo-zero-dimension objects with a size usually lower than 10 nm and come under various shapes such as rectangle, square, triangle and ribbon.[72] They exhibit great biocompatibility, high photothermal conversion ability in NIR-I (700-1200)[73,74] making them promising photothermal agents.

2.3. Organic nanoparticles

2.3.1. Liposomes

Liposomes (or vesicles) are probably the most studied and developed organic nanoparticles as of today. They were discovered in the 1960s and are spherical supramolecular assemblies with sizes that can greatly vary from nanoliposomes (20-100 nm), to large liposomes (100-1000 nm) and giant liposomes (larger than 1000 nm). These are classified as unilamellar liposomes, however multilamellar and multivesicular liposomes also exist with sizes similar to giant liposomes. Vesicles (spherical bilayers) are formed after the self-assembly of lipid molecules in water. Liposomes are bilayered structures constituted of amphiphilic molecules containing a hydrophilic head and a hydrophobic tail (**Fig. 10**). A major class of natural amphiphiles is phospholipids. They bear two hydrophobic chains usually composed of 14 to 24 carbon atoms with one of the tails being unsaturated with one (oleic acid) or more double bonds (arachidonic acid).

[72] N. Mohanty et al., Nature Communications, 2012, https://doi.org/10.1038/ncomms1834.
[73] S. Li et al., ACS Applied Materials & Interfaces, 2017, https://doi.org/10.1021/acsami.7b07267.
[74] H. Liu et al., Biomaterials, 2020, https://doi.org/10.1016/j.biomaterials.2019.119700.

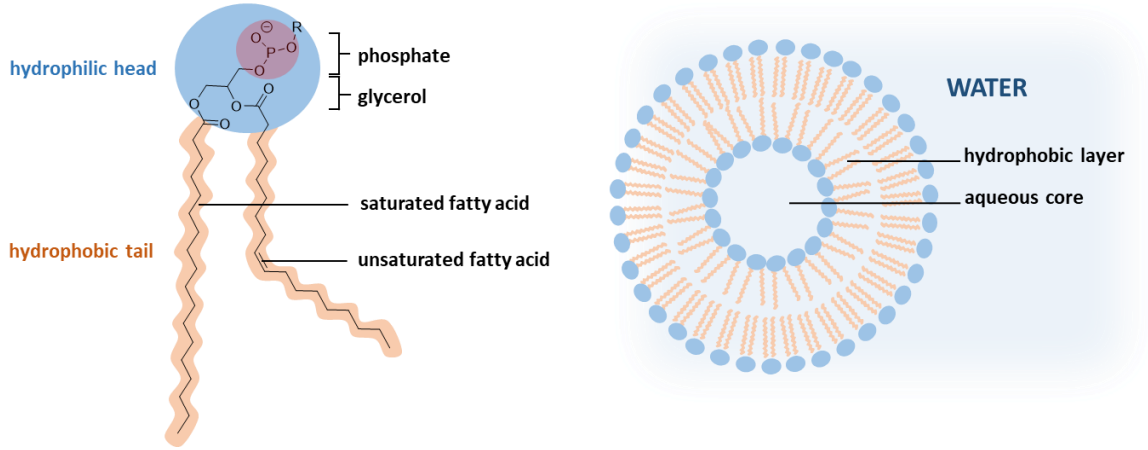

Fig. 10: General structures of a phospholipid (left) and liposomes (right).

These chemical characteristics give the phospholipids the small twist that is important for the molecules to pack against one another consistently. Most phospholipids are constituted of: **i)** the hydrophilic head containing a phosphate moiety, **ii)** a glycerol moiety as a linker and **iii)** the two fatty chains. The surface charge being a crucial parameter for the cellular uptake and clearance of nanoparticles, it can be easily tuned in case of liposomes by modifying the hydrophilic head group. It was shown that negatively charged liposomes had much lower clearance than their neutral or positively charged counterparts.[75] Indeed, negatively charged liposomes were taken up by macrophages of the reticuloendothelial system 2 and 4 times more than positively and neutrally charged liposomes.[76] In biology, phospholipids are particularly important as they are the main constituent of cell membranes. The most predominant phospholipids that occur in many mammalian cells, including human cells, are phosphatidylethanolamine, phosphatidylcholine, and phosphatidylserine. Hence, liposomes made of these phospholipids are typically used as mimics of cell membranes for the study of particle-cell interaction. Such liposomes are inherently biocompatible, biodegradable, and well-tolerated.

[75] R. L. Juliano and D. Stamp, Biochemical and Biophysical Research Communications, 1975, https://doi.org/10.1016/S0006-291X(75)80433-5.
[76] M. J. Hsu and R. L. Juliano, Biochimica et Biophysica Acta (BBA) - Molecular Cell Research, 1982, https://doi.org/10.1016/0167-4889(82)90120-3.

Liposomes are made of three regions: The first one is the hydrophilic part facing the aqueous media, the second is the hydrophobic bilayer, and the third and last one is the aqueous core. Bearing a hydrophobic layer allows the entrapment of hydrophobic drugs while the aqueous core can host hydrophilic molecules. Being able to encapsulate either hydrophobic or hydrophilic drugs makes liposomes very versatile and appealing nanoparticles. Indeed, Doxil® and many other liposome-based anticancer drugs have been FDA-approved since the early 2000s.[77] Typically, the formulation of Doxil® is a mixture of a PEG_{2000}-phosphatidylethanolamine (3.19 mg/mL), phosphatidylcholine (9.58 mg/mL), cholesterol (3.19 mg/mL) and doxorubicin (2 mg/mL). Other liposomal drug delivery systems for cancer treatment such as Myocet® (2000) and Onivyde™ (2015) are based on phosphatidylcholine and phosphatidylethanolamine by encapsulation of doxorubicin and irinotecan respectively.

2.3.2. Polymeric nanoparticles

Polymeric nanoparticles are made of polymers only. Polymers are composed of many repeating low-molecular-weight subunits. For instance, polystyrene can be obtained from the radical polymerization of styrene. Polymers, as opposed to small molecules, are characterized by a high molecular weight (from a few thousand to several hundreds of thousand) and extended molecular chains resulting in strong inter- and intramolecular interactions such as van der Waals and hydrogen bonds that would be weak within small molecules. In addition, polymer chains are intertwined and thus, create knot points that keep the polymer as one unit and form the polymer matrix. The latter can either be hydrophobic or hydrophilic (swellable) depending on the solvent and constitution of the polymer. Polymeric particles can create a core-shell structure that is either hydrophilic-hydrophobic (block copolymer) or hydrophilic-hydrophilic (single polymer or block copolymer). They can also be fully hydrophobic such as poly(ε-caprolactone). These properties specific to polymers are used to prepare spherical polymeric nanoparticles for drug delivery systems. Indeed, drugs can be adsorbed, dissolved, encapsulated, or entrapped within the polymer.

There are two main categories of polymeric nanoparticles, namely nanospheres and nanocapsules (**Fig. 11**). They differ in terms of structure arrangement according to the method

[77] U. Bulbake et al., Pharmaceutics, 2017, https://doi.org/10.3390/pharmaceutics9020012.

of formulation.[78] Nanospheres are solid spheres where the polymer matrix plays the role of shell and core at the same time. They are prepared by solvent evaporation or emulsification and drugs can either be entrapped inside the matrix (which protects them from the environment due to the high density of polymer chains) or be adsorbed at the surface. Nanocapsules are vesicle-like and are synthesized by nanoprecipitation. They contain a shell made of polymers with an inner core that can be oily or aqueous. The oily core can either constitute the medium for the encapsulation of an active drug[79] or be the active pharmaceutical molecule itself.[80] An aqueous core can host hydrosoluble compounds such as DNA,[81] enzymes[82] and water-soluble drugs.[83] In all cases, conjugation of active or targeting molecules can be performed at the surface of the nanocapsule to provide additional effects. Several polymers used for the nanoformulation of polymeric nanoparticles are FDA-approved. Common synthetic polymers are polyglycolide, poly(ε-caprolactone), polylactide, and poly(lactide-co-glycolide). Biopolymers, namely polysaccharides such as chitosan, dextran, pullulan or alginate, are also used due to their high biocompatibility and biodegradability, low toxicity, easy preparation, and nonimmunogenicity.[84] Polymeric nanoparticles are extremely efficient in drug delivery systems thanks to their high stability and ability to load drugs and many studies showed their capabilities as nanocarriers for cancer treatment.

[78] A. Zielińska et al., Molecules, 2020, https://doi.org/10.3390/molecules25163731.
[79] L. A. Frank et al., European Journal of Pharmaceutics and Biopharmaceutics 2019, https://doi.org/10.1016/j.ejpb.2019.01.001.
[80] K. Yang et al., Food Control, 2021, https://doi.org/10.1016/j.foodcont.2020.107783.
[81] E. Haladjova et al., Colloid and Polymer Science, 2017, https://doi.org/10.1007/s00396-017-4193-7.
[82] F. Ishizuka et al., Macromolecules, 2018, https://doi.org/10.1021/acs.macromol.7b02377.
[83] D. Cosco et al., European Journal of Pharmaceutics and Biopharmaceutics, 2015, https://doi.org/10.1016/j.ejpb.2014.11.012.
[84] M. Madej et al., Applied Sciences, 2022, https://doi.org/10.3390/app12199479.

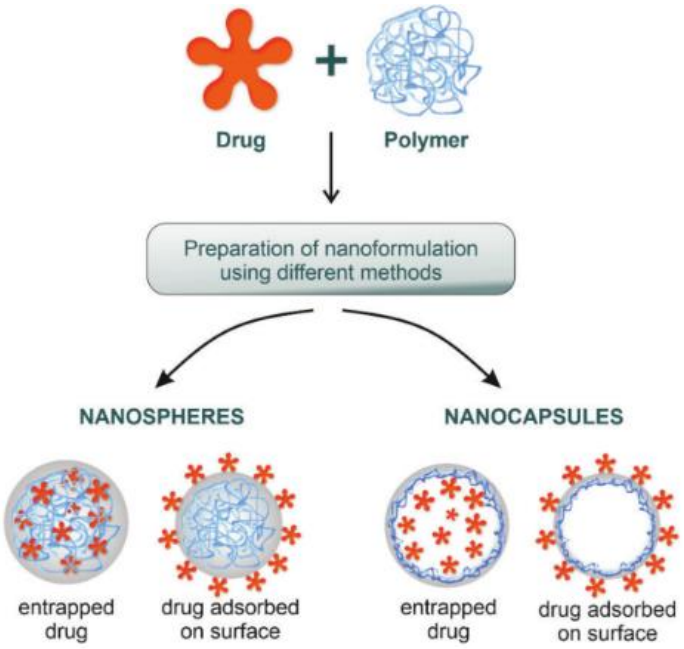

Fig. 11: Structures of nanospheres and nanocapsules with drug loading.[84]

2.3.3. Dendrimers

Dendrimers were discovered in 1978 by Fitz and Vogtle. They were named arborols, which means trees in Latin due to their hyperbranched three-dimensional structure. They are composed of a core made of a group of atoms, usually a small molecule, and branches that radiate from it called dendrons. Dendrimers are macromolecules composed of several subunits, or monomers, repeated throughout the structure. Each branching step is called the n^{th} generation (or generation n (noted Gn)), with the core being the 0^{th} generation (**Fig. 12**). The more dendrons, the more dense the packing of the growing chains is. As a consequence, dendrimers are unable to expand indefinitely and their growth usually comes to an end near the 10^{th} generation which limits their diameter to a maximum of 15–20 nm. This phenomenon, called 'de Gennes dense packing effect' arises from the steric hindrance within the molecules which reduces the reactivity of surface groups (amines in case of PAMAM).[85] Larger dendrimers are possible but result in lesser stability and more difficulties to control the growth.

To illustrate this effect, 2^{nd} generation polyamidoamine (PAMAM) dendrimers have 16 amino groups at the surface with a 3 nm diameter, while 6^{th} generation have 256 amino groups for 7

[85] B. Zhang et al., Nature Communications, 2013, https://doi.org/10.1038/ncomms2993.

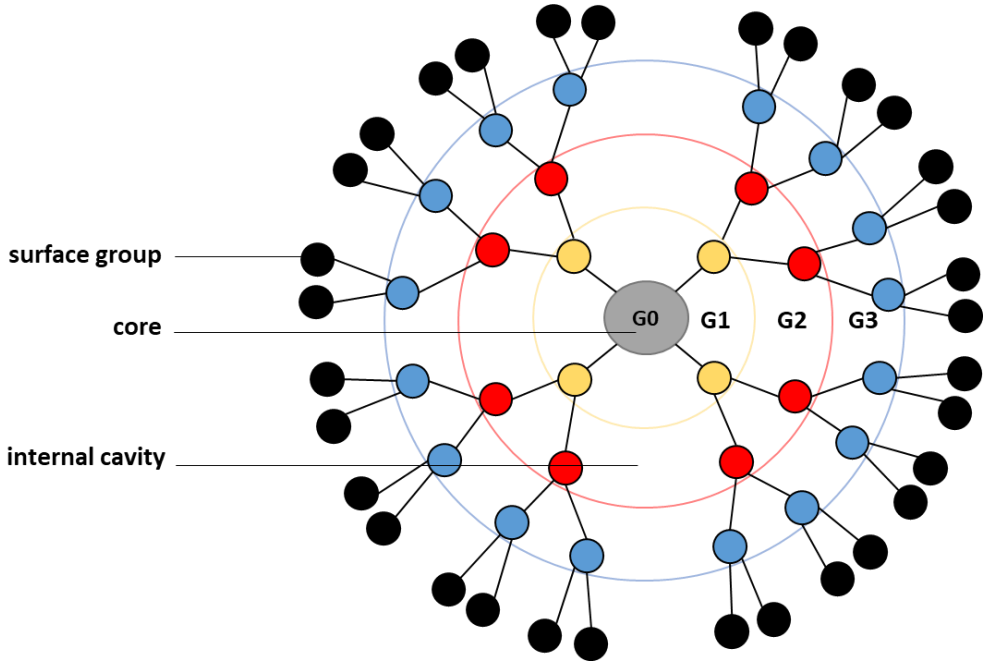

Fig. 12: General structure of dendrimers.

nm.[86] This is due to the fact that for each branching step, two new branching sites are introduced for the following step, thus doubling the amount of reactive groups. A 10th generation dendrimer has 4096 functional groups. This shows how dense the outer region becomes as the dendrimer gets larger. However, besides their limited size, dendrimers are prepared with extremely high control, giving almost monodisperse samples which is very difficult to attain with other spherical nanoparticles that are usually polydisperse.[87] Highly monodisperse dendrimers are attainable via convergent or divergent synthesis. The former is the growth from the core to the outside, while the latter is the opposite, limiting the number of generations. For instance, amino-terminated dendrimers can be prepared by sequential addition and aminolysis reactions between ethylenediamine and methyl acrylate. Amino and hydroxyl-terminated dendrimers are called complete dendrimers while those terminated with carboxylic acid group are named half-dendrimers. The many surface functional groups allow the introduction of multiple conjugates for imaging or therapy.[88] Furthermore, the empty volume between the dendrons is called an internal void, or cavity, and can easily entrap either

[86] D. A. Tomalia, Progress in Polymer Science, 2005, https://doi.org/10.1016/j.progpolymsci.2005.01.007.
[87] E. Abbasi et al., Nanoscale Research Letters, 2014, https://doi.org/10.1186/1556-276X-9-247.
[88] I. J. Majoros et al., Biomacromolecules, 2006, https://doi.org/10.1021/bm0506142.

hydrophobic or hydrophilic molecules depending on the dendrimer's chemistry.[89] This concept was introduced in 1982 by Maciejewski who suggested that hyperbranched structures should be able to act as molecular hosts. For example, hydrophilic PAMAM dendrimers proved to be able to increase the solubility of hydrophilic molecules. Dendrimers with hydrophilic surfaces but hydrophobic cavities are also developed and used as drug carriers for lipophilic molecules such as paclitaxel. Salimi et al. developed iron oxides nanoparticles coated with 4th generation PAMAM dendrimers and successfully induced breast cancer magnetic hyperthermia.[47] Majoros and coworkers built a multiconjugated 5th generation PAMAM dendrimer on which they successively introduced fluorescein isothiocyanate (FITC) for imaging, folic acid (FA) for targeting of cancer cells and paclitaxel as anticancer drug.[88] This multifunctional dendrimer displayed increased internalization and therapeutic effect. Dendrimers fill many requirements as nanoparticles to be used in cancer treatment, namely their high drug loading via the internal void space, the high amount of functional groups at the surface and their adapted size, shape and stability to be used as nanovectors.

2.3.4. Micelles

Micelles are probably the simplest form of organic nanoparticles. Micelles result from the self-assembly of amphiphiles into a spherical monolayer, as opposed to liposomes, in which amphiphiles are assembled to form a vesicular bilayer (**Fig. 13**). Amphiphiles can be of different natures, namely polymeric and non-polymeric and their polar region can be either charged or neutral. The nature of the amphiphiles has a huge impact on the nanoparticles regarding their stability and behavior toward the environment. Non-polymeric micelles are small (d around 10–15 nm) and poorly stable due to their high CMC and non-glassy core. Polymeric micelles are usually bigger (d can reach several hundreds of nm) and composed of amphiphiles based on at least two polymers, one hydrophilic, and one hydrophobic. These types of polymers are called block copolymers and can be diblock (A-B), triblock (A-B-C or A-B-A), quadrablock, pentablock and so on. In nanomedicine, the most commonly used copolymers are diblock and triblock copolymers.[90] The hydrophilic block is usually made of poly(ethylene oxide) (PEO), poly(*N*-vinyl-2-pyrrolidone) (PVP), poly(2-oxazoline)s or polysaccharides. The hydrophobic

[89] M. Ina, Journal of Drug Delivery and Therapeutics, 2011, https://doi.org/10.22270/jddt.v1i2.46.
[90] A. Bose et al., IET Nanobiotechnology, 2021, https://doi.org/10.1049/nbt2.12018.

part is most of the time composed of polyesters such as poly(lactic acid) (PLA) or poly(ε-caprolactone) (PCL) which are FDA-approved for human biological applications.[91] Saturated fatty chains can also be used as substitutes.

Small micelles are great nanoparticles for passive targeting. In aqueous media, the polar head faces the solvent while the hydrophobic part faces toward the interior of the micelles. These are called regular micelles. In apolar organic solvent such as toluene, the hydrophobic chains face the solvent while the hydrophilic head constitutes the inner core. These are called reverse micelles. For biological applications such as cancer treatment, regular micelles are much more studied because of their solubility in water. However, a few studies developing modified-reverse micelles for drug delivery exist and will be discussed later. Normal micelles, similar to other nanoparticles, can be functionalized on the surface and encapsulate hydrophobic molecules for drug delivery in tumor tissues by either active or passive targeting.

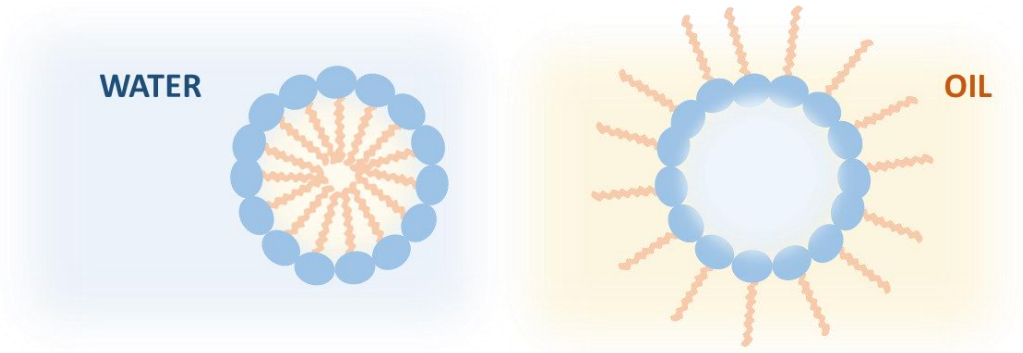

Fig. 13: Structure of regular micelle (left) and reverse micelle (right).

3. Micelles

3.1. Micellization

3.1.1. Dynamics of micelles

Micellization is the process by which amphiphilic molecules start to aggregate to form micelles. This phenomenon of aggregation is driven by a highly favourable entropic factor (**Fig. 14**).

[91] G. Gaucher et al., Journal of Controlled Release, 2005, https://doi.org/10.1016/j.jconrel.2005.09.034.

Entropy (S) can be defined as the state of disorder and is closely related to enthalpy (H) and Gibbs free energy (G). The change in Gibbs free energy for a given system (ΔG_{system}) determines if the reaction or process is spontaneous ($\Delta G_{system} < 0$) or nonspontaneous ($\Delta G_{system} > 0$) and is defined as follows:

$$\Delta G_{system} = \Delta H_{system} - T\Delta S_{system} \quad \textbf{(Eq. 1)}$$

with ΔH_{system} and ΔS_{system} referring respectively to the change of enthalpy and entropy of the system. Nonspontaneous processes require external energy to occur, as opposed to spontaneous processes that occur naturally. ΔS_{system} is equal to the sum of the change of entropy of water molecules (ΔS_{water}) and the change of entropy of the surfactant ($\Delta S_{surfactant}$).[92] In the liquid phase, water molecules are randomly interacting with each other by hydrogen bonds. Upon introduction of a surfactant molecule, the water molecules are forced to assume a certain orientation around the hydrophobic tail, decreasing ΔS_{water} due to a more ordered structure (ice-like) of the water molecules than in bulk water. Alternatively, $\Delta S_{surfactant}$ increases due to the loss of hydrophobic interactions between surfactant molecules. The overall interaction of water with the hydrophobic chain is unfavorable in contrast with the solvation of the hydrophilic head. As a consequence, the hydrophobic tail is expelled from the aqueous phase, leading to the hydrophilic head in water, and the hydrophobic chain directed at the water-air interface. This phenomenon is spontaneous as hydrophobic-water interactions disappear and only the favorable interaction with the hydrophilic head remains. As more surfactant molecules are added, more are pushed toward the surface. However, at one point, the surface becomes saturated and the excess of amphiphiles remains in water, solvated by the water molecules. To stabilize the system, the spontaneous process consists of expelling not the

[92] G. Liu et al., Physical Chemistry Chemical Physics, 2016, https://doi.org/10.1039/C6CP01042C.

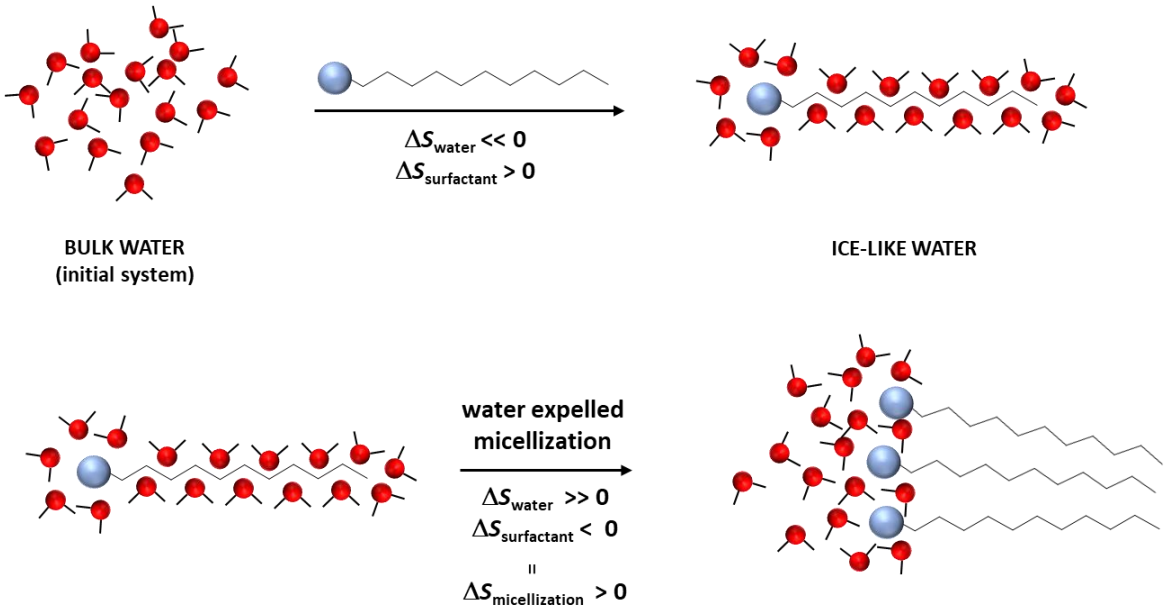

Fig. 14: Evolution of entropy change of water and surfactant during micellization.

surfactant but the water molecules from the hydrophobic tails by association of multiple hydrophobic chains from different surfactant molecules. Amphiphiles aggregate by combining their hydrophobic regions in a central core shielded by the associated polar head groups. This results in favorable interactions between the water molecules and hydrophilic parts, while hydrophobic chains are separated in a different compartment. Consequently, the expulsion of well-ordered water molecules around the hydrophobic tail back to the bulk solution increases ΔS_{water} while $\Delta S_{surfactant}$ decreases due to hydrophobic interactions creating micelles that are more ordered than free unimers. The contribution of ΔS_{water} being more important than $\Delta S_{surfactant}$, the change of entropy of the system ΔS_{system} increases. According to the equation of ΔG_{system}, for the micellization to be spontaneous with ΔS_{system} positive, ΔH_{system} has to be either negative, in which case the reaction is always spontaneous or be positive with an absolute value lower than ΔS_{system}. Reported values of both ΔH_{system} and ΔS_{system} of several nonionic, anionic and cationic surfactants show that the absolute values of ΔS_{system} are much higher than those of ΔH_{system}.[93] Therefore, the process of micellization is spontaneous. The same process happens in apolar organic solvents such as toluene, except that the unfavorable interaction is the hydrophilic-toluene interaction, giving rise to reverse micelles.

[93] C. Jolicoeur and P. R. Philip, Canadian Journal of Chemistry, 1974, https://doi.org/10.1139/v74-262.

Micelles are dynamic objects, meaning that their structure is subject to change in the medium. Indeed, they are in a constant dynamic equilibrium with their unimer state.[94] Environmental conditions such as temperature, ionic strength and pH also influence their dynamics. A general misconception of micelles is to assume that their core is entirely hydrophobic or hydrophilic, deprived of solvent molecules. However, it is known that micelles' cores contain a certain percentage of solvent molecules depending on the chemical composition. In the case of regular micelles, this phenomenon is called hydrophobic hydration. The more hydrophobic the core is, the lesser the hydration is.[95] However, hydrophobic hydration is difficult to assess experimentally, and computational studies are usually necessary.

3.1.2. Reverse micelles: water in the oil system

Reverse micelles are water droplets dispersed in an organic solvent from surfactant molecules. The lipophilic part is in direct contact with the solvent while the polar part makes the inner core. The hydrophilic core of the micelle allows the encapsulation of hydrosoluble molecules such as fluorescein salts, proteins, and active drugs like doxorubicin. Reverse micelles are thermodynamically stable and are specially used in biomimetism, namely the interactions and behaviours of biological components, such as proteins, in a more realistic environment.[96] Studies on structure-function relationships in bulk aqueous solutions are different from those in a micro- or nanoscale level which are much more confined and crowded. Moreover, it was shown that the pH, viscosity, and polarity differ.[96] The aqueous core, more commonly named water pool varies depending on the surfactant concentration and nature of polar head during nanoformulation. The size of reverse micelles is proportional to the molar ratio of water to surfactant, also known as w_o.[96,97] This parameter increases as the micelles get larger, and influences the degree of solvation and encapsulation efficiency of drugs. As an example, it was shown for dioctyl sodium sulfosuccinate (AOT) reverse micelles that at low w_o (< 4), the water molecules are strongly bound to surfactant polar heads. However, when w_o value is higher than 10, unbound water molecules start to be available. Therefore, small micelles (low w_o) may not

[94] H. Hoffman, Berichte Der Bunsengesellschaft Für Physikalische Chemie, 1978, https://doi.org/10.1002/bbpc.19780820962.
[95] U. R. Dahal et al., The Journal of Chemical Physics, 2019, https://doi.org/10.1063/1.5089251.
[96] E. P Melo et al., Biotechnology Annual Review, 2001, https://doi.org/10.1016/S1387-2656(01)07034-X.
[97] W. D. Van Horn et al., Journal of the American Chemical Society, 2009, https://doi.org/10.1021/ja901871n.

encapsulate as efficiently as larger micelles (high w_o) as the number of free water molecules is crucial for better solvation and thus, better encapsulation efficiency of hydrosoluble molecules.

A major application of reverse micelles is their use as nanoreactors for catalytic reactions. The reactions are performed in the water pool, greatly increasing the kinetic of the reaction due to the restricted volume of the reaction.[98] Another example is the inverse emulsion polymerization reaction, allowing the polymerization of hydrophilic monomers to occur inside the micelles, providing great control over the dispersity of the final polymer due to the limited volume.[99] In general, reverse micelles are used as nanoreservoirs in a hydrophobic environment. However, in biological applications, their utilization is very limited due to them being hydrophobic, making them much less appealing than their water-soluble counterparts. Nonetheless, reverse micelles are not completely excluded from the field of nanomedicine and a few studies have shown promising results regarding their utilization in drug delivery and possible applications in cancer treatment.

As mentioned earlier, the main drawback is their water solubility. To circumvent this issue while preserving the properties of reverse micelles intact, the main idea is to associate them to another water-soluble supramolecular assembly. This leads to multiple levels of structuration and more complex systems than just the micelle itself. In 2007, Qiu et al., synthesized reverse micelles based on the self-assembly of amphiphilic polyphosphazenes for the encapsulation of fluorescein sodium and trypan blue, two water-soluble dyes. After successful encapsulation, they showed that the dye-loaded reverse micelles could be entrapped into poly(lactic-co-glycolic acid) (PLGA) microspheres. Confocal imaging confirmed the dye's location in microdomains inside the PLGA microparticles attributed to the reverse micelles.[100] A few years later, Vrignaud et al. developed an innovative system in a two steps preparation. Firstly, doxorubicin was encapsulated into Span 80® reverse micelles. Then, small nanolipids of Solutol HS15® were prepared by nanoemulsion which were then mixed with the Span 80® micelles. By using the phase inversion temperature method, they managed to obtain stable spherical 90 nm nanoparticles. Docetaxel was then encapsulated inside the hydrophobic core of the Solutol HS15® micelles, resulting in the double encapsulation of the hydrophilic doxorubicin and

[98] K. Bhargavi et al., Bulletin of Chemical Reaction Engineering & Catalysis, 2022, https://doi.org/10.9767/bcrec.17.1.12732.157-162.
[99] L. García-Uriostegui et al., Polymer Engineering & Science, 2017, https://doi.org/10.1002/pen.24499.
[100] L. Qiu et al., Nanotechnology 2007, https://doi.org/10.1088/0957-4484/18/47/475602.

hydrophobic docetaxel drugs.[101] More recently, Yao and coworkers associated the hydrophobic tails of crosslinked reverse micelles with the lipophilic cavity of (2-hydroxypropyl)-β-cyclodextrin.[102] Rhodamine B could be encapsulated in the water pool while carmofur, a hydrophobic anticancer drug, was entrapped in the alkyl hydrophobic region, giving spherical nanoparticles of 15 nm. In vitro results showed very promising results regarding their internalization via confocal imaging provided by rhodamine B, and their cytotoxicity induced by the release of carmofur against A549 cells.

The use of reverse micelles in nanomedicine is not as direct as other nanoparticles. Indeed, their insolubility in water requires the use of different and larger water-soluble supramolecular assemblies to stabilize the reverse micelles in a stable environment. The common procedure as of now usually follows a three-step formulation. The first step consists of preparing the reverse micelles system with the encapsulation of hydrophilic drugs. Then, the second step is to make the water-soluble supramolecular assembly containing a hydrophobic core to accommodate the reverse micelles. The last step is the assembly of both objects by incorporating the reverse micelles into the hydrophobic core of the host structure. These assemblies can be likened to liposomes, wherein they possess a hydrophilic shell (resembling the host's shell), an inner hydrophobic layer (resembling the host's core), and ultimately, a hydrophilic core (resembling the core of a reverse micelle). These supramolecular structures are complex and require great control over each step, from the preparation of the micelles to the final object. In vivo tests are yet to be done to assess the efficacy and stability of these nanoformulations in biological conditions. Studies and development of reverse micelles for cancer treatment are still very limited. Nonetheless, the presented results are very promising and may lead to alternative approaches to cancer treatment in the future.

3.1.3. Regular micelles: oil in water system

Regular micelles are obtained by dispersing surfactant molecules into an aqueous phase. They are composed of an outer hydrophilic shell and an inner hydrophobic core used to entrap lipophilic drugs. As opposed to reverse micelles, regular micelles are widely studied as they are

[101] S. Vrignaud et al., European Journal of Pharmaceutics and Biopharmaceutics, 2011, https://doi.org/10.1016/j.ejpb.2011.02.015.
[102] Y. Yao et al., Langmuir, 2019, https://doi.org/10.1021/acs.langmuir.9b00607.

easy to produce, cheap to formulate and do not require extensive methods in order to be used in biological applications. The system is prepared in water and no phase transfer is necessary. All these reasons make regular micelles much easier to prepare and manipulate, making them highly appealing for research. Their main feature is their ability to host hydrophobic drugs in their core. Indeed, many commonly used antineoplastic drugs are hydrophobic due to their chemical structure generally composed of aromatic rings such as camptothecin, paclitaxel or docetaxel. Furthermore, it was shown that micelles drastically increase the water solubility of hydrophobic molecules from 10 to 500 fold[103], making micelles excellent drug carriers. The hydrophilic shell is usually made of poly(ethylene oxide) or poly(*N*-vinyl-2-pyrrolidone) due to their bulkiness and high hydrophilicity, providing great solubility and stealth properties. The hydrophobic chains are commonly made of polyesters, polyethers and saturated or unsaturated lipids such as stearic acid and oleic acid, respectively. For instance, chitosan could be functionalized with stearic acid, providing amphiphilic properties for the preparation of spherical micelles.[104] These types of micelles have very low critical micellar concentration, making them stable even under a high dilution factor, resulting in good supramolecular stability in the bloodstream for enhanced circulation time. Besides the encapsulation of hydrophobic molecules, regular micelles can also host hydrophobic nanoparticles such as metal nanoparticles. Indeed, instead of functionalizing the metal nanoparticles' surface using PEO for instance, these can be encapsulated inside the micelles' core. The advantage of associating different objects is to benefit from the properties of both nanoparticles and obtain a multifunctional object. Typically, gold nanoparticles and active drugs can be encapsulated inside micelles to provide imaging and anticancer activity properties to the system while conserving the characteristics of micelles.[105] These systems are called hybrid micelles and allow to obtain multipurpose nanoobjects for improved theranostic approaches.

According to the micelle structure, cargo release can be triggered under specific conditions depending on the environment. Internal factors such as pH[106], oxidants[107] or enzymes[108] as well

[103] O. Soga et al., Journal of Controlled Release, 2005, https://doi.org/10.1016/j.jconrel.2004.12.009.
[104] H. Yuan et al., Molecular Pharmaceutics, 2011, https://doi.org/10.1021/mp100289v.
[105] W. Lin et al., Acta Biomaterialia, 2017, https://doi.org/10.1016/j.actbio.2017.06.003.
[106] C. Y. Zhang et al., Biomaterials, 2012, https://doi.org/10.1016/j.biomaterials.2012.05.025.
[107] C. Sun et al., International Journal of Biological Macromolecules, 2018, https://doi.org/10.1016/j.ijbiomac.2018.01.136.
[108] D. Wan et al., Nano Research, 2023, https://doi.org/10.1007/s12274-022-4967-1.

as external parameters such as ultrasound[109], illumination[110] or heating[111] can cause the release of the cargo. Typically, acid-labile moieties such as hydrazones, acetals or orthoesters are used to conjugate active molecules. In acidic medium, hydrolytic cleavage occurs and the drug is released. For instance, Bae et al. prepared PEGylated micelles in which doxorubicin was conjugated to the hydrophobic chain using a hydrazone link.[112] Chen and coworkers also prepared PEGylated micelles but this time by taking advantage of the acid-labile property of carbonate, resulting in the efficient release of 63% of the encapsulated doxorubicin.[113] Nanosystems based on acidic conditions are especially convenient due to the fact that tumor tissues are slightly more acidic than healthy tissues. Moreover, if combined with active targeting ligands such as folic acid, micelles can be internalized more efficiently into tumor cells by recognizing he overexpressed folate receptors FOLR1 and FOLR2.[114] Furthermore, lysosomes and endosomes are known to have pH between 4.5 and 6.5[115], making pH-sensitive systems even more efficient after internalization into target cells.

Besides pH-sensitive micelles, thermoresponsive micelles are also widely studied. These systems are typically based on polymers and their cloud point temperature in aqueous millieu. The concept of thermosensitive micelles can be classified into two categories. The first one describes micelles made of block copolymers, usually a diblock A-B where A is hydrophilic and B hydrophobic. These micelles are based on the lower critical solution temperature (LCST) of the hydrophilic block, which corresponds to the minimum temperature in the concentration-dependant cloud point temperature curve (**Fig. 15**).

[109] X. Liu et al., International Journal of Pharmaceutics, 2021, https://doi.org/10.1016/j.ijpharm.2021.121052.
[110] Y. Zhao, The Chemical Record, 2007, https://doi.org/10.1002/tcr.20127.
[111] F. Kohori et al., Colloids and Surfaces B: Biointerfaces, 1999, https://doi.org/10.1016/S0927-7765(99)00070-3.
[112] Y. Bae et al., Bioconjugate Chemistry, 2005, https://doi.org/10.1021/bc0498166.
[113] W. Chen et al., Journal of Controlled Release, 2013, https://doi.org/10.1016/j.jconrel.2013.01.001.
[114] L. E. Kelemen, International Journal of Cancer, 2006, https://doi.org/10.1002/ijc.21712.
[115] Y. -B. Hu et al., Translational Neurodegeneration, 2015, https://doi.org/10.1186/s40035-015-0041-1.

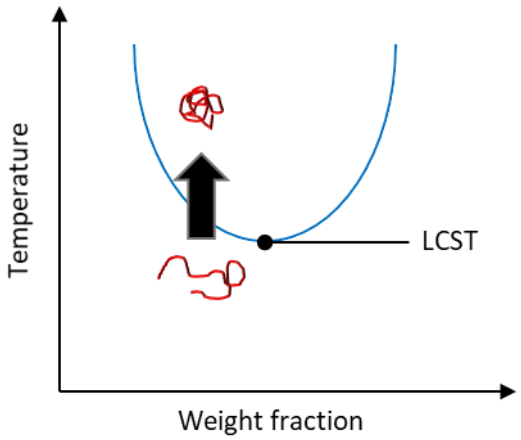

Fig. 15: Cloud point temperature curve showing the solvation and desolvation of polymer chains at temperature below and above the lowest critical solution temperature (LCST).

Above the LCST, the polymers constituting the micelles become insoluble in water, leading to the release of the cargo. Such thermosensitive micelles are mostly made of poly(*N*-isopropylacrylamide) (PNIPAAm)) which has a LCST of 32 °C. However, due to the LCST lower than body temperature, copolymers are utilized in combination with hydrophilic monomers such as acrylamide (AAm), *N*,*N*-dimethylacrylamide (DMAAm) or hydroxymethylacrylamide (HMAAm). In 1999, Kohori et al. showed that poly(NIPAAm-co-DMAAm)-*b*-PLGA micelles could release adriamycin above the LCST (40 °C) at 42.5 °C, drastically enhancing the cytotoxic effect against bovine aorta cells compared to the same experiment at 37 °C.[111] In 2007, Liu et al. developed similar micelles made of poly(NIPAAm-co-AAm)-*b*-PDLLA block copolymers. Free docetaxel could be released above the LCST (41 °C) at 43 °C while having minimum cytotoxicity at 37 °C in Kunming mice.[116] Even though thermosensitive micelles are promising, the main issue is that the LCST is a variable parameter based on polymer-polymer and polymer-solvent hydrogen bond interactions. Hydrogen bonds are highly impacted by the molecular weight and length of the polymer chains and their concentration.

The second class of thermoresponsive micelles describes hydrophilic block copolymers. A great example are Pluronic triblock copolymers (PEO_x-PPO_y-PEO_x). Their high amount of oxygen atoms allows multiple hydrogen bonds with water molecules, making them hydrosoluble.

[116] B. Liu et al., European Journal of Pharmaceutics and Biopharmaceutics, 2008, https://doi.org/10.1016/j.ejpb.2008.01.015.

However, as the temperature rises, the polymer-polymer interactions become more predominant and results in aggregation to micelles due to a lesser solubility in water. This phenomenon occurs at temperatures above the cloud point.[117,118]

To improve the therapeutic effects, external stimuli can be used, such as ultrasound or light illumination. Ultrasound is based on frequencies higher than 20 kHz to generate hyperthermia and cavitating bubbles. Ultrasound is interesting due to its high tissue penetration and localized waves. Extensive research has demonstrated the effectiveness of ultrasound in enhancing tissue permeability. Pulsed ultrasound has been shown to significantly increase the permeability of blood vessels, leading to improved accumulation in the targeted area. The reason is that microbubbles, naturally present in the blood stream, collapse under the fast compression and expansion caused by the ultrasounds, leading to the high shear stress of the fluid that can damage cell membranes. As a consequence, affected cell membranes present higher permeability and allow the passive diffusion of nanoparticles. Pluronic P105 is the most common copolymer used in combination with ultrasound. Pluronic P105 is a triblock copolymer made poly(ethylene oxide) and poly(propylene oxide) of formula PEO_{37}-PPO_{56}-PEO_{37} that assembles into micelles of 5 to 20 nm diameter, ideal for passive targeting. The first example using micelles combined with ultrasound was performed by Munshi et al. in 1997.[119] In vitro experiments on HL-60 cells showed that Pluronic P105 micelles loaded with doxorubicin displayed an IC_{50} of 1.25 µg/mL against 0.19 µg/mL using ultrasounds, depicting a clear effect of the ultrasounds on the therapeutic effect. Marin and coworkers reported a similar study a few years later and showed the increased accumulation of Pluronic micelles into cell nuclei by fluorescent microscopy.[120] Nelson et al. showed that encapsulated doxorubicin in stabilized Pluronic micelles induced a significant decrease in size in subcutaneous tumors of BDIX rats compared to the control group.[121] The use of ultrasound for cancer therapy is very promising due to its non-invasive nature, to its easiness to application and control for targeted treatment.

Light-responsive micelles are designed to release their cargo, as a result of their degradation, upon illumination. Ultraviolet (UV) and near-infrared (NIR) are commonly used for biological

[117] N. Pandit et al., Journal of Colloid and Interface Science, 2000, https://doi.org/10.1006/jcis.1999.6628.
[118] P. Linse, Journal of Physical Chemistry, 1993, https://doi.org/10.1021/j100153a072.
[119] N. Munshi et al., Cancer Letters, 1997, https://doi.org/10.1016/S0304-3835(97)00218-8.
[120] A. Marin et al., Journal of Controlled Release, 2001, https://doi.org/10.1016/S0168-3659(01)00363-7.
[121] J. L. Nelson et al., Journal of Controlled Release, 2001, https://doi.org/10.1016/S0168-3659(01)00363-7.

applications. However, UV light suffers from poor tissue penetration associated to its high energy (potentially responsible for side effects) and therefore is used for topical treatments only. To reach deeper tissues while being harmless, NIR light is preferred. Indeed, water and lipids are almost transparent (little to no absorption) in the 700–900 nm region, which makes NIR perfectly adapted for biological applications. However, the use of light-sensitive micelles is only reported in a few studies. Light-sensitive micelles sometimes rely on the switch of the hydrophobic part under illumination to become hydrophilic and create an unbalance between the hydrophilicity and hydrophobicity, leading to the disassembly of the micelles to release the cargo. Jiang et al. prepared PEO-*b*-PNBMA micelles that are photodegraded due to the photolysis of the 2-nitrosobenzyl chromophore.[122] Zhang and coworkers developed PEGylated upconversion micelles that can be photodegraded in 30 min to release 84% of the encapsulated doxorubicin.[123]

Regular micelles have a wide range of applications due to their high versatility and robustness. Their tunable surface offers various possibilities of conjugation, their chemical structure can be modified in order to respond to specific conditions, their small size is ideal for passive targeting and their hydrophobic core allows the encapsulation of active molecules for drug delivery. While being among the easiest and fastest nanoparticles to produce, regular micelles contain a certain number of crucial parameters to take into account during their formulation and application in biology.

3.2. Characteristics of micelles

3.2.1. Critical micellar concentration

The critical micellar concentration (CMC) is defined as the concentration at which the surfactant molecules start to self-assemble to form micelles. Below the CMC, surfactant molecules are located at the water-air interface, where the hydrophobic part points away from the aqueous phase. At a certain concentration, the surface is saturated with surfactant molecules, clusters start to appear and micelles are formed. This exact concentration is the CMC. This is an important consideration especially for drug delivery. Indeed, upon injection in vivo, the

[122] J. Jiang et al., Macromolecules, 2006, https://doi.org/10.1021/ma060142z.
[123] Y. Zhang et al., Journal of Controlled Release, 2021, https://doi.org/10.1016/j.jconrel.2021.06.028.

supramolecular assemblies are quickly diluted in the bloodstream, leading to micelle disassembly into monomeric units and causing the premature release of the cargo.[124] Therefore, developing micelles that have the lowest possible CMC is essential in order to increase their supramolecular stability. As stated earlier, micellization is a process driven by the interactions between water molecules and both hydrophilic and hydrophobic chains. The more water-soluble the surfactant molecules are, the less they tend to aggregate to form micelles. Solubility in aqueous medium can be increased either by reducing the length of the hydrophobic chain or by increasing the length of the hydrophilic part. For example, nonionic alkyl poly(ethylene oxide) surfactants (noted C_nPEO_m with n the number of carbon atoms in the alkyl chain and m the number of oxyethylene units), $C_{10}PEO_5$ and $C_{10}PEO_8$, have CMC values of 900 µM and 1000 µM at 25 °C, respectively, showing the effect of the length of the hydrophilic chain. $C_{12}PEO_5$ has a CMC value of 65 µM as opposed to the 900 µM from $C_{10}PEO_5$ where the carbon chain is only two carbon atoms shorter. The CMC is drastically affected by the length of the hydrophobic chain while the change in hydrophilic chain has less impact. These experimental values are in accordance with the thermodynamic process of micellization that is driven by the hydrophobic effect. In case of ionic surfactants, the trend is the same regarding the hydrophobic chain for a given ionic chain. Sodium dodecyl sulfate and sodium octyl sulfate have CMC values of 8.3 mM and 133 mM respectively.[125] However, the CMC trend in ionic surfactants is more difficult to predict due the influence of the counter ions and the type of ionic polar head, whether it is cationic or anionic. Ammonium and sulfonate polar heads, or chloride and bromide counter ions have their own influence on the CMC value. Nonetheless, it's worth noting that in general, ionic surfactants have much higher CMC than their nonionic counterparts due to their higher water solubility.

Multiple methods were developed in order to determine the CMC value of a surfactant.[126,127] All methods are based on the switch of properties from monomer units to micelles nanoparticles. A first approach is by tensiometry which consists of measuring the surface tension of the aqueous solution at different concentrations of surfactant. Below the CMC, the

[124] Y. Lu et al., Nature Biomedical Engineering, 2018, https://doi.org/10.1038/s41551-018-0234-x.
[125] K. Holmberg, Ullmann's Encyclopedia of Industrial Chemistry, 2019, https://doi.org/10.1002/14356007.a25_747.pub2.
[126] Ö. Topel et al., Journal of Molecular Liquids, 2013, https://doi.org/10.1016/j.molliq.2012.10.013.
[127] D. R. Perinelli et al., Langmuir, 2020, https://doi.org/10.1021/acs.langmuir.0c00420.

water-air interface is not saturated and surface tension decreases as the surfactant concentration increases. When the concentration of surfactant is equal or above the CMC, surface tension remains stable due to the saturated surface. A simple plot allows the determination of the CMC value. Another method commonly used is static (SLS) or dynamic light scattering (DLS). In a similar manner to tensiometry, light scattering involves measuring the light scattering properties of surfactant solutions at various concentrations. Below the CMC, minimal light scattering occurs, indicating the absence of colloidal structures such as micelles, and only individual molecules of small size are observed. As micelles form above the CMC, it is leading to a significant increase in light scattering intensity. The signal becomes more intense with higher concentrations of surfactants, indicating a higher concentration of micelles. Additionally, DLS can detect larger objects, such as micelles, when the surfactant concentration exceeds the CMC. A third approach is based on the encapsulation of pyrene, a hydrophobic fluorescent probe. The latter has specific emission peaks that display more or less intensities depending on the polarity of the environment. Pyrene has five peaks, among which the first (I_1) and third (I_3) are highly dependent on their environment. In polar medium, I_1 increases while in apolar medium I_3 is dominant. Below the CMC, pyrene is not encapsulated, however, above the CMC, pyrene starts to get encapsulated in the hydrophobic core of the micelles. By plotting the I_1/I_3 ratio against the concentration of surfactant, one can determine the CMC.

Micelles are thermodynamic nanoparticles, meaning that they are temperature-dependent. Indeed, for a given surfactant, cooling down or heating up the solution can drastically change the surfactant's behaviour.

3.2.2. Temperature effect on surfactant solubility

Temperature affects surfactant solubility and can thus affect CMC value and micelle formation. In general, nonionic surfactants become less soluble in water as the temperature increases. At some point, the solution becomes cloudy and a phase separation occurs. This exact moment is called the lower critical temperature T_c, or cloud point. This phenomenon is unusual as in the majority of cases, an increase in temperature results in a higher solubility of the solute. The reason is that, when reaching T_c, the dehydration of the polymer chains is such that they start forming their own phase. In other words, the intermolecular hydrogen bonds between the water molecules and the polymer chains are cleaved, reducing their water solubility. As a

consequence, the surfactant molecules tend to aggregate more as the temperature increases, yielding larger micelles giving the cloudy appearance. Consequently, the CMC value decreases as well due to a higher hydrophobicity. From a macromolecular point of view, before T_c, water is considered as a good-to-ideal solvent (or theta solvent) that completely solvates the polymer chains. However, as the temperature increases, the polymer chains are less and less solvated and the solvent-polymer interactions decrease until T_c is reached, turning water into a poor solvent. This results in a decrease of the second virial coefficient A_2 and leads to conformational changes of the polymer chains from extended coil to globule conformation.[128] This phenomenon is mostly observed with poly(ethylene oxide) and poly(acrylamide) based polymers. Polysaccharides like cellulose, although nonionic, do not have a cloud point. However, once ethoxylated, a cloud point can be measured.[125] Typically, PEO-based surfactants have high cloud points such as the commercially available TWEEN 80 (T_c = 90 °C) and Triton X-100 (T_c = 65 °C). Surfactants that are not based on PEO, like SPAN 80, have low T_c around 40 °C which can be problematic when heating.[129] When utilizing polymers with even lower T_c such as PNIPAAm (T_c = 32 °C) for biological applications, the use of hydrophilic comonomers can increase the T_c value while hydrophobic comonomers will have the opposite effect.[130] However, in reality, applications in biological environment do not require high temperatures, and mitigate the importance of the cloud point for polymers with high intrinsic T_c. In fact, T_c is mainly an issue for surfactants that have low cloud point value as stated for PNIPAAm and is usually not considered when using surfactants based on polymers with high cloud point such as PEO.

In the case of ionic surfactants, water solubility increases with temperature and cloud point is not an issue. In fact, as mentioned previously, the CMC values of ionic surfactants are much higher than those of nonionic surfactants due to their much higher hydrophilicity, making them less susceptible to aggregate and form micelles. However, if the temperature is below a certain value, ionic surfactants do not form micelles, even above the CMC value. This exact temperature is called Krafft temperature (or Krafft point) in honor of Friedrich Krafft, who discovered this phenomenon in 1895. The Krafft temperature (T_k) is defined as the point where the solubility curve of the surfactant intercepts the curve of temperature dependence of the CMC. In other

[128] K. Kubota et al., Journal of Physical Chemistry, 1990, https://doi.org/10.1021/j100375a070.
[129] S. Chatterjee et al., Journal of Food Science and Technology, 2017, https://doi.org/10.1007/s13197-017-2906-z.
[130] H. Wei et al., Journal of Physical Chemistry B, 2010, https://doi.org/10.1021/jp100901p.

words, at T_k, the solubility of the surfactant equals the value of the CMC, and below T_k, the CMC does not exist. Typically, SDS and CTAB have Krafft temperatures of around 16 °C and 26 °C respectively.[131] Below T_k, the surfactant molecules crystallize, forming a similar turbid phase as for nonionic surfactants above the cloud point. Analogous to T_c, the Krafft point is highly dependent on the length of the hydrophobic chain. Crystallization occurs due to the increased packing of the hydrophobic chains and decreased motion at low temperature. The type of ionic head as well as the counterions also have their influence. As an example, a surfactant with an anionic head combined with divalent cations as counterions will have a higher T_k than the same surfactant with monovalent counterions. As for cationic surfactants, the Krafft point is higher with iodides than with chlorides as counterions. Modifying the structure of the surfactant can reduce the Krafft point and circumvent these problems, mainly by introducing oligo(ethylene oxide) units between the hydrophobic chain and the ionic head, or by reducing the length of the hydrophobic chain (using a branched tail instead of a linear one). A general rule of thumb to reduce the Krafft temperature for a given surfactant is to insert any modifications that induce a distortion of the hydrophobic chains to prevent them from packing. In biological medium, phospholipids and most fatty acids contain unsaturated hydrophobic chains, resulting in a twist in their structure making them less likely to pack and thus, lower their Krafft point.[125]

Whether the micelles are ionic or nonionic, temperature plays an important role in their dynamics and thus, their stability. On the other hand, these particular temperature conditions, namely the cloud point and Krafft temperature, are rarely an issue during biological applications as the T_c and T_k of surfactants are far from the body temperature, except for a few examples.

3.2.3. Aggregation number and packing parameter

A parameter that is closely related to the critical micellar concentration is the micellar aggregation number *N*. For spherical micelles, *N* can be calculated using the following formula:

$$N = \frac{4\pi r^2}{a_0} \qquad \textbf{(Eq. 2)}$$

[131] C. Vautier-Giongo and B. L. Bales, Journal of Physical Chemistry B, 2003, https://doi.org/10.1021/jp0270957.

with *r* being the radius of the micelle and a_0 the optimal surface area of the polar head.[132] The aggregation number is the number of surfactant molecules per micelle, usually comprised between 50 to 100. For a given surfactant molecule, a micelle of 20 nm will have a higher amount of unimers than a 10 nm micelle. The effects of temperature depicted previously for the CMC follow the same trend for the aggregation number. For nonionic surfactants, the aggregation number increases as the temperature rises. This is coherent with the decrease of CMC and the tendency of surfactants to aggregate more easily due to a higher hydrophobic character. This effect was indeed observed in 1985 by Malliaris et al. where they showed the temperature dependence of the aggregation number for Triton X-100. The results showed an increase of N at about 30 °C below the cloud point which is in accordance with the dehydration process during heating. Moreover, they studied the aggregation number of various ionic surfactants and showed that N mainly depends on three parameters: the ionic head, the chain length and the counter ion.[133] The aggregation number decreases as the polar head becomes less hydrophilic. On the other hand, a longer hydrophobic chain and a larger counter ion increase the N value. In the majority of cases, the aggregation number of ionic surfactant decreases as the temperature increases. As mentioned previously for the CMC, ionic surfactants have more complicated behaviors than nonionic amphiphilic molecules and the prediction of their behavior may be complex. In any case, amphiphiles only aggregate into structures in which their polar head is close to the optimal surface area a_0. Aggregates result from a favored thermodynamic process driven by the entropy of the system. In other words, the optimal value of a_0 is obtained when the minimum free energy per amphiphile is reached in the aggregate.

Surfactants can adopt several types of structures depending on their chemical composition, temperature, concentration, salinity, pH and so on. In general, any system seeks to be in its lowest possible energy as it is the most thermodynamically stable state. In the case of surfactants, entropy favors the structure that will minimize the aggregation number, leading to the smallest possible structure that allows each amphiphile to have the same optimal surface area while taking into account their structural constraints. The resulting structure is

[132] J. N. Israelachvili et al., Journal of the Chemical Society, Faraday Transactions, 1976 https://doi.org/10.1039/f29767201525.
[133] A. Malliaris et al., Journal of Physical Chemistry, 1985, https://doi.org/10.1021/j100258a054.

energetically and entropically favoured. The type of structure in which the amphiphiles self-assemble can be predicted by the dimensionless critical packing parameter P_c defined as:

$$P_c = \frac{v}{a_0 l_c} \quad \textbf{(Eq. 3)}$$

where v is the volume of the hydrophobic chain, a_0 the optimal surface area of the polar head and l_c the critical length of the hydrophobic chain which corresponds to the length of the fully extended chain. To obtain spherical micelles, the radius must fill the following requirement $l_c \geq 3v/a_0$. However, if the critical length of the hydrophobic chain is lower than $3v/a_0$, then the surfactants molecules will not be able to pack into spherical micelles. This happens when P_c is higher than 1/3. If the critical length of the hydrophobic chains fills the condition $3v/a_0 \geq l_c \geq 2v/a_0$, and if P_c is higher than 1/3 but lower than 1/2, then the amphiphiles will form worm-like micelles instead. Apart from these two examples, other geometrical shapes exist depending on the value of P_c. Vesicles are obtained for $1/2 < P_c < 1$, planar bilayers are formed when P_c is around 1 and reverse micelles are achieved for a value above 1.[132,134] A general rule of thumb is that surfactants with monohydrophobic chains tend to form micelles due to their small volume and large polar head. Surfactants that contain two hydrophobic tails per molecule, such as phospholipids, mostly form bilayers. The reason is that their carbon chains are too bulky to pack into small micelles without disrupting the optimal surface area a_0 of the polar head. Bilayers can either be planar or spherical (vesicle), however, thermodynamically, spherical shapes are more stable thanks to their smaller size and reduced aggregation number while preserving their optimal surface area.

Although the critical packing parameter allows the prediction of the structure resulting from the self-assembly of surfactants, the different values are approximative and certainly not absolute. Several other factors have to be taken into account, such as the temperature, the ionic strength of the solution and the type of surfactant used.

[134] R. Nagarajan, Langmuir, 2002, https://doi.org/10.1021/la010831y.

3.3. Nature of surfactant

Surfactants may be classified into three different ways: if they are synthetic or natural, by the origin of their raw source material (petroleum or vegetable oils), or by their type of polar head. The latter is related to the amphiphiles' properties and is more common and allows the classification of different surfactants into two broad categories: ionic and nonionic (**Fig. 16**).

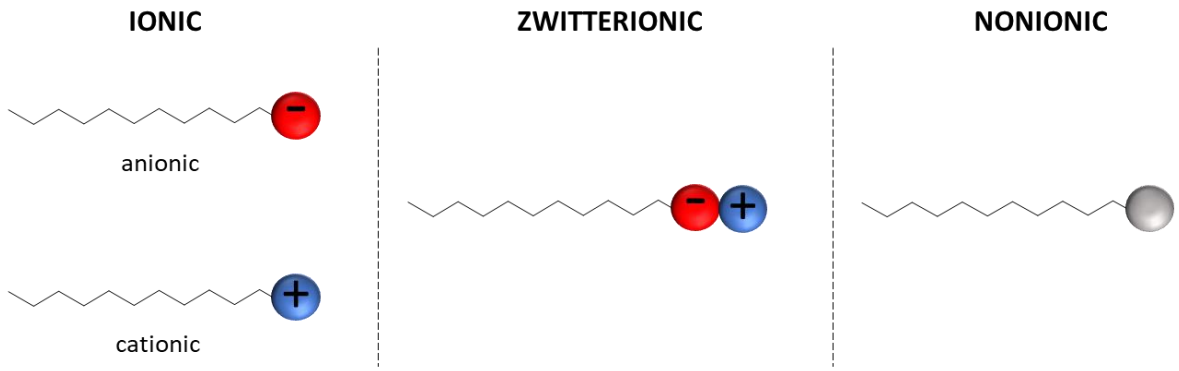

Fig. 16: Different classes of surfactant based on the hydrophilic head charge.

3.3.1. Ionic

Anionic surfactants are the most predominant ionic surfactants. In everyday life, these are commonly called 'soaps'. They are salty fatty acid composed of a linear saturated carbon chain with a terminal anionic group. These surfactants are extremely common. Indeed, evidences proved that around 2800 BC, ancient Babylonians already discovered soap by treating vegetable oils such as cassia oil with alkaline salts to heal skin diseases. Anionic surfactants, in general, are used in many different fields due to their low cost and ease of production. A typical anionic surfactant is sodium dodecyl sulfate (SDS) that has a CMC of 8.2 mM at 25 °C[125] and an aggregation number of 60 (**Fig. 17**).[135]

Fig. 17: Structure of SDS surfactant.

[135] N. J. Turro and A. Yekta, Journal of the American Chemical Society, 1978, https://doi.org/10.1021/ja00486a062.

However, these common surfactants are not tailored for biological applications and are scarcely used in the field of nanomedicine. They have low in vivo stability due to high CMC and are associated with high nonspecific cytotoxicity. In fact, these surfactants are used as detergents and can disaggregate cell walls by solubilizing the phospholipids, hence their use in cell lysis.[136,137] These properties are also observed with cationic surfactants and more rarely with nonionic amphiphiles. Anionic nanoparticles show lower cellular uptake due to repulsive interaction with the overall negatively charged membranes, leading to longer blood circulation.[138] Yamamoto et al. compared the uptake of Tyr-PEO-PDLLA (neutral) and Tyr-Glu-PEO-PDLLA (anionic) micelles and showed that the anionic micelles had lower uptake in the liver and spleen.[139] The reason is the combined effect of steric hindrance provided by the PEO chains and the repulsive interaction with cells due to the negative surface charge. Mazumdar and coworkers studied the effect of surface charge on the different cellular internalization pathways. They prepared a series of 6 analogous polymeric micelles with different surface charges and concluded that the uptake of all anionic micelles were the most compromised when endocytic inhibitors were used in comparison with cationic and neutral micelles.[6] However, as mentioned previously, negatively charged micelles have lower cellular uptake due to the overall negative charge of the cell membranes which is problematic for therapeutic applications. Therefore, micelles with temporary negative charges were developed.[140] The aim of these anionic micelles is to be able to switch off the charge in the vicinity of the tumor tissue to facilitate the cellular uptake. These systems are pH-sensitive and rely on the difference of pH in healthy and tumor tissues, in which the extracellular environment is slightly more acidic. As opposed to the conventional anionic surfactants, pH-sensitive micelles are based on polymeric surfactants that can either be neutral or ionic depending on the pH and functional groups. The anionic nature is temporary, as opposed to SDS whose negative charge is persistent. A common design of temporary anionic micelles is the incorporation of carboxyl groups onto the polymer chains. Neutral pH is enough to deprotonate them while slight acidic pH, between 6 and 7, is enough to protonate them into the corresponding acids. In this

[136] Z. Pang et al., ELECTROPHORESIS 27, 2006, https://doi.org/10.1002/elps.200500732.
[137] F. Shafa and M. R. J. Salton, Journal of General Microbiology, 1960, https://doi.org/10.1099/00221287-23-1-137.
[138] J. S. Suk et al., Advanced Drug Delivery Reviews, 2016, https://doi.org/10.1016/j.addr.2015.09.012.
[139] Y. Yamamoto et al., Journal of Controlled Release, 2001, https://doi.org/10.1016/S0168-3659(01)00451-5.
[140] P. Zhang et al., Journal of Nanobiotechnology, 2022, https://doi.org/10.1186/s12951-021-01221-8.

framework, Zhao et al. reported the preparation of crosslinked micelles based on poly(L-glutamic acid) (PGA) to modify the surface charge.[141] Similarly, Deng et al. proposed PEO-*b*-PCL micelles with grafted β-carboxylic amides as pH-sensitive moieties.[142] Taking advantage of the tumor microenvironment allows the easy charge conversion from anionic to neutral (or cationic) to benefit from a higher circulation time and thus, a better tumor accumulation.

Cationic surfactants are much more restricted in term of chemical structure. Their polar head is made of a cation such as ammonium, phosphonium, sulfonium or sulfoxonium. However, these are more expensive and less convenient to produce, with the exception of ammonium salts which are, as a consequence, the only cationic surfactants that are actually studied. They can either be primary, secondary, tertiary or quaternary ammoniums. The latter have a permanent positive charge (**Fig. 18**) whereas the other three are pH-dependant by protonation in acidic conditions.

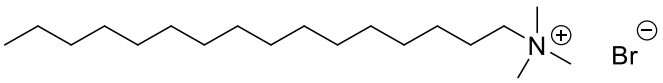

Fig. 18: Structure of the quaternary ammonium surfactant cetyltrimethylammonium bromide (CTAB).

Similar to anionic surfactants, common cationic surfactants are made of a single saturated carbon chain with an ammonium polar head. Due to their positive charge, they are commonly used to interact with negatively charged surfaces. They can be used against metal corrosion, as hair conditioner, dispersant for inorganic pigments or as bactericides.

In nanomedicine, nanoparticles with positive surface charge are known to have higher clearance and cellular uptake than anionic and neutral particles.[143] Indeed, as opposed to anionic nanoparticles, cationic ones express strong electrostatic interactions with cells. As a consequence, they undergo faster cellular internalization compared to neutral and anionic nanoparticles. However, the positive surface charge also greatly increases the nonspecific interactions with serum proteins leading to higher rates of phagocytosis. In fact, most proteins are negatively charged in blood. Their isolectric point, value that defines the pH at which the net charge of a protein is zero, is usually less than 7. As their isoelectric point is lower than the

[141] C. Zhao et al., Journal of Colloid and Interface Science, 2011, https://doi.org/10.1016/j.jcis.2011.04.037.
[142] H. Deng et al., Journal of Materials Chemistry B, 2015, https://doi.org/10.1039/C5TB01939G.
[143] E. Fröhlich, International Journal of Nanomedicine, 2012, https://doi.org/10.2147/IJN.S36111.

physiological pH of 7.4, proteins are overall negatively charged. As an example, human serum albumin has an isoelectric point of 4.7.[144] Unspecific interactions with proteins can lead to side effects. Analogously to anionic surfactants, systems based on cationic surfactants rely on charge conversion phenomenon. As stated previously, negatively charged micelles are designed to retain their charge until they reach the tumor to switch it off. In case of positively charge micelles, the idea is the same except that the cationic property is turned on in the tumor tissue to enhance cellular uptake. Cationic amphiphiles revolve around primary, secondary and tertiary amines. Quaternary ammonium, due to their permanent cationic nature, are not used in charge conversion micelles. A widely used cationic polymer is poly(ethyleneimine) (PEI) which can either be linear or branched. In both cases, amines can be protonated in acidic environment, leading to ammonium cations. In 1999, Vinogradov et al. showed that PEO-*b*-PEI micelles loaded with oligonucleotides had significantly increased efficiency compared to free oligonucleotides against multidrug resistant human oral epidermoid carcinoma cells.[145] In 2006, PLGA-*b*-PEI nanoparticles synthesized by Sutton et al. and showed efficient release of entrapped β-lapachone as the pH decreases.[146] Later on, Shi and coworkers reported the effective co-delivery of doxorubicin and gene Msurvivin T34A loaded in triblock copolymer PEO-PCL-*g*-PEI micelles against B16F10 tumor bearing mice.[147]

Cationic and anionic surfactants have opposite properties: i) anionic micelles suffer from lower cellular uptake while cationic ones benefit from an increased internalization and ii) anionic micelles have higher circulation time improving the passive targeting whereas cationic nanoparticles have higher cytotoxicity and clearance due to increased unspecific interactions. On the basis of these facts, micelles benefiting from the advantages of both categories were developed. The surface charge can be reversed from negative in circulation to positive in the tumor microenvironment. This process is commonly coined as 'charge reversal'. These hybrid systems mainly utilize amino conjugates of 2,3-dimethylmaleic anhydride (DMA) as an anionic and acid-labile moiety. At physiological pH and above, DMA is negatively charged due to the carboxylate group. From pH 7 and below, the amide bond is hydrolyzed, leading to the

[144] I. M. Vlasova and A. M. Saletsky, Journal of Applied Spectroscopy, 2009, https://doi.org/10.1007/s10812-009-9227-6.
[145] S. Vinogradov et al., Colloids and Surfaces B: Biointerfaces, 1999, https://doi.org/10.1016/S0927-7765(99)00080-6.
[146] D. Sutton et al., Journal of Applied Polymer Science, 2006, https://doi.org/10.1002/app.22636.
[147] S. Shi et al., Biomaterials, 2014, https://doi.org/10.1016/j.biomaterials.2014.02.010.

cleavage of DMA and restoration of the amine group from the polymer. Protonation of the latter turns it to an ammonium that modifies the surface charge of the micelle. Zhou et al. reported in 2009 the synthesis of poly(L-lysine) (PLL) conjugated with camptothecin as neoplastic drug, folic acid for active targeting, and DMA for the charge conversion. Results showed successful internalization of the nanoparticles and induced cytotoxicity. A similar system was developed in 2015 by Han et al. in which DMA was used to induce charge reversal for better circulation and cellular uptake.[148] More recently, Huo and coworkers showed increased cytotoxicity and internalization of PEO-*b*-PLL grafted with DMA and paclitaxel against MCF-7 and ADR cells.[149]

Lowering the clearance and enhancing the tumor cellular uptake are two parameters that are crucial for cancer treatment. These can be achieved by smartly designing micelles to activate/deactivate certain functions to trigger the desired effect. Although the results using these micelles are promising, the charge conversion is based on pH, hydrolysis, and protonation. This phenomenon is not quantitative and can take up to a few hours to reach its maximum. Moreover, pH can be different from one tumor to another, making this approach less reliable. For instance, the reported values of the protonation state of the cationic PEI polymer varies greatly from 20% to 90% of amines being protonated.[150] This can have a drastic impact on the solubility and cationic property of the nanoparticle. And finally, ionic surfactants are easily detected and eliminated compared to nonionic surfactants due to strong electrostatic interactions. However, zwitterionic surfactants are ionic, yet neutral, and display interesting properties.

3.3.2. Zwitterions

Zwitterionic surfactants are situated in between ionic and nonionic surfactants. Chemically wise, they are comparable to ionic amphiphiles, however, their physicochemical properties are more related to nonionic surfactants. Zwitterionic amphiphiles contain a polar head, called zwitterion, with both positive and negative charges resulting in a neutral net charge but highly polar character, allowing them to self-assemble into different structures such as micelles and vesicles.

[148] S. -S. Han et al., Small, 2015, https://doi.org/10.1002/smll.201402865.
[149] Q. Huo et al., International Journal of Nanomedicine Volume, 2017, https://doi.org/10.2147/IJN.S144452.
[150] J. D. Ziebarth and Y. Wang, Biomacromolecules, 2010, https://doi.org/10.1021/bm900842d.

As opposed to anionic and cationic surfactants, zwitterionic surfactants do not have counter ions as they form their own salt, hence their designation 'inner salts'. Zwitterions usually display high biocompatibility whereas anionic and cationic surfactants display more unspecific interactions. This is due to the fact that ions in zwitterions are closely interacting with each other, reducing their reactivity with the environment. Phospholipids which bear ammonium and phosphate groups are a great example of naturally occurring zwitterionic amphiphiles. Zwitterionic amphiphiles are ionic but have antifouling properties similar to nonionic surfactants such as PEO and thus show high resistance to opsonization. Generally, zwitterionic surfactants have lower CMC than ionic ones, but higher than nonionic amphiphiles. The reason is their neutral net charge and relatively weak repulsion interactions within the polar head. Like cationic and anionic surfactants, zwitterions are mostly composed of ammonium and carboxylate groups due to their sensitive nature toward pH variation. If the zwitterion contains a quaternary ammonium as cationic group, it is classified as "betaine". Betaines have permanent positive charge and thus, are not pH-dependant. Trimethylglycine is a naturally occurring amino acid involved in cell reproduction or in liver functioning and is the smallest betaine. Both ionic groups are located on the same chain and many zwitterionic micelles were developed using betaines. Lin et al. reported the synthesis of zwitterionic micelles using carboxybetaine as polar head for the delivery of doxorubicin while having excellent biocompatibility.[151] Liu and coworkers recently published the synthesis of a triblock copolymer using G3 dendrimer PAMAM-graft-poly(diethylamino) ethyl methacrylate (PDEAEMA)-block-poly(betaine sulfonate) (PSMBA). This copolymer could assemble into micelles and displayed excellent stability against serum proteins and high dilution rate.[152] Betaine is a zwitterion bearing both charges close to each other onto the same carbon chain. However, zwitterionic micelles using polymers with both positive and negative charges on two different chains are also developed. This type of micelles is zwitterionic in character but are not bearing zwitterions in the strict sense of the term as both charges are located in two different chains. However, to preserve the zwitterionic properties, both charges have to be somewhat close to each other. In 2012, Yuan et al. prepared zwitterionic micelles by grafting side chains containing an ammonium and carboxylate (DMA) and showed reduced opsonisation and increased in vivo

[151] W. Lin et al., Colloids and Surfaces B: Biointerfaces, 2014, https://doi.org/10.1016/j.colsurfb.2013.12.020.
[152] W. Liu et al., Langmuir, 2020, https://doi.org/10.1021/acs.langmuir.0c00206.

cellular internalization.[153] A few years later, Zhihui and coworkers loaded doxorubicin in zwitterionic micelles using similar ionic groups for drug delivery against KB cells, displaying high cytotoxicity thanks to the reduced adsorption of serum proteins.[154]

Zwitterionic surfactants are drawing more and more attention in the development of new nanocarriers. The acidic pH in the tumor environment can result in the protonation of the carboxylate group, leading to an unbalance in the zwitterionic character of the surfactant, making it more cationic for an increased cellular uptake. Furthermore, the main characteristic is their high stability and ability to greatly reduce opsonisation. Indeed, zwitterionic amphiphiles are often compared with nonionic surfactants such as PEO-based polymers as their antifouling properties are very similar.

3.3.2. Nonionic

Nonionic surfactants are the second class of surfactants. As the name suggests, they do not contain any ions, making them neutrally charged. They are commonly used in household as detergents like anionic surfactants. For biological applications, they find their use as coating and hydrophilic agents due to their low electrostatic interactions compared to their ionic counterparts. Moreover, nonionic amphiphiles have much lower CMC due to a lesser water solubility[125], making them less likely to be in monomeric state which is usually the cause of nonspecific toxicity of surfactants. They also feature high steric hindrance that prevents adsorption of proteins.

[153] Y. -Y. Yuan et al., Advanced Materials, 2012, https://doi.org/10.1002/adma.201202296.
[154] Z. Qin et al., Langmuir, 2019, https://doi.org/10.1021/acs.langmuir.8b00471.

3.4. Hydrophilic polymers

3.4.1. Polysaccharides

Polysaccharides are common natural nonionic polar polymers. Dextran, cellulose or pullulan are all biopolymers and as a result, showcase high biodegradability, biocompatibility, no toxicity and high water solubility (**Fig. 19**). [155] Polysaccharides can be easily biodegraded by enzyme catalysis such as glycosidase, hyaluronidase and esterase which cleave the glycosidic bonds, breaking the polymer into oligomers and monomers that are then easily eliminated. Polysaccharides contain many reactive groups, namely hydroxyl, carboxyl and amines, making them easy to modify. Indeed, the anomeric positions or the C_6 carbon atoms are the most reactive sites and allow easy introduction of a hydrophobic chain such as cholesterol, poly(ε-caprolactone) or stearic acid. Although they present interesting properties, polysaccharides usually present high dispersity and contamination with bioactive molecules. Furthermore, research on polysaccharide-based micelles are still quite limited in terms of clinical applications.

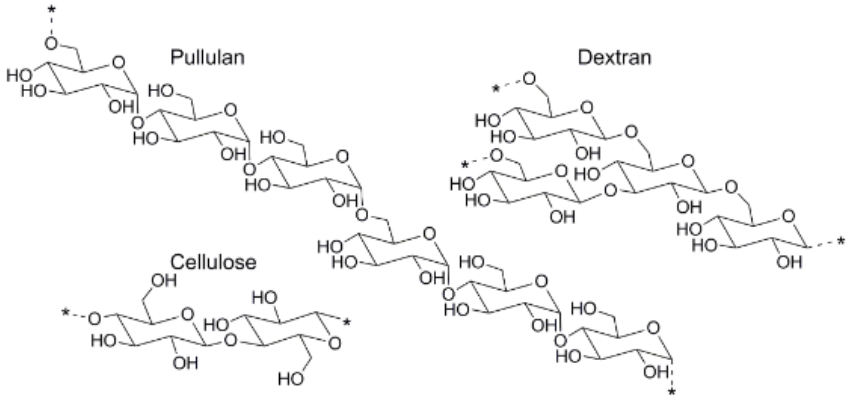

Fig. 19: Stucture of nonionic polysaccharides.

3.4.2. Poly(*N*-vinyl-2-pyrrolidone)

Another common nonionic polymer is poly(*N*-vinyl-2-pyrrolidone) (PVP). It shares the common properties with other nonionic polymers: good biocompatibility, biodegradability, water solubility and no toxicity. PVP was FDA-approved which makes it an interesting polymer for biological applications. Overall, it's quite inert chemically and expresses high resistance to pH

[155] N. Zhang et al., Pharmaceutics, 2013, https://doi.org/10.3390/pharmaceutics5020329.

and temperature variations. PVP is used in many biological fields such as regenerative medicine, gene delivery and targeted delivery which makes it a versatile polymer. In the work of Hira et al., the cytotoxicity of 49 nm PCL-*b*-PVP micelles loaded with doxorubicin was assessed in vitro and in vivo. The results show high decrease in tumor growth compared to free doxorubicin and low toxicity toward healthy cells.[156] Low cytotoxicity and ability to deliver active molecules were also reported by Wang and coworkers by synthesizing polypeptides-*b*-PVP micelles against pancreatic cancer cells.[157]

3.4.3. Poly(2-oxazoline)s

Currently emerging nonionic polymers are poly(2-oxazoline)s (POxs). These polymers are synthesized by cationic ring opening polymerization of the corresponding 2-oxazoline monomers. POxs are stable, biocompatible, provide stealth properties and are synthesized with low dispersity. Similar to polysaccharides, properties of POxs can be finely tuned. Indeed, position 2 of the monomer can be substituted prior to the polymerization step. The hydrophilic-hydrophobic balance can be modified in order to change the water solubility of the resulting polymer. For instance, the polymerization of 2-methyl-2-oxazoline (PMeOx) gives highly hydrophilic POx while linear chains longer than 4 carbons usually result in water-insoluble POx. Typically, PMeOx has no LCST while the *n*-propyl equivalent, PnPOx, has a LCST value of 25 °C (**Fig. 20**).[158]

[156] S. Kumar Hira et al., PLoS ONE 9, 2014, https://doi.org/10.1371/journal.pone.0094309.
[157] L. Wang et al., Colloids and Surfaces B: Biointerfaces, 2009, https://doi.org/10.1016/j.colsurfb.2009.07.032.
[158] R. Luxenhofer et al., Macromolecular Rapid Communications, 2012, https://doi.org/10.1002/marc.201200354.

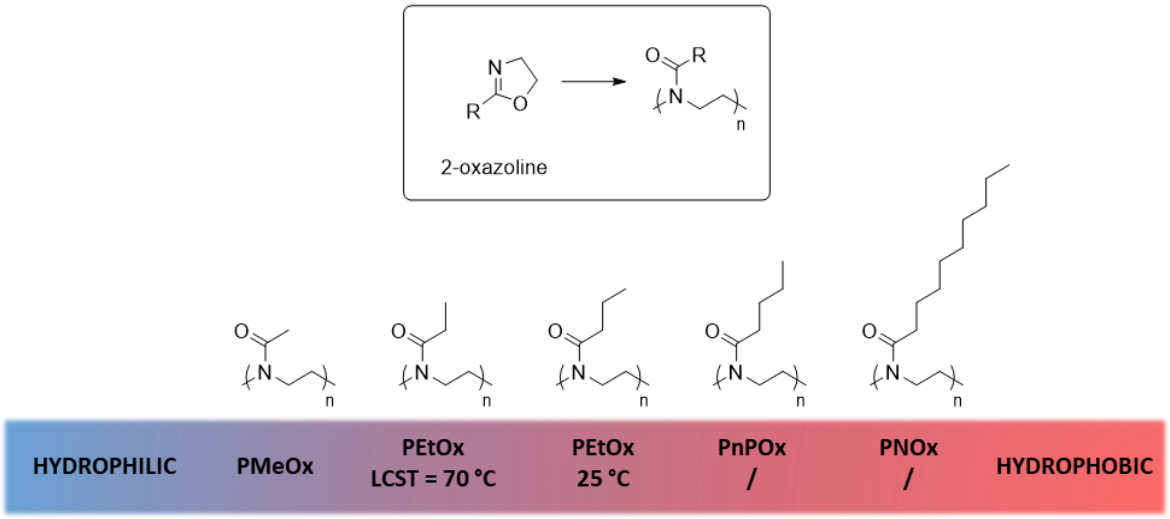

Fig. 20: Structure of 2-oxazoline and the effect of the carbon chain length regarding the final polymer's properties.

Besides substitution on position 2, telechelic POx can be prepared by rational selection of the electrophilic initiator (alkyl halides, acid halides, tosylates and triflates derivatives) and the nucleophilic terminating agent (carboxylates, amines, thiolates, alkoxides). Therefore, POxs provide a broad range of possibilities for potential functionalization while preserving their nonionic coating properties. Their high versatility has lately drawn a lot of attentions in pharmaceutical fields, especially in drug delivery. Qiu et al. reported the high efficacy of POx-*b*-PCL micelles for the delivery doxorubicin against HeLa, KB, A549 and MCF-7 cell lines. In vivo experiments on mice bearing KB tumors showed inhibition of tumor growth and reduced cytotoxicity compared to free doxorubicin.[159] Luxenhofer and coworkers prepared triblock copolymers based on POx displaying excellent drug loading capacity (45 wt%) for paclitaxel. In vivo experiments demonstrated the efficient drug delivery and inhibition of tumor growth compared to the free drug.[160] POx have already demonstrated their high robustness in various fields especially in drug delivery. They provide high biocompatibility, no toxicity, antifouling and possibilities of conjugations. Hence, POx are often compared to PEO regarding their physicochemical properties in biological environment.

[159] L. -Y. Qiu et al., International Journal of Pharmaceutics, 2013, https://doi.org/10.1016/j.ijpharm.2013.08.071.
[160] R. Luxenhofer et al., Biomaterials, 2010, https://doi.org/10.1016/j.biomaterials.2010.02.057.

3.4.4. Poly(ethylene oxide)

Poly(ethylene oxide) (PEO) or poly(ethylene glycol) (PEG) is a nonionic polymer resulting from the ionic ring opening of ethylene oxide commonly called oxirane. PEO and PEG refer to the same polymer, but strictly speaking, the correct name is PEO. In polymer chemistry, a polymer is named after its monomer used during polymerization. In that case, the monomer is ethylene oxide and not ethylene glycol. However, the use of the term PEG is much more common as it is more convenient and has given rise to derived expressions such as 'PEGylation' or 'PEGylated' nanoparticles. Low molecular weight polymers below 25 kDa also often referred to as PEG and those above are classified as PEO. Nonetheless, in this thesis, PEO will be used for all polymers regardless their size, for scientific accuracy. PEO is considered as the gold standard for biological applications. It's the most common polymer for the synthesis of nonionic surfactants as it provides high biocompatibility, biodegradability and antifouling properties, low dispersity, low cost of production and toxicity while providing high water solubility.[161] PEO is a polyether with only saturated bonds resulting in high chain flexibility and low glass transition temperatures (below −60 °C). The particularity of PEO compared to other polyethers is the close location between two oxygen atoms in the carbon chains. Indeed, only two carbon atoms are in between two consecutive oxygen atoms. The high water solubility from PEO, as opposed to other polyethers, comes from the ability of the polymer chains to form efficient hydrogen bonds with water molecules.[162] PEO has long been approved by the FDA (Adagen®, a macromolecular drug developed by Enzon, was approved in 1990). With the rise of nanomedicine at that time, an immense amount of studies using PEO were reported.

PEO has been used in the all types of nanoformulations for drug delivery and cancer treatment. Indeed, from metal nanoparticles such as gold and iron oxides to liposomes and micelles, PEO was the first choice regarding nanoparticle's coating. Although this was the case for a couple decades, recent studies show that PEO may induce cytotoxicity to some degrees and trigger immunogenic responses.[163] In fact, it was found that some patients develop anti-PEO immunity, with or without prior exposure to PEO. As a consequence, PEO might not be such an ideal polymer for the coating of nanoparticles intended for drug delivery, hence the research on

[161] J. Herzberger et al., Chemical Reviews, 2016, https://doi.org/10.1021/acs.chemrev.5b00441.
[162] R. Kjellander and E. Florin, Journal of the Chemical Society, Faraday Transactions 1: Physical Chemistry in Condensed Phases 77, 1981, https://doi.org/10.1039/f19817702053.
[163] N. d'Avanzo et al., Advanced Therapeutics, 2020, https://doi.org/10.1002/adtp.201900170.

various different nonionic polymers such as PVP and POx, mentioned previously. Despite these questionings, the use of PEO for drug delivery is still very popular and shows truly promising results in terms of efficacy, thanks to the long circulation time and low toxicity of PEGylated nanoparticles.

4. Conclusion and objectives of the PhD thesis

In the history of medical sciences, nanomedicine is a novel and innovative field that opens new possibilities and strategies to treat various diseases such as cancer. The main objective is to achieve a specific therapeutic effect at the desired area to significantly reduce side effects and increase the potency of the administrated drug. This is achieved by using supramolecular assemblies such as micelles in which the active drug can be encapsulated, protecting it from the environment and preventing it from harming healthy tissues. Since the early 2000s, after the development of Doxil® in 1995, a wide range of nanoparticles was reported, featuring different sizes, shapes and surface chemistries of all sorts. Studies show that these nanosystems can be used as efficient nanovectors for the specific delivery of active molecules into solid tumors by either taking advantage of the EPR effect and/or the specific characteristics of the tumor microenvironment such as the overexpressed enzymes and receptors to perform active targeting. In this context, micelles are perfect candidate nanocarriers. They present numerous advantages such as easy production and efficient encapsulation of lipophilic molecules such as anticancer drugs (e.g. paclitaxel) or imaging agents (e.g. Nile Red). Among the hydrophilic polymers used for drug delivery, nonionic are the most desired as they provide neutral surface charge, low toxicity, biocompatibility and prevent serum proteins from adsorbing onto the micelles' surface. This PhD project was focused on the development of PEGylated micelles for drug delivery against solid tumor by EPR effect.

The first and second chapters are dedicated to PEGylated micelles based on a photoactivatable ferrocene moiety intended for the treatment of solid tumors.

The former is mainly focused on the design and organic synthesis of the amphiphilic molecules, describing the different approaches that led to the final products before their self-assembly into micelles.

The second chapter describes the photochemical properties of the formulated ferrocene-based micelles. Their ability to photodecompose under blue and red lights as well as their capability to encapsulate and release hydrophobic drugs were assessed. Finally, their cytotoxicity was tested against breast cancer MCF-7 cells, showing very promising results regarding their controlled cytotoxicity triggered by illumination (while being harmless without light activation).

The third and last chapter is about the synthesis and *in vivo* application of PEGylated and polymerized radiolabeled micelles for bi-modal imaging of the EPR effect in U87-MG tumor-bearing mice. The micelles were polymerized to increase their *in vivo* stability and reduce their cytototoxicity while DiD, a hydrophobic red emitter dye, was successfully encapsulated inside the micelles. Deferoxamine (DFO) ligands at the surface of the micelles were used to chelate radioactive Zirconium [^{89}Zr]. The association of DiD and [^{89}Zr] allowed the *in vivo* tracking of the micelles using a bi-modal method combining fluorescence and positron electron microscopy (PET). Sonoporation, the use of localized ultrasounds to increase the permeability of the tissues, was performed in order to improve and homogenize the accumulation of the micelles inside the tumors.

CHAPTER 1. MOLECULAR ENGINEERING, SYNTHESIS AND CHARACTERIZATION OF FERROCENE-BASED MICELLES

Chapters 1 and 2 describe degradable micelles that take advantage of the oxidation of ferrocene to ferricenium. Ferrocene was specifically selected to serve as a redox linker enabling micelle degradation and cargo release. This choice was guided by several features of ferrocene: i) its stability under most conditions, ii) its degradation under oxidative conditions, iii) its ability to induce oxidative damage through the Fenton reaction. The following chapter begins with an introduction on the state-of-the-art of ferrocene in anticancer treatments and then describes the work that I carried out on the synthesis of ferrocene-based amphiphiles, including the various obstacles encountered and the different pathways explored.

1. Theoretical introduction to ferrocene, a potent candidate for cancer treatment

1.1. From discovery to cancer therapy

1.1.1. Discovery and properties

Ferrocene was unexpectedly discovered in 1951 by Thomas J. Kealy and Peter L. Pauson at Duquesne University in Pittsburgh. In 1950, R. D. Brown from the University of Melbourne hypothesized that fulvalene, an unstable isomer of naphthalene and azulene, was a non-benzenoid compound. As an attempt to verify this hypothesis, Pauson assigned the synthesis of such molecule to his student Kealy, who proceeded by reacting cyclopentadienyl magnesium bromide with iron (III) trichloride ($FeCl_3$). For this type of reaction, one would normally use cobalt dichloride instead, however, it was not available in that time, so they used $FeCl_3$. After the reaction, an orange solid with a melting point of 173 °C was obtained.[164] By elemental analysis, it was found that the compound contained iron up to 30%, with a molecular weight of 186.5 g mol^{-1}. Pauson and Kealy thus proposed the famous structure of the iron atom sandwiched between two cyclopentadiene rings, also named iron biscyclopentadienyl, but doubted and never considered to publish it as no other similar structures were known at that time. One year later, Wilkinson, Rosenblum, Woodward and Whiting published the structure of the sandwiched structure based on multiple analysis (**Fig. 21**).[165] After this

[164] T. J. Kealy and P. L. Pauson, Nature, 1951, https://doi.org/10.1038/1681039b0.
[165] G. Wilkinson et al., Journal of the American Chemical Society, 1952, https://doi.org/10.1021/ja01128a527.

publication, several scientists confirmed the structure by X-ray diffraction.[166,167] Woodward, Rosenblum, Whiting and Wilkinson then studied the aromatic nature of the cyclopentadiene rings. They assumed that, according to the structure, the two double bonds in each ring should be delocalized throughout the rings. In this matter, they compared the structure to benzene, hence the given name "ferrocene".[168]

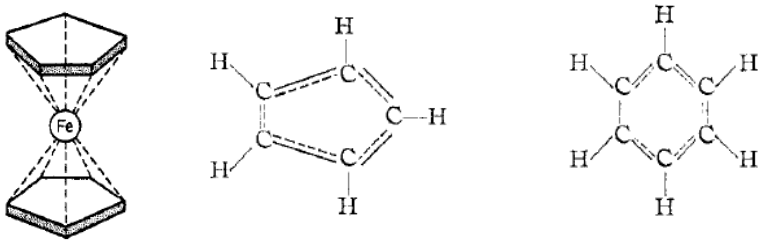

Fig. 21: Suggested structure of ferrocene (left) and comparison of aromaticity in cyclopentadiene (middle) and benzene (right) by Wilkinson et al.

Although ferrocene presented a high degree of unsaturation, it did not react with the highly electrophile maleic anhydride nor was reduced by hydrogenation over platinum oxide which were two typical reactions of conjugated unsaturated compounds such as polyolefins. It thus appeared that both rings were aromatic like benzene. The high stability was also assessed by Pauson and Kealy who tested various conditions. Ferrocene was left in concentrated hydrochloric acid, concentrated sulfuric acid or 10% NaOH solution without reacting.[164] It was noticed that ferrocene was also stable under air, against moisture, did not degrade under light and could resist pyrolysis up to 470 °C. It was clear that ferrocene was extremely stable. To confirm the similarities with benzene, Wilkinson et al. proceeded to the Friedel–Crafts acylation by treating ferrocene with acetyl chloride in the presence of aluminium chloride ($AlCl_3$) and obtained a crystalline red product that corresponded to the diacetylated ferrocene.[165] Reaction with hypoiodite yielded ferrocene dicarboxylic acid. Wilkinson et al. also suggested that during the acylation reaction, the resulting acetyl groups could not be on the same ring but one per cyclopentadiene. Finally, attempting to solubilize ferrocene, Pauson and Kealy found that the use of concentrated nitric acid or sulfuric acid changed the color from orange to blue. This

[166] J. D. Dunitz et al., Acta Crystallographica, 1956, https://doi.org/10.1107/S0365110X56001091.
[167] W. L. Baun, Analytical Chemistry, 1959, https://doi.org/10.1021/ac60152a017.
[168] R. B. Woodward et al., Journal of the American Chemical Society, 1952, https://doi.org/10.1021/ja01133a543.

observation was confirmed by Wilkinson and attributed to the oxidation of ferrocene to ferricenium cation.

Ferrocene undoubtedly changed chemistry due to its original structure and properties. Indeed, the unique structure displays high stability toward various conditions. This was totally unusual when it was discovered and its reactivity involves two main reactions: electrophilic aromatic substitution and redox reactions. The discovery of ferrocene led to the development of similar compounds using different metals called metallocenes, such as ruthenocene, osmocene, zirconocene, cobaltocene and nickelocene. Ferrocene was the first metallocene to be discovered but also the most stable among all and is nowadays used in many fields including nanomedicine for therapeutic applications.

1.1.2. Development of ferrocene in tumor therapy

Due to its high stability and easy functionalization, ferrocene found its use in biological applications. Anticancer studies were first published in 1978 by Fiorina et al. who reported the use of ferrocenyl polyamines as DNA binding agents to induce an immune response in tumor cells.[169] The different compounds presented low toxicity but a slightly higher tumor growth inhibition than polyamines without ferrocene. Although they did not know the exact reason for the higher anticancer activity, their study showed the potential use of ferrocene for anticancer treatments. At the same time, Yashchenko et al. also published a study on the toxicity of alkylating ferrocene derivatives.[170] They concluded that the presence of ferrocene did not increase the cytotoxicity of the alkylating agents. These two early studies from Florina and Yashchenko highlighted the low toxicity of ferrocene. A few years later, Köpf-Maier, Köpf and Neuse, who studied the anticancer activity of various metallocenes, decided to focus their research on ferrocene. They compared the survival time of mice bearing Ehrlich ascites tumor (EAT) treated with ferrocene and various ferricenium salts.[171] They first noticed that ferrocene did not display any differences in terms of survival compared to untreated mice, showing the lack of antitumor activity of ferrocene. Concerning the ferricenium salts, four out of five showed incredible tumor growth inhibition. Indeed, ferricenium chloroferrates led to the survival of

[169] V. J. Fiorina et al., Journal of Medicinal Chemistry, 1978, https://doi.org/10.1021/jm00202a016.
[170] G. N. Yaschenko et al., Pharmaceutical Chemistry Journal, 1978, https://doi.org/10.1007/bf00779217.
[171] P. Köpf-Maier et al., Journal of Cancer Research and Clinical Oncology, 1984, https://doi.org/10.1007/BF00390468.

67% of mice while mice treated with ferricenium picrate showed an outstanding 100% survival rate. To prove that ferricenium was indeed the reason of the anticancer activity and not the associated anions, they performed the same experiments using the corresponding ammonium salts and no survivability was observed. Therefore, Köpf-Maier, Köpf and Neuse disclosed the high anticancer activity of ferricenium as well as the low toxicity of ferrocene. This high toxicity was assumed to be the combination of the great water solubility and the direct linkage to DNA due to its positive charge. As for the observed low toxicity of ferrocene, it was mainly explained by its low water solubility. In 1991, Houlton and coworkers hypothesized that the high antitumor activity could be attributed to the redox behaviour of ferrocene/ferricenium in cells instead of the the direct binding to DNA.[172] In 2000, Osella et al. confronted these theories by testing ferrocene and ferricenium salts to inhibit EAT cell implants. As ferrocene is insoluble in water, it was entrapped in heptakis(2,6-di-O-methyl)-β-cyclodextrin (dmβ-CD) as an inclusion complex to deliver ferrocene to the target. For the same concentrations in tumor, only ferricenium salts showed potent inhibition effect while others did not.[173] This experiment demonstrated that the solubility was not the reason for the difference in activity between ferrocene and ferricenium as they equally penetrated the cell membrane. To assess whether ferricenium was directly interacting with DNA or not, it was mixed with either ferrocene or ferricenium. In the case of ferrocene, no binding or intercalation was detected and DNA was intact. However, in the case of ferricenium, DNA was highly fragmented. Therefore, they concluded that the mechanism was probably an indirect interaction between ferricenium and DNA by oxidative damage that was already known with ferric salts. To prove it, they proceeded to electron spin resonance (ESR) and indeed detected the generation of hydroxyl radical. This mechanistic study showed that the cytotoxicity was due to the formation of reactive oxygen species (ROS) generated by the ferricenium in the biological environment that would degrade DNA. This was an important finding as ROS can react with DNA but also with other biological components such as proteins and lipids resulting in more biological damage.

Since the discovery of ferrocene and its unique redox properties, various studies regarding the development of ferrocene-based anticancer drugs were reported. Joy et al. published the use of two ferricenium salts as *in vitro* and *in vivo* radiosensitizers and showed enhanced inhibition

[172] A. Houlton et al., Journal of Organometallic Chemistry, 1991, https://doi.org/10.1016/0022-328X(91)86350-Y.
[173] D. Osella et al., Inorganica Chimica Acta, 2000, https://doi.org/10.1016/S0020-1693(00)00147-X.

of KHT tumor growth in mice.[174] Ong's group described the synthesis of ferrocene linked to acridine, a potent DNA intercalator, and compared the *in vitro* cytotoxicity of the ferrocenylacridine to the intercalator-free analog as control against four different cell lines. Results showed high potency of the tested molecule against all four cell lines while the control did not induce any toxicity, depicting the synergy of ferrocene and acridine.[175] Topoisomerase II, an enzyme responsible for the correct topological changes of DNA overexpressed in cancer cells, is a prominent target for tumor growth inhibition. Vashisht et al. synthesized four different ferrocene derivatives that showed topoisomerase II inhibition activities.[176] Kondapi and coworkers also reported the inhibition effect of azalactone and thiomorpholid amido methyl ferrocenes against topoisomerase II.[177]

A widely studied class of ferrocene derivatives are ferrocifens, i.e. tamoxifen analogs where one phenyl is substituted with ferrocene. The Jaouen group was the first to introduce such compounds in 1996 when they synthesized ferrocenyl hydroxytamoxifen. The molecule was tested on breast cancer cells MCF-7 and showed higher cytotoxicity than hydroxytamoxifen demonstrating the added effect of ferrocene.[178] Indeed, different metallocifens were synthesized and it turned out that ferrocifen displayed the highest potency. Ferrocifens are currently in preclinical studies for anticancer treatments.

Despite outstanding anticancer properties, some studies described ferricenium as unstable in aqueous media (detailed in chapter 2), resulting in low *in vivo* half-lives and limiting its therapeutic effect. Several reports described efficient tumor growth inhibition using ferrocene, the reduced form of ferricinium. However, the insolubility of ferrocene in aqueous media is a serious drawback as it prevents intravenous or intraperitoneal injections. Furthermore, the ferrocene/ferricenium redox couple is reversible in most cases, which mainly depends on the pH and whether the environment is reductant or oxidant. Indeed, in the cellular environment, ROS can oxidize ferrocene to the corresponding ferricenium, which can then be reduced back to ferrocene. This cycle of oxidation-reduction by ROS is called the Fenton reaction, responsible

[174] A. M. Joy et al., International Journal of Radiation Oncology Biology Physics, 1989, https://doi.org/10.1016/0360-3016(89)90914-0.
[175] C. -W. Ong et al., Bioorganic and Medicinal Chemistry Letters, 1992, https://doi.org/10.1016/S0960-894X(00)80590-9.
[176] Y. N. Vashisht Gopal et al., Archives of Biochemistry and Biophysics, 2000, https://doi.org/10.1006/abbi.1999.1692.
[177] A. K. Kondapi et al., Archives of Biochemistry and Biophysics, 2006, https://doi.org/10.1016/j.abb.2006.04.003.
[178] S. Top et al., Chemical Communications, 1996, https://doi.org/10.1039/CC9960000955.

for the oxidative stress found in many cases of iron overload. Therefore, from a therapeutic point of view, it would be more interesting to administer the drug as ferrocene and deliver it to the target where ferricenium can be generated to induce the desired cytotoxicity

1.2. Fenton reaction in anticancer treatment

1.2.1. Oxidative damage

The original Fenton reaction, discovered by H. J. H. Fenton in 1876, is a homogenous catalytic process in which Fe^{2+} salts react with H_2O_2 to generate the highly oxidant hydroxyl radical and oxidized Fe^{3+} (**Eq. 4**). The latter can be reduced back to Fe^{2+} by H_2O_2 or hydroxyperoxyl radical to catalyze the reaction (**Eq. 5** and **6)**. This process is most efficient under acidic conditions from pH 2 to 4 due to the insolubility of the Fe^{3+} salts in neutral and basic aqueous media, which results in the precipitation of Fe^{3+} hydroxide species. The highly oxidant hydroxyl radical formed during the first step can undergo various reactions. Oxidation of Fe^{2+} terminates the cycle by producing hydroxide anion and Fe^{3+} (**Eq. 7**). Reaction with hydrogen peroxide is also possible and results in the generation of a hydroperoxyl radical (**Eq. 8**). The latter can oxidize Fe^{2+} to Fe^{3+} to terminate the cycle by formation of the corresponding hydroperoxide (**Eq. 9**). Hydroxy radical can also react with itself and form hydrogen peroxide (**Eq. 10**) or react with any nearby organic molecules (**Eq. 11**).

Fenton reaction

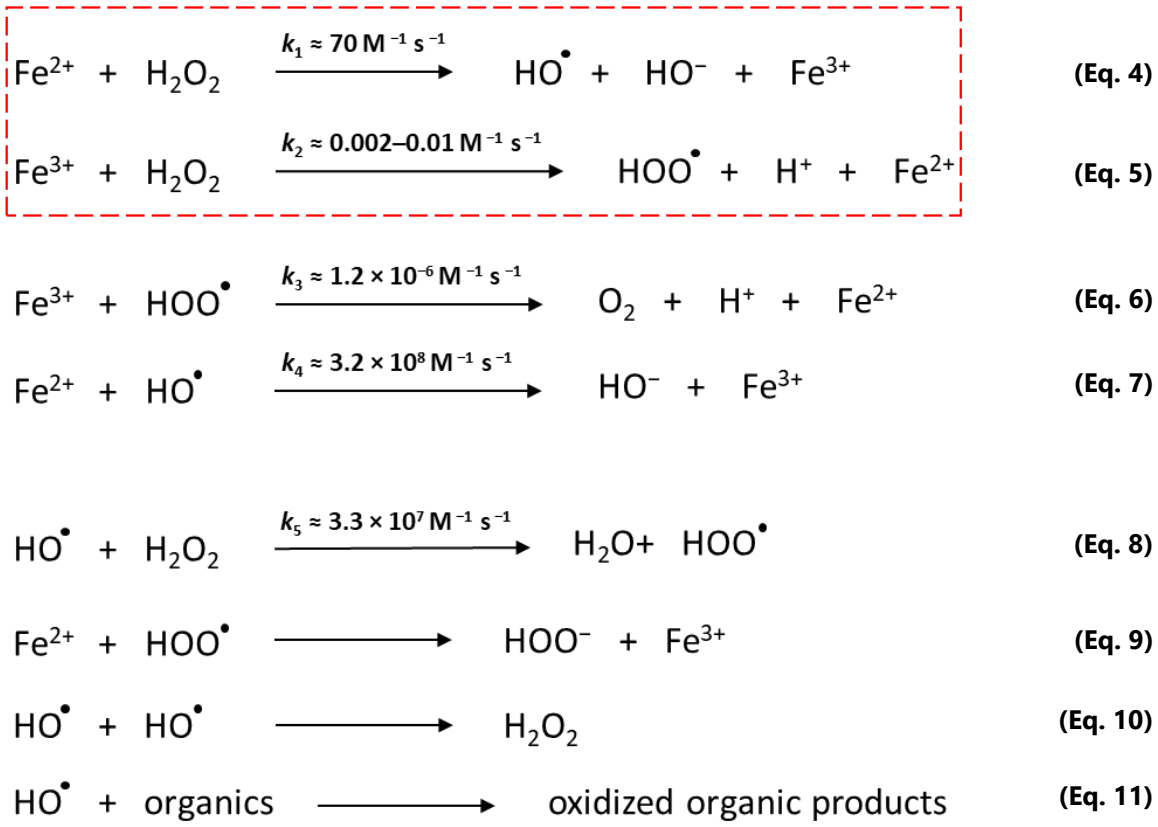

This process exists within cells, however, to prevent the over-production of ROS and to protect the cells, proteins that sequester iron such as transferrin and ferritin finely regulate the amount of free iron in the extra- and intracellular environment.[179] The initial oxidation of Fe^{2+} by H_2O_2 is very fast ($k_1 \approx 70\ M^{-1}\ s^{-1}$), generating hydroxyl radical and Fe^{3+} at a high rate. This step is the most important as both hydroxyl radical and Fe^{3+} are cytotoxic to cells. Indeed, ROS can actively react with lipids, proteins and DNA to induce oxidative damage, while Fe^{3+} is cationic and oxidant as well. Therefore, the Fenton reaction is an interesting means of treating tumors. Several studies and reviews can be found on the use of various iron-based drugs to trigger cell death by oxidative damage via the Fenton reaction. The concept of such drugs is to be able to deliver the iron species to the tumor tissues by passive or active targeting. As the amount of intracellular iron is strictly regulated,[180] creating an imbalance in the iron homeostasis leads to uncontrolled oxidation within the cell as reported by Wang et al.[181] However, as mentioned

[179] S. Tokoyuni, Redox Report, 2002, https://doi.org/10.1179/135100002125000596.
[180] D. Galaris et al., Biochimica et Biophysica acta. Molecular Cell Research, 2019, https://doi.org/10.1016/j.bbamcr.2019.118535.
[181] Q. Wang et al., Industrial and engineering Chemistry Research, 2013, https://doi.org/10.1021/ie403402q.

previously, Fe^{3+} salts readily precipitate if the pH is higher than 4, greatly affecting the kinetic of the reaction. It's reported pH below 4 can be attained in endosomes and lysosomes.[182] However, pH in the cytosol is similar to that of normal cells and only slightly more acidic in the extracellular tumor tissue. Although Fe^{3+} salts can precipitate, heterogenous Fenton-like reactions proved to be capable of inducing cell damage by generating ROS utilizing iron oxides species such as Fe_3O_4.[183,184] Other transition metals that have oxidation states differed by one electron also show Fenton activity such as copper (Cu(I) and Cu(II)) and cobalt (Co(II) and Co(III)).[185]

Ferrocene is known to be reversibly oxidized into ferricenium by ROS, and especially hydrogen peroxide. High concentrations of ferrocene are required in order to induce oxidative damage, because of its low water solubility and limited cellular uptake. Some ROS are located in the intracellular part of the cell and are referred to as "endogenous ROS". The solubility and ability of ferrocene to reach the cytoplasmic compartment are two key points for ROS-induced oxidative damage promoted by the Fenton reaction. Acevedo-Morantes and coworkers studied the cytotoxicity of ferrocene and ferricenium tetrafluoroborate against MCF-7 and MCF-10A cell lines.[186] Concentrations from 25 to 3000 µM for ferrocene and 2.5 to 300 µM for ferricenium were used. The higher concentrations used for ferrocene reflect the much more potent effect of ferricenium. It was reported that the IC_{50} values of ferrocene and ferricenium against MCF-7 cells were 1422 and 262 µM, respectively. In the experiment with MCF-10A, the respective IC_{50} values were 1251 and 126 µM. The cytotoxic gap between ferrocene and ferricenium mainly came from the fact that ferricenium is more easily internalized, thanks to electrostatic interactions with the negatively charged cell membranes. The study showed that both ferrocene and ferricenium, at concentrations above 1000 and 100 µM respectively, induced cytotoxicity due to significant generation of intracellular ROS. Quenching of ROS by the cell-permeable antioxidant *N*-acetylcysteine (NAC) could greatly improve the cell survivability.

Most of ferrocene cytotoxicity studies use either pristine ferrocene, ferricenium salts or conjugated molecules with an already bioactive compound such as tamoxifen,[178] camphor

[182] Y. -B. Hu et al., Translational Neurodegeneration, 2015, https://doi.org/10.1186/s40035-015-0041-1.
[183] H. Huijie et al., Biomedical Technology, 2023, https://doi.org/10.1016/j.bmt.2022.12.004.
[184] H. Hou et al., ACS Applied Materials and Interfaces, 2019, https://doi.org/10.1021/acsami.9b09671.
[185] W. Cao et al., Journal of Biotechnology, 2021, https://doi.org/10.1186/s12951-021-01074-1.
[186] C. Y. Acevedo-Morantes et al., Journal of Cancer Science and Therapy, 2012, https://doi.org/10.4172/1948-5956.1000154.

sulfonamide[187] or acridine.[175] However, very few studies reported the actual cytotoxicity of ferrocene itself. Ludwig et al. studied the cytotoxic effect of 1,1′-ferrocenedicarboxylic acid and different integrin-ligand ferrocene (ILF) conjugates to specifically target tumor cells that overexpress specific integrins. The purpose of ILF conjugates is to increase the solubility of ferrocene and actively target cancer cells to bring ferrocene into the intracellular compartment in which endogenous ROS are located. The study showed that free 1,1′-ferrocenedicarboxylic acid had little to no effect on the cell's proliferation when used without integrin ligands. The inherent cytotoxicity of the integrin-ligands was determined to be negligible as well. Hence, both components of the integrin-ligand ferrocene conjugates showed very little cytotoxicity toward cells when used separately. However, when ferrocene is conjugated to certain integrin ligands, high inhibition of cell proliferation was observed with reported IC_{50} values below 20 nM. The high cytotoxicity of ILF conjugates was attributed to their efficient cellular uptake, and as a consequence, to their ability to generate ROS by Fenton reaction in the intracellular compartment. As a result, DNA damage and cell death could be observed in contrast with free 1,1′-ferrocenedicarboxylic acid. Věžník et al. reported the cytotoxicity of ferrocenyliminoboronate. Under acidic conditions, the imine bond was hydrolysed and led to the degradation of the compound by releasing the corresponding aminoferrocene and boronate. The induced cytotoxicity was ascribed to the low oxidation potential of the generated aminoferrocene (−0.120 V vs CE, as opposed to +0.280 V for $Fc(COOH)_2$), which makes it easily oxidizable into ferricenium upon addition of hydrogen peroxide (100 μM).[188] Zhou et al. developed covalent organic framework nanodrugs functionalized with ferrocene. After internalization of the nanoparticles by different cancer cell lines, redox dyshomeostasis by Fenton reaction with endogenous hydrogen peroxide could induce lipid peroxidation and ultimately lead to cell death.[189]

[187] M. Schröder et al., Pharmaceutics, 2023, https://doi.org/10.3390/pharmaceutics15030791.
[188] J. Věžník et al., Journal of Inorganic Biochemistry, 2021, https://doi.org/10.1016/j.jinorgbio.2021.111561.
[189] L. -L. Zhou et al, Small, 2021, https://doi.org/10.1002/smll.202101368.

1.2.2. Ferricenium for drug release

The ability of ferrocene to undergo oxidation to give the corresponding ferricenium was exploited by several groups for the release of active molecules in nanodrugs. Levels of endogenous ROS in tumor cells are difficult to assess due to the heterogeneity of the tumor tissue. Indeed, the production of ROS requires oxygen. Hypoxic cells have a lower ROS concentration than other cells. However, it was estimated that the level of ROS could reach up to 200 × 10^{-6} M as opposed to normal cells (20 × 10^{-9} M).[190,191] The oxidation of ferrocene to ferricenium induces a change from hydrophobic to hydrophilic, disturbing the nanoparticle's structure and leading to the release of the cargo.[192] Cationization also helps disassembly by Coulombic repulsions among the chains. Kang et al. prepared a redox-responsive supramolecular assembly containing a ferrocene-camptothecin compound.[193] *In vitro* experiments showed that the structures could release 42% of the ferrocene active compound within 48 h in the presence of 50 µM of H_2O_2 (79% was released at 100 µM of H_2O_2 for the same duration). *In vivo* experiments showed a 3-fold inhibition of the tumor growth compared to the control group. Zuo et al. reported the synthesis of micelles containing a hydrophobic PCL core conjugated with ferrocene. The ferrocene unit could be oxidized using 200 µM of sodium hypochlorite (NaClO), a strong oxidant that is more abundant in cancer cells, leading to the release of 20 to 30% of the encapsulated doxorubicin.[194] Although these experiments were not performed with endogenous ROS, the use of biologically-relevant concentrations of oxidant (< 200 µM) to mimic the oxidant environment of tumor cells proved to efficiently oxidize ferrocene to ferricenium, inducing a clear increase in the release of the active molecule. The concept is based on the disturbance of the hydrophilic-lipophilic balance by switching the hydrophobic ferrocene to hydrophilic ferricenium. Additionally, in the case of packed ferrocene groups such as in the micelle's core, the multiple cationic centers create electrostatic repulsion between the ferricenium units, leading to the structure's disruption and eventually to irreversible degradation.

---

[190] A. A. Qutub et al., Molecular and Cellular Biology, 2008. https://doi.org/10.1128/MCB.00060-08.
[191] T. P. Szatrowski and C. F. Nathan, Cancer Research, 1991, https://aacrjournals.org/cancerres/article/51/3/794/497502/Production-of-Large-Amounts-of-Hydrogen-Peroxide?searchresult=1
[192] T. Saji et al., Journal of the American Chemical Society, 1985, https://doi.org/10.1039/C39850000865.
[193] Y. Kang et al., ACS Applied Materials and Interfaces, 2017, https://doi.org/10.1021/acsami.6b14640.
[194] C. Zuo et al., Journal of Colloid and Interface Science, 2018, https://doi.org/10.1016/j.jcis.2017.12.022.

The redox couple ferrocene/ferricenium was shown to be an outstanding candidate for cancer therapy. While ferrocene presents low toxicity and high stability in non-oxidant conditions, the oxidized state, ferricenium, is less stable but much more biologically active. Used as drug derivative or as part of the nanocarrier, ferrocene is a unique and robust molecule that can be easily functionalized.

1.3. Chemical reactivity of ferrocene

Ferrocene being aromatic, it can mainly react with electrophiles. The most common functionalization methods are the Friedel–Crafts acylation and alkylation reactions, which are electrophilic aromatic substitutions. Ferrocene can be compared to its other metallocenes containing the lower transition metals from the same period, namely ruthenocene and osmocene. Indeed, the two latter present the same features as ferrocene that are the parallel cyclopentadiene rings sandwiching the metal atom and the high stability toward various conditions. Other metallocenes such as titanocene, vanadocene or zirconocene are either unstable or imply other ligands such as halides or carbonyls, leading to different geometries, stabilities, reactivities and properties. For instance, acylation of nickelocene or metalation of cyclopentadienylmanganese tricarbonyl result in degradation of the complexes due to instability toward the experimental conditions.[195] Ferrocene, ruthenocene and osmocene are comparable in terms of reactivity.[196] The reactivity of ferrocene is well documented since its discovery as well as other metallocenes. Ferrocene, ruthenocene and osmocene can undergo Friedel–Crafts acylation using acyl chloride and aluminium trichloride. When an excess of $AlCl_3$ and acyl chloride is used, only the diacetylated ferrocene is obtained, while a mixture is observed with ruthenocene. In the case of osmocene, only the monoacylated product is detected. By pushing the conditions with ruthenocene and osmocene by introducing large excess of $AlCl_3$ and acyl chloride, only the diacetylated ruthenocene is obtained while the monosubstituted compound is still the only isolated product with osmocene. Therefore, the reactivity between these three metallocenes is as follow: ferrocene > ruthenocene > osmocene, with ferrocene being the most reactive in electrophilic aromatic substitution. Ruthenocene has an intermediate behaviour while osmocene presents the lowest rate of acylation.

[195] M. D. Rausch, Canadiann Journal of Chemistry, 2011, https://doi.org/10.1139/v63-182.
[196] M. D. Rausch et al., Journal of the American Chemical Society, 1960, https://doi.org/10.1021/ja01486a016.

This difference in reactivity can be related to the acidity of their monocarboxylic acid derivative. Acidity dissociation constant K_a of ferrocene monocarboxylic acid and ruthenocene monocarboxylic acid could be measured and showed respective values of 1.89×10^{-6} and 3.71×10^{-6}.[196] The lower acidity of ferrocene corroborates with its higher reactivity implying that the electronic density around the Cp rings is higher than in ruthenocene. As a consequence, the Cp rings are less tightly bonded to the iron atom than to ruthenium, and even less than to osmium. In other words, the cationic nature of the metal in ferrocene is much more pronounced than in ruthenocene or in osmocene. This has a huge impact on the ability of the metal to be oxidized and on the stability of its oxidized state. Indeed, ferrocene is known to be easily oxidized while osmocene is particularly resistant. Chronopotentiometry measurements of ferrocene, ruthenocene and osmocene provide the quarter wave oxidation potential ($E_{1/4}$) which are respectively 0.307, 0.693 and 0.633 V vs. saturated calomel electrode (SCE).[197] These values depict how much easier it is to oxidize ferrocene with a $E_{1/4}$ value twice as low as the others'. The chronopotentiometric plots use the follow equation:

$$E = E_{1/4} + \frac{\mathrm{RT}}{\mathrm{nF}} \ln \frac{\tau^{1/2} - t^{1/2}}{t^{1/2}} \qquad \textbf{(Eq. 12)}$$

where $E_{1/4}$ is the quarter-wave potential, τ the transition potential and t the time. For a one-electron process to be considered as completely reversible, the slope $\ln \frac{\tau^{1/2}-t^{1/2}}{t^{1/2}}$ must be equal to the ideal value of 0.059. In the case of ferrocene, the value was reported to be 0.057, which confirms the redox reversibility behaviour of ferrocene/ferricenium, as opposed to ruthenocene and osmocene. Therefore, the transition metal has a crucial role in the reactivity of the metallocene.

Besides the transition metal center, substituents can have drastic consequences in the redox properties and reactivity of the metallocene.[198,199] The Friedel–Crafts acylation only produces mono and disubstituted ferrocene, even by adding a large excess of catalyst and acyl chloride.

[197] T. Kuwana et al., Journal of the American Chemical Society, 1960, https://doi.org/10.1021/ja01507a011.
[198] M. Rosenblum et al., Journal of the American Chemical Society, 1963, https://doi.org/10.1021/ja00893a015.
[199] M. Emilia N. P. R. A. Silva et al., Journal of Organometallic Chemistry, 1994, https://doi.org/10.1016/0022-328X(94)87105-1.

Additionally, in the disubstituted product, the heteroannular is almost exclusively obtained. It is well-known that acylation heavily decreases the reactivity of the affected ring, directing the second substitution to occur on the second ring which is deactivated afterwards. It is reported that the homoannular diacetylated ferrocene only contributes for < 1% of the total disubstituted products after reaction with acetyl chloride.[200] Moreover, the first acylation reduces the efficacy of the second reaction, depicting a direct dependance regarding the electron density of both rings over the whole structure. The Friedel–Crafts acylation using alkylferrocenes shows higher reactivity due to the donor groups increasing the nucleophilic character of the Cp rings. For instance, 1,1′-diethylferrocene undergoes acylation reaction 1.7 times faster than ferrocene. However, the enhanced reactivity provided by both ethyl groups is not that high. As a comparison, toluene is 128 times more reactive than benzene in a competitive acylation.[201] As a direct consequence of the type of substituent, the ability of the metal center to be oxidized is also greatly affected. Electron withdrawing groups reduce the electron density on the Cp rings while donor groups have the opposite effect. Increasing the electron density of the Cp rings will decrease the oxidation potential while substitution with electron withdrawing groups will increase the oxidation potential, making the metal more resistant to oxidation. For instance, 1,1′-diethylferrocene and 1,1′-diacetylferrocene have respective $E_{1/4}$ of 0.194 and 0.796 V vs. SCE.[197] With $E_{1/4}$ = 0.307 V for ferrocene, the effect of substitution plays a major role in the resistance to oxidation, electron withdrawing groups conjugated with the Cp rings increase the oxidation potential, while donor groups such as alkyl groups slightly decrease it. The reason is that the π-electrons from unsaturated substituents can readily participate in the electron density of the redox center by resonance, thus the much greater effect than σ-groups. The ability of ferrocene to be easily and reversibly oxidized in a one-electron process can be used as a redox catalyst combined with ROS to induce oxidative damage.

[200] A. N. Nesmeyanov et al., Journal of Organometallic Chemistry, 1975, https://doi.org/10.1016/S0022-328X(00)83557-3.

[201] H. C. Brown and Y. Okamoto, Journal of the American Chemical Society, 1957, https://doi.org/10.1021/ja01565a039.

1.4. Objectives

In the aim of developing micelles with the ability to induce Fenton-like reactions, ferrocene is a great candidate as it can easily react with electrophiles by Friedel–Crafts acylation to give access to heteroannular disubstituted ferrocene derivatives.

2. First approach: direct acylation of PCDA chain

2.1. Diyne-bearing micelles

G. Wegner discovered the polymerization of diynes in 1969. Under UV (254 nm), diynes can polymerize by 1,4 addition to form a highly conjugated ene-yne polymer that has a characteristic deep blue color. To allow the photopolymerization to occur, the diynes have to be closely packed, therefore, bulky groups impact the polymerization as they hinder the packing. Diyne-containing amphiphilic molecules have been shown to form bilayers in aqueous medium. After self-assembly into bilayers, they can be photopolymerized while retaining their packing structure. A very common amphiphilic molecule for that purpose is 10,12-pentacosadiynoic acid (PCDA).[202] The carboxylic acid constitutes the hydrophilic head while the lipophilic part is made of the remaining 24 carbon atoms. PCDA is a cheap and commercially available molecule. The carboxylic acid allows easy functionalization to introduce different hydrophilic groups for complexation,[203] PEGylation,[204] or antibodies[205] in a few steps only, making PCDA a very robust molecule.

Our group has been working on PCDA-based micelles for drug delivery since 2005. The hydrophilic head was composed of a nitrilo triacetic acid and was pH-dependant as the protonation state plays a major role in the self-assembly of the amphiphiles in either bilayers or micelles.[206] Indeed, between pH 4 and 10, the tertiary amine was protonated leading to a more compact polar head due to intramolecular hydrogen bonds with the carboxylates, which gave the classic bilayer packing. At pH superior to 10, the amine was neutrally charged while the carboxyl groups were anionic. The electrostatic repulsion between the three carboylates

[202] C. Bubec et al., Molecular Crystals and Liquid Crystals, 1983, https://doi.org/10.1080/00268948308074697.
[203] R. A. Kumar et al., Advanced Synthesis and Catalysis, 2020, https://doi.org/10.1002/adsc.202000795.
[204] A. Doerflinger et al., Chemical Communications, 2018, https://doi.org/10.1039/C8CC00553B.
[205] J. -p. Jeong et al., Polymers, 2017, https://doi.org/10.3390/polym9040127.
[206] E. Gravel et al., Chemistry - A European Journal, 2011, https://doi.org/10.1002/chem.201102769.

created a bulkier polar head resulting in the decrease of the critical packing parameter and thus, to the formation of micelles. The 7 nm micelles could be photopolymerized at 254 nm providing polymerized micelles (pPCDA-NTA) which were yellow-colored. As opposed to bilayers where the color is blue, a yellow color indicates a lower delocalization of the π electrons in micelles than in bilayers. This is due to the fact that the micelles are much smaller and spherical, constraining the overlap of the molecular orbitals to allow the motion of electrons throughout the system. Nonetheless, the resulting micelles showed high stability over several months and were stable under high dilution rate compared to non-polymerized micelles. Even after polymerization, they could still effectively encapsulate active molecules as shown with paclitaxel, camptothecin and flavone analogs. However, the main drawback of these micelles was their limited half-life in blood due to the ionic surface charge and their pH-dependant instability. Consequently, PEGylated micelles were developed in order to benefit from a lower clearance, thanks to their neutral surface. Polymerized micelles (pPCDA-PEO) showed much higher tumor uptake and better circulation time than pPCDA-NTA micelles, as expected.[207]

On the basis of these results and the literature, we decided to synthesize pPCDA-Fc-PEO micelles as drug carriers with enhanced stability and lower non-specific toxicity provided by the photopolymerization of the diyne moiety. By bringing stabilized micelles to the tumor by EPR effect, ferrocene would be oxidized to ferricenium by endogenous ROS. The oxidation to ferricenium was expected to generate electrostatic repulsion between nearby ferricenium units in the micellar assembly and disturb the hydrophilic-lipophilic balance to destabilize the micelles and release the cargo. The biocompatibility provided by the PEO chain would allow such micelles to passively target the tumor tissue and eventually be internalized. The presence of intracellular ROS would activate the micelles by oxidizing ferrocene to ferricenium, inducing a dual therapeutic effect by releasing the encapsulated active molecule and generating the potent ferricenium species leading to oxidative damage by Fenton reaction. In this framework, using ferrocene as a linker for the synthesis of surfactant molecules seemed very interesting as both hydrophilic and lipophilic chains could be introduced one at a time by acylation. Although the acylation increases the redox potential of the ferrocene derivative and therefore its resistance to oxidants, ROS have high reduction potentials which are strong enough to easily

[207] E. Gravel et al., Nanoscale, 2013, https://doi.org/10.1039/C2NR34149B.

oxidize ferrocene. Typically, the reported standard reduction potential of $HO^{\bullet}/H_2O$ is 2.72 V.[208] During the syntheses, photopolymerizable micelles obtained from amphiphiles bearing a lipophilic diyne moiety and a PEO2000 chain for enhanced stability were prepared based on previous development in our group. Indeed, PEO2000 and PEO750-based micelles were compared *in vivo* and showed significant higher retention time in blood with the larger PEO than with smaller one, which led to a better accumulation in tumor tissue. Therefore, PEO2000 was selected as hydrophilic chain for the synthesis of the amphiphiles.

2.2. Retrosynthesis

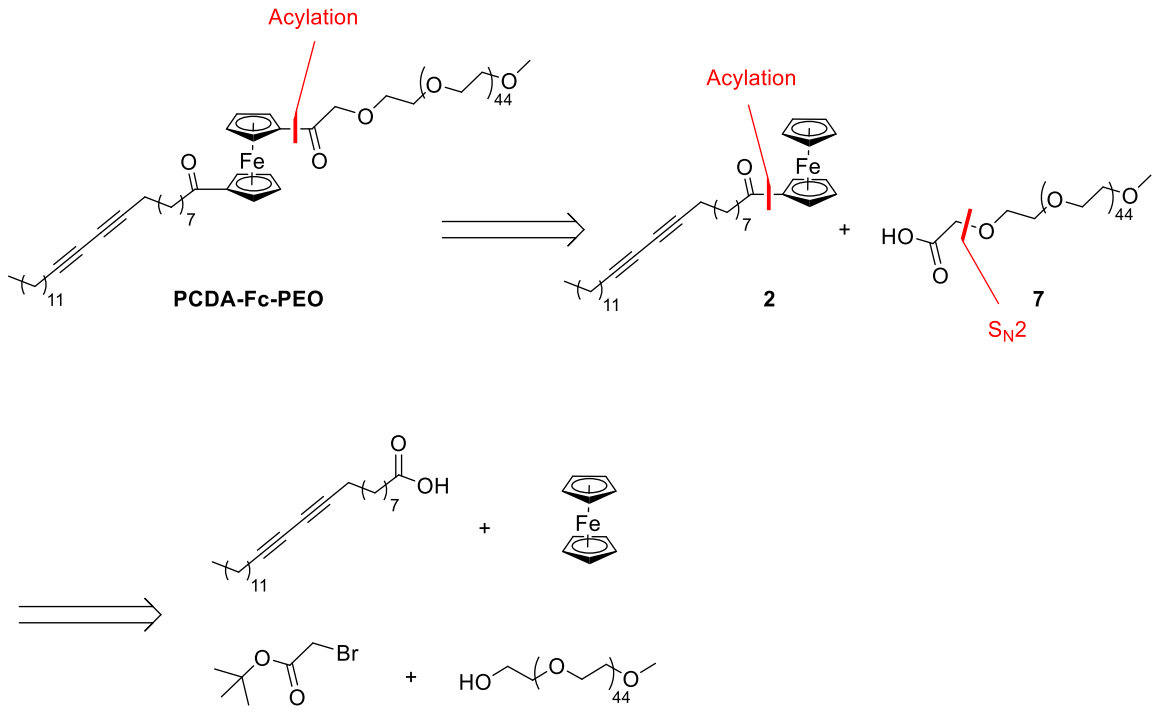

Fig. 22: Retrosynthesis of PCDA-Fc-PEO.

The retrosynthetic approach (**Fig. 22**) was based on two successive acylation reactions. The strategy consisted in introducing the PEO chain at the last step for ease of purification. Thus, the desired molecule PCDA-Fc-PEO would be obtained by acylation of intermediate **2** with the carboxylic acid-functionalized PEO chain **7**. Compound **2** could be synthesized by acylation of

[208] P. M. Wood., Biochemistry Journal, 1988, https://doi.org/10.1042/bj2530287.

ferrocene with 10,12-pentacosadiynoic acid, both commercially available. However, Friedel–Crafts acylation proved to be incompatible with PCDA, which pushed us toward the use of Lewis acid-free conditions. In the case of intermediate **7**, it could be prepared by nucleophilic substitution of tert-butylbromoacetate by methoxy(polyethylene oxide) 2000 followed by a deprotection step under acidic conditions.

2.3. 10,12-pentacosadiynoic acid as hydrophobic chain

2.3.1. Friedel–Crafts

The synthesis consisted of starting from the inexpensive and commercially available unsubstituted ferrocene from which successive acylation reactions would allow the introduction of the lipophilic and hydrophilic chains. The first attempts were performed using the Friedel–Crafts acylation under classic experimental conditions with an acyl chloride and aluminium chloride in dichloromethane at room temperature.

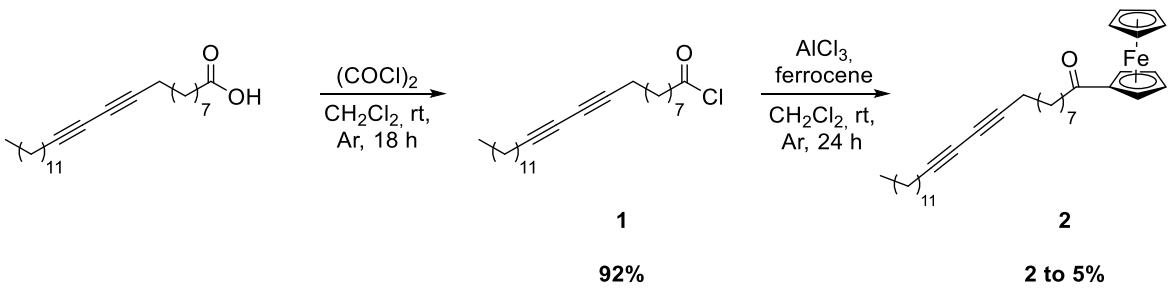

Fig. 23: Friedel–Crafts acylation of ferrocene with 10,12-pentacosadyinoyl chloride.

Starting from the commercially available 10,12-pentacosadiynoic acid, the first step was the activation of the carboxyl group into the corresponding acyl chloride using an excess of oxalyl chloride in dichloromethane at room temperature. The reaction gave the corresponding acyl chloride **1** in high yield, as expected from this type of procedure. Although diyne photopolymerization is reported to be done under UV at 254 nm, if left too long under visible light, a color change could be seen, reflecting the slow polymerization of the diynes. Therefore, the synthesized intermediate **1** was immediately engaged in the Friedel–Crafts acylation of ferrocene. In order to favour the monosubstituted product and limit the formation of the

symmetrical one, the reaction was carried out using 1.2 equiv. of $AlCl_3$ as Lewis acid and 1.0 equiv. of ferrocene and acyl chloride **1**. Unfortunately, acylated product **2** was obtained in extremely low yields, ranging from 2 to 5% within three attempts (**Fig. 23**), despite reported yields for monosubstituted ferrocenes being usually around 60–70%. The reaction was performed using 2.1 equiv. of $AlCl_3$ instead of 1.2 equiv. but no changes were observed. An initial hypothesis was that $AlCl_3$ was poorly reactive due to possible hydrolysis of the batch, but the use of freshly bought reagent did not improve the reaction. Another reason could be that, as a Lewis acid, $AlCl_3$ could chelate the diyne moiety resulting in the consumption of $AlCl_3$. However, even using an excess did not improve the reaction. To identify the issue, a simple saturated acyl chloride, lauroyl chloride, was used instead and the Friedel–Crafts acylation was performed.

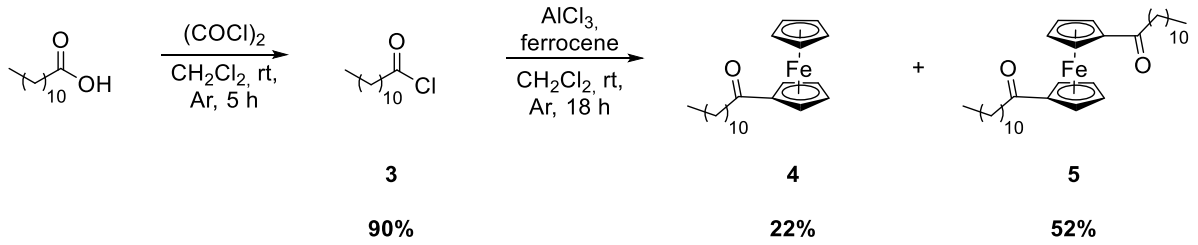

Fig. 24: Friedel–Crafts acylation of ferrocene using lauroyl chloride.

Lauric acid was first activated into the corresponding lauroyl chloride **3**. Then, the Friedel–Crafts acylation was performed using 1.0 equiv. of $AlCl_3$. Two distinct products could be detected and purified, the monoacylated **4** and disubstituted **5** products (**Fig. 24**). As opposed to the diyne acylation, the reaction with lauroyl chloride afforded both expected products that could be easily identified by ^1H NMR. This reaction was a proof of concept and confirmed that the Friedel–Crafts reaction gave the expected results with a simple substrate. Therefore, the reason for failure with the diyne substrate probably came from a possible interaction between the triple bonds and $AlCl_3$.

2.3.2. Mild acylation using TfOH/TFAA

As the Friedel–Crafts acylation was not successful with 10,12-pentacosadiynoyl chloride, different experimental conditions without the need of aluminium chloride were explored. The method is based on mild conditions using trifluoroacetic acid (TfOH), trifluoroacetic anhydride (TFAA) and a carboxylic acid derivative.[209] Apart from the mild conditions, the acylation does not require the preparation of the corresponding acyl chloride which is unstable. Thus, PCDA was reacted with with TfOH, TFAA and ferrocene in dichloromethane to provide intermediate **2** in acceptable yield (**Fig. 25**). The reaction proved to be much more successful than the Friedel–Crafts acylation. By not using $AlCl_3$, the reaction proceeded smoothly with ease of purification and no disubstituted product was observed.

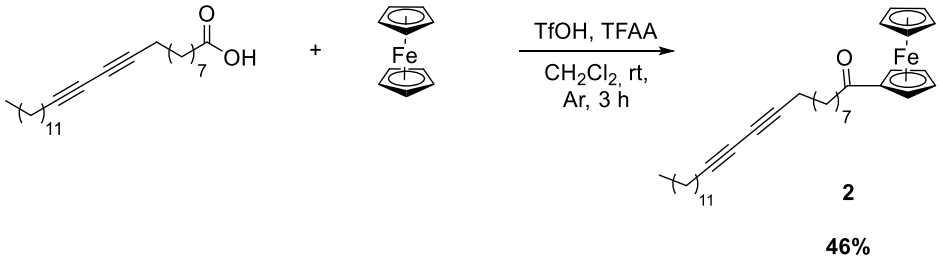

Fig. 25: Mild acylation of ferrocene using PCDA.

To further study the incompatibility of $AlCl_3$ and the diyne substrate, the monoacylated product **2** underwent Friedel–Crafts acylation with lauroyl chloride **3**. However, the desired product was not observed in this case, but instead, a mixture of products was observed on TLC. Mass spectrometry of the reaction mixture showed a gaussian type profile instead of a few peaks. We did not study the mechanism of reaction between $AlCl_3$ and the diyne moiety, but it was clear that both could somehow react together, explaining why the reaction was not working as intended. There is, however, no report in the literature regarding this issue. As a consequence, the Friedel–Crafts acylation was left aside during the syntheses.

As the conditions with TfOH/TFAA successfully provided **2**, the last step in order to obtain the desired molecule was the second acylation of the methoxypoly(ethylene glycol) 2000

[209] D. Plazuk and J. Zakrzewski, Journal of Organometallic Chemistry, 2009, https://doi.org/10.1016/j.jorganchem.2009.01.007.

(PEO2000) chain. The carboxyl terminated PEO2000-COOH was first synthesized from the commercially available PEO2000-OH (**Fig. 26**).

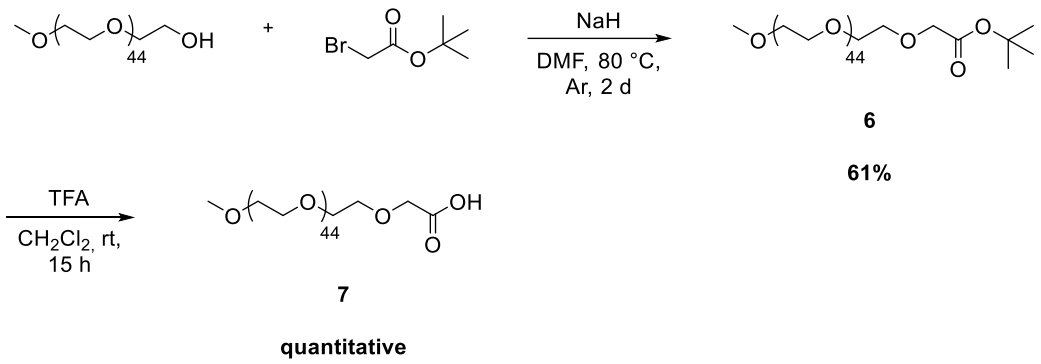

Fig. 26: Synthesis of PEO2000-COOH.

PEO2000-OH was first deprotonated by sodium hydride and reacted with tert-butylbromoacetate under heating at 80 °C. Intermediate **6** could be obtained in relatively good yield and the deprotection of the carboxyl group by trifluoroacetic acid (TFA) quantitatively provided the desired PEO2000-COOH **7**. The acylation of **2** by **7** under mild conditions with TfOH/TFAA resulted in a failure as no product was detected. The reason was that these conditions are too mild, and the conjugation of the first ketone greatly reduced the reactivity of the second unsubstituted ring. This was coherent with the reaction to obtain **2** in which no disubstituted product was observed.

To narrow down the reasons why exactly the second acylation could not operate, an already functionalized intermediate was used as study base. Instead of ferrocene, the commercially available ferrocenemonocarboxylic acid was utilized as starting material. Carboxylic acids and ketones are both electron withdrawing groups with possibility of delocalization of electrons in a π-system by resonance. Therefore, their electronic effects are very similar toward the Cp rings. However, in the acylation conditions with TfOH/TFAA, the carboxylic acid could possibly react as acylating reagent and form ferrocene oligomers. To prevent that, it was transformed into the corresponding amide (**Fig. 27**).

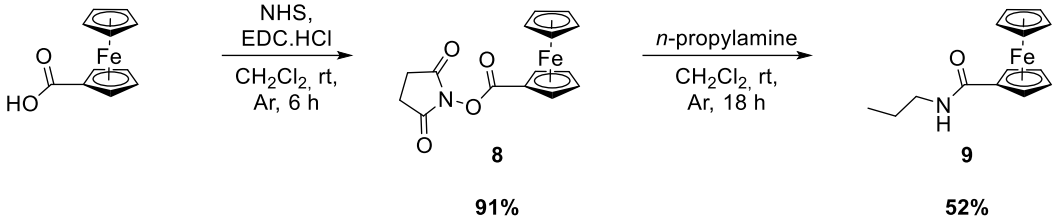

Fig. 27: Synthesis of the model monoacylated ferrocene using *n*-propylamine

The first step consisted of activating the carboxyl group using *N*-hydroxysuccinimide (NHS). After obtaining **8**, it was reacted with *n*-propylamine, a simple amine for study purposes, providing the intermediate **9** with decent yield. The acylation of **9** with PCDA was then performed in the same experimental conditions, but no product was observed. Once more, these mild conditions were not strong enough to overcome the deactivation of the second ring due to the amide group. It was clear that the use of TfOH/TFAA was specific to the monosubstituted product, causing the failure of the attempt with PEO2000-COOH.

Knowing that the deactivating effect of any carbonyl derivative group was too strong to allow the second acylation, a two-step pathway to introduce the first chain was investigated in order to reduce the electronic effect affecting the Cp rings. Carboxyl group can be functionalized and have its electronic properties modified. To preserve the functionality while reducing its strong electron withdrawing effect, an attempt of acylating the activated ester derivative **8** was performed before the amidation reaction. NHS is used as activating group for carboxylic acids because of the electronic properties of the resulting esters. Indeed, the strong electron withdrawing effect reduces the electron density of the carbonyl by resonance effect. The idea was to assume that the attracting effect of the NHS group would mainly affect the carbonyl group while having minimal effect on the Cp ring. As a consequence, the reactivity of the nearby Cp ring would be higher and possibly lead to the second acylation. Thus, the activated NHS intermediate **8** was engaged in the acylation reaction with PCDA in the presence of TfOH/TFAA and the desired product **10** was isolated in very low yield (2%, **Fig. 28**).

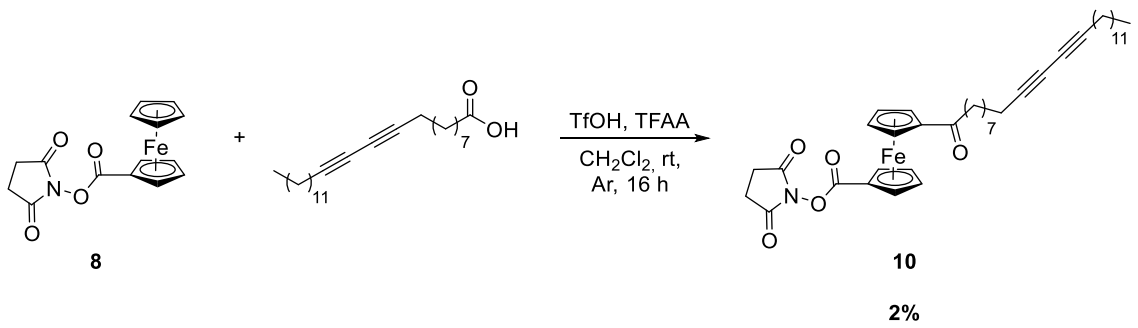

Fig. 28: Acylation in mild conditions of ferrocenemono NHS ester **8** using PCDA.

The desired product could be isolated and characterized by ^{1}H NMR. The isolation of the product, even if the yield was extremely low, possibly showed the effect of NHS toward the carboxyl group. However, this effect was minor. The process was clearly not efficient enough and was therefore abandoned and new conditions were explored.

3. Second approach: indirect incorporation of PCDA chain

3.1. Retrosynthesis

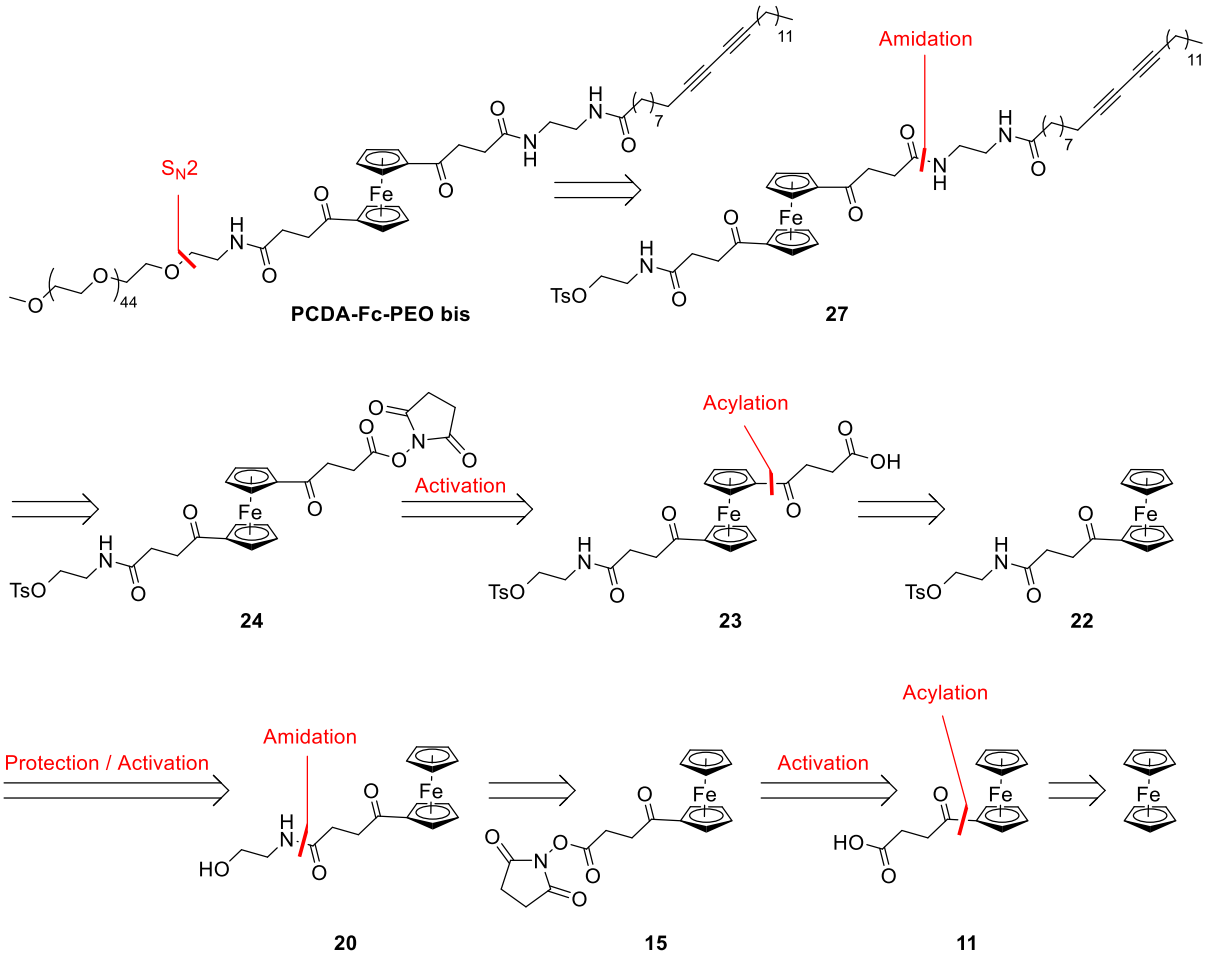

Fig. 29: Retrosynthesis of the second strategy by late incorporation of PCDA and PEO chains.

Since the first strategy failed due to complications regarding the acylation steps, the structure of the target compound was modified by introducing linkers between the ferrocene moiety and the PEO and PCDA chains (**Fig. 29**). Similar to the first strategy, it was decided to introduce the PEO chain at last for ease of purification. Thus, PCDA-Fc-PEO bis would be obtained by nucleophilic substitution of the tosylate intermediate **27**. The latter could be prepared by amidation between the NHS-ester intermediate **24** with the primary amine-functionalized PCDA derivative. Coupling reactions between NHS-ester and primary amines are known to be

very efficient, with high conversion and kinetics. The carboxylic acid-containing precursor **23** could be synthesized by acylation using succinic anhydride. The latter was selected as it was reported to efficiently undergo Friedel–Crafts acylation with no side reactions in contrast with PCDA. The tosylated monoacylferrocene **22** could be synthesized by tosylation of the primary alcohol **20**. The latter could be obtained by amidation in the same way as for compound **27** by reacting the NHS-ester **15** with ethanolamine. Finally, **15** could be easily prepared by Friedel–Crafts acylation using succinic anhydride and ferrocene.

3.2. Acylation using succinic anhydride

As both Friedel–Crafts and TfOH/TFAA acylations did not yield the desired molecules, another pathway was explored using succinic anhydride as electrophile. It is reported that the acylation of ferrocene with succinic anhydride provides both expected products, with the disubstituted being the major product in the case of excess of reagents. The reaction was set using an excess of $AlCl_3$ and succinic anhydride in dichloromethane. Although published articles report that the major product is the diacylated ferrocene, in our case only the monoacylated **11** was isolated in high yield (80%, **Fig. 30**). Published data mentioned the insolubility of the diacylated product while the monoacylated should be soluble in dichloromethane. However, it turned out that the precipitate in the reaction mixture only contained the monosubstituted ferrocene. The soluble fraction was purified on silica gel and proved to be the monoacylated ferrocene as well. The diacylated ferrocene was detected neither by mass spectrometry nor by ^{1}H NMR. However, even though only the monoacylated product was obtained, this method was much more efficient than the two previous ones. Moreover, even if the diacylated ferrocene was not observed, we decided to proceed with the second acylation using the same conditions.

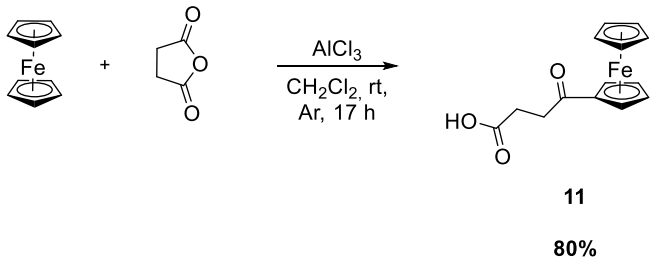

Fig. 30: Acylation of ferrocene using succinic anhydride.

After obtaining intermediate **11**, we first attempted to introduce the PEO chain first. Indeed, we knew that it would not be possible to do the second acylation in the presence of the diyne-containing chain using $AlCl_3$. Therefore, the strategy was to first introduce the PEO chain and then do the acylation. Hence, prior to the coupling reaction with **11**, PEO2000-NH_2 **14a** and PEO750-NH_2 **14b** were prepared from commercially available PEO2000-OH and PEO750-OH, respectively. The shorter PEO chain was selected to simplify the different purification steps of future syntheses (**Fig. 31**).

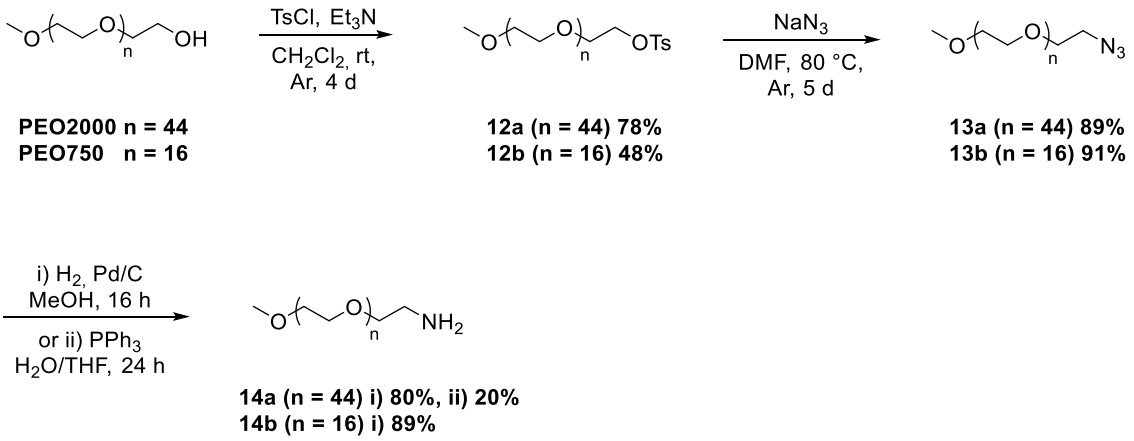

Fig. 31: Synthesis of PEO2000-NH_2 and PEO750-NH_2.

The first step consisted in activating the terminal hydroxyl group into the corresponding tosylate using tosyl chloride (TsCl) in the presence of an organic base. The reaction provided both **12a** and **12b** in decent yields and was followed by the nucleophilic substitution of the tosylate with sodium azide (NaN_3). The reaction proceeded smoothly with high efficiency, yielding **13a** and **13b** with 89 and 91% yields respectively. To synthesize the desired amine, two reduction pathways were explored. The first one was a hydrogenation using Pd/C as catalyst in methanol. Hydrogenation of azides into amines is a well-known method as it usually does not require any complicated purification but only a filtration of the heterogeneous catalyst. In our case, the reduction was quantitative but the obtained product **14a** was grey and did not match the white color of commercially available PEO polymers. The dark color clearly came from Pd/C and attempts of washing on silica gel allowed only partial removal of the grey color. It is known that amines are considered as poisons of palladium due to their high

affinity with the metal center, but this color issue was not observed with the smaller PEO chain **14b**. Although the color with **14a** clearly showed the presence of the catalyst, the product was easily identified by ^{1}H NMR, confirming the total reduction of the azide. However, for purity reasons in the case of **14a**, another reduction pathway was tested. we thus used the classic conditions for the Staudinger reduction of azides. By reacting the azide **13a** with triphenylphosphine (PPh_3) in a mixture of water and THF, the amine-terminated PEO **14a** could be isolated. In this case, the product was white as expected, but the yield was relatively low (20%, **Fig. 31**) and required purification. Thus, both methods in the synthesis of the longer PEO did not provide satisfying results due to low yield or impurities.

A more direct approach was tried, involving the direct amination of the tosylate intermediate **12a**. A 38% (w/w) solution of ammonia in water was used to directly substitute the tosylate. This method provided the desired product **14a** in relatively good yield and showed total conversion of the tosylate. No purification was needed as simple extraction and precipitation in diethyl ether were performed to quickly recover the desired product (**Fig. 32**).

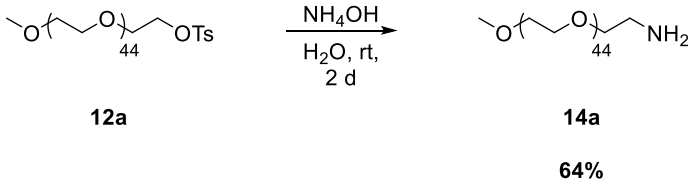

12a **14a**

64%

Fig. 32: Synthesis of PEO2000-NH_2 by direct amination.

After obtaining **14a**, the next step was to graft it onto the monoacylated ferrocene prior to the second acylation step (**Fig. 33**). Thus, **11** was first activated into the corresponding NHS ester to provide **15** which underwent a coupling reaction with either primary amine **14a** or **14b**. The PEGylated intermediates **16a** and **16b** were obtained with low yields due to difficulties in purification on silica gel.

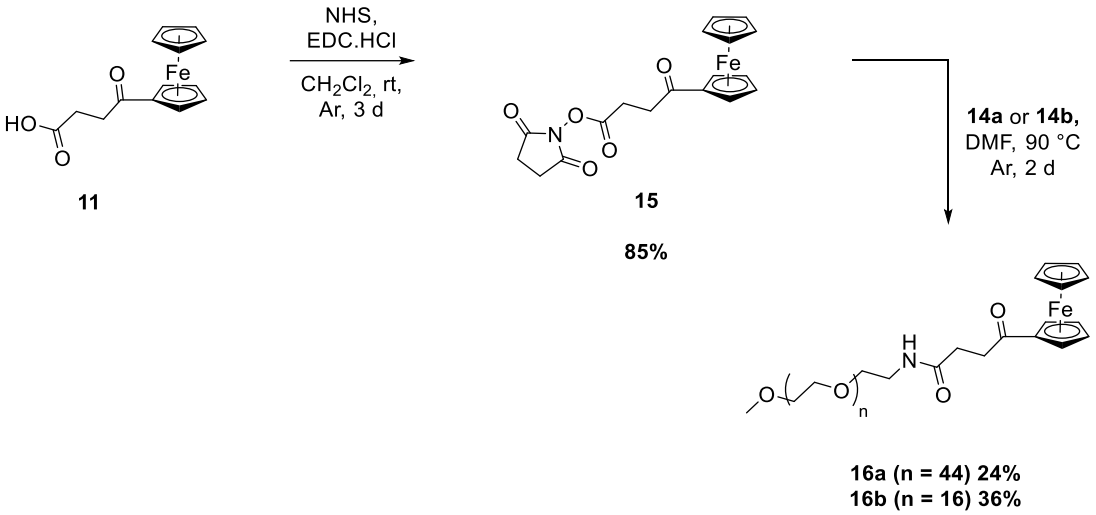

Fig. 33: PEGylation of **11** with PEO750 and PEO2000.

Then, the next step was to substitute the second ring. From previous experiments, it was clear that the second acylation was much more challenging than the first one. Succinic anhydride with $AlCl_3$ were used to acylate **16a** or **16b** but did not yield the desired acylated products. In fact, acylation using $AlCl_3$ in the presence of PEO already resulted in failure in the attempt with PEO2000-COCl and $AlCl_3$ as mentioned previously. The presence of PEO seemed to somehow induce a complete deactivation of $AlCl_3$, perhaps by coordination of PEO to aluminium As both attempts with PEO chains failed, *n*-propylamine was once again taken as model amine to assess the potential effect of PEO interfering with the acylation (**Fig. 34**).

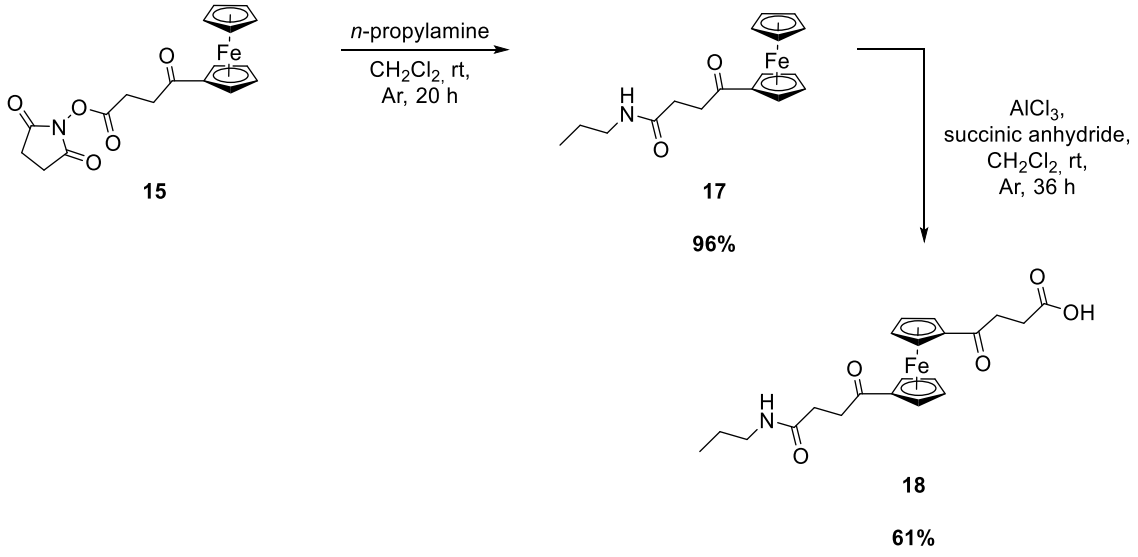

Fig. 34: Synthesis of diacylated ferrocene using succinic anhydride after amidation with *n*-propylamine.

The coupling reaction between the NHS ester **15** and *n*-propylamine provided the intermediate **17** with almost quantitative yield. The difference in yields compared with PEO derivatives **14a** and **14b** resides in the much easier purification with *n*-propylamine. Then, monosubstituted derivative **17** was acylated using succinic anhydride and $AlCl_3$, which resulted in the isolation of the desired product **18** in good yield. By replacing the PEO chain by *n*-propylamine, the acylation proved to work as intended, concluding that PEO could most likely interfere with $AlCl_3$ by possible chelation. However, no article was found on this matter.

3.3. Protecting group for acylation

$AlCl_3$ proved to be incompatible with PCDA and PEO, therefore, a new strategy had to be found in order to do the two acylations before introducing either the lipophilic or hydrophilic chain. To do so, the introduction of a linker with a functionalizable end was used. In this matter, *N*-Boc-ethylenediamine was first chosen to react with intermediate **15** to give molecule **19** in decent yield (**Fig. 35**).

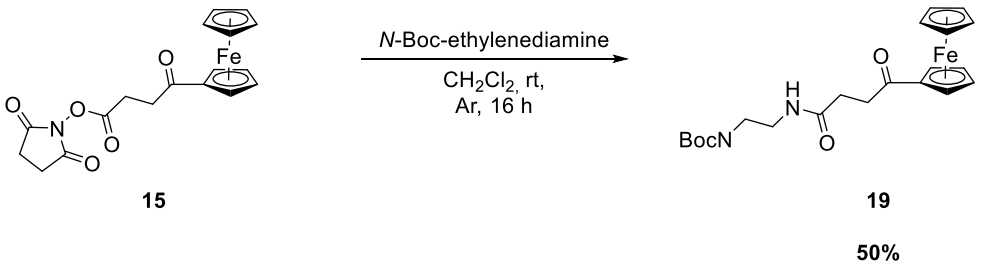

Fig. 35: Synthesis of *N*-Boc protected ferrocene derivative.

Ethylenediamine is an excellent linker due to its high nucleophilic nature via the primary amines, where one can be used to do a first conjugation and the other for extending the chain by typically reacting with another electrophile. In this case, the strategy was to first introduce the linker while having the second amine protected to prevent dimerization. Another important point was to acylate after this step, which would introduce a carboxyl group. If not protected, acido-basic reactions would occur with the primary amine leading to possible solubility issues

in organic solvent as well as risks of side reactions during the NHS ester activation. Therefore, one of the amine was protected to prevent any undesired reactions. However, attempt of acylation of **19** failed and showed in mass spectrometry the deprotected product, without trace of the desired acylated ferrocene. Commonly, Boc protecting groups are deprotected using strong acidic conditions such as TFA or HCl. However, it is also reported that Lewis acid such as $FeCl_3$ or $AlCl_3$ can also selectively deprotect Boc groups.[210,211] Therefore, the use of the Boc group was not compatible with the experimental conditions and the terminal amine was changed.

Thus, *N*-Boc-ethylenediamine was substituted with ethanolamine. Even if NHS ester is a reactive acylation agent, its reactivity is moderate with primary alcohols compared to primary amines. The competitiveness between both is highly directed in favour of the primary amine due to its better nucleophilicity and higher stability of the resulting conjugate (amide against ester). Thus, **15** was reacted with ethanolamine in similar conditions as previously described to provide **20** in good yield (**Fig. 36**).

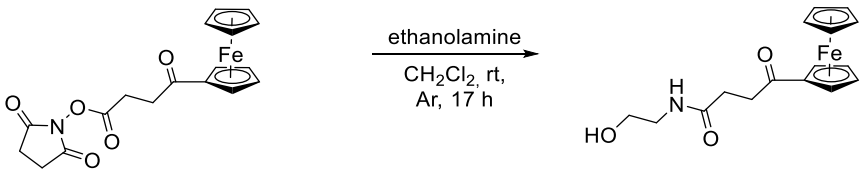

15 **20**

85%

Fig. 36: Synthesis of free hyroxyl ferrocene derivative using ethanolamine.

During the purification, no dimers nor esters were observed, showing the limited reactivity of the hydroxyl end toward NHS ester compared to the primary amine. Then, acylation of **20** was attempted with succinic anhydride and $AlCl_3$. After isolation and characterization of the product, it turned out that the acylation did not proceed, but instead the esterification with the primary alcohol occurred. The molecular weight being identical for the esterification and acylation products, mass spectrometry could not determine which one was formed during the

[210] R. S. Giri et al., ChemistrySelect, 2020, https://doi.org/10.1002/slct.201904617.
[211] D. S. Bose and V. Lakshminarayana, Synthesis, 1999, https://doi.org/10.1055/s-1999-3694.

reaction. ^{1}H NMR confirmed the formation of ester adduct **21** due to the characteristic singlet proton peak of the unsubstituted Cp ring accounting for 5 protons (**Fig. 37**).

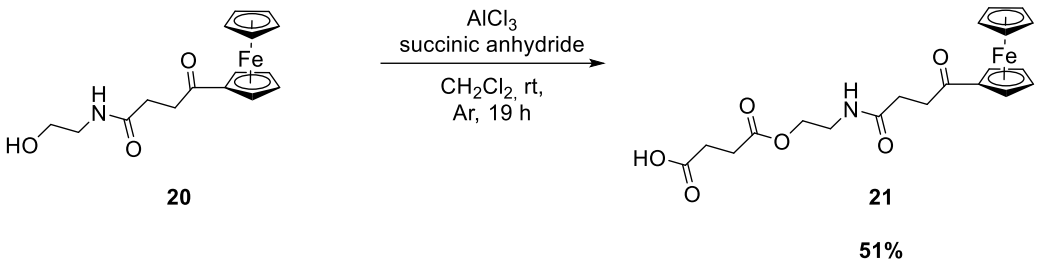

Fig. 37: Attempt of second acylation of **20** with succinic anhydride resulting in the esterification.

To prevent esterification and promote acylation, the reactivity of the hydroxyl group had to be disabled. We figured the best method would be using a protecting group resistant to acidic conditions as opposed to Boc. To limit the total amount of steps of the synthesis, *O*-tosyl was selected. Indeed, while being a strong electrophile, it can also be used as a protecting group. The purpose was to take advantage of the fact that it could be used as a protecting group and leaving group, which allowed to skip the deprotection step commonly done with most protecting groups. Therefore, **20** was reacted with tosyl chloride and triethylamine, providing intermediate **22** in decent yield (**Fig. 38**).

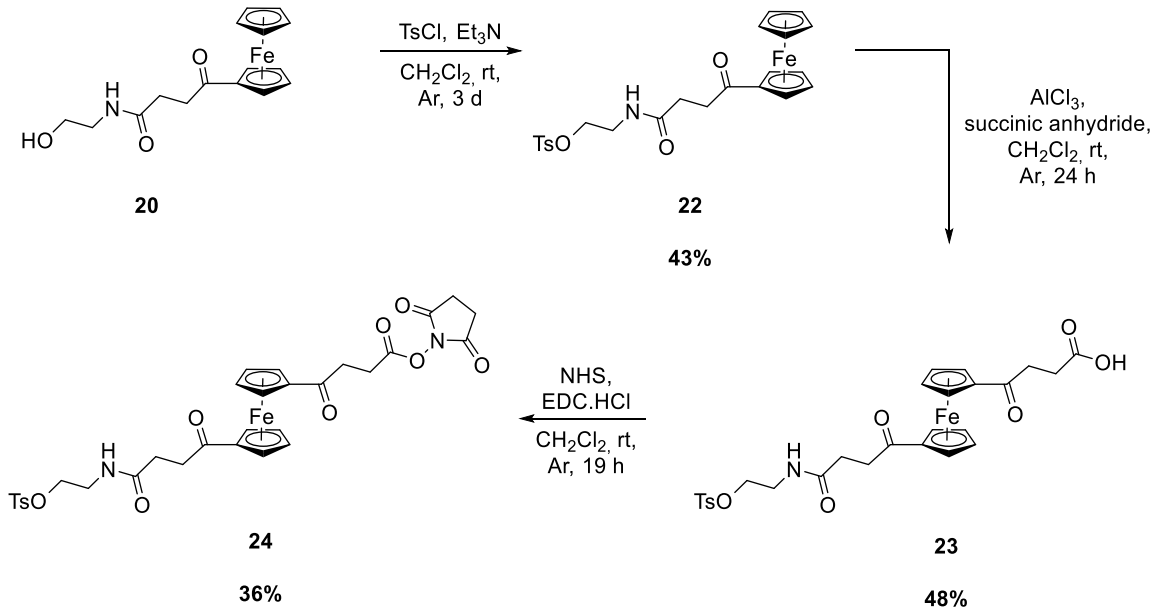

Fig. 38: Synthesis of bifunctionalized-end ferrocene derivative bearing NHS ester and tosyl group.

Then, acylation was performed in the presence of succinic anhydride and $AlCl_3$. This time, the desired product **23** was obtained and isolated (48%). ^1H NMR showed the characteristic peaks of the tosyl group as well as the splitting of the ferrocene signals, confirming the successful acylation of the second ring. After obtaining **23**, the carboxyl group was activated into the corresponding NHS ester to give **24**.

From this point, two options were considered, as to which chain, PCDA or PEO, would be introduced first. From a synthetic point of view, it was decided to PEGylate at the last step for ease of purification. Therefore, PCDA chain was first conjugated with the NHS ester. To make the reaction possible, PCDA was modified with ethylenediamine to introduce a primary amine (**Fig. 39**). PCDA was activated with NHS and EDC.HCl to obtain the corresponding derivative **25**. Then, large excess of ethylenediamine in dichloromethane allowed the monosubstitution to provide the desired amine derivative **26** with good overall yield.

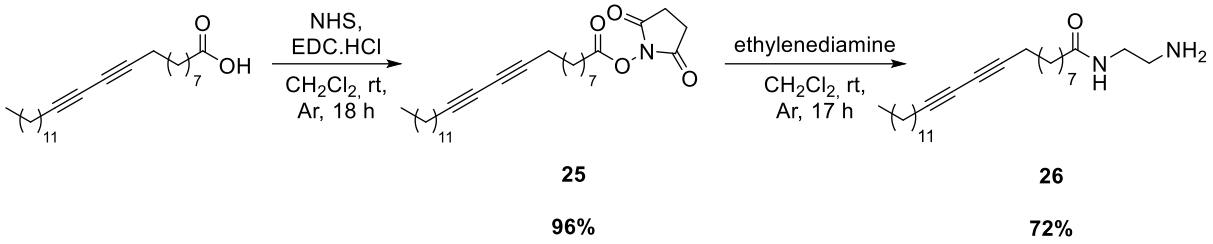

Fig. 39: Synthesis of amine terminated PCDA **26**.

Finally, the diacylated **24** and the primary amine **26** were reacted in DMF at 90 °C (required because of poor solubility of the reagents), which provided the desired product **27** in 37% yield (**Fig. 40**). Even if primary amines are relatively nucleophilic, no displacement of the tosyl group was observed.

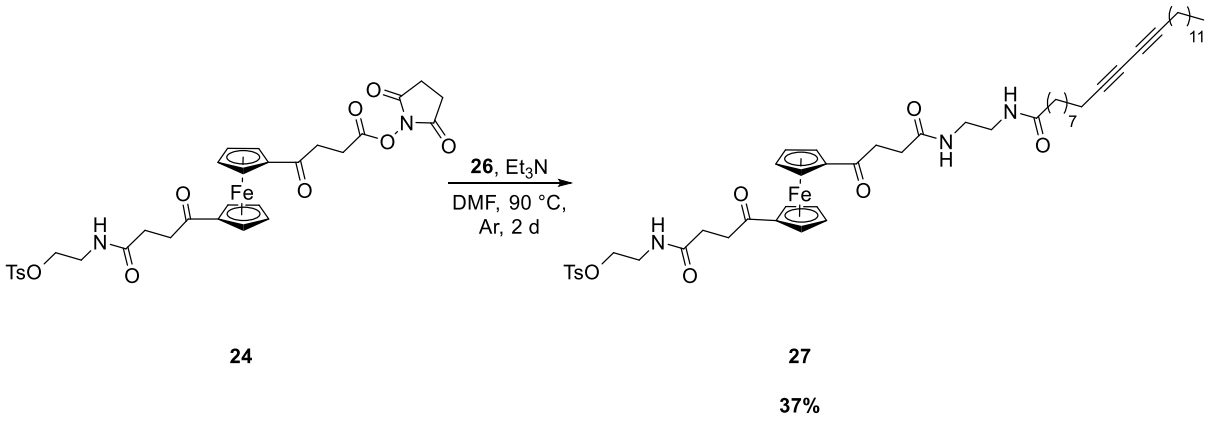

Fig. 40: Incorporation of the lipophilic chain by amidation of **24**.

To obtain the final product, PEGylation of the molecule by substitution of the tosyl group was attempted. Tosyl groups are sensitive to nucleophiles such as alkoxides. Thus, the alkoxide from 1.2 equiv. of PEO2000-OH was first prepared by deprotonation with 2.0 equiv. of sodium hydride (60% (w/w)) before addition of the tosylate **27**. The reaction was left stirring for two days but no product was detected.

The synthesis was tried again but starting this time from the commercially available ferrocene monocarboxylic acid that was previously used for the acylation with TfOH/TFAA. Moreover, since small molecules seemed to be more reactive than PEO chains, it was decided to introduce the latter first, and then proceed to the substitution of the tosyl group with the lipophilic chain (**Fig. 41**). Thus, the synthesis followed the pattern used for compound **24**. The activated ferrocene **8** was reacted with ethanolamine to provide the primary alcohol **28**. Activation into the corresponding tosylate yielded the intermediate **29** which was then acylated with an excess of succinic anhydride and $AlCl_3$. The resulting disubstituted ferrocene **30** could be isolated and activated by NHS and EDC.HCl providing the compound **31** in good yield. Finally, the PEGylation step was performed by reacting PEO2000-NH_2 **14a** and **31** in the presence of triethylamine, in order to give the intermediate **32**.

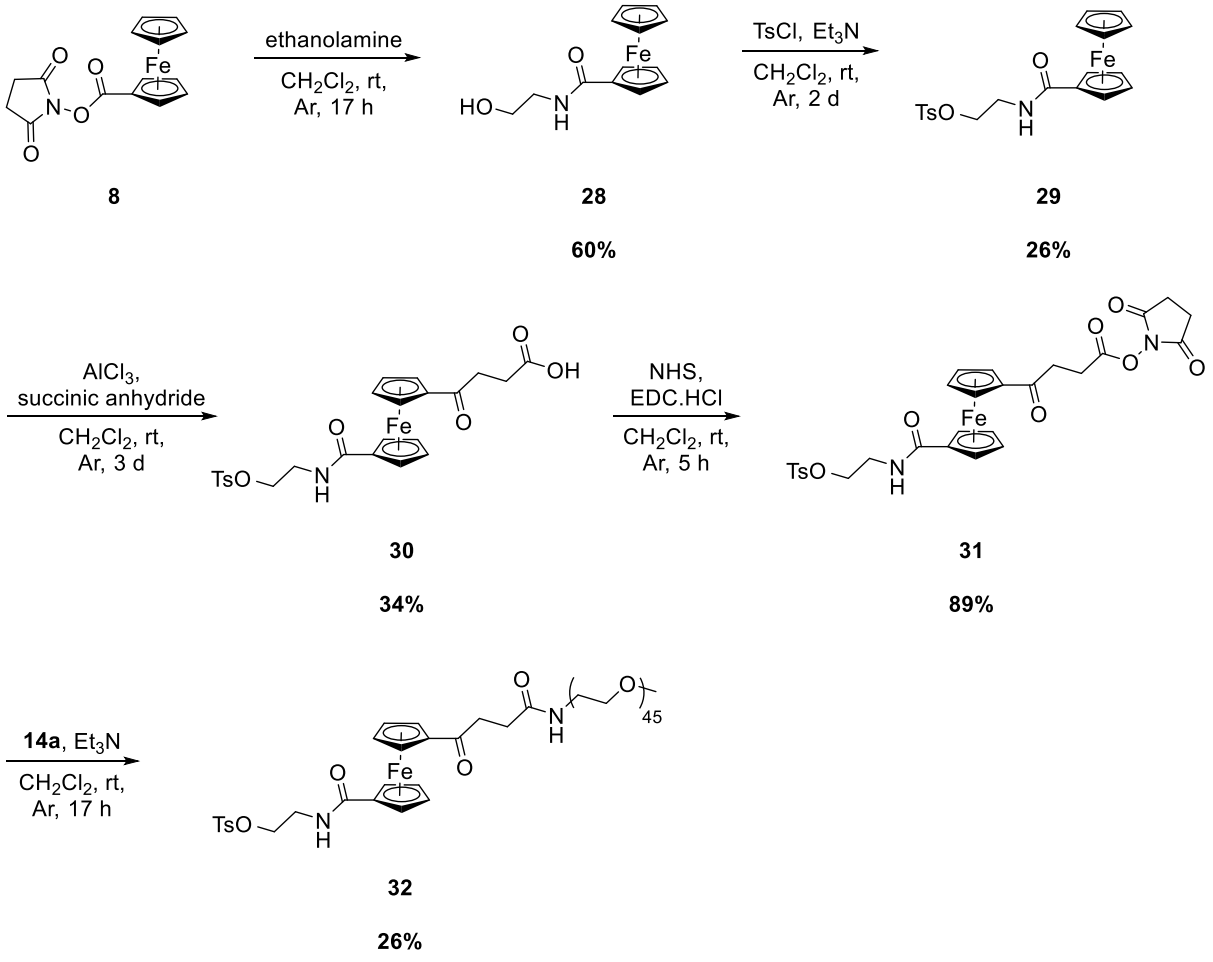

Fig. 41: Synthesis of PEGylated intermediate **32** bearing a tosyl group.

The last step to possibly obtain the desired amphiphile was the substitution of the tosyl group by the lipophilic chain. As mentioned before, alkoxides are great nucleophiles for this type of reaction. The carboxyl group in PCDA was reduced to form the corresponding alcohol. To do so, PCDA was reacted with lithium aluminium hydride ($LiAlH_4$) in diethyl ether at 0 °C. The reduction was total and provided the alcohol intermediate **33** in high yield (**Fig. 42**).

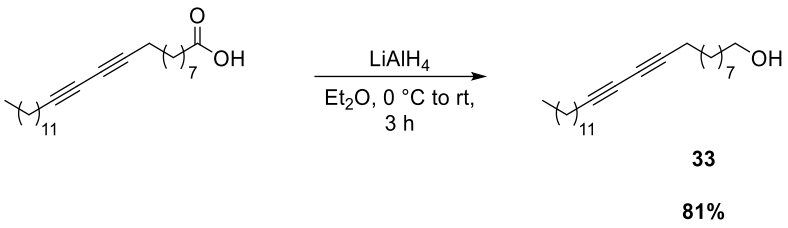

Fig. 42: Reduction of PCDA into the corresponding alcohol.

The reaction of substitution between the tosylate intermediate **32** and the primary alcohol **33** was attempted with large excess of NaH (6.0 equiv.) but same as the first attempt, the reaction failed and no product was detected. Since ferrocene has a very characteristic yellow-orange color, it is easy to monitor reactions involving ferrocene by TLC. In the case of this last step, no newly formed product was detected, even after work-up and purification on silica gel. The reason of the failed attempts was not identified. After trying to synthesize the desired amphiphilic molecule by various means of acylations, ferrocene could be successfully acylated twice. However, the substitution of the tosyl group turned out to be difficult, resulting in failed attempts as no products could be detected. It was decided to take an easier approach which consisted in starting from an already bifunctionalized ferrocene, namely 1,1'-ferrocenedicarboxylic acid.

4. Third approach: starting from 1,1′-ferrocenedicarboxylic acid

4.1. Retrosynthesis

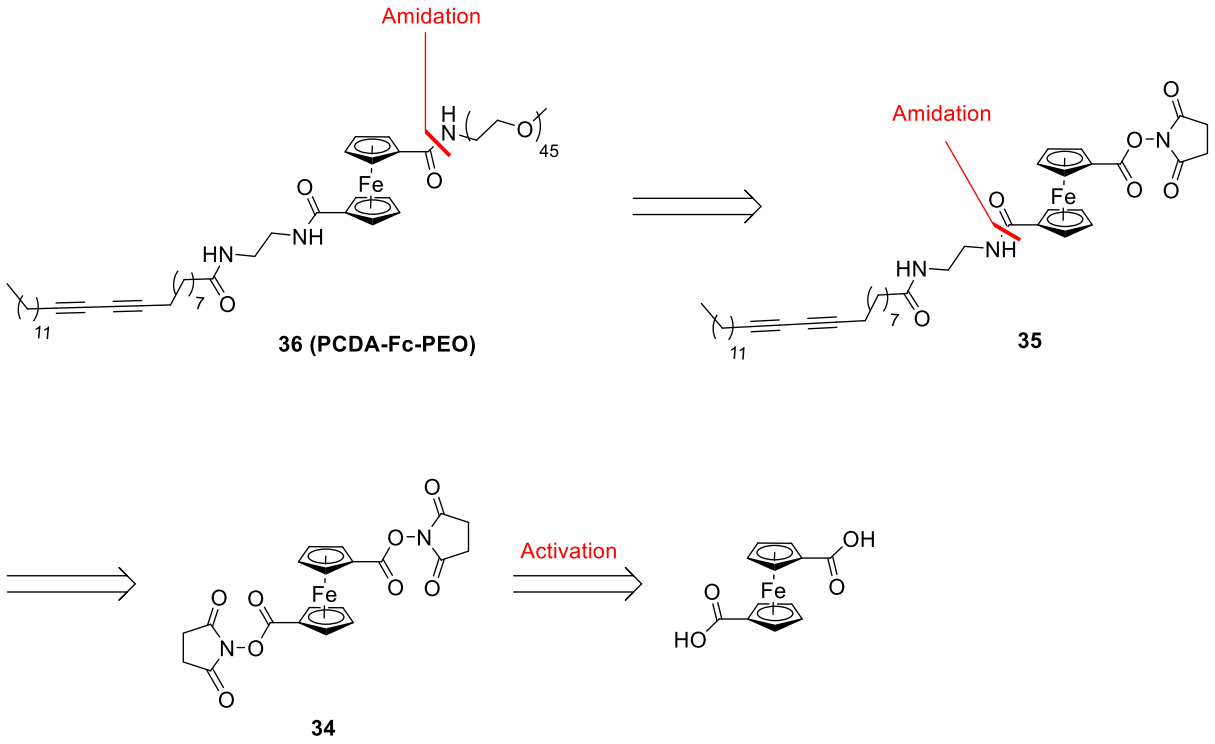

Fig. 43: Retrosynthesis of PCDA-Fc-PEO amphiphile starting from 1,1′-ferrocenedicarboxylic acid.

The third strategy relies on the modification of commercially available 1,1′-ferrocenedicarboxylic acid with simple amidation reactions (**Fig. 43**). The desired molecule PCDA-Fc-PEO could be synthesized by introducing the PEO chain at the last step by amidation reaction of the methoxypoly(ethylene oxide) amine 2000 with the activated intermediate **35**. The latter could be prepared by similar reaction but with the amine-terminated PCDA chain and the diNHS-ester **34** which was obtained from the double activation of 1,1′-ferrocenedicarboxylic acid.

4.2. Synthesis of PCDA-Fc-PEO amphiphile

1,1′-ferrocenedicarboxylic acid is commercially available but is more expensive than ferrocene or ferrocenecarboxylic acid. However, the molecule is already bifunctionalized, which makes the derivatization much easier and decreases the number of steps to the target compound.

Thus, only coupling reactions have to be carried out to obtain the desired amphiphile. However, 1,1'-ferrocenedicarboxylic acid is symmetrical while our objective is to synthesize unsymmetrical ferrocene derivatives. Therefore, the main challenge was to favor the single amide while limiting as much as possible the formation of the doubly substituted product.

From the previous presented syntheses, the activation by NHS ester proved to work efficiently with primary amines. Therefore, both carboxylic acids were activated into NHS esters to provide intermediate **34** (**Fig. 44**). Reaction with the amine-terminated PCDA derivative **26** provided the first amide intermediate **35**. This step was done using 1.0 equiv. of each reactant and dropwise addition of the primary amine to a solution of **34** was necessary to limit the formation of the diamide product. However, the reaction was not truly successful, affording the desired product in low yield along with the diamide product as well as unreacted **34**. These three products could be separated on silica gel. Even if the yield was low, it was sufficient to carry out the last step.

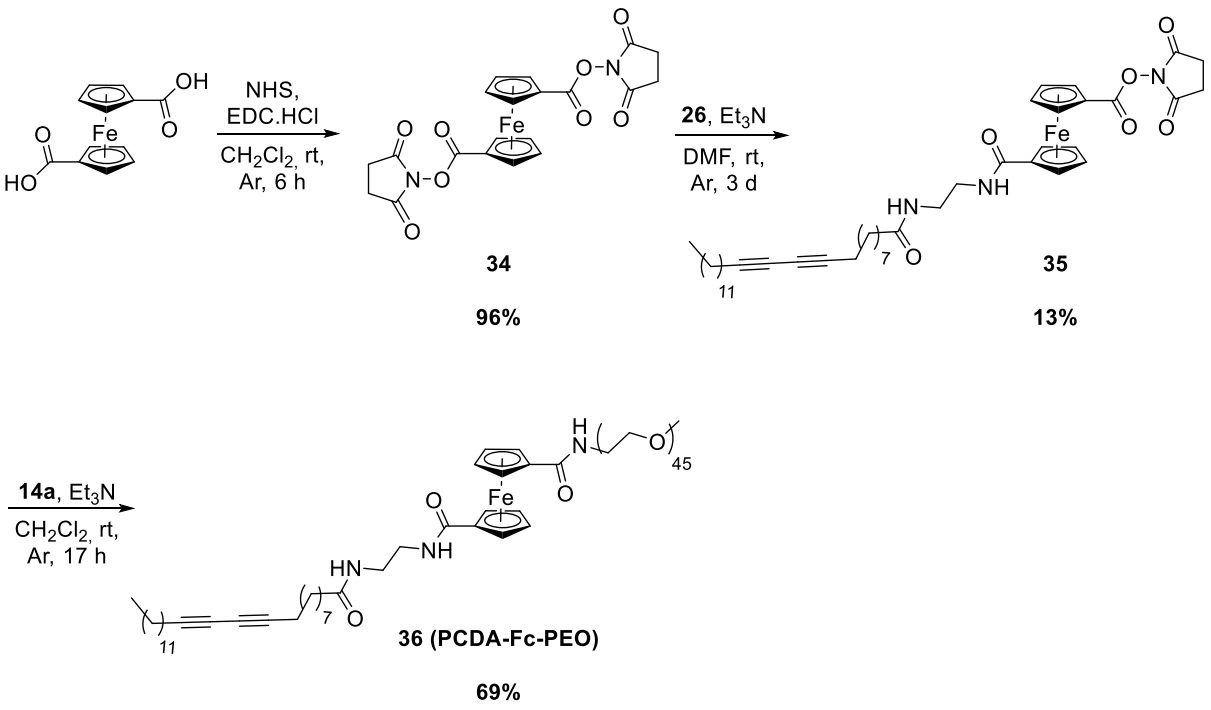

Fig. 44: Synthesis of amphiphile **36** starting from 1,1'-ferrocenedicarboxylic acid.

The last step to obtain the target molecule was the coupling reaction to introduce the PEO chain. **35** was reacted with PEO2000-NH_2 **14a** and triethylamine in dichloromethane. The

reaction mixture was easily purified on silica gel to afford the final molecule **36** (PCDA-Fc-PEO) in good yield. A control amphiphile was also prepared to study the effect of ferrocene on micelles properties. To this end, activated PCDA **25** was reacted with PEO2000-NH_2 **14a** to form the desired molecule **37** (PCDA-PEO, **Fig. 45**). Both amphiphiles **36** and **37** were then self-assembled into micelles in aqueous medium.

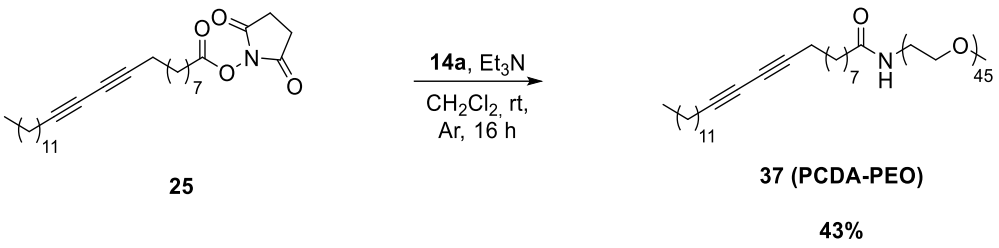

Fig. 45: Synthesis of amphiphile **37** without ferrocene.

4.3. Micelle formulation

Amphiphiles **36** and **37** were dispersed in ultrapure water (Milli-Q®, 18.2 MΩcm at 25 °C) and lyophilized to obtain fine yellow and white solids, respectively. Then, micelle samples were prepared by dispersing 10 mg of the amphiphiles in 1 mL of ultrapure water to obtain a final concentration of 10 mg mL^{-1}. This concentration was based on previous studies that demonstrated that the CMC of micelles assembled from PCDA-PEO2000 amphiphiles was 0.095 mg mL^{-1}. Thus, a concentration of 10 mg mL^{-1} is around 10 times higher than the CMC, which secures the formation of micelles. Once dispersed, the samples were sonicated either by ultrasonic probe (40% output, 10 min total time) or simply using an ultrasound bath. Then, filtration on 0.2 µm nylon syringe filter was performed to eliminate any large aggregates or dust particles. The hydrodynamic diameter was measured for PCDA-PEO micelles which displayed a narrow distribution with a mean value of 14 nm. The PCDA-PEO micelles could be photopolymerized under 254 nm UV light for 2 h, resulting in a yellow solution reflecting the formation of a conjugated system.

However, in the case of PCDA-Fc-PEO micelles, the first DLS measurement showed relatively good results but the colloid started to display higher scattered intensity when the measurement duration was extended. Macroscopically, an opaque cloud started to form and a

brown to dark precipitate appeared. The DLS set-up used in our laboratory uses a 450 nm diode laser, close to the absorption maximum of ferrocene (442 nm), and it appears that, despite the low intensity of the DLS laser, the micelles were photodegraded during the measurment. In addition to that, the photopolymerization of the PCDA-Fc-PEO micelles at 254 nm unexpectedly proved to induce a photodegradation of the micelles as well, but to a lesser extent, compared to the 450 nm laser. In fact, in late 1960s, A. N. Nesmeyanov from Lomonosov Moscow State University published several articles on the photolysis of ferrocene derivatives bearing acyl groups. He observed the photodegradation of ferrocene dicarboxylic acid in water by visible light, yielding insoluble ferric hydroxides and dimer of cyclopentadienecarboxylic acid.[212] These results were confirmed by A. M. Tarr followed by more in-depth studies in the late 1960s.[213] In short, several reports showed that acylferrocenes could be photodegraded by illumination in the visible absorption band of ferrocene at 442 nm. Our observations were very similar to that of Nesmeyanov and Tarr, which made us assume that our micelles underwent intense photodegradation during the DLS measurements.

As a result, ferrocene and photopolymerization of the diyne chains appeared not to be compatible in our case. However, these findings led us to explore the photolability of the micelles to develop an original light-triggered drug delivery system. As a consequence, the idea of crosslinking the micelles was abandoned and the lipophilic chain was modified to a simple stearyl moiety.

5. Modification of the fatty chain: C_{18}-Fc-PEO and C_{18}-PEO

5.1. Previous C_{18}-NB-PEO micelles

Our group already reported the use of micelles containing a stearyl lipophilic chain instead of PCDA.[214] The amphiphile was made of a C_{18} tail, a photo-labile nitrobenzyl group, and a PEO2000 chain. The 2-nitrobenzyl group was known to be photo-cleavable under UV light by generating 2-nitrosobenzaldehyde and PEO2000-COOH. The amphiphile could self-assemble into 12 nm C_{18}-NB-PEO micelles in aqueous media, characterized by a CMC value of 0.085

[212] A. N. Nesmeyanov et al., Bulletin of the Academy of Sciences of the USSR, Division of chemical science, 1965, https://doi.org/10.1007/bf01083826.
[213] A. M. Tarr and D. M. Wiles, Canadian Journal of Chemistry, 1968, https://doi.org/10.1139/v68-449.
[214] P. Anilkumar et al., Advanced Functional Materials, 2014, https://doi.org/10.1002/adfm.201400840.

mg mL^{-1}. After encapsulation of DiO dye within the micelles, their uptake by MDA-MB-231 cells was studied by epifluorescence microscopy. Indeed, the DiO-loaded micelles were located within the cells, displaying their ability to be internalized.

MDA-MB-231 cells were incubated with micelles at various concentrations from 0.2 to 60 µM for 12 h. *In vitro* cytotoxicity studies showed no significant effect on the cells without illumination. However, cells that were illuminated by UV light (350 nm) showed a completely different behaviour. Illuminated micelles did not induce any cytotoxicity at concentrations lower than 0.2 µM. Above that, a decrease in cell viability was observed and became significant at 2 µM where 62% of cells were killed. At 6 µM, 90% of the cells did not survive, highlighting the high potency of the micelles under illumination. The reported IC_{50} was 1.7 µM in contrast with Taxol that had an IC_{50} of 15 µM under the same experimental conditions.

Therefore, the study showed that micelles bearing a photo-labile linker with stearyl and PEO2000 chains could be used as effective drug carriers. On the basis of this study, it was decided to replace the PCDA chain by a stearyl chain.

5.2. Synthesis of C_{18}-based micelles

The synthesis was performed using the strategy described for amphiphiles **36** and **37** but using a stearoyl carbon chain instead of the 10,12-pentacosadyinoyl one. 1,1'-ferrocenedicarboxylic acid was doubly activated into the corresponding NHS esters. However, in this case, different conditions were used that greatly improved the work-up step, decreased the reaction time and limited the formation of impurities due to the excess of free NHS. This new method consisted in using a different source of NHS that is N,N'-disuccinimidyl carbonate (DSC). The activation of the dicarboxylic acid with DSC in the presence of triethylamine was performed in acetonitrile. As the reaction proceeded, the desired product **34** precipitated. By filtration and washing with acetonitrile, the product could be easily isolated in good yield. Then the activated derivative **34** was reacted with *n*-octadecylamine to perform the first amidation reaction and introduce the lipophilic tail. Intermediate **38** was obtained in decent yield as opposed to **36** which was isolated with 13% yield only. Then, from **38**, the PEGylation step was performed and provided the target molecule **39** (C_{18}-Fc-PEO) (**Fig. 46**).

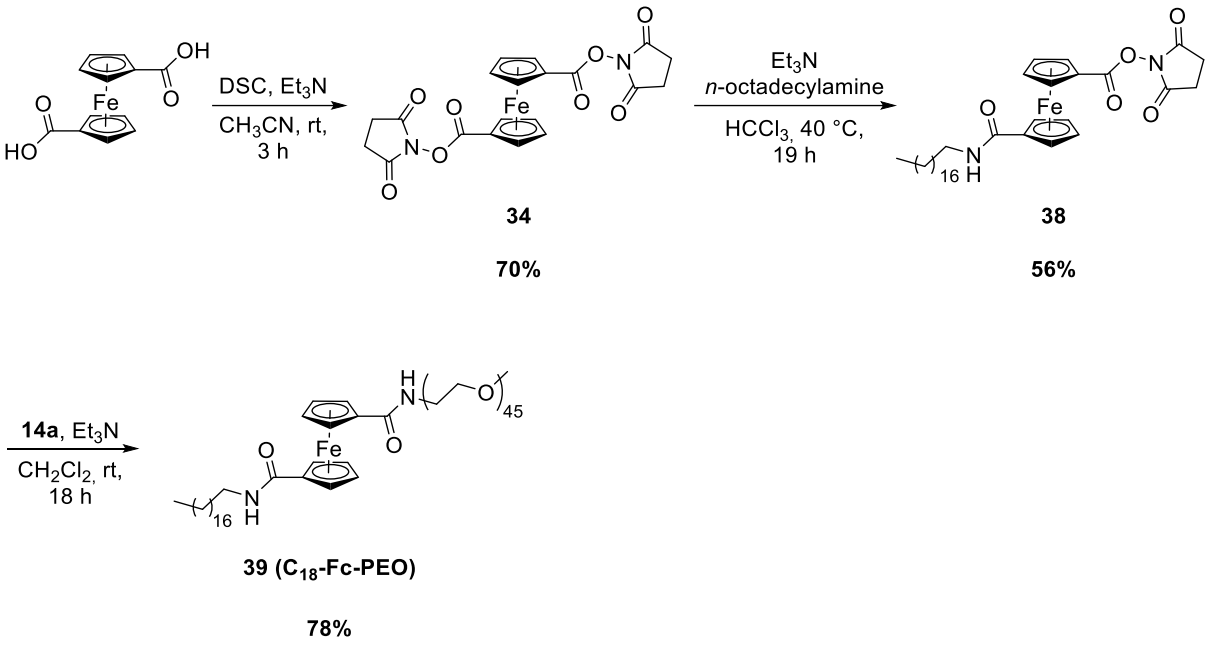

Fig. 46: Synthesis of amphiphile **39** (C_{18}-Fc-PEO).

The control molecule was also synthesized following the scheme described for **37** (**Fig. 47**). In short, stearic acid was activated into the corresponding NHS ester using the classic conditions with NHS and EDC.HCl to obtain intermediate **40**. Then, the PEO chain was introduced by amidation reaction to provide the desired amphiphile **41** (C_{18}-PEO).

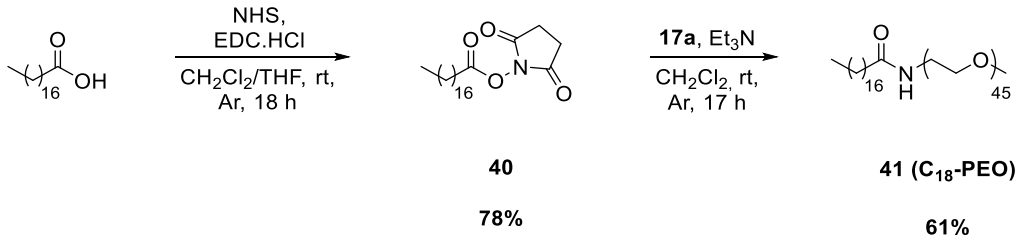

Fig. 47: Synthesis of amphiphile **41** (C_{18}-PEO).

Both amphiphiles C_{18}-Fc-PEO and C_{18}-PEO were successfully synthesized with great overall yields and in a limited amount of steps. Their structure was confirmed by full characterization and their ability to form micelles upon aqueous dispersion was further studied.

6. Formulation of micelles

6.1. Self-assembly

Micellization followed the usual protocol. In short, 10 mg of either C_{18}-PEO or C_{18}-Fc-PEO were dispersed in 1 mL of ultrapure water (Milli-Q®, 18.2 MΩ cm at 25 °C). The dispersion was sonicated using either an ultrasonic probe (40% output, 10 min) or ultrasound bath. Then, filtration on a 0.2 µm nylon syringe filter was performed to remove large aggregates and dust particles, which led to a 10 mg mL^{-1} solution of C_{18}-PEO and C_{18}-Fc-PEO micelles used in subsequent experiments. As these micelles had the same lipophilic and hydrophilic chains as the previously reported C_{18}-NB-PEO, the CMC of which was 0.095 mg mL^{-1}, the properties of C_{18}-PEO and C_{18}-Fc-PEO micelles were expected to be similar.

6.2. Characterization of micelles

6.2.1. DLS measurements

C_{18}-PEO and C_{18}-Fc-PEO aqueous colloids were first characterized by DLS at a concentration of 10 mg mL^{-1} to assess whether or not micelles were formed (**Fig. 48**). The advantage of checking by DLS is the fast process which allows the verification of the presence of nanoparticles before further characterizations. The hydrodynamic diameters were measured by DLS using a 640 nm laser, compatible with ferrocene. As expected ferrocene showed photostability during the measurements as the intensity of the scattered light was stable and the sample remained unaltered even after long exposure to the laser.

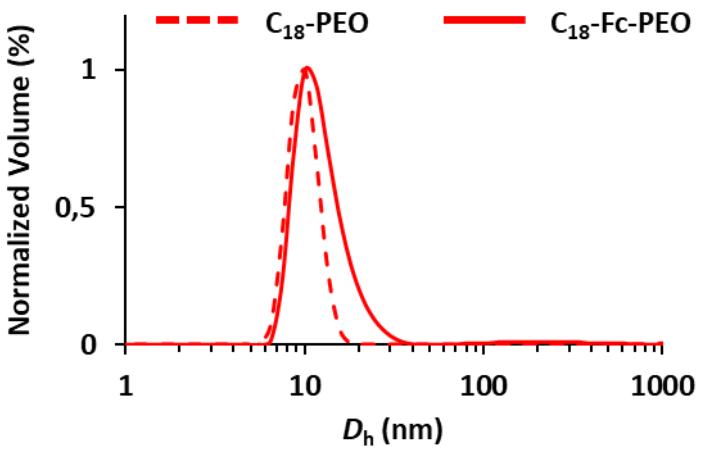

Fig. 48: Hydrodynamic diameter of C_{18}-PEO and C_{18}-Fc-PEO micelles.

Multiple measurements provided the hydrodynamic diameters (D_h) of C_{18}-Fc-PEO and C_{18}-PEO micelles that were both found to be 10 nm. The fact that both micelle types have the same hydrodynamic diameter indicates that the ferrocene moiety does not influence the packing of the molecules. Moreover, their small size of 10 nm is in agreement with all previous studies carried out in our group related to similar micelles. Therefore, DLS measurements showed that C_{18}-PEO and C_{18}-Fc-PEO amphiphiles could easily self-assemble into micelles in aqueous media. To assess the colloidal stability of the micelles, DLS measurements were performed every 7 days over a 3 week period and showed no significant changes, demonstrating the good stability of the objects. In the case of C_{18}-Fc-PEO, storage in the dark was crucial due to the photodegradability of the ferrocene moiety under visible light.

6.2.2. Zeta potential

The surface of nanoparticles can be either positively charged, negatively charged or neutral. Depending on their ionic or nonionic nature, the surface interactions of particles greatly change. Zeta potential (ζ) measurements provide the mean surface charge of a given nanoparticle. Experimentally, ζ is obtained with a sign, positive or negative, and an amplitude. Typically a colloidal solution is considered stable for an absolute value of zeta potential bigger than 30–40 mV (i.e, the particles are strongly negatively or strongly positively charged, repelling each other by Coulombic repulsion). Particles with zeta potentials close to 0 mV are considered as electrostatically unstable, resulting in sedimentation or aggregation. However, this rule does not apply in the case of nonionic nanoparticles such as PEGylated micelles, as the surface charge is known to be neutral, due to steric stabilization. Thus, after confirming the presence of micelles with C_{18}-PEO and C_{18}-Fc-PEO, zeta potentials were measured (**Fig. 49**). The measurements proceeded at 25 °C using 10 mg mL^{-1} suspensions of micelles. As expected, the value for both micelles was just slightly negative (−1 mV) and can be considered neutral. This negligibly negative value is assumed to come from the numerous oxygen atoms constituting the hydrophilic shell.

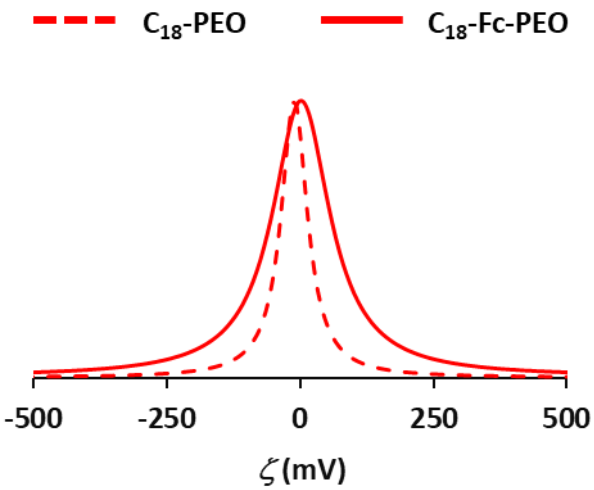

Fig. 49: Zeta potentials of C_{18}-PEO and C_{18}-Fc-PEO micelles.

6.2.3. Determination of CMC

The critical micellar concentration is a crucial parameter to determine as it depicts the aggregation state of amphiphiles (self-assembled micelles or individual unimers) at a given concentration. In biology, intravenously administrated micelle-based drugs face high dilution upon injection and during circulation in the blood stream. Therefore, the CMC values of both amphiphiles were measured. Several techniques can be used and tensiometry was the one selected for its simplicity and ease of access in the laboratory. Tensiometry relies on the change of surface tension as a function of the concentration of surfactant in the suspension. In pure water, the surface tension is equal to 72 mN m^{-1} at 25 °C. As surfactant is added, the surface tension lowers gradually until the air-water interface is saturated with surfactant. The concentration required to saturate the water-air interface is known as the CMC. Surfactant molecules added beyond this concentration aggregate into micelles and have no further impact on surface tension, which becomes constant. Experimentally, the CMC is determined by plotting the surface tension against the concentration which gives two straight lines. The x-axis value of the intersection of these two lines corresponds to the CMC.

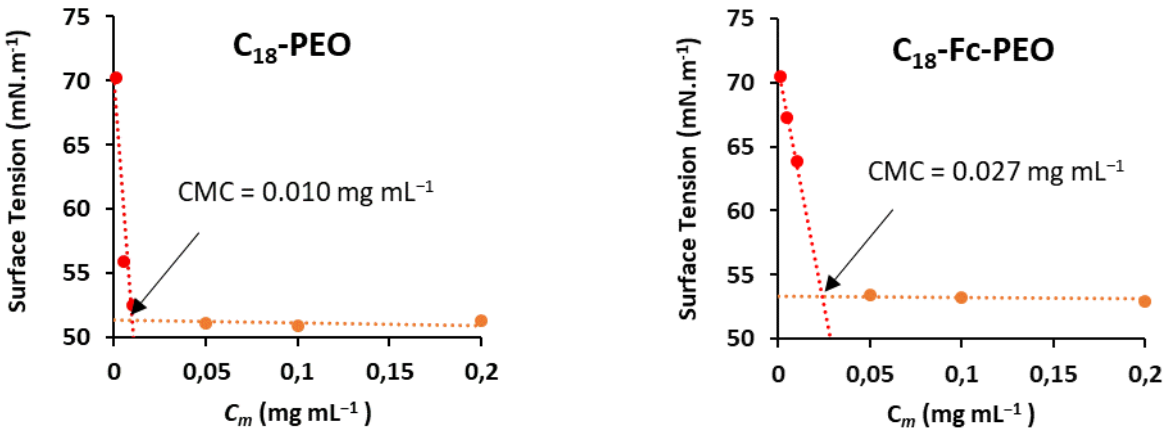

Fig. 50: Determination of the CMC of C_{18}-PEO and C_{18}-Fc-PEO micelles by tensiometry.

Thus, the CMC value of C_{18}-PEO and C_{18}-Fc-PEO amphiphiles were determined using tensiometry (**Fig. 50**). Dispersions of amphiphiles were prepared at concentrations of 0.001, 0.005, 0.01, 0.05, 0.1 and 0.2 mg mL^{-1}. Surface tension was measured in triplicate for each concentration and the mean values were plotted versus the concentration. The calculated CMC values for C_{18}-PEO and C_{18}-Fc-PEO were 0.010 mg mL^{-1} and 0.027 mg mL^{-1}, respectively. In comparison, the CMC of C_{18}-NB-PEO micelles was found to be slightly higher (0.085 mg mL^{-1}), probably because fluorescence was used instead of tensiometry in that case and both methods have different degrees of accuracy regarding the calculation of the CMC value. Nonetheless, the results are in the same order of magnitude and fall within the range of referenced CMC values of C_nPEO_m type surfactants.[215]

7. Conclusion

In this chapter, the synthesis of photopolymerizable micelles containing the unsaturated 10,12-pentacosadiynoyl chain was shown. The Friedel–Crafts acylation of ferrocene quickly faced issues regarding the reactivity of the dyine moiety with the Lewis acid $AlCl_3$. The monoacylated product could be isolated only up to 5% while the disubstituted ferrocene could not be detected. It was assumed that $AlCl_3$ and the diyne could somehow react together which impeded with the acylation. Therefore, an alternative was found.

[215] K. Holmberg, Ullmann's Encyclopedia of Industrial Chemistry, 2019, https://doi.org/10.1002/14356007.a25_747.pub2.

Acylation under mild conditions using TfOH/TFAA could successfully provide the monoacylated ferrocene in good yields. However, due to the deactivation effect of the electron withdrawing substituent on the first ring, the second acylation in similar conditions could not yield the desired diacylated ferrocene. We thus decided to start with an already functionalized ferrocene containing a carboxyl group. In the idea of tuning down the deactivating effect of the carboxyl group and allow the second acylation, the latter was transformed into the corresponding NHS ester. The acylation in the presence of the NHS ester under mild conditions afforded the isolation of the desired product but only in very low yield (2%). As a consequence, this pathway was also abandoned.

The third strategy of acylation was performed with succinic anhydride in the presence of $AlCl_3$. These conditions were the most successful as the mono and disubstituted ferrocenes could be detected and isolated in relatively good yields. However, after multiple activation and coupling reactions, the desired product could not be obtained due to reactivity issues to displace the tosyl group.

The amphiphilic molecules were finally synthesized using the already bifunctionalized 1,1'-ferrocenedicarboxylic acid. The synthesis could be achieved in a limited amount of steps and amphiphiles were self-assembled in water. However, we found out that the micelles underwent intensive photodegradation during DLS measurements, even though the laser intensity was low. The same observation was made during the photopolymerization step at 254 nm, but to a lesser extent. Consequently, the diyne chain was changed to a saturated fatty chain.

A stearyl chain was selected, based on previous studies. The amphiphiles were synthesized and self-assembled into micelles. The physico-chemical characterization of the nanoparticles confirmed that the molecules were indeed aggregated into micelles.

After the successful synthesis and characterization of the micelles, the following chapter will present the study and characterization of the photodegradation process under illumination at different wavelengths. In this framework, two different light sources were used, a blue (460 nm) and a red (740 nm) LED lamp. In the first case, we showed that the micelles could be quickly photodegraded while in the second case, a photosensitizer was needed. *In vitro* studies were performed and displayed very promising triggered cytotoxicity upon illumination.

CHAPTER 2. PHOTODEGRADATION AND CYTOTOXICITY STUDIES

This chapter follows on from the previous one describing the ability of the ferrocene–based micelles to be photodegraded under blue (460 nm) light. Characterization of the photoadducts was performed, showing that ferrocene undergoes dissociation and photooxidation upon illumination. *In vitro* cytotoxicity assays against MCF-7 breast cancer cells were performed and showed very promising dose-response effects. Finally, a modified system using a bacteriochlorin for the generation of singlet oxygen ($^1O_2$) under red illumination (740 nm) proved to also induce a similar photodegradation due to ferrocene oxidation by $^1O_2$. Therefore, this chapter focuses on the behaviour of ferrocene derivatives under illumination.

1. Introduction to photodecomposition of ferrocene derivative:

1.1. Pristine ferrocene

After its discovery in 1951, ferrocene was heavily studied with special attention paid to its redox properties. The ability of ferrocene to be quickly oxidized to the active cationic intermediate ferricenium by oxidant species, such as ROS, allowed the development of a wide range of nanodrugs for chemotherapeutic applications. Ferrocene/ferricenium was long described as a reversible one-electron redox couple for the catalysis of various reactions. Studies concerning ferrocene behaviour toward light started to be reported a few years after its discovery. In 1957, Brand and Snedeen reported the illumination of ferrocene in carbon tetrachloride (CCl_4) under UV light (365 nm) (**Fig. 51**), resulting in the precipitation of a solid identified as ferric chloride ($FeCl_3$).[216] The oxidation state of the iron atom in the latter being +3, they assumed that a photooxidation occurred during the illumination from oxidation state +2 to +3. In fact, this was confirmed by the detection of an absorption band at 615 nm during the first 30 s of illumination, characteristic of ferricenium. The formation of ferricenium and $FeCl_3$ indicated that ferrocene was oxidized and dissociated during the process. This photo-induced phenomenon was ascribed as a ground state donor-acceptor complex (ferrocene-solvent) characterized by a charge transfer to solvent (CTTS) absorption band in the UV region.[217] In 1970, Traverso and Scandola reconducted the experiments and confirmed the observations made by Brand and Snedeen. Additionally, experiments in deoxygenated and oxygenated environments were compared and showed slightly enhanced photooxidation in saturated oxygen solutions,

[216] J. C. D. Brand and W. Snedden, Transactions of the Faraday Society, 1957, https://doi.org/10.1039/tf9575300894.
[217] L. A. Peña et al., Transition Metal Chemistry, 2009, https://doi.org/10.1007/s11243-008-9169-5.

suggesting the implication of oxygen in the photooxidation of ferrocene.[218] The photochemical reaction occured according to the following process:

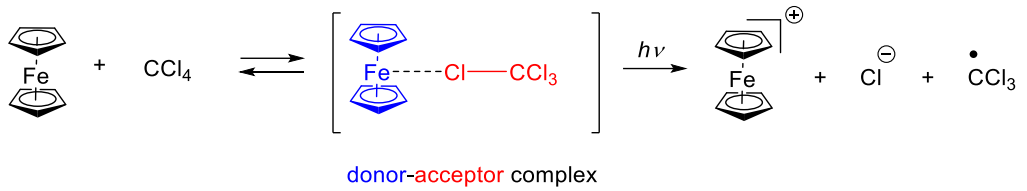

Fig. 51: Photodecomposition of ferrocene with formation of a CTTS with carbon tetrachloride under UV light.

by which ferricenium, chloride anion and trichloromethyl radical were formed. The formation of the radical was demonstrated by the radical polymerization of acrylamide by Traverso (**Fig. 52**).

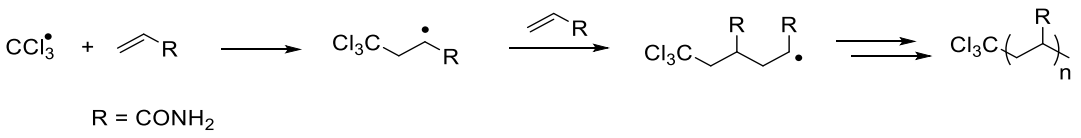

Fig. 52: Radical polymerization of acrylamide using trichloromethyl radical as initiator.

Ferrocene in CCl_4 did not show any photooxidation when illuminated in the visible absorption band of ferrocene at 442 nm.[219] Photooxidation of ferrocene to ferricenium could only be observed in acceptor solvents (e.g. halogenated solvents, CCl_4, $HCCl_3$ and CH_2Cl_2) using UV light due to the CTTS absorption band from the donor-acceptor complex, depicting the importance of the solvent.

Ferrocene possesses a low oxidation potential and is a great electron donor that allows the formation of charge transfer complexes (CTC).[220] Comparable with the photooxidation of

[218] O. Traverso and F. Scandola, Inorganica Chimica Acta, 1970, https://doi.org/10.1016/S0020-1693(00)93335-8.
[219] P. Borrell and E. Henderson, Inorganica Chimica Acta, 1975, https://doi.org/10.1016/S0020-1693(00)89863-1.
[220] M. Rosenblum et al., Journal of the American Chemical Society, 1964, https://doi.org/10.1021/ja01077a025.

ferrocene in halogenated solvents, alkyl/aryl chlorides can form CTC with ferrocene (**Fig. 53**).[221] The generated radical can then initiate the radical polymerization in the presence of acrylate derivatives for instance.

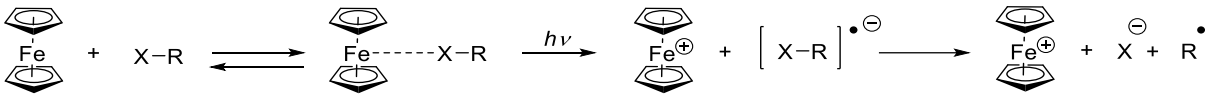

Fig. 53: Formation of ferricenium by CTC with a halide derivative

Besides alkyl/aryl chlorides, electron-poor alkenes, usually acrylates substituted with an electron withdrawing group on position 2, can also be used directly for photopolymerization. Sanderson et al. reported the use of ferrocene as initiator in neat ethyl 2-cyanoacrylate (CA) under ~ 300 nm UV light, where the electron transfer from ferrocene to CA provided the corresponding radical anion.[222] Then, polymerization occurred by addition onto another CA unit and the newly formed active anionic center could grow the chain to obtain the final polymer poly(ethyl 2-cyanoacrylate) (**Fig. 54**). Although ferrocene can be used as photoinitiator and shows rapid photodecomposition, the scope of substrates is quite limited due to the necessity to form a charge transfer complex and the process only occurs under UV illumination.

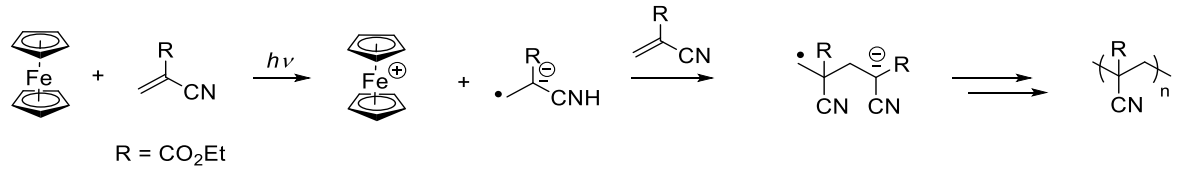

Fig. 54: Anionic polymerization of 2-cyanoacrylate using ferrocene as photoinitiator.

[221] J. A. Anderson et al., Journal of Coatings Technology and Research, 2007, https://doi.org/10.1007/s11998-007-9008-1.
[222] C. T. Sanderson et al., Macromolecules, 2002, https://doi.org/10.1021/ma0212238.

1.2. Cyclopentadienyl iron(II) arene salts $[CpFeAr]^+,X^-$

In early 1960s, Nesmeyanov et al. first reported the synthesis of cyclopentadienyl iron(II) arene [CpFeAr],X starting from the commercially available ferrocene by reaction with an excess of aluminium chloride and arene derivative (benzene, toluene, mesitylene etc.) (**Fig. 55**).[223] The reaction allowed the substitution of one Cp ring, forming the corresponding $[CpFeAr]^+,X^-$ salt, with X being a non-nucleophilic counterion (usually PF_6 or BF_4). $[CpFeAr]^+,X^-$ salts are rather stable but sensitive to nucleophiles as these can displace the arene ring. This is typically observed with water, acetonitrile and alcohols, which limits the solvent choice. The yield of ligand exchange highly depends on the type of substituents on the nucleophile arene ring. Indeed, substituents containing heteroatoms (mainly acyl groups) prevent the reaction to proceed due to chelation of the Lewis acid. Electron donor groups, such as methyl, increase the exchange rate due to the enhanced nucleophilicity of the arene that facilitates the displacement of the Cp ring.[224]

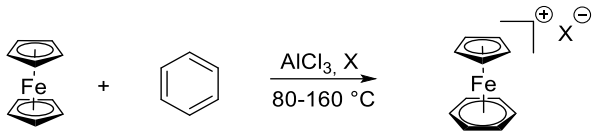

Fig. 55: Ring substitution with benzene.

This substituent effect is also observed for the Cp rings. Indeed, Nesmeyanov reported a much slower reaction with 1,1′-diacetylferrocene compared to ferrocene while 1,1′-diethylferrocene showed the fastest exchange rate among the three. Due to the lability of the arene ring, $[CpFeAr]^+,X^-$ can undergo a second exchange with a new arene ring that is more electron-rich than the one to displace. Gill and Mann, as well as Nesmeyanov, studied the photolysis of $[CpFeAr]^+,PF_6^-$ and $[CpRuAr]^+,PF_6^-$.[225] They showed that in the presence of a mild nucleophilic solvent (S), such as acetonitrile, while illuminating with visible light, the arene ring could be progressively displaced by the solvent molecules by reducing the hapticity of the arene from η^6 to η^4. As a consequence, the arene-metal bond was greatly weakened which, in the end, led

[223] A. N. Nesmeyanov et al., Tetrahedron Letters, 1963, https://doi.org/10.1016/S0040-4039(01)90903-7.
[224] A. N. Nesmeyanov, Pure and Applied Chemistry, 2009, https://doi.org/10.1351/pac196817020211.
[225] T. P. Gill and K.R. Mann, Inorganic Chemistry, 1983, https://doi.org/10.1021/ic00156a011.

to the total dissociation and replacement of the arene by three solvent molecules to form a coordinatively saturated cyclopentadienyl iron cationic complex (**Fig. 56**). The authors were the first to report the photolability of these arene-complexes in the presence of nucleophilic solvents. This method could be extended to different aromatic compounds such as naphthalene and anthracene.[226]

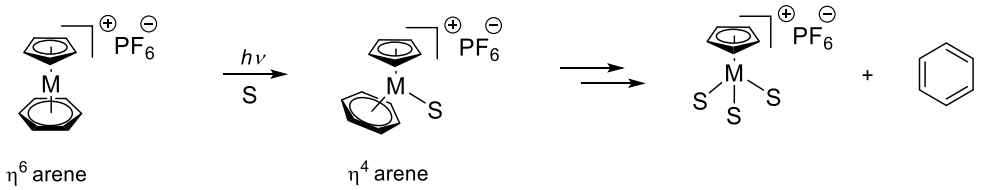

Fig. 56: Typical photolysis of arene-iron compounds by ligand exchange between the arene and solvent molecules.

This exchange reaction was reported for the cationic photopolymerization of epoxides.[227,228] Epoxides can coordinate the iron atom, just like solvent molecules, according to the previously described mechanism, eventually displacing the arene. The newly formed oxygen-iron bonds weaken the oxygen-carbon bonds of the epoxides, which are thus activated, leading to cationic polymerization (**Fig. 57**).

[226] E. P. Kündig et al., Inorganica Chimica Acta, 2004, https://doi.org/10.1016/j.ica.2003.11.022.
[227] A. Roloff et al, Pure and Applied Chemistry, 1986, https://doi.org/10.1351/pac198658091267.
[228] K. M. Park and G. B. Schuster, Journal of Organometallic Chemistry, 1991, https://doi.org/10.1016/0022-328X(91)86249-P.

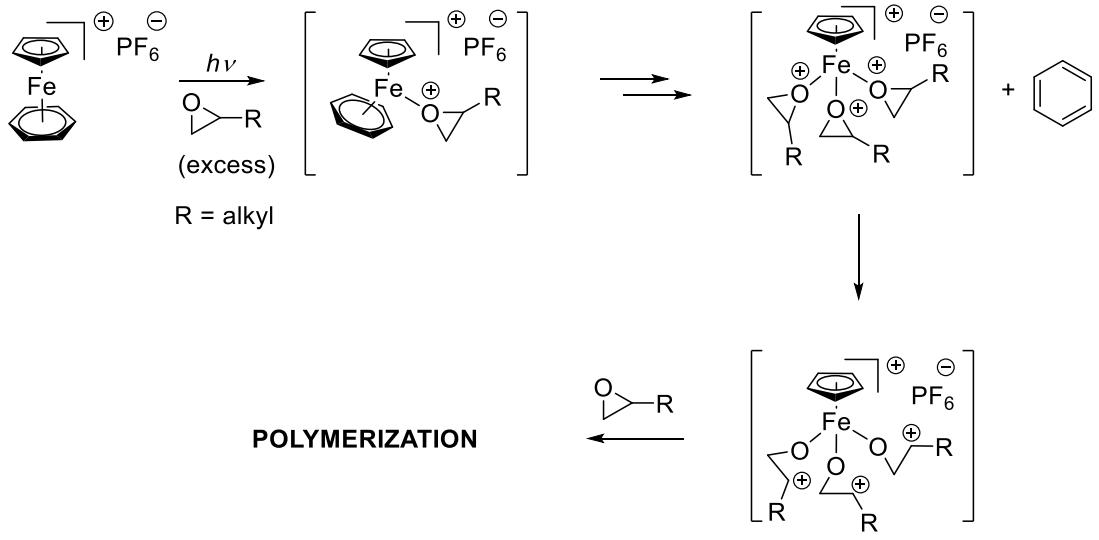

Fig. 57: Epoxide polymerization using arene-iron as photoinitiator.

This experiment shows that oxygen is a great ligand to coordinate iron. In fact, among the nucleophilic solvents, water is the most efficient to displace the arene ring followed by methanol. It's worth noting that in case of water, the coordination in neutral to basic pH conditions results in the precipitation of $Fe(OH)_3$ species as reported by Pearson et al.[229]

These arene-iron complexes also find their use in organic chemistry for synthethic purposes. Indeed, the coordination of the arene ring to the metal atom increases the electrophilicity of the arene, allowing it to undergo nucleophilic substitution reactions. Indeed, the ferricenium cation induces a strong electron withdrawing effect on both rings. This effect was tested by Nesmeyanov by trying various common reactions of electrophilic aromatic substitution, namely nitration, acylation, mercuration as well as metallation.[224] All these reactions were known to work with ferrocene but failed in that case, depicting the lower electronic density around the aromatic rings. This was confirmed by comparing the nucleophilic aromatic substitution of chlorobenzene and the chlorobenzene-iron equivalent by various nucleophiles. The common reaction condition with chlorobenzene requires strong heating and the presence of a catalyst. In case of clorobenzene-iron, the reaction proceeded under milder conditions by mild heating around 30–60 °C for a few hours. The reaction occurred even at room temperature with ethoxylate as nucleophile. The electron density of the arene is decreased due to the presence

[229] A. J. Pearson and L. Sun, Journal of Polymer Science Part A: Polymer Chemistry, 1997, https://doi.org/10.1002/(SICI)1099-0518(199702)35:3<447::AID-POLA7>3.0.CO;2-P.

of ferricenium which allows the nucleophilic substitution to proceed. These results were later on used for cross-coupling reactions. Indeed, arylchloride hardly reacts in Pd-catalyzed cross-coupling reactions due to the low electrophilic nature of the carbon atom in the carbon-chlorine bond to allow the insertion of the palladium during the oxidative addition step. In case of arylchloride-iron complex, the arylchloride ring could successfully react with palladium as demonstrated by Zhao et al. in the Suzuki-Miyaura cross-coupling reaction.[230] The desired molecule could be smoothly released by photolysis of the iron-containing product. This approach is interesting as the electron withdrawing group (here $FeCp^+$) can be easily removed by simple illumination as opposed to the traditional method of adding an attracting group as substituent.[231] Sartor et al. reported the use of arene-iron for the synthesis of dendrimers that showed to be quicker and less tedious than the conventional method.[232]

The use of arene-iron complexes relies on the electron withdrawing effect of the $FeCp^+$ moiety for arene modifications. Their ease of removal by illumination allows the recovery of the desired product free of metal. As opposed to pristine ferrocene, photodissociation can be observed with visible light in different solvents and does not require a charger transfer complex.

1.3. Substituted ferrocene

As stated previously, the photodissociation of pristine ferrocene is only observed when a charge transfer complex is possible with the substrate, giving rise to a specific absorption band in the UV region. Illumination in the CTC absorption band results in an electron transfer from ferrocene to a substrate, leading to the oxidation of ferrocene to ferricenium and eventually to its decomposition. Traverso tested the same process by illuminating in the visible absorption band of ferrocene (442 nm) without any noticeable changes, attesting the photostability of ferrocene under visible light. However, in early 1960s, Nesmeyanov et al. reported the photolysis of substituted ferrocene derivatives containing electron withdrawing groups.[224,233] The group synthesized a ferrocenetriethylammonium salt and discovered the photosensitivity

[230] Jie Zhao et al., Industrial & Engineering Chemistry Research, 2014, https://doi.org/10.1021/ie403413r.
[231] N. V. Shvydkiy and D. S. Perekalin, Coordination Chemistry Reviews, 2020, https://doi.org/10.1016/j.ccr.2020.213238.
[232] V.Sartor et al., Journal of the American Chemical Society, 1999, https://doi.org/10.1021/ja983868m
[233] A. N. Nesmeyanov et al., Bulletin of the Academy of Sciences, USSR Division of Chemical Science, 1965, https://doi.org/10.1007/BF01083826.

of such compounds by visible light in water. They first reported the photolysis of the ferrocene unit where the triethylammoniumcyclopentadienyl could be isolated. The resulting photoadduct could react in electrophilic aromatic substitution to provide the tetrabrominated product for instance. A similar compound with pyridinium resulted in the same observation. They concluded that the presence of an ammonium close to ferrocene could induce drastic photophysic modifications of ferrocene that allow the photolysis. Attempts of distancing the ammonium group from ferrocene using an ethylene group as spacer resulted in the compound photolysis as well (**Fig. 58**).

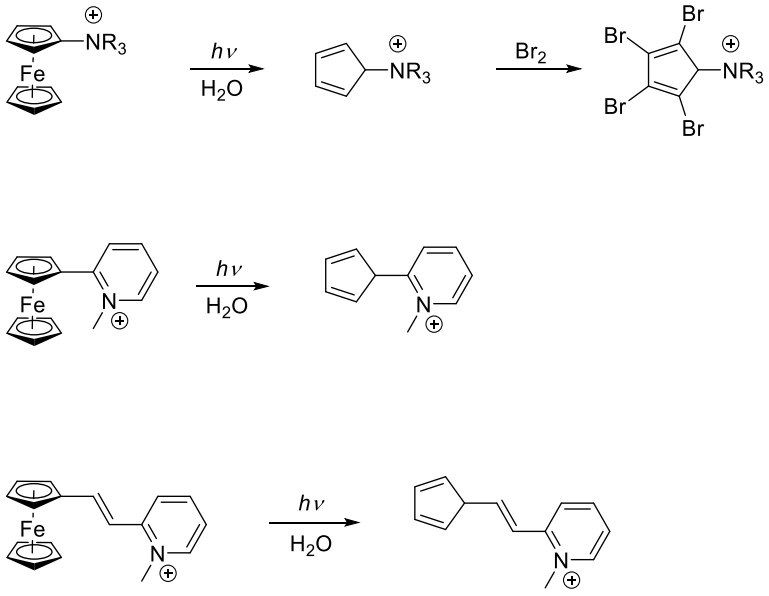

Fig. 58: Photodissociation of different ferrocene derivatives substituted with ammonium groups.

At the same time, Nesmeyanov discovered the photolysis of 1,1'-ferrocenecarboxylic acid in basic aqueous solution under ordinary light bulb or sunlight. In that case, ferric hydroxide $Fe(OH)_3$ and the dimer of cyclopentadienecarboxylic acid could be isolated. The observation was very similar to the photolysis of arene-iron complexes previously described. Indeed, photolysis of arene-iron in water yields $Fe(OH)_3$ by reducing the hapticity of the aromatic rings through coordination of solvent molecules. In case of substituted ferrocene, the carboxylic acids were changed to different electron withdrawing groups, i.e. sulfonic acid and ketone (**Fig. 59**). The corresponding derivatives were also unstable under visible light.

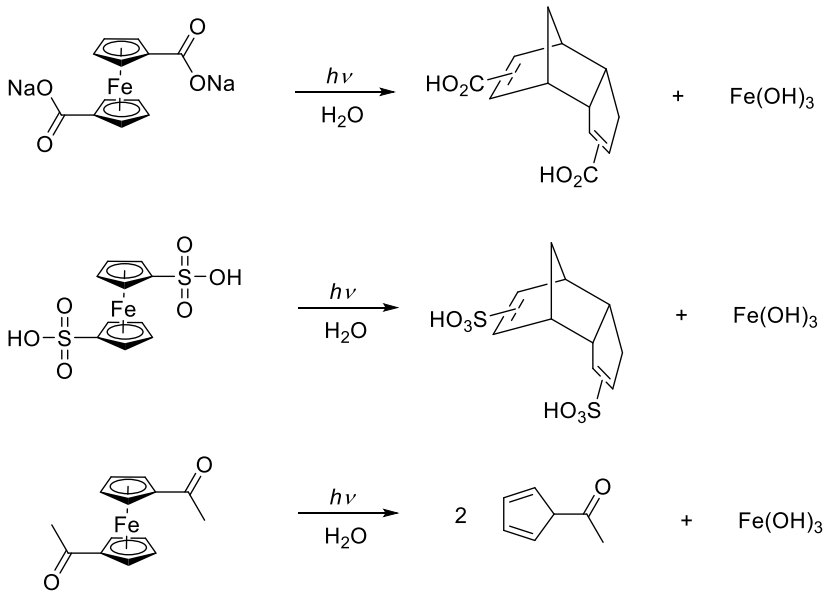

Fig. 59: Photodissociation of different ferrocene derivatives substituted with various acyl groups.

These results confirmed the words of Wilkinson et al. that mentioned the photolability of acylferrocenes back in 1952 when ferrocene was still under investigation. Nesmeyanov was the first to study the photoreactivity of ferrocene substituted with electron withdrawing groups. In contrast, when octamethylferrocene, an electron-rich ferrocene, was illuminated with visible light no decomposition was observed. These results caught the attention of many scientists regarding this new behaviour of ferrocene and several studies were reported.

Tarr and Wiles reported, in the late 1960s, more in depth studies about the photostability of ferrocene substituted with electron withdrawing groups,[234] such as benzoylferrocene (BFc) and dibenzoylferrocene (DBFc) (**Fig. 60**). BFc and DBFc didn't show any decomposition in hydrocarbon solvents. However, solutions exposed to sunlight in methanol became cloudy and turned into heterogenous suspensions with a colorless supernatant and a dark-brown precipitate, presumed to be inorganic iron species. The photochemical nature of the process was confirmed by the stability of the solutions in the dark. In case of DBFc, 17 different solvents were tested and alcohol solvents such as methanol, 1-propanol and ethylene glycol provided similar photodegradation observations, namely the brown precipitate and a colorless supernatant. Other solvents such as acetone, DMF, THF or pyridine allowed the

[234] A. M. Tarr and D. M. Wiles, Canadian Journal of Chemistry, 1968, https://doi.org/10.1139/v68-449.

photodegradation of BFc but to a lesser extent, with alteration of the color and with or without precipitate. Only the solutions in hydrocarbon solvents were photostable.

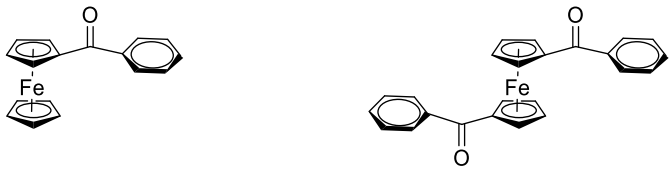

BFc **DBFc**

Fig. 60: Structures of benzoylferrocene (BFc) and dibenzoylferrocene (DBFc).

It is therefore obvious that the solvent plays a major role in the photodecomposition of ferrocene substituted with electron withdrawing groups, similar to the arene-iron compounds previously described by Nesmeyanov. It was assumed that alcohols could interact with the carbonyl groups by hydrogen bonding as observed by infrared peak broadening. Tarr and Wiles confirmed the hypothesis by photodegrading DBFc, which was slow in pure THF, but faster in the presence of dextrose or dihydroxyacetone (DHA), with DHA providing the most efficiency. When the solvent was changed to a 1:1 mixture of water/methanol, the rate of photodecomposition was as fast as the one with DHA in THF. Water seems to play an important role in the photodecomposition process and solvents that are not miscible with it (CCl_4, CS_2, dimethyl phtalate, isooctane) barely showed photodegradation. Therefore, hydrogen bond donor solvents play a crucial role in the photodecomposition of ferrocene substituted with ▪-carbonyl groups. This observation was confirmed by Ali et al. a few years later by comparing the illumination of BFc in wet or freshly dried solvents. DMSO, pyridine, DMF, THF, methanol and 1,4-dioxane were used as solvents. Solutions in rigorously and freshly distilled solvents showed little to no photodecomposition, but addition of water quickly promoted the photodegradation of BFc.[235]

The multiple reports of photolysis of ferrocene substituted with electron withdrawing groups raised many questions toward the mechanism and photophysics involved in the

[235] L. H. Ali et al., Journal of the Chemical Society, Dalton Transactions, 1973, https://doi.org/10.1039/dt9730001468.

photodegradation of these compounds as the process greatly differed from the photodecomposition by UV illumination of charge transfer complexes.

1.4. Spectroscopy and electronic structure

Ferrocene is a coordination complex in which both cyclopentadiene rings are ionically bonded to the iron atom. Ferrocene exists under two different conformers that are eclipsed (D_{5h}) or staggered (D_{5d}). It was determined that the staggered conformer was the dominant form of ferrocene in the crystal structure as opposed to solution where the eclipsed form is the most stable. However, due to their very similar structures, the differences in properties of eclipsed and staggered ferrocenes can't be measured. Moreover, the rotational barrier between both conformations was determined to be 4 kJ mol^{-1}.[236] As a comparison, the rotational barrier in ethane is 12 kJ mol^{-1},[237] showing how fast the conformational change happens in ferrocene.

Ligand-metal orbital interactions, bondings and reactivity of coordination complexes can be described using the ligand field theory (LFT). In short, LFT results from the combination of molecular orbital theory and crystal field theory and explains the consequences of the inner orbitals splitting of the transition metal surrounded by its ligands. Metallocenes, including ferrocene, are perfectly adapted for the study by LFT (**Fig. 61**).[238] In the case of ferrocene, the staggered conformer D_{5d} is commonly used due to the simplified electronic structure. Cp^- ligand has three π-bonds delocalized around the five carbon atoms constituting the ring. Therefore, Cp^- contains five 2p orbitals (one per carbon atom). Both Cp^- can be described as one unit by linearly combining the π-orbitals pairwise. Applying the operations of point group D_{5d} to the 2p valence atomic orbitals gives rise to three sets of ligand molecular orbitals of gerade ("*g*", symmetrical) and ungerade ("*u*", unsymmetrical) that constitute a bonding pair (A_{1g} and A_{2u}), a weakly bonding pair (E_{1g} and E_{1u}) and an anti-bonding pair (E_{2g} and E_{2u}). For the iron atom, applying the same operations to the 4*s*, 4*p* and 3*d* valence atomic orbitals provides the metal orbitals with the following representations: A_{1g} (s, d_z^2), E_{1g} (d_{yz}, d_{xz}), E_{2g} (d_x^2-d_y^2, d_{xy}), A_{2u} (p_z) and E_{1u} (p_x, p_y). By appropriate interactions of the metal orbitals with the

[236] C. -H. Wang et al., Chemical Science, 2021, https://doi.org/10.1039/D0SC06876D.
[237] R. F. Quijano-Quiñones et al., Molecules, 2012, https://doi.org/10.3390/molecules17044661.
[238] H. B. Gray et al., Journal of the American Chemical Society, 1971, https://doi.org/10.1021/ja00744a011.

ligand molecular orbitals of same symmetry, the electronic structure of ferrocene using LFT can be obtained. Each combination of a metal orbital with a ligand molecular orbital leads to a bonding molecular orbital and a corresponding anti-bonding molecular orbital. For instance, the metal orbital 4*s* of A_{1g} representation can combine with the ligand molecular orbital of the same symmetry, leading to the formation of the low lying filled bonding molecular orbital $1a_{1g}$ and its corresponding anti-bonding unfilled molecular orbital $3a^{*}_{1g}$. When there is no symmetry matching from both metal and ligands, the lone orbital, such as the metal orbital d_{z^2} or e_{2u} ligand molecular orbitals, constitutes its own molecular orbital with little to no change of energy level. The closer the energy level of the resulting molecular orbitals with respect to the energy levels of the parent metal orbital and ligand molecular orbital, the better the overlap is. The best overlap occurs with the e_{1g} ligand molecular orbital and the ($3d_{xz}$, $3d_{yz}$) metal orbitals, leading to the formation of the molecular orbital $1e_{1g}$ that contains two strong π-bonds. $1e_{1g}$ is mostly ligand in character while the unoccupied anti-bonding $2e^{*}_{1g}$ is mainly metallic. The remaining metal orbitals (d_{x^2}-d_{y^2}, d_{xy}) and d_{z^2} are essentially nonbonding. In fact, there is no available orbital to correctly interact with d_{z^2} and the overlap of the ligand molecular orbital e_{2g} with the metal orbital of same symmetry (d_{x^2}-d_{y^2}, d_{xy}) is poor. The resulting molecular orbitals $2a_{1g}$ and $1e_{2g}$ are therefore mainly metal in character. $2e^{*}_{1g}$, $2a_{1g}$ and $1e_{2g}$ constitute the main molecular orbitals behind ferrocene's reactivity and electronic properties, with $2e^{*}_{1g}$ also named as the lowest unoccupied molecular orbital (LUMO) and $2a_{1g}$ the highest occupied molecular orbital (HOMO). The ground state molecular occupation of ferrocene is $(1a_{1g})^2(1a_{2u})^2(1e_{1g})^4(1e_{1u})^4(1e_{2g})^4(2a_{1g})^2$. The promotion of a $2a_{1g}$ or $1e_{2g}$ electron to the empty $2e^{*}_{1g}$ molecular orbital leads to an excited state E_{1g}. The resulting spin-allowed electronic transitions give rise to the 442 nm and 325 nm absorption bands. Ferrocene, in the D_{5d} conformation, is centrosymmetric, meaning that Laporte rule applies to the observed electronic transitions. The two observed transitions are weak in intensity because the excited electron moves from a gerade molecular orbital to another one, which is forbidden according to Laporte rule.

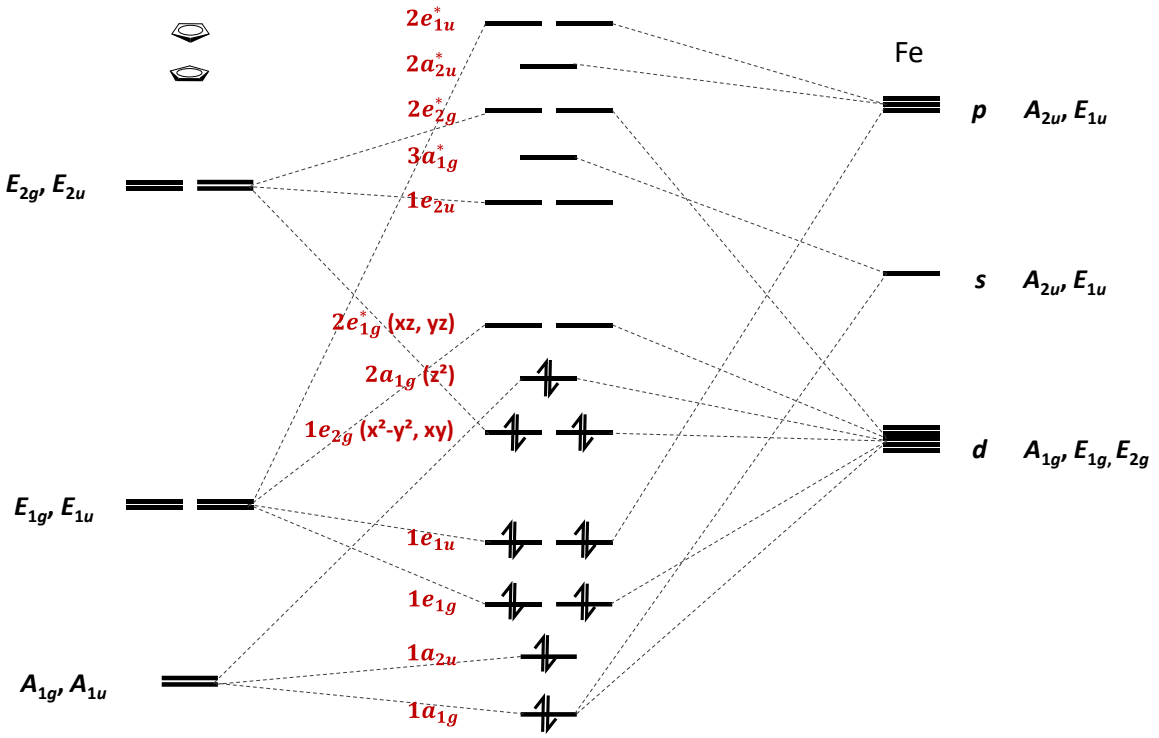

Fig. 61: Electronic structure of ferrocene by ligand field theory.[238]

The photostability of simple ferrocene in non-halogenated solvents suggests that the photoexcited state undergoes very fast relaxation to the ground state, preventing further reactions.[239] However, ferrocenes substituted with electron-withdrawing groups are highly photosensitive. Many reported studies tried to explain the difference of photostability between ferrocene and its derivatives using BFc and DBFc as models.[235,240] However, Kutal et al. refuted the multiple hypotheses and demonstrated that the mechanism involved a heterolytic cleavage of metal-ligand bond as the first step (**Fig. 62**).[241] Illumination at a wavelength close to the 442 nm absorption band of ferrocene leads to the photoexcitation of a $2a_{1g}$ or $1e_{2g}$ electron to the $2e^*_{1g}$ molecular orbital. As a consequence, a vacancy is formed in either $2a_{1g}$ or $1e_{2g}$, resulting in the weakening of the iron-ring bond which facilitates the nucleophilic attack of the solvent molecules as observed with water or methanol. Moreover, the conjugation between the

[239] Y. Yamaguchi et al., Coordination Chemistry Reviews, 2007, https://doi.org/10.1016/j.ccr.2006.02.028.
[240] E. K. Heaney et al., Journal of the Chemical Society, Faraday Transactions 1: Physical Chemistry in Condensed Phases, 1977, https://doi.org/10.1039/f19777300699.
[241] Y. Yamaguchi and C. Kutal, Inorganic Chemistry, 1999, https://doi.org/10.1021/ic990173t.

carbonyl group and Cp ring introduces a metal-to-ligand charge transfer (MLCT) character in the photoexcited state, decreasing the electronic density of the Cp ring by reducing its hapticity from η^5 to η^4. As a result, the Cp ring is less bound to the iron atom, weakening the iron-ring bond. As stated previously, $2a_{1g}$ and $1e_{2g}$ are mainly metal in character. Therefore, the promoted electron to the empty $2e^*_{1g}$ is mainly affecting the iron atom. Kutal suggested that the photodegradation of BFc and DBFc implies the heterolytic cleavage of one iron-ring bond by photolysis, oxidizing iron(II) to iron(III) followed by the coordination of solvent molecules to satisfy the 18 electron rule. Then, further illumination eventually leads to the formation of inorganic iron species and the release of various organic by-products such as the cyclopentadiene ligands.

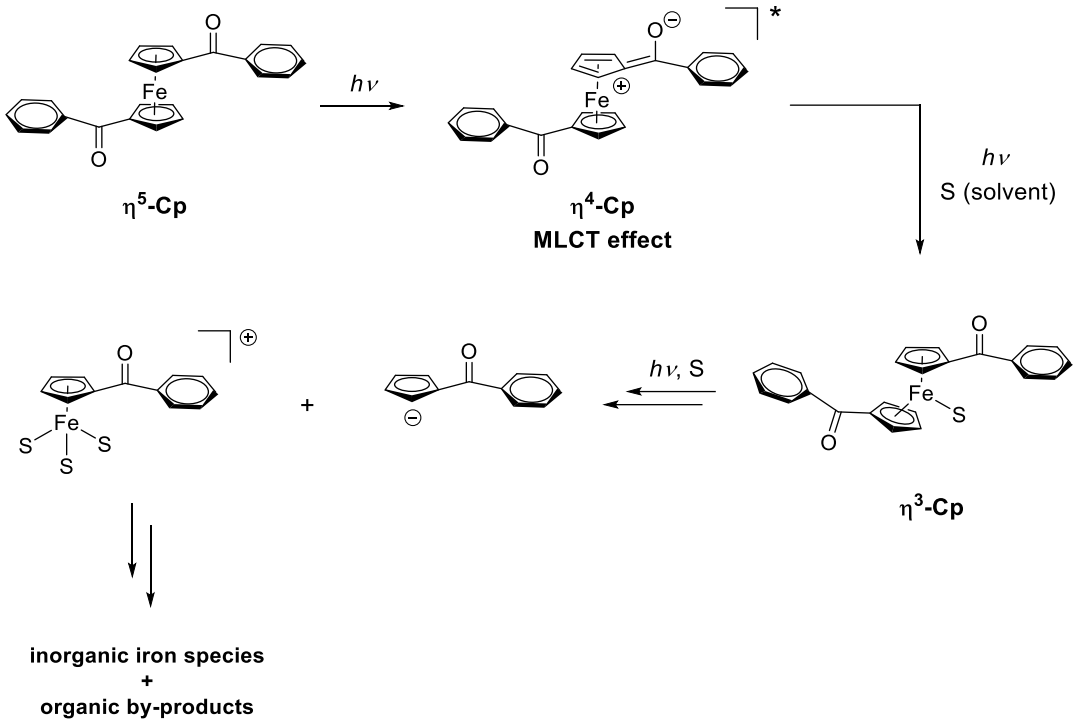

Fig. 62: Mechanism of photodegradation of DBFc proposed by Kutal.[241]

The ability of ferrocene substituted with electron withdrawing groups to undergo quick photolysis by illumination in the visible absorption band was reported by Nesmeyanov and coworkers. The work of Kutal et al. demonstrated the process involved in the photodegradation in case of BFc and DBFc, which requires a metal-to-ligand charge transfer that greatly participates in the weakening of the iron-ring bond.

1.5. Ferricenium decomposition

Ferricenium is the result of an oxidative process by which one electron from the iron atom is removed. Ferricenium can be obtained by chemical oxidation or photooxidation involving the electrons in the metal character molecular orbitals. Indeed, it was reported that ionization of ferrocene to ferricenium involved the removal of an electron from the weakly bonding $1e_{2g}$ orbital,[242,243] making the positive charge mainly located on the iron atom. Therefore, the ground state is defined as $(1a_{1g})^2(1a_{2u})^2(1e_{1g})^4(1e_{1u})^4(1e_{2g})^3(2a_{1g})^2$. Prins and Kotbeek reported the decomposition of ferricenium against various ligands and solvents, providing different products such as ferric and ferrous complexes. In their work, they showed that ferricenium was decomposed by chloride and bromide anions to give the corresponding iron tetrahalide complex and the release of the Cp rings.[244] Similar observations were made using strong donor solvents such as DMSO and HMPTA which resulted in the displacement of the Cp rings by the solvent molecules giving a fully coordinated iron complex. In weak donor solvents such as acetonitrile, acetone and nitromethane, ferricenium displayed much higher stability over a few hours. They assumed that the decomposition took place by progressive coordination of the donor molecules (anionic or neutral) to displace the Cp rings. They concluded that the better the nucleophile, the faster the decomposition.

In the same work, the authors reported the good stability of unsubstituted ferricenium in acidic aqueous solution. However, at basic pH, in presence of hydroxide, the decomposition could be observed. Thus, one can assume that the mechanism of decomposition of ferricenium and photoexcited ferrocene derivatives substituted with electron withdrawing groups are very similar. During the photoexcitation of these ferrocene derivatives in their visible absorption band, the excited state could be characterized but no data on the formation of a ferricenium species was reported. The d ground state of ferricenium is known to be $(1e_{2g})^3(2a_{1g})^2(2e^*_{1g})^0$ while the photoexcited state of ferrocene is $(1e_{2g})^3(2a_{1g})^2(2e^*_{1g})^1$. In both cases, the removed electron comes from the weakly bonding $1e_{2g}$ molecular orbital that is mainly metal in character (**Fig. 63**).

[242] H. B. Gray et al., Inorganic Chemistry, 1971, https://doi.org/10.1021/ic50102a001.
[243] E. M. Shustorovich and M. B. Dyatkina, Journal of Structural Chemistry, 1967, https://doi.org/10.1007/bf00739262
[244] R. Prins et al., Journal of Organometallic Chemistry, 1972, https://doi.org/10.1016/S0022-328X(00)80459-3.

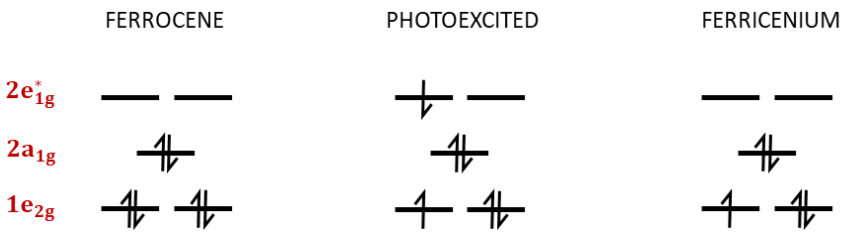

Fig. 63: *d* ground state of ferrocene, photoexcited ferrocene and ferricenium.

Although no positive charge exists in the photoexcited state, as opposed to ferricenium, the electrophilic nature of the iron atom is highly promoted by MLCT as described by Kutal. Therefore, the consequence on the weakening of the iron-ring bond is very similar in unsubstituted ferricenium and in photoexcited ferrocene bearing attracting groups. One can probably make the assumption that the decomposition of photoexcited electron-poor ferrocene could be even greater due to the fact that water in neutral conditions is enough to decompose the ferrocene moiety, as opposed to ferricenium that is stable. Even if ferricenium can't be identified in the photodecomposition process, the isolation of inorganic ferric species clearly suggests the oxidation of the iron atom at some point as proposed by the mechanism of Kutal et al.[241]

1.6. Photodynamic therapy

1.6.1. General principle

Photodynamic therapy (PDT) is an approach to treat various cancers by combining molecular oxygen, a photosensitizer (PS), and a light source. PDT treatments are considered to be less invasive than other conventional radiotherapy or chemotherapy.[245] Indeed, PDT is based on a specific and localized illumination to reduce side effects. The photo-activation of the photosensitizer in the tumor tissue generates radical oxygen species (ROS) that can quickly oxidize biological components leading to cell death.[246] Commonly used photosensitizers are porphyrin, chlorin and lately bacteriochlorin derivatives.[247,248] The first application of porphyrin in the human body was carried out in 1912 by Friedrich Meyer-Betz, who self-injected 200 mg of hematoporphyrin and became extremely sensitive to sunlight through noticeable swelling of exposed skin. More recently, several photosensitizers were approved such as Photofrin (1995), a porphyrin-based molecule, Temoporfin (2000), a chlorin-based photosensitizer, and Tookad (2017), a palladium-bacteriochlorin photoactive molecule.

A photosensitizer relies on photoexcitation and de-excitation processes and can be described by the Jablonski diagram (**Fig. 64**).[249] In standard conditions, almost all molecules are in their singlet ground state S_0 which is the lowest and most stable electronic state. All electrons are paired and thus the spin is zero. When illuminated, a molecule can absorb a photon and promote electrons to higher orbitals.[250] This electronic transition turns the molecule from a ground state S_0 to an excited state S_n according to the Franck-Condon principle. This excited state is higher in energy and less stable than the ground state. To release the excess of energy and return to the ground state, the excited system undergoes rapid release of a portion of the absorbed energy by successive vibrational relaxation (VR) and internal conversion (IC). These relaxation processes allow the system to reach the lowest excited state S_1. VR and IC are nonradiative as no photons are emitted. Typical time for VR and IC is around 10^{-12} s. This time is dependent on the energy gap between the two states. From S_1 to S_2 the energy gap is lower

[245] K. N. Maloth et al., Journal of Lasers in Medical Sciences, 2016, https://doi.org/10.15171/jlms.2016.07.
[246] D. L. Sai et al., Experimental & Molecular Medicine, 2021, https://doi.org/10.1038/s12276-021-00599-7.
[247] J. Kou et al., Oncotarget, 2017, https://doi.org/10.18632/oncotarget.20189.
[248] R. R. Cheruku et al., Journal of Medicinal Chemistry, 2021, https://doi.org/10.1021/acs.jmedchem.0c01735.
[249] M. H. Abdel-Kader, Book entitled "Photodynamic Therapy, From Theory to Application", 2014, 10.1007/978-3-642-39629-8.
[250] B. M. Aveline, Comprehensive Series in Photosciences, 2001, https://doi.org/10.1016/S1568-461X(01)80106-X.

than the one from S_0 to S_1. This is true for most molecules, and the IC process from S_1 to S_0 is around 10^{-9} s. At the S_1 excited state, three main relaxation pathways can be observed. The first one is the IC from S_1 to S_0, which simply results in the return to the ground state. The second possibility is the emission of a photon called fluorescence. This is a radiative process and the emitted photon is always red-shifted compared to the absorbed photons due to the lower energy. The third process implies a change of spin multiplicity of the electronic state S_1 (singlet) to a triplet state (T_1). This phenomenon, called intersystem crossing (ISC), implies a spin flip of one of the unpaired electron in the S_1 excited state. Such feature is normally obtained by applying a strong magnetic field (such as in NMR and MRI). However, in case of photoexcitation, this phenomenon is still observed even without strong magnetic field. ISC is possible due to spin-orbit coupling. In short, the motion of the nucleus seen by the electrons orbiting around corresponds to a magnetic field that the electron spins tend to align with. Moreover, the spin-orbit coupling scales up with the atomic number to the fourth power (Z^4), meaning that the larger the atom, the better the ISC.[251] The reason is that the magnetic field from the nucleus is directly proportional to its positive charge, and thus, to its atomic number. As a result, heavy atoms (metals, iodine, bromine…) favour the formation of the triplet state with a reduced lifetime.[252] Similarly to IC and VR, ISC is also nonradiative and depends on the energy gap between S_1 and T_1. The lifetime of the triplet state is generally around 1000-fold longer than the lifetime of the singlet state.[253] Indeed, the T_1 to S_0 electronic transition is spin-forbidden, meaning that the de-excitation by phosphorescence or IC from T_1 to S_0 is slow. Therefore, the probability for a molecule to react in its triplet state is much higher than in its singlet state. This is particularly important in PDT as it gives enough time for the photosensitizer to interact with neighbouring molecules such as molecular oxygen. In fact, the photochemistry of most molecules occurs in the lowest excited levels, namely S_1 and T_1. This phenomenon is coined as Kasha's rule and is the direct consequence of the very rapid relaxation from S_n to S_1 and T_n to T_1 by VR and IC.[254]

[251] R. Pellow and M. Vala, The Journal of Chemical Physics, 1989, https://doi.org/10.1063/1.456414.
[252] J. Najbar, Journal of Luminescence, 1975, https://doi.org/10.1016/0022-2313(75)90015-0.
[253] C. E. Avalos et al., The Journal of Physical Chemistry A, 2020, https://doi.org/10.1021/acs.jpca.0c03498.
[254] J. Carlos del Valle and J. Catalan, Physical Chemistry Chemical Physics, 2019, https://doi.org/10.1039/C9CP00739C https://doi.org/10.1039/C9CP00739C

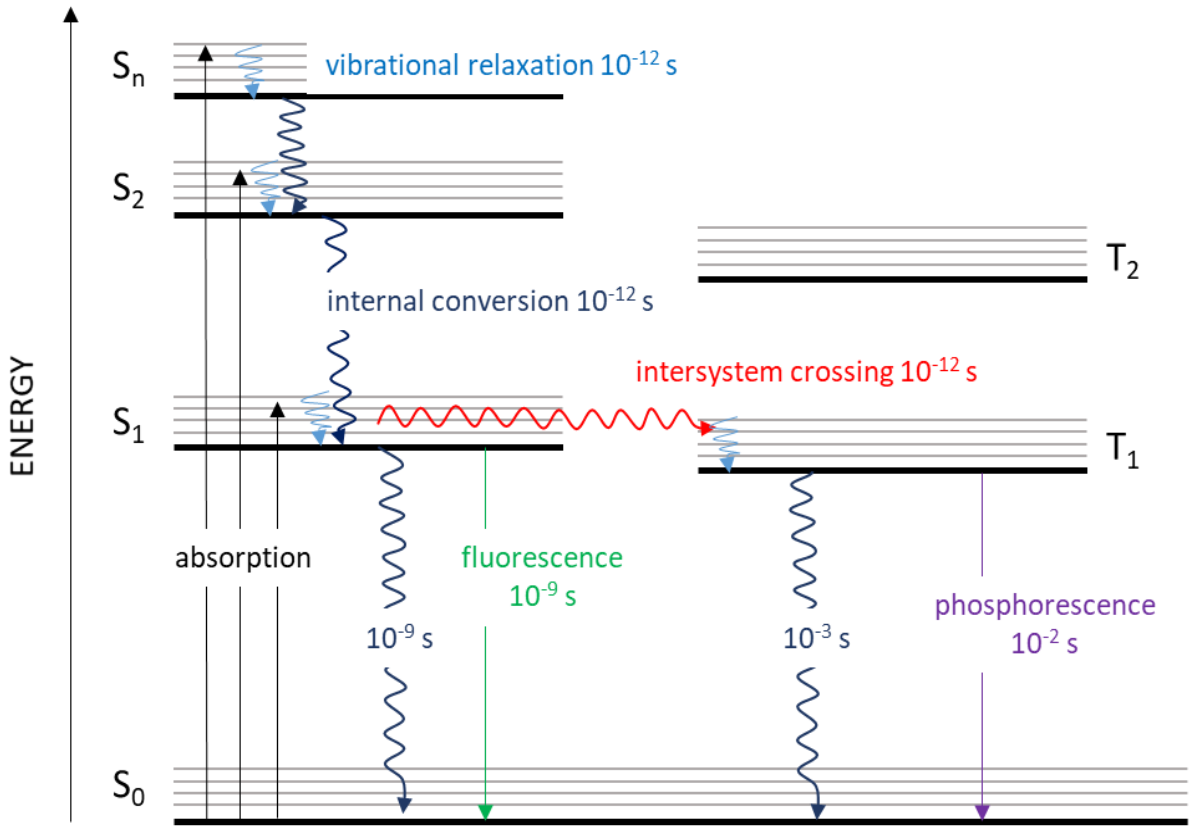

Fig. 64: Jablonski diagram with approximate constant rates of different nonradiative and radiative processes in the photoexcitation of a photosensitizer.

1.6.2. Photosensitization mechanism

Beside phosphorescence and IC, the triplet state PS can react with another molecule in its ground state by charge (type I) or energy (type II) transfer (**Fig. 65**). The former process involves the transfer of an electron or hydrogen atom between the triplet photosensitizer (^{3}PS) and a substrate molecule (A) or molecular oxygen. Type I reactions consist of complex mechanisms and generate various ROS such as superoxide anion ($O_2^{\bullet-}$), hydroxyl radical ($HO^{\bullet}$) and hydrogen peroxide (H_2O_2). Type II photoreactions are based on the generation of the highly reactive singlet oxygen ($^1O_2$), known to be a potent oxidant against biomolecules.

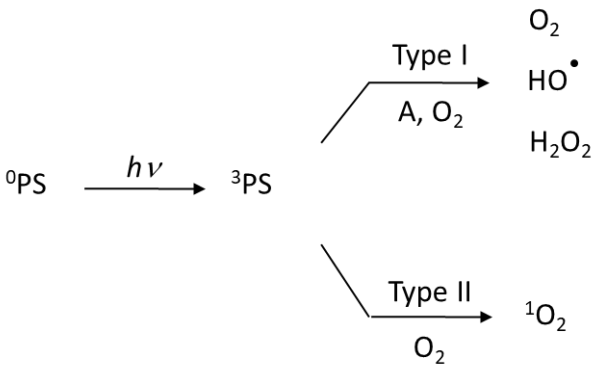

Fig. 65: Different pathways of photosensitizing, leading to the generation of different reactive oxygen species.

Type I reactions involve the direct charge transfer of the triplet state PS to an organic molecule A or molecular oxygen. As a result, a pair of radical ions is formed (**Eq. 13** and **15**). The superoxide anion can also be obtained from direct oxidation of molecular oxygen by the radical anion photosensitizer (**Eq. 14**). However, $O_2^{\bullet-}$ in water spontaneously undergoes dismutation to form hydrogen peroxide (**Eq. 16**). H_2O_2 has a higher lifetime compared to other ionic ROS and can readily diffuse through cell membranes. H_2O_2 is known as a main reagent in the Fenton reaction generating more oxidant species such as hydroxy radical. $HO^{\bullet}$ can also be formed by the reaction of $O_2^{\bullet-}$ or ^3PS with H_2O_2, with additional release of molecular oxygen and hydroxide (**Eq. 17** and **18**).

$$^3PS + A \longrightarrow {}^3PS^{\bullet-} + A^{\bullet+} \quad \textbf{(Eq. 13)}$$

$$^3PS^{\bullet-} + O_2 \longrightarrow PS + O_2^{\bullet-} \quad \textbf{(Eq. 14)}$$

$$^3PS + O_2 \longrightarrow PS^{\bullet+} + O_2^{\bullet-} \quad \textbf{(Eq. 15)}$$

$$O_2^{\bullet-} + O_2^{\bullet-} + 2H^+ \longrightarrow O_2 + H_2O_2 \quad \textbf{(Eq. 16)}$$

$$H_2O_2 + O_2^{\bullet-} \longrightarrow O_2 + HO^{\bullet} + HO^- \quad \textbf{(Eq. 17)}$$

$$H_2O_2 + PS^{\bullet-} \longrightarrow PS + HO^{\bullet} + HO^- \quad \textbf{(Eq. 18)}$$

Besides the direct charge transfer, the photoexcited PS can also undergo hydrogen abstraction, in which case the photosensitizer can be the donor or acceptor of hydrogen (**Eq. 19** and **20**). As a consequence, two radicals are formed and can react further with oxygen. In case of the radical substrate, the reaction with molecular oxygen gives the corresponding peroxyl radical (**Eq. 21**) that can then abstract a hydrogen atom from another substrate molecule to continue the cycle (**Eq. 22**).

$$^3PSH + A \longrightarrow {}^3PS^{\bullet} + HA^{\bullet} \qquad \textbf{(Eq. 19)}$$

$$^3PS + HA \longrightarrow {}^3PSH^{\bullet} + A^{\bullet} \qquad \textbf{(Eq. 20)}$$

$$A^{\bullet} + O_2 \longrightarrow AOO^{\bullet} \qquad \textbf{(Eq. 21)}$$

$$AOO^{\bullet} + HA \longrightarrow AOOH + A^{\bullet} \qquad \textbf{(Eq. 22)}$$

As mentioned previously, type I photosensitizing is a complex process and involves several reactions due to the high reactivity of radical species. The different reactions discussed here show the main possibilities that lead to biological damage by generating highly oxidant ROS ($HO^{\bullet}$ and H_2O_2) in addition to peroxidation of biomolecules (protein, lipid, DNA).[255]

Type II photosensitizing is based on the energy transfer from the photoexcited PS to molecular oxygen (**Fig. 66**). This pathway consists in reacting the triplet state ^3PS directly with molecular oxygen by energy transfer. This process is more oxygen-dependent than type I. Type II is possible when the energy gap between the triplet state and ground state of the photosensitizer is higher than the energy gap from $^3O_2$ to $^1O_2$. This requirement is fulfilled by most photosensitizers, including porphyrin and its derivatives. Moreover, the kinetics of energy transfer ($10^9\ M^{-1}\ s^{-1}$) is faster than that of charge transfer ($10^7\ M^{-1}\ s^{-1}$) in the case of oxygen.[256] Therefore, type II mechanisms are more common than type I.

[255] D. B. Min and J. M. Boff, Comprehensive Reviews in Food Science and Food Safety, 2002, https://doi.org/10.1111/j.1541-4337.2002.tb00007.x.

[256] L. N. An, Thesis dissertation entitled "Development of porphyrinoid-based photosensitisers as potentially dual acting agents for photodynamic therapy and crosslinkable polymeric contrast agent for high-resolution x-ray imaging of the vascular system", 2020, https://doi.org/10.5167/UZH-194324.

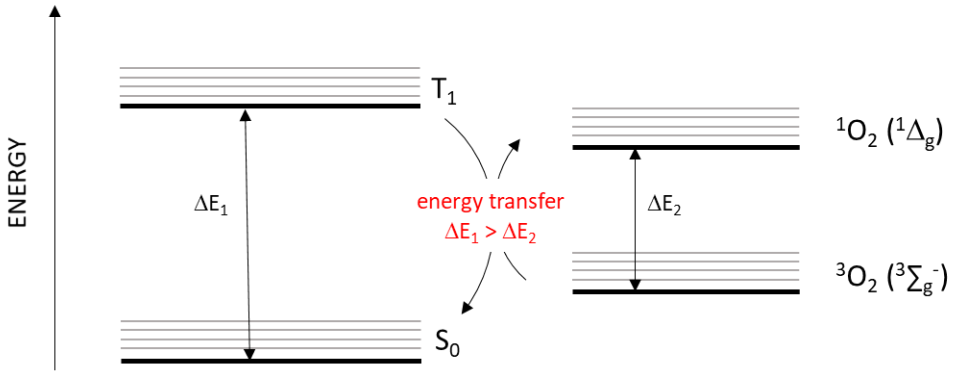

Fig. 66: Energy transfer from the triplet photosensitizer and triplet ground state molecular oxygen.

Molecular oxygen has three electronic states. The first one is the ground triplet state ($^3\sum_g^-$) which is the most stable electronic configuration. After excitation by energy transfer, oxygen can reach two different singlet excited states named "closed-shell" ($^1\Delta_g$) and "open-shell" ($^1\sum_g^+$) (**Fig. 67**). The energy gaps with respect to the ground state are respectively 95 kJ mol^{-1} and 158 kJ mol^{-1}.[257] However, $^1\sum_g^+$ is unstable and rapidly transitions to either $^1\Delta_g$ or $^3\sum_g^-$ states. The singlet-triplet transitions ($^1\sum_g^+$ to $^3\sum_g^-$ and $^1\Delta_g$ to $^3\sum_g^-$) are forbidden by spin and Laporte selection rules. The singlet-singlet transition is spin allowed but Laporte forbidden. Therefore, the transition from $^1\sum_g^+$ to $^1\Delta_g$ is favored.

[257] P. R. Ogilby, Accounts of Chemical Research, 1999, https://doi.org/10.1021/ar980005p.

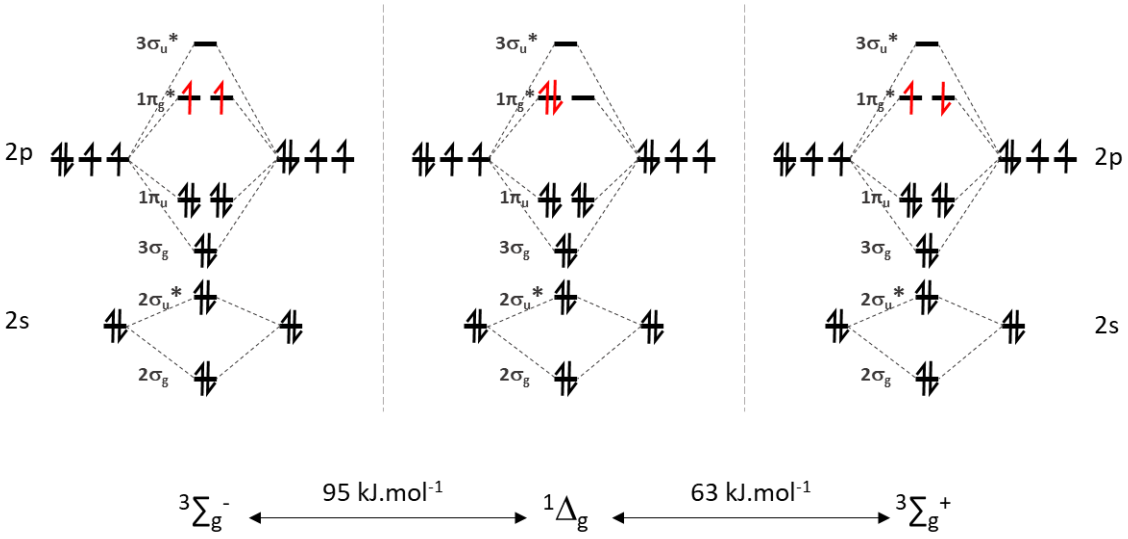

Fig. 67: Electronic structures of triplet oxygen (left), lower energy singlet oxygen (middle) and higher energy singlet oxygen (right).

The electronic configuration shows two unpaired electrons of same spin (+1/2) in the $^3\sum_g^-$ state, explaining the triplet ground state of oxygen. In the lowest energy singlet state $^1\Delta_g$, both electrons occupy the same orbital, thus the singlet state. The presence of the unoccupied antibonding π_g^* orbital makes $^1O_2$ highly reactive toward electron-rich molecules. Indeed, singlet oxygen can actively react with lipids and amino acids to form hydroperoxides and endoperoxides, leading cell death.[258,259,260]

In fact, type I and type II photosensitizing pathways are in competition, however, most photosensitizers mainly involve type II process due to the higher kinetic of energy transfer compared to charge transfer. This is the case for porphyrins, chlorins and bacteriochlorins for which hydroxyl radical, superoxide anion and singlet oxygen can be detected during photosensitizing.

[258] T. Homma et al., Biochemical and Biophysical Research Communications, 2019, https://doi.org/10.1016/j.bbrc.2019.08.073.
[259] R. L. Jensen et al., Journal of the American Chemical Society, 2012, https://doi.org/10.1021/ja303710m.
[260] I. O. L. Bacellar and M. S. Baptista, ACS Omega, 2019, https://doi.org/10.1021/acsomega.9b03244.

1.7. Porphyrinoid photosensitizers

1.7.1. Porphyrins

The most commonly used family of photosensitizers is porphyrins. The family includes porphin (the simplest porphyrin) and its substituted derivatives. They are heteromacrocyclic compounds and have the advantage to be rather photostable and can be chemically modified to change their solubility, giving access to hydrosoluble and liposoluble derivatives. These compounds are naturally found in plants (chlorophyll) and human body (heme). Porphyrins that chelate a metal ion are called metalloporphyrins (such as heme) and those free of metal are named free-base porphyrins. Porphyrins are characterized by five differents absorption bands.[261] The most intense band located at 418 nm is called the Soret (or B) band and corresponds to the electronic transition from the singlet ground state S_0 to the second singlet excited state S_2. Then, the four remaining absorption bands, far less intense than the Soret band, correspond to weak transitions from S_0 to the first excited state S_1. These transitions give rise to four absorption bands named Q bands (Q_{1y}, Q_{0y}, Q_{1x}, Q_{0x}) and are visible from 500 to 650 nm (**Fig. 68**). The use of porphyrins in PDT takes advantage of the last Q band (Q_{0x}) due to the absorbance in the red region, more suitable for biological application. Although the intensity is relatively low, porphyrins are clinically approved and are still widely used as photosensitizers for cancer treatments by PDT due to their high efficiency, decent photostability and many accessible commercial derivatives are available.

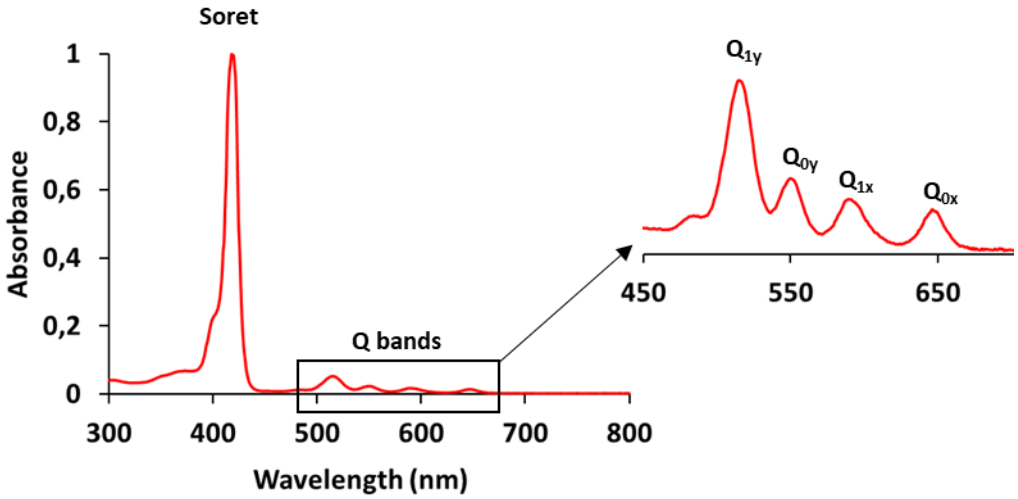

Fig. 68: UV-vis spectroscopy of *meso*-tetraphenylporphyrin (TPP) in chloroform.

[261] M. Gouterman, Journal of Molecular Spectroscopy, 1961, https://doi.org/10.1016/0022-2852(61)90236-3.

1.7.2. Chlorins

Chlorin derivatives (or dihydroporphyrins) can be obtained by reducing one pyrrole ring from porphyrin compounds. As a consequence, the energy gap between the ground state S_0 and excited state S_1 decreases due to the alteration of the π-electrons delocalization. Therefore, as the energy lowers, the associated wavelength of that transition is slightly red-shifted to 660 nm.[262] Chlorin-based compounds are characterized by more intense Q bands, as observed with the most red-shifted one at 660 nm. Due to the disturbance of the resonance pathway of the π-electrons, the Q bands are mostly affected while the Soret band remains unchanged. The higher intensity of the Q bands allow chlorins to absorb more light for an increased photosensitizing effect. Chlorins benefit from the same properties as porphyrins, mainly the decent photostability, the photoexcitation in the red region and the functionalization with different substituents. Chlorin-based compounds are also commonly used in PDT and clinically approved.

1.7.3. Bacteriochlorins

Bacteriochlorins are obtained by reduction of two pyrrole rings in porphyrins. Similar to chlorins, the reduction of a second ring leads to greater bathochromic effect of the Q bands (**Fig. 69**). Indeed, bacteriochlorins display a very sharp and intense absorption band at 740 nm in the NIR region, making them very appealing for biological applications as water absorbs the least in the 700–1000 nm region.[263] *meso*-Tetraphenylbacteriochlorin (TPBC), obtained by reduction of *meso*-Tetraphenylporphyrin (TPP), shows high triplet state quantum yield formation (0.83) and good quantum yield in singlet oxygen formation (0.43 in air-saturated and 0.62 in oxygen-saturated methanol).[264] The important absorption band at 740 nm and the high quantum yields of triplet state and singlet oxygen make TPBC a promising photosensitizer. However, in contrast with porphyrins and chlorins, bacteriochlorins suffer from faster photobleaching. This phenomenon is common with photosensitizers and results from self-photosensitizing. Indeed, the generated ROS react with nearby molecules, including the photosensitizer, leading to the degradation and loss of photo-activity. Because of the high

[262] A. Naumenko and N. Kutsevol, International Journal of Polymer Science, 2021, https://doi.org/10.1155/2021/8842052
[263] B. Pucelik et al., Coordination Chemistry Reviews, 2020, https://doi:10.1016/j.ccr.2020.213340.
[264] R. Bonnett et al., Journal of the Chemical Society, Perkin Transactions 2, 1999, https://doi.org/10.1039/A805328F

reactivity of ROS, photobleaching is a complex process that mainly involves oxidation and bond dissociation. Rovers et al. showed that photobleaching of TPBC in mice under illumination was 20-times greater than TPC.[265] Bonnett et al. reported a 90-fold greater photobleaching of TPBC in water-methanol compared to TPC.[266] To reduce photobleaching, the chelation of a heavy metal improves the oxidation potential of bacteriochlorins.[267] The clinically approved bacteriochlorin-based drug Tookad uses palladium instead of magnesium for better photostability. In case of free base bacteriochlorins (without metal), the use of electron-withdrawing groups increase the oxidation potential, which makes bacteriochlorins less sensitive to photooxidation as reported for perfluorinated derivatives.[268]

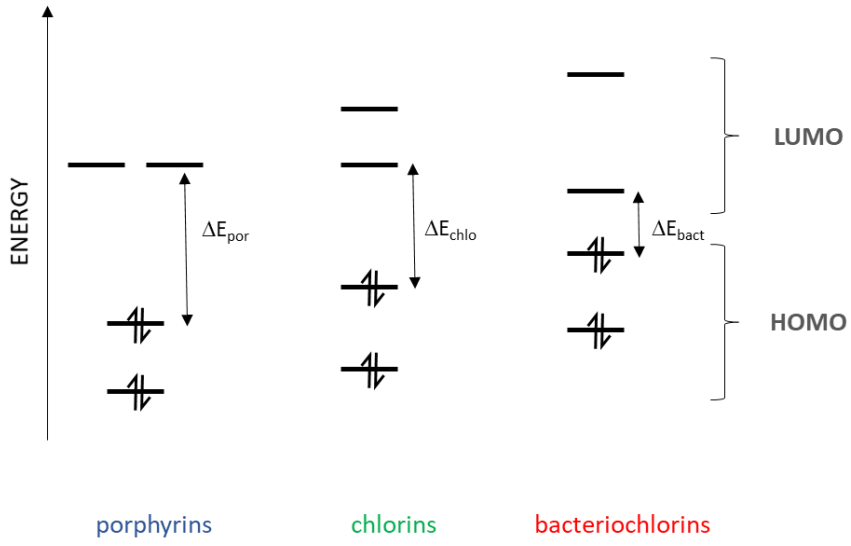

Fig. 69: Simplified electronic structures of porphyrins, chlorins and bacteriochlorins showing the energy gap between the HOMO and LUMO.

1.8. Ferrocene and photosensitizer interactions

Ferrocene is an electron-rich compound that can easily promote an electron to a higher orbital by photoexcitation. Its triplet excited state has an energy value of 167 kJ mol^{-1}, lower than its

[265] J. P. Rovers et al., Photochemistry and Photobiology, 2000, https://doi.org/10.1562/0031-8655(2000)072<0358:ivpcot>2.0.co;2.
[266] H. -P. Lassalle et al., Photochemical and Photobibological Sciences, 2004, http://doi.org/10.1039/b405138f.
[267] C. -Y. Chen et al., Inorganic Chemistry, 2012, https://doi.org/10.1021/ic301262k.
[268] S. Singh et al., Bioconjugate Chemistry, 2010, https://doi.org/10.1021/bc100356z.

singlet excited state which has an energy of 267 kJ mol^{-1}.[269,270] The quantum yield of the T_1 state was measured to be 0.66 in air-saturated DMSO.[270] Therefore, excited ferrocene is more prone to be in the triplet state than in the singlet state. Interestingly, ferrocene was reported to be able to quench triplet states of various organic compounds. Kikuchi et al. reported the quenching of triplet methylene blue by ferrocene and concluded that the quenching process was due to electron transfer by reductive quenching from ferrocene.[271] Indeed, triplet states of higher energy than T_1 state of ferrocene (167 kJ mol^{-1}) are mainly quenched by energy transfer while T_1 with energy lower than 167 $kJ.mol^{-1}$ are quenched by different ways, assuming electron transfer. This was confirmed by Ohno et al. who studied the quenching of triplet state of chloroaluminum phtalocyanine (AlPcCl) by various compounds including ferrocene and concluded that the quenching by ferrocene proceeded through electron transfer.[272] In order to have efficient triplet energy transfer, the quencher's triplet state must be lower in energy. Otherwise, quenching by electron transfer is favored, as discussed with molecular oxygen for type I and II photosensitizing. In case of AlPcCl, the triplet state energy value was reported to be around 106 kJ mol^{-1}. These observations were made by Farmilo and Wilkinson who reported the quenching rate constants (K_q) of the T_1 state of various compounds by ferrocene (**Table 1**).[273] According to their results, the lower the energy of the T_1 state, the lesser the quenching rate constant by ferrocene. For values lower than 120 kJ mol^{-1}, the quenching rate constants were 100 to 1000 folds lower than those of higher triplet state.

[269] J. J. Dannenberg and J. H. Richards, Journal of the American Chemical Society, 1965, https://doi.org/10.1021/bc100356z.
[270] A. Jaworska-Augustyniak et al., Chemical Physics Letters, 1987, https://doi.org/10.1016/0009-2614(87)80318-4.
[271] K. Kikuchi et al., Bulletin of the Chemical Society of Japan, 1975, https://doi.org/10.1246/bcsj.48.1378.
[272] T. Ohno et al., Journal of Physical Chemistry, 1983, https://doi.org/10.1021/j100228a016.
[273] A. Farmilo and F. Wilkinson, Chemical Physics Letters, 1975, https://doi.org/10.1016/0009-2614(75)85565-5.

Table 1: Quenching constant rates (K_q) of various organic compounds by ferrocene with their corresponding triplet state energy in benzene.

Compound	$E(T_1)$ (kJ mol^{-1})	K_q (L mol^{-1} s^{-1})
Benzophenone	293	8.6×10^9
Chrysene	238	5.7×10^9
Anthracene	176	4.4×10^9
Methylene blue	144	5.1×10^9
Naphtalene	123	3.6×10^7
Pentacene	96	$\leq 1.5 \times 10^6$
β-carotene	76	$\leq 1.0 \times 10^6$

Another interesting study was published by Maiya et al. on the intra- and intermolecular quenching rate of the triplet state of germanium porphyrins by ferrocene (**Fig. 70**).[274] In the former case, ferrocene was a ligand of germanium whereas in the intermolecular study, ferrocene was added as a free solute. In both cases, the photoreaction quantum yields greatly decreased, mainly attributed to the energy transfer from the triplet porphyrin to ferrocene. Interestingly, the intramolecular quenching was more noticeable due to a better orbital overlap between porphyrin and ferrocene. In fact, energy transfer is more efficient as the distance between the donor and acceptor is short. Therefore, the proximity and energy of the triplet state of the transferring compound to ferrocene are two key parameters in order to have an optimal energy transfer from the triplet state photosensitizer to ferrocene.

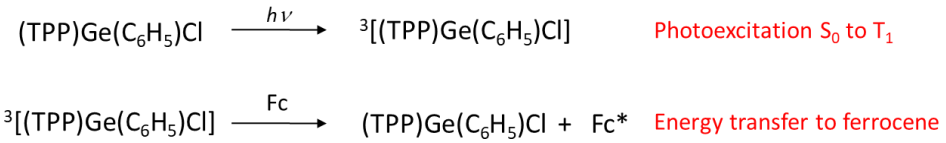

Fig. 70: Quenching of the triplet germanium porphyrin by free ferrocene leading to an excited state ferrocene.

[274] G. B. Maiya et al., Inorganic Chemistry, 1989, https://doi.org/10.1021/ic00312a006.

1.9. Objectives

As far as we know, utilizing the photolability of substituted ferrocene for the controlled disassembly of nanoparticles has yet to be reported. The synthesized C_{18}-Fc-PEO micelles could be used as nanocarriers able to release their cargo upon illumination in the visible absorption band of ferrocene at 442 nm. In addition to that, the photogenerated iron oxide species could possibly act as Fenton catalyst to induce oxidative damage in a biological environment as described in the previous chapter. Thus, the use of C_{18}-Fc-PEO micelles has two main goals: the delivery of a hydrophobic compound (dye or active molecule) and the formation of cytotoxic ferric species by photo-activation. Herein, the study focuses on the photodegradation of C_{18}-Fc-PEO micelles for anticancer applications.

2. Photodegradation study of C_{18}-Fc-PEO micelles at λ_{exc} = 460 nm

2.1. Photodegradation

The characteristic visible absorption band of ferrocene results from the spin-allowed electronic transition state A_{1g} to the excited state E_{1g}. This HOMO-LUMO transition is Laporte forbidden, leading to a low intensity absorption band (ε = 95 L mol^{-1} cm^{-1}).[275] As reported by Kutal et al., BFc and DBFc display a 40 nm bathochromic shift on their visible absorption band in polar solvents such as methanol.[239] Hence, to determine whether any similar shift occurred with C_{18}-Fc-PEO amphiphiles, they were self-assembled into micelles in ultrapure water (10 mg mL^{-1}) and the UV-visible absorption spectrum was recorded. The expected visible absorption band was observed, with a maximum at 442 nm as reported for unsubstituted ferrocene. The relatively large band from 400 to 600 nm displayed no solvatochromic effect in our case. After determining the exact absorption band of the C_{18}-Fc-PEO micelles, the photodegradation process was performed using the appropriate light source. A blue light emitting diode (LED) was selected for its broad emission spectra. Indeed, its emission spectra overlaps with the absorption spectra of the C_{18}-Fc-PEO micelles, with a maximum emission at 460 nm. The 400–600 nm region of the ferrocene's visible absorption band is mostly covered by the LED's emission spectra providing an optimized photoreaction (**Fig. 71**).

[275] A. Paul et al., ACS Omega, 2019, https://doi.org/10.1021/acsomega.9b01341.

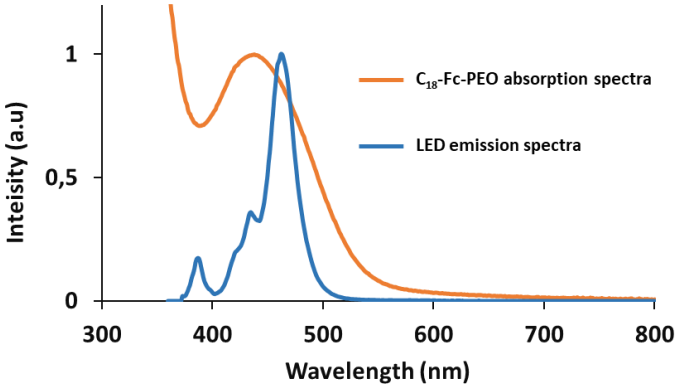

Fig. 71: Overlap of the visible absorption band of ferrocene with the emission spectra of the blue LED.

Thus, C_{18}-Fc-PEO micelles in water were exposed to the LED for 5 min. Prior to light exposure, the solution was clear and orange. However, after illumination, the solution quickly became heterogeneous, with a dark precipitate and a pale-to-colorless supernatant (**Fig. 72a**). These observations were in accordance with the literature on this matter.[223,] Indeed, the insoluble dark precipitate was most likely inorganic iron species and the loss of color in the supernatant was the result of the dissociation of the iron-ring bonds. The latter was confirmed by UV-visible spectroscopy of the supernatant, showing a drastic decrease of the visible absorption band of ferrocene (**Fig. 72b**). According to the electronic structure of ferrocene, a specific decrease of this absorption band reflects the fact that the Cp and metal orbitals no longer overlap with each other. Such observation results in no bonding between the iron atom and the Cp rings, and consequently, photodissociation occurs, in compliance with the proposed mechanism by Kutal.[241]

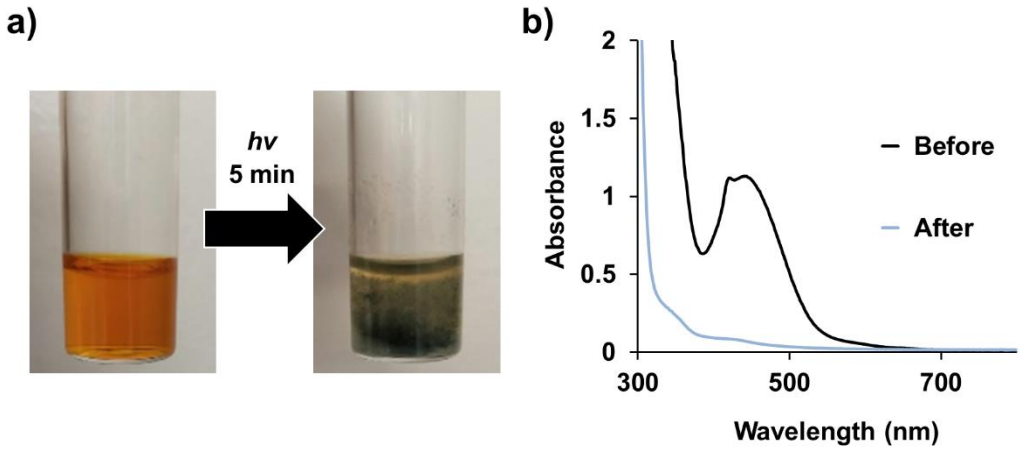

Fig. 72: **a)** Macroscopic view of a C_{18}-Fc-PEO micelles before and after illumination. **b)** UV-vis specstroscopy of the same sample before and after illumination.

Knowing that C_{18}-Fc-PEO micelles could be easily photodegraded in water in less than 5 min, we decided to monitor the kinetics of photodecomposition (**Fig. 73**). A 10 mg mL^{-1} solution was thus illuminated and the UV-vis spectrum was measured at different time points, from 0 to 15 min. After 30 s of light exposure, a noticeable 40% decrease of the absorbance at 442 nm could be observed, and the maximum decrease was obtained after 4 min. Illumination up to 15 min didn't induce any further modification of the UV-vis profile, suggesting that the photodegradation process had come to an end. This monitoring allowed us to determine the kinetic of photodegradation of the micelles which is an important feature for the release of encapsulated hydrophobic molecules.

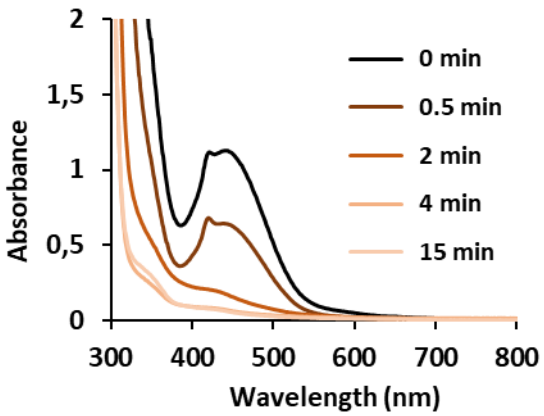

Fig. 73: Kinetics of photodegradation of C_{18}-Fc-PEO micelles monitored by UV-vis spectroscopy.

2.2. Mechanism and characterization

2.2.1. Supernatant

The photodegradation of several ferrocene derivatives is well documented, with detection and/or isolation of the photoadducts. In simple and small ferrocene derivatives such as BFc, DBFc and 1,1'-ferrocenedicarboxylic acid, systematic release of the Cp rings with their substituent is observed after the iron-ring bond dissociation. In case of the photodegradation of C_{18}-Fc-PEO micelles, analysis of the supernatant by mass spectrometry and ^{1}H NMR didn't allow conclusive characterization. In fact, the performed analyses were hardly exploitable due to the overwhelming signals of PEO. Mass spectrometry showed the characteristic Gaussian-like profile of PEO with a 44 m/z increment between each peaks. In ^{1}H NMR, the typical broad signal of PEO was also observed but the characteristic signals of the Cp ring was not visible. Therefore, organic by-products couldn't be accurately detected, however, the presence of PEO in the supernatant and the loss of color of the latter comfort the idea of the ring loss during the photodegradation. Based on previous reports, the by-products would hypothetically be Cp-PEO and Cp-C_{18}. In case of Cp-PEO, its solubility should be close to that of PEO, which makes it soluble in the aqueous phase, explaining the detection of PEO by mass spectrometry and ^{1}H NMR. On the other hand, Cp-C_{18} should be highly hydrophobic and should undergo precipitation in aqueous phase. This might partly explain why Cp-C_{18} couldn't be detected in the supernatant. To confirm the reported observation by Nesmeyanov, the experiment was reconducted using 1,1'-ferrocenedicarboxylic acid in presence of potassium carbonate in water. After illumination using the blue LED, the same precipitate and pale supernatant were observed. After centrifugation, mass spectrometry of the supernatant indicated a unique peak of m/z = 219, corresponding to the dimer of the cyclopentadienecarboxylic acid, as published by Nesmeyanov and other groups (**Fig. 74**).[223,276,277] Although the organic by-products couldn't be clearly identified, other observations seemed to point toward the fact that the photodegradation of C_{18}-Fc-PEO micelles most likely followed the photodecomposition process described for acyl-substituted ferrocene derivatives by releasing monomeric Cp rings.

[276] L. Zhang et al., ACS Applied Materials and Interfaces, 2013, https://doi.org/10.1021/am402189s.
[277] D. Peters, Journal of the Chemical Society, 1959, https://doi.org/10.1039/JR9590001761.

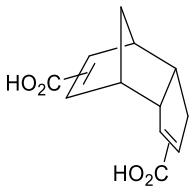

Fig. 74: Structure of the dimeric cyclopentadienecarboxylic acid.

2.2.2. Precipitate

The dark precipitate could not be solubilized in any organic solvent, comforting the hypothesis of an inorganic species. The insolubility of the precipitate prevented its analyses by common methods. Hence, to determine the nature of the precipitate, x-ray photoelectron spectroscopy (XPS) was used. XPS is a technique based on the photoelectric effect in solid state. The illumination of the sample by an x-ray beam results in the emission of core electrons from the different elements in the sample (Fe and O in our case). Depending on the orbital of the electron, the energy necessary to eject that electron is variable and thus, serves as footprint for the determination of the material's composition. Electrons that are located close to the nucleus of the atom have higher binding energies than those on outer shells. For instance, electrons in the 2s orbital have higher binding energy than 2p electrons. The photon-matter interaction provides information regarding elemental composition and oxidation state. Therefore, XPS was performed to determine the nature of the precipitate. XPS measurements were performed before illumination using C_{18}-Fc-PEO amphiphile (yellow solid) and 1,1'-ferrocenedicarboxylic acid ($Fc(COOH)_2$, orange solid) as comparison. The corresponding precipitates were obtained by illuminating a solution of ferrocene derivative in water under blue LED. The precipitates were centrifuged and washed several times with water and dried in the oven. XPS measurements of inorganic iron(II) and iron(III) species are well-documented and references can be found in the literature.[278,279] Typically, the binding energy of the 2p core electrons is specifically observed in order to determine the oxidation state of the iron atom. Indeed, the peak positions of Fe $2p_{1/2}$ and Fe $2p_{3/2}$ highly depend on the oxidation state of the iron atom as reported by Roosendaal.[280] Electrons in iron(0) are less tightly bound than those in iron(II) followed by

[278] M. Preisinger et al., Physical Review B, 2005, https://doi.org/10.1103/PhysRevB.71.165409.
[279] A. P. Grosvenor et al., Surface and Interface Analysis, 2004, https://doi.org/10.1002/sia.1984.
[280] S. J. Roosendaal et al., Surface Science, 1999, https://doi.org/10.1016/S0039-6028(99)01006-7.

iron(III). The same observation is made for the satellite peaks of lower intensities. XPS measurements focusing on Fe $2p_{1/2}$ and Fe $2p_{3/2}$ of iron contain four different peaks, noted from one to four, corresponding to the lowest binding energy to the highest. The first one is attributed to the main Fe $2p_{3/2}$ peak, the second to the satellite Fe $2p_{3/2}$ peak and third and fourth correspond to the main and satellite Fe $2p_{1/2}$ peaks respectively (**Fig. 75**, **Table 2**).

XPS measurements before illumination provided the expected values of binding energies for both C_{18}-Fc-PEO and $Fc(COOH)_2$. The main peaks 1 and 3 at 711 and 721 eV respectively, followed by their corresponding low intensity satellite peaks 2 (~ 716 eV) and 4 (~ 729 eV), are characteristic of Fe(II). The XPS spectra of the precipitates after illumination show a shift of all peaks to higher binding energies. This observation is in accordance with the higher oxidation state of Fe(III). Indeed, the respective peak positions of Fe $2p_{3/2}$ and Fe $2p_{1/2}$ at 711 and 724 eV are typical from Fe(III). The rise in intensity of the satellite peaks 2 and 4 also confirms the presence of Fe(III). Furthermore, the XPS spectra of the precipitates are much broader than those of the samples before illumination. This broadening effect is reported in the literature and attributed to spin-orbit couplings and multiplet splitting that are systematically observed with iron(II) and iron(III) oxide species. In Nesmeyanov's work, the formation of ferric hydroxide ($Fe(OH)_3$) species was reported during the photolysis of $Fc(COOH)_2$ in basic aqueous solution. Even if the XPS measurements didn't allow the attribution of a precise structural composition of the iron species, the XPS spectra of the precipitates from $Fc(COOH)_2$ and C_{18}-Fc-PEO are almost perfectly matching, strongly suggesting that the photodegradation of C_{18}-Fc-PEO micelles also generates $Fe(OH)_3$ as a by-product, even in neutral aqueous solution. Reference XPS spectra of $Fe(OH)_3$ can be found in the literature and correspond to our experimental values.[281]

[281] H. Chen et al., Ceramics International, 2021, https://doi.org/10.1016/j.ceramint.2021.09.047.

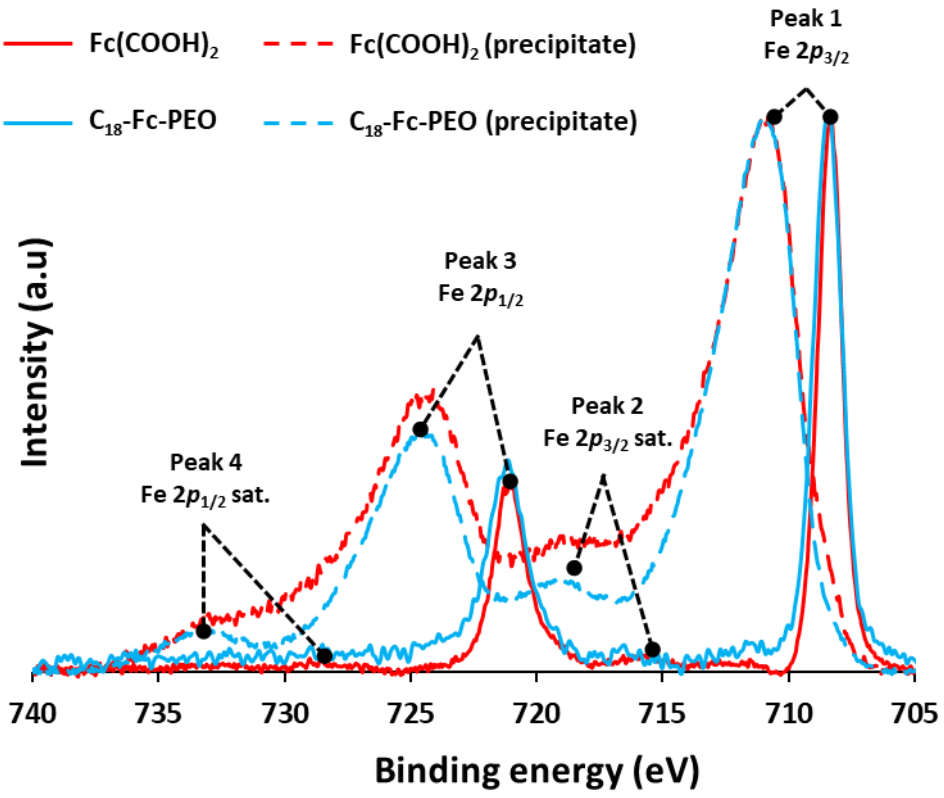

Fig. 75: XPS measurements of $Fc(COOH)_2$ (red) and C_{18}-Fc-PEO (blue) before (solid lines) and after (dashed lines) illumination.

Table 2: Values of the different binding energies (eV) observed for the four samples.

	binding energy (eV)			
	Peak 1	Peak 2	Peak 3	Peak 4
$Fc(COOH)_2$	708.3	715.5	721.6	728.5
$Fc(COOH)_2$ (PRECIPITATE)	711.0	719.6	724.2	733.0
C_{18}-Fc-PEO	708.3	715.9	721.1	728.7
C_{18}-Fc-PEO (PRECIPITATE)	711.0	719.2	724.3	733.0

Thus, we showed that illumination of C_{18}-Fc-PEO micelles in the visible absorption band led to the decomposition and oxidation of the ferrocene moiety (Fe^{2+}) to generate ferric oxide/hydroxide species (Fe^{3+}).

To further study the photodegradation process, the illumination of C_{18}-Fc-PEO micelles was conducted in the presence of Fe^{3+}-binding chelators, to prevent the formation of insoluble iron(III) species. Deferiprone (DFP) and deferoxamine (DFO), two commonly used molecules for the chelation of free Fe^{3+} and are used in medicine to treat iron-related diseases,[282] were selected as model chelators. Solutions of C_{18}-Fc-PEO micelles were prepared at 10 mg mL^{-1} and a large excess of DFP or DFO was introduced. DFP is known to form a bright red complex with Fe^{3+} in a 3:1 ratio (DFP:Fe^{3+}),[283] while DFO forms a 1:1 ratio yellow-orange complex.[284] No color change was observed after introducing DFP or DFO, implying that the chelation of iron didn't occur before illumination. The samples, containing either DFP or DFO, were exposed to the blue LED for 5 min. The micelles solution with DFP quickly turned from a clear yellow to a clear red solution and no precipitate was observed. In case of DFO, the solution's color remained yellow-orange but without any sign of precipitate.

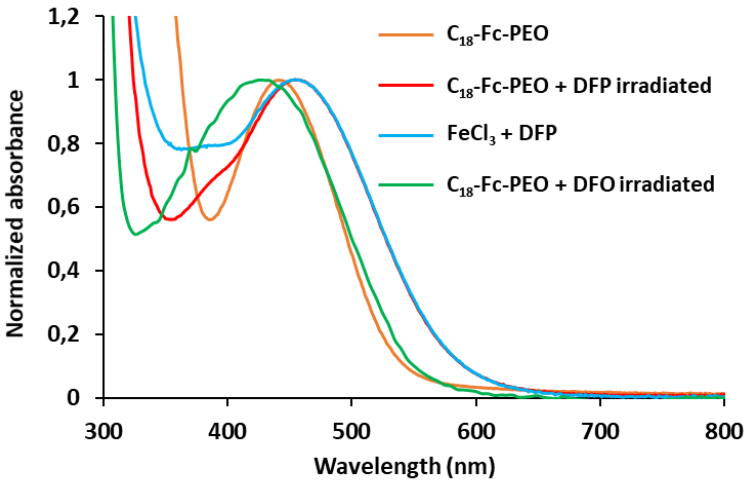

Fig. 76: UV-vis spectroscopy of C_{18}-Fc-PEO micelles before illumination (yellow), after illumination with DFP (red) and DFO (green), $FeCl_3$ with DFP (blue).

[282] R. Origa et al., Journal of Clinical Medicine, 2022, https://doi.org/10.3390/jcm11072010.
[283] V. A. Timoshnikov et al., Free Radical Biology and Medicine, 2015, https://doi.org/10.1016/j.freeradbiomed.2014.10.513.
[284] V. M. Nurchi et al., Molecules, 2021, https://doi.org/10.3390/molecules26113071.

Thus, the use of chelators of Fe^{3+} prevented the formation of the precipitate and confirmed once more that ferrocene is photo-oxidized during upon illumination. The red complex DFP:Fe^{3+} could be characterized by UV-visible spectroscopy and showed a maximum absorption at 460 nm (**Fig. 76**). Its absorption band is similar to that of ferrocene but the 18 nm bathochromic shift and the broader band gives the specific red color instead of the yellow-orange color of ferrocene. To assure that the observed complex was indeed DFP:Fe^{3+}, an aqueous solution of ferric trichloride ($FeCl_3$) in presence of DFP was also analyzed by UV-vis spectroscopy. The UV-vis profile of the control solution proved to be exactly the same as the one from the illuminated solution. Hence, the complex formed during the photodegradation of C_{18}-Fc-PEO micelles with DFP was confirmed to be DFP:Fe^{3+}. For DFO, UV-vis spectroscopy provided an absorption band with a maximum absorption at 430 nm, in agreement with reported values of DFO:Fe^{3+} complex at neutral pH.[284] According to Kutal's photodegradation mechanism and the absence of precipitate, one can hypothesize that, during the displacement of the Cp ring, DFP and DFO complex iron faster than water, due to their greater nucleophilic character. Indeed, water coordinates to iron with its oxygen atom while DFP and DFO engage multiple heteroatoms. Therefore, they should be better coordinating molecules than water, which prevents the latter from generating the ferric hydroxide species that precipitates. In fact, the complex constant formation log(β) for DFP, DFO and H_2O with Fe^{3+} are respectively 37.4,[285] 30.4[286] and 12.0.[287] Log(β) measures the stability of the complex. The higher the value, the more stable the complex is. Compared to water, the complex constant formations are around 3-fold higher for DFP and DFO, which could explain the predominant formation of the colored complexes instead of the inorganic ferric species.

2.2.3. Effect of solvent

After assessing the photodegradation of C_{18}-Fc-PEO micelles in water, the study was extended to different organic solvents. The experiments were conducted in DMF, methanol, acetonitrile, acetone and chloroform, at 10 mg mL^{-1} with 5 min illumination. The purpose of these experiments was to determine the influence of the solvent in the photodecomposition process

[285] G. Crisponi et al., PLoS One, 2015, https://doi.org/10.1371/journal.pone.0133050.
[286] E. Farkas et al., Polyhedron, 1999, https://doi.org/10.1016/S0277-5387(99)00144-8.
[287] D. B. Jaynes et al., Water Resources Research, 1984, https://doi.org/10.1029/WR020i002p00233.

of the C_{18}-Fc-PEO amphiphiles as described by other groups. According to the literature, water and methanol are the two solvents that induce the most photodecomposition with generation of a dark precipitate and discoloration of the supernatant. Therefore, the illumination was first performed in methanol. As expected, the photodecomposition occurred very quickly and the same result as with water was obtained. In the case of DMF, a very dark brownish solution was obtained but no apparent precipitate could be observed. Although no precipitate was detected, it was clear that the photodecomposition had occurred.

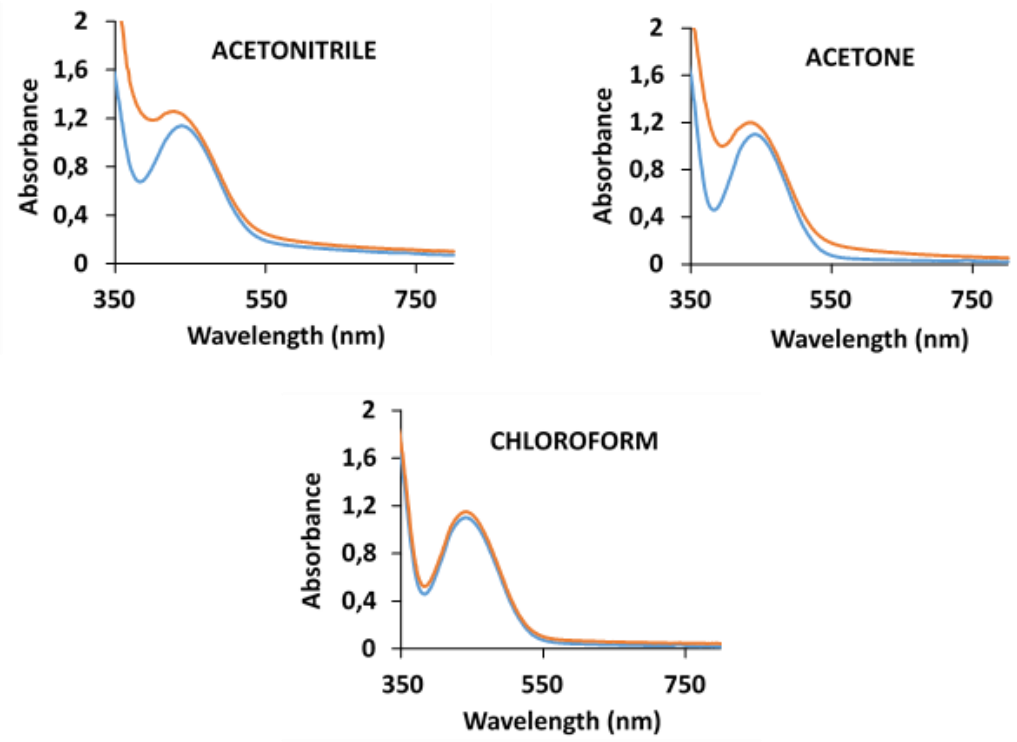

Fig. 77: UV-vis spectroscopy of before (blue) and after (orange) illumination of C_{18}-Fc-PEO in different organic solvents.

The same experiment was also performed in acetonitrile, acetone and chloroform. In these solvents, no macroscopic changes were noticed and the solutions retained their initial yellow-orange color (**Fig. 77**). To support this observation, UV-visible spectra of the solutions before and after illumination were recorded. Following the illumination in acetonitrile and acetone, a slight hypsochromic shift was observed while maintaining the same absorbance intensity, suggesting that no major structural modification of the ferrocene moiety had taken place.

Despite a noticeable increase of the absorbance at 386 nm, more pronounced in acetonitrile than acetone, the absorption band of interest at 442 nm was not majorly affected by the illumination, as the curvature and maximum absorption remained the same. In chloroform, not a single shift or decrease in absorbance was observed. Spectra obtained before and after illumination were identical. From these experiments, the nucleophilic character of the solvent clearly appears to play an important role in the photodecomposition of C_{18}-Fc-PEO, as reported by Tarr et al.

2.3. Proof of concept: Encapsulation and release of Nile Red

To evaluate the ability of our micelles to encapsulate and release hydrophobic molecules, we selected Nile Red (NR) as a model hydrophobic compound. The NR is a dye that is strongly fluorescent in lipophilic environment, but precipitates in water and gets quickly quenched.[288] Bearing that in mind, these properties are perfectly suited for the encapsulation into C_{18}-Fc-PEO micelles, as the hydrophobic core allows the solubilization of the dye. Upon illumination of the micelles, their degradation is expected to induce the release and aggregation/precipitation of Nile Red in the aqueous medium, leading to the decrease of its absorbance.

Nile Red (0.3 wt%, λ_{abs} = 555 nm) was loaded into C_{18}-Fc-PEO micelles following the standard procedure used in our laboratory (see Experimental section). After sonication and filtration over 0.45 µm filter, the colloidal suspension of NR@C_{18}-Fc-PEO was illuminated and the degradation was monitored by UV-vis spectroscopy (**Fig. 78a**). In this case, exposure to light with λ_{exc} = 460 nm triggered photodegradation of the micelles similar to what was observed with C_{18}-Fc-PEO micelles. Indeed, after only 30 seconds of illumination, around 40% of the NR signal was lost, which can be correlated to the photodegradation of the ferrocene unit, leading to the disruption of the micelles and thus, the release of NR in the aqueous medium. NR's absorption band totally disappeared after 4 min of illumination, which is in accordance with the kinetic of C_{18}-Fc-PEO micelles photodegradation.

[288] P. Greenspan and S. D. Fowler, Journal of Lipid Research, 1985, https://doi.org/10.1016/S00222275(20)34307-8.

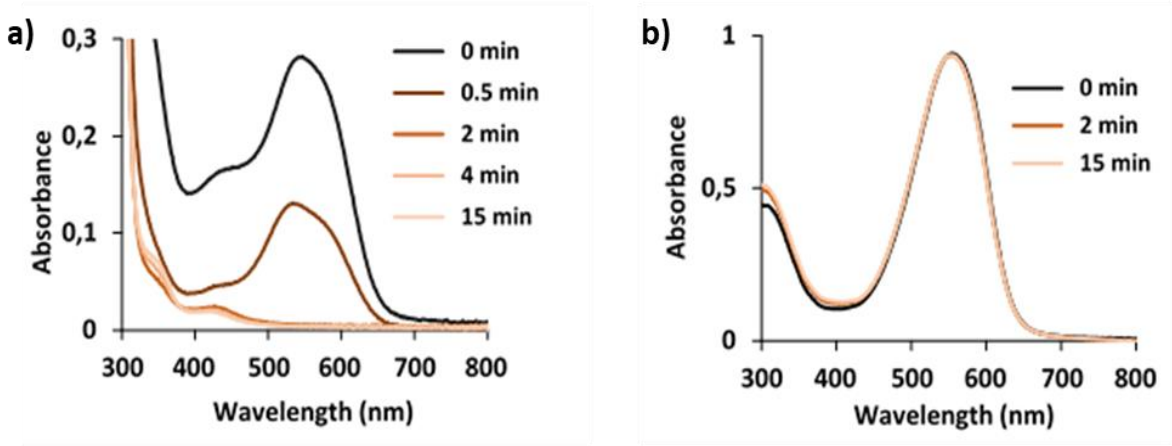

Fig. 78: Illumination of NR@C_{18}-Fc-PEO **a)** and NR@C_{18}-PEO **b)** micelles in water up to 15 min.

Even though the results seem to show that NR is being released from the micelles during the photo-illumination experiment, photodegradation of NR itself could not be excluded at that point. As a matter of fact, illuminating at 460 nm could potentially induce photobleaching of the dye, as it is a very common issue when using fluorophores in this type of experiments. While NR has minimum absorption in the blue region, the energy delivered by the light to NR may alter the dye's structure which would lead to a decrease of the measured NR absorbance.

To rule out the possibility of NR photobleaching during the illumination process, the same experiment was carried out using micelles without ferrocene obtained from the self-assembly of C_{18}-PEO. To this end, NR was encapsulated in C_{18}-PEO micelles. The aqueous solution of NR@C_{18}-PEO was then exposed to 460 nm light for 15 min. The absorbance corresponding to NR remained the same, indicating that NR is stable under these conditions (**Fig. 78b**). As a conclusion, we can doubtlessly state that the decrease in NR's absorbance is due to its release from the micelles that are gradually degraded under 460 nm light, leading to NR precipitation and quenching in aqueous media.

2.4. *In vitro* experiments

2.4.1. Cell uptake

After proving that C_{18}-Fc-PEO micelles could efficiently be photodegraded by light to generate insoluble ferric species and release Nile Red at the same time, *in vitro* experiments were performed to assess the internalization of the micelles in cancer cells. For these experiments, MCF-7 human breast cancer cells were selected, as they are commonly used for early testing of phototherapies. The cells were seeded in 96-well plates and incubated in a culture medium for 3 days. NR-loaded micelle were then added at different concentrations (0, 20, 50, and 100 µM) and cells were incubated at 37 °C for 2 h. After removal of the supernatant, cells were treated with paraformaldehyde (fixation) and Hoechst 33342 (nuclei staining) for 20 min at room temperature, before fluorescence quantification and confocal imaging. Confocal imaging showed the presence of Nile Red in the cytosol surrounding the nuclei for both NR@C_{18}-Fc-PEO and NR@C_{18}-PEO micelles (**Fig. 79a** and **79b**). Moreover, the internalization is concentration-dependant: the higher the concentration of micelles is, the higher the intracellular fluorescence is (**Fig. 79d**). Both C_{18}-Fc-PEO and C_{18}-PEO micelles were effectively uptaken by MCF-7 cells, which is an important prerequisite for the photo-triggered release of toxic species in tumor cells.

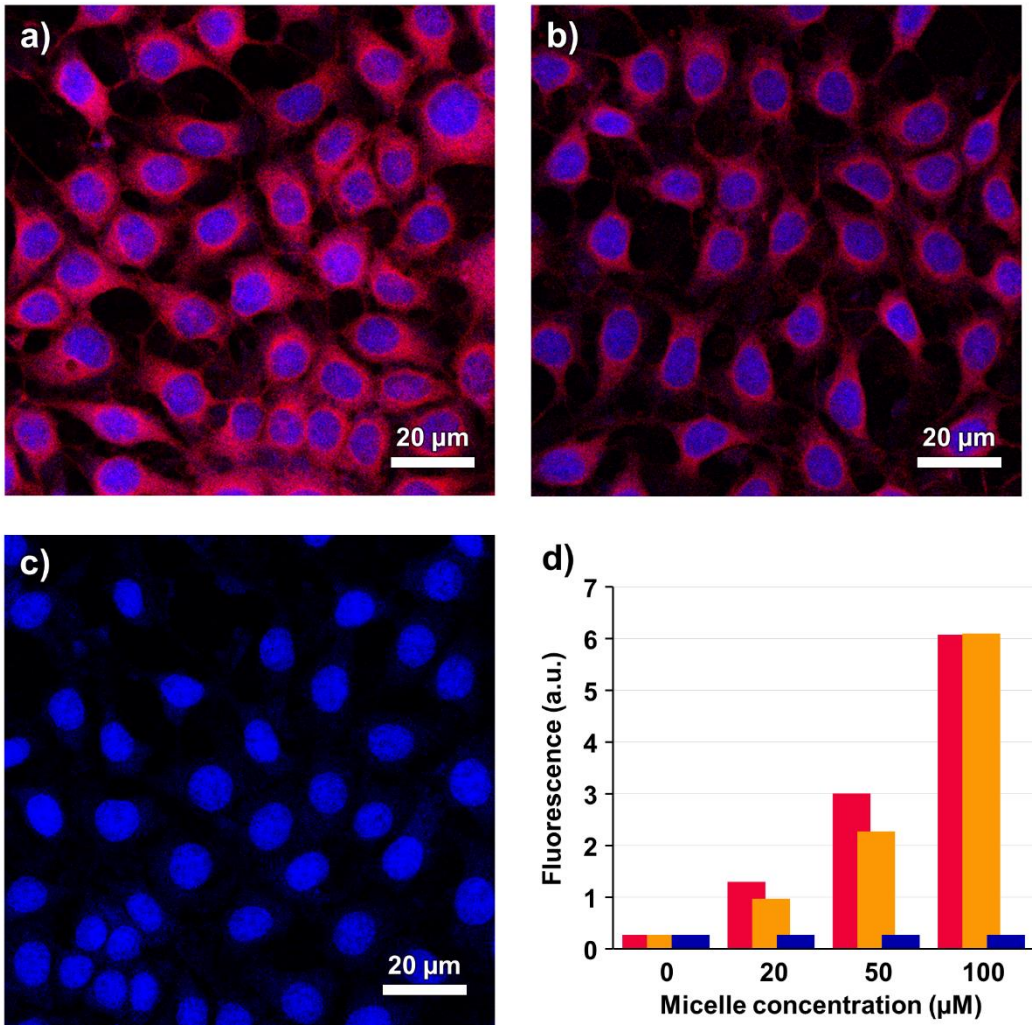

Fig. 79: **a)**, **b)** and **c)** Confocal imaging of NR@C_{18}-Fc-PEO, NR@C_{18}-PEO and C_{18}-Fc-PEO micelles at 100 µM. **d)** Cytosolic fluorescence at different concentrations for NR@C_{18}-Fc-PEO (red), NR@C_{18}-PEO (orange) and C_{18}-Fc-PEO (blue).

2.4.2. Cytotoxicity assays

We first decided to investigate whether C_{18}-Fc-PEO micelles exhibited non-specific cytotoxicity in the absence of light illumination. Thus, MCF-7 cells were treated with either C_{18}-PEO (control) or C_{18}-Fc-PEO (photo-active) micelles at different concentrations, from 2 to 200 µM. In both cases and at all concentrations, no decrease in cell viability was observed, indicating that both micelle types were biocompatible (**Fig. 80**, black bars).

However, when combined with illumination, a net cytotoxicity could be observed for C_{18}-Fc-PEO micelles while no effect was observed with C_{18}-PEO micelles. In fact, cell viability gradually decreased as the concentration of C_{18}-Fc-PEO micelles increased, with an IC_{50} value of 49 µM.

Importantly, MCF-7 cells treated with photostable C_{18}-PEO micelles showed no cytotoxicity under illumination (**Fig. 80**, blue bars). Indeed, cell viability remained constantly high regardless of the concentration. These results indicate that light itself has no direct impact on the cells and that the cytotoxicity of C_{18}-Fc-PEO micelles under illumination is solely mediated by photo-activation of the ferrocenyl group. It's worth noting that the choice of the cell line is quite important. For instance, HeLa cells exposed to blue light under the same conditions but without micelles proved to be extremely sensitive, with less than 20% of cells surviving 72 h post-illumination. In the case of MCF-7 cells, no damage was observed as demonstrated with the control group.

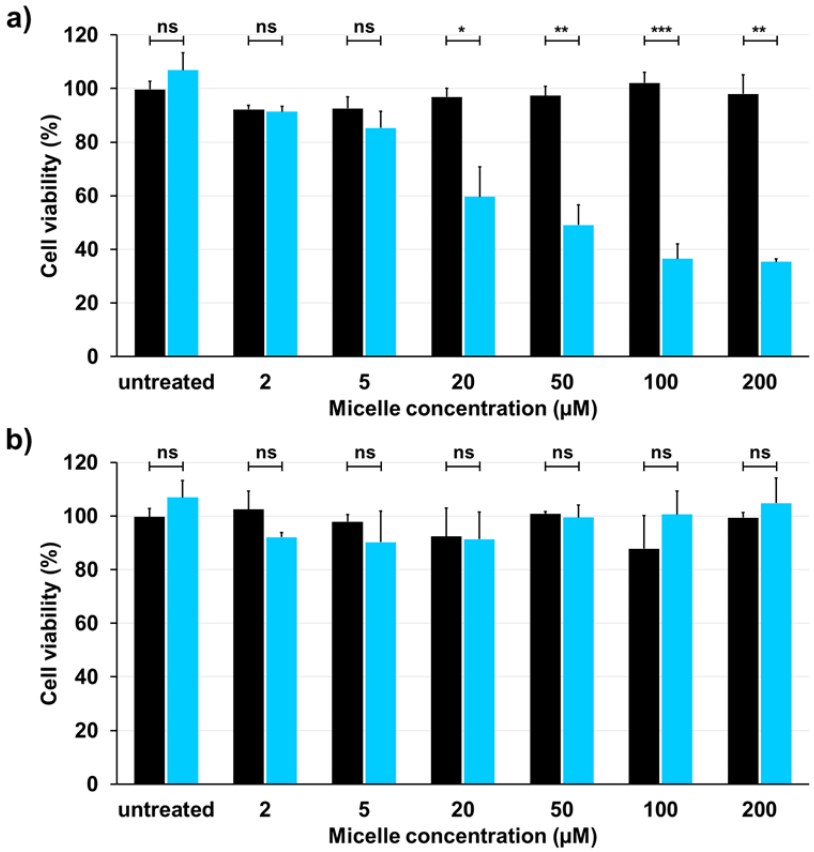

Fig. 80: MCF-7 cells treated with **a)** C_{18}-Fc-PEO and **b)** C_{18}-PEO without (black) and with (blue) illumination at 460 nm for 10 min. Statistical analysis was performed using Excel, Student's T-test (* $p \leq 0,05$; ** $p \leq 0.01$; *** $p \leq 0.001$; ns = non-significant).

The two hypotheses can be put forward to account for the observed cytotoxicity of C_{18}-Fc-PEO micelles upon photo-activation: i) the insoluble iron that is released in the intracellular compartment can be directly toxic to cells; ii) iron can also contribute to redox reactions and increase intracellular oxidative stress. In fact, iron species are well-known Fenton catalysts involved in intracellular redox processes, leading to lipid peroxidation and ultimately to cell death. To comfort the latter hypothesis, the oxidative stress induced upon photo-activation of C_{18}-Fc-PEO micelles was investigated using CellROX™ Deep Red. CellROX is a fluorogenic reporter probe used for measuring oxidative stress in cells. The cell-permeant dye is non-fluorescent in its reduced state and becomes brightly fluorescent (absorption/emission maxima ~644/665 nm) upon ROS-mediated oxidation. MCF-7 cells were incubated with C_{18}-Fc-PEO or C_{18}-PEO micelles (100 µM) for 1 h and either subjected to illumination (460 nm) for 10 min or left in the dark for 10 min. Cells were then incubated with the CellROX™ probe for 8 h and cytoplasmic fluorescence (red channel) was quantified using an Operetta microscope (**Fig. 81**).

Cells treated with C_{18}-Fc-PEO or C_{18}-PEO micelles in the dark showed no increase in ROS production, compared to the untreated cells (conditions: no micelle/dark) (**Fig. 81a**). This experiment confirmed that the two pristine micelles were not pro-oxidant species by themselves. However, cells treated with the activatable C_{18}-Fc-PEO micelles and submitted to blue light for 10 min displayed a significant increase of the CellROX signal (**Fig. 81b**, blue bars)). In fact, we observed an 8-fold increase of the amount of intracellular ROS production, compared to the non-activatable C_{18}-PEO micelles, under the same conditions. This experiment unambiguously demonstrated the generation of an oxidative stress mediated by the photo-degradation of the ferrocene-containing micelles. These results suggest that the in situ production of ROS could account for the cytotoxic effect observed when cells were treated with C_{18}-Fc-PEO micelles under illumination.

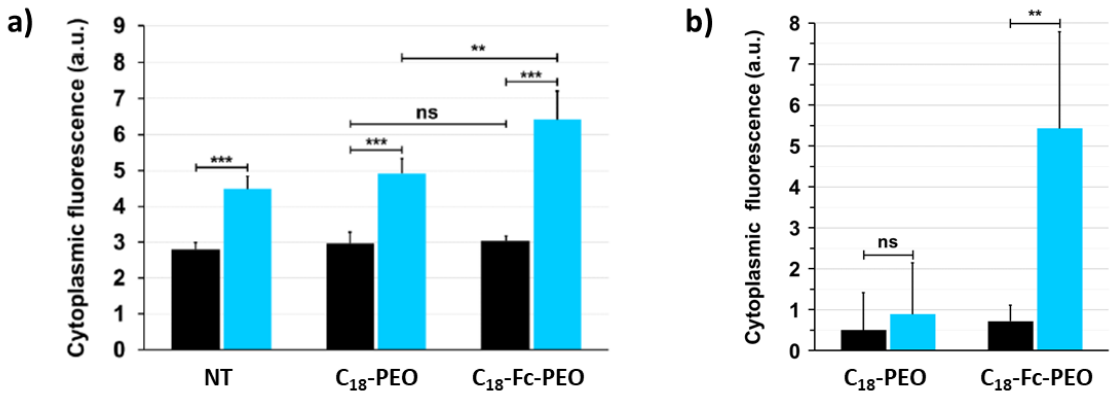

Fig. 81: **a)** Detection of light-triggered oxidative stress: CellROX cytoplasmic fluorescence induced by treatment with different micelles (100 µM) either in the dark (black bars) or after illumination at 460 nm for 10 min (blue bars). Student's T-test (** $p \leq 0.01$; *** $p \leq 0.001$; ns = non-significant). **b)** Detection of light-triggered oxidative stress: Increase of CellROX cytoplasmic fluorescence compared to control cells, induced by treatment with different micelles (100 µM) either in the dark (black bars) or after illumination at 460 nm for 10 min (blue bars) – The background fluorescence signal of CellROX in blank cellular experiments, i.e. no micelles/dark and no micelles/illumination, was subtracted from the signal of CellROX measured for cells treated with micelles/dark and micelle/illumination, respectively. Statistical analysis was performed using Excel, Student's T-test (** $p \leq 0.01$; ns = non-significant).

Although the C_{18}-Fc-PEO micelles showed very promising results regarding their phototriggered cytotoxicity, they are ultimately intended to treat solid tumors *in vivo*, and the utilization of blue light is not suitable for such purpose as the penetration through biological tissue is limited. There is one wavelength window of high tissue penetration in the near-infrared (NIR) region which comprises wavelengths from 700 to 1200 nm. We thus decided to encapsulate a photosensitizer in order to assist the photodegradation of C_{18}-Fc-PEO micelles under NIR light illumination. For this purpose, we decided to work with *meso*-Tetraphenylbacteriochlorin (TPBC) that can be photo-activated at 740 nm.

3. Photodegradation study at λ_{exc} = 740 nm

3.1. TPBC and C_{18}-Fc-PEO micelles

No data was found in the literature regarding the quenching of triplet chlorin and bacteriochlorin derivatives by ferrocene. TPP is reported to have a triplet state at 137 kJ mol^{-1}. In the case of TPC and TPBC, no values have been published, but respective estimations of 141 kJ mol^{-1} and 119 kJ mol^{-1} were made.[264] Comparing these values to the triplet state energies of **Table 2**, the quenching rate constants of TPC and TPBC by ferrocene could be estimated to be in the order of 10^9 and 10^6–10^7 L mol^{-1} s^{-1} respectively. By analogy with the values of **Table 2** and the studies of AlPcCl by Ohno and methylene blue by Kikuchi, we could hypothesize that the quenching of the triplet state of TPC by ferrocene would mainly proceed by energy transfer while an electron transfer process would be more favored with TPBC due to the lower triplet state energy value.

In addition to the lack of data on the quenching of bacteriochorins and chlorins by ferrocene, no experiments were performed using substituted ferrocene with electron-withdrawing groups. One can hypothesize that, in the case of energy transfer, the excited triplet state ferrocene formed after receiving the triplet energy from the photosensitizer is very similar to the transient excited state during the photodegradation using visible light as described by Kutal et al. Indeed, the illumination of electron-poor ferrocene in the visible absorption band generates a transient excited state that results from the promotion of an electron from the LUMO to the HOMO. The excitation by triplet energy transfer also arises from the promotion of an electron. Therefore, it may be possible that ferrocene excited by triplet energy transfer undergoes decomposition similar to that of the photoexcited ferrocene in the presence of nucleophiles such as water. In the case of reductive quenching of a photosensitizer by ferrocene through electron transfer, a direct oxidation of ferrocene would occur, leading to the formation of ferricenium species. Combined with the electron-withdrawing substituents, such mechanism would decompose the ferrocene moiety. Finally, the generation of type I or II reactive oxygen species by illumination of a photosensitizer could also oxidize the ferrocene unit and potentially lead to its degradation.

Thus, *meso*-Tetraphenylbacteriochlorin (TPBC) was selected as photosensitizer. The intense Q band in the NIR region at 740 nm is perfectly suited for biological applications. The high quantum yields of singlet oxygen and triplet state formation make TPBC a great PDT agent.

Quenching of triplet state of TPBC by ferrocene would either lead to an excited triplet state ferrocene (energy transfer) and/or ferricenium species (charge transfer). In both cases, the ferrocene moiety represents a highly electrophilic nature likely to undergo decomposition. Furthermore, the distance between the ferrocene unit and the photosensitizer being a crucial parameter in quenching, the encapsulation of TPBC into C_{18}-Fc-PEO micelles (10 nm) should greatly improve the efficiency of energy and/or charge transfer between both groups for enhanced activation of ferrocene. All these reasons prompted us to select TPBC as potential photosensitizer for the photodegradation of the micelles in the NIR region.

3.2. *meso*-Tetraphenylbacteriochlorin (TPBC)

3.2.1. Synthesis

The synthesis of TPBC can be performed in one step by reduction of the corresponding TPP by hydrogenation using an in situ generation of diimide. The diimide is formed during the thermolysis of *p*-toluenesulfonylhydrazine (*p*-TsN_2). The latter is decomposed at 110 °C, giving p-toluenesulfonyl acid and diimide. In the presence of an electron-rich double bond, the diimide can readily react to reduce it by hydrogenation and release nitrogen gaz (**Fig. 82**).

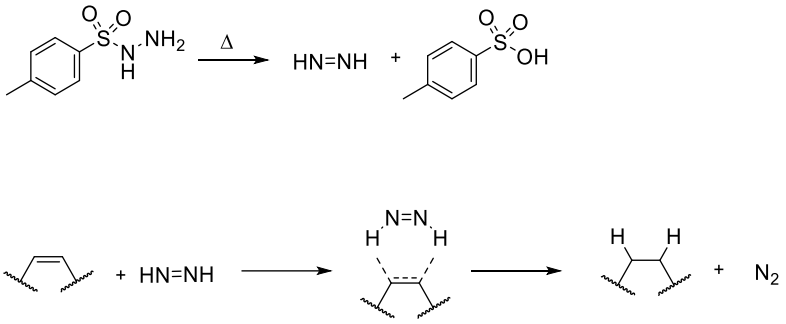

Fig. 82: General mechanism of the reduction of double bond by in situ generation of diimide using *p*-TsN_2.

In case of porphyrins, the hydrogenation by diimide selectively reduces two double bonds. Porphyrins have 18 π-electrons that constitute an aromatic macrocycle (in bold, **Fig. 83**) following the Hückel's rule of (4n + 2) π electrons. In this case, the shortest aromatic macrocycle

in porphyrins in which all bonds have the same length corresponds to n = 4. The two remaining double bonds in two of the four pyrrole rings have a more localized character. Indeed, these two bonds were reported to undergo cycloaddition reactions, proving their much higher reactivity.[289,290] Thus, the reduction by hydrogenation using diimide either reduces one or two double bonds, providing TPC and TPBC respectively.

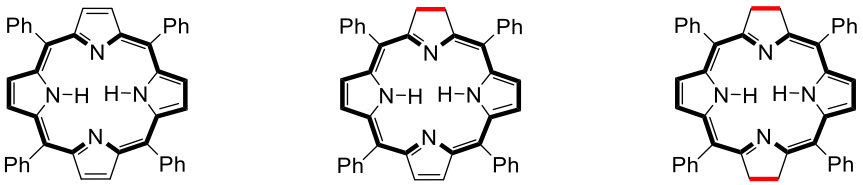

Fig. 83: Structures of TPP, TPC and TPBC, showing the reduced double bonds (red) and the 18 π aromatic macrocycle (bold).

The synthesis of TPBC (**Fig. 84**) was adapted following the protocole of Whitlock et al.[291] Starting from the commercially available TPP, the reduction by in situ generated diimide from p-toluenesulfonylhydrazine at 110 °C yielded a mixture of unreacted TPP, partially reduced TPC and totally reduced TPBC. Although these compounds have very similar chemical structures, their UV-vis spectra greatly differ, especially for TPBC (**Fig. 85**). TPP has very low intensity Q bands from 500 to 650 and an intense Soret band at 418 nm, TPC has more intense red-shifted Q bands, especially at 660 nm, and TPBC is characterized by very intense bands at 358, 378, 522 and 740 nm. Therefore, by monitoring these bands by UV-vis spectroscopy, the purity and conversion rate could be assessed. The crude mixture obtained after the reaction contained all the described absorption bands from TPP, TPC and TPBC, showing the partial reduction of TPP. The three compounds could not be separated on silica gel, however, acidic treatment with concentrated phosphoric acid could selectively protonate TPP and TPC due to their higher basicity, leaving TPBC in the organic phase.[291]

[289] A. M. G. Silva et al., Journal of Organic Chemistry, 2006, https://doi.org/10.1021/jo0611770.
[290] A. C. Tomé et al., Journal of Porphyrins and Phtalocyanines, 2009, https://doi.org/10.1142/S1088424609000619.
[291] H. Whitlock et al., Journal of the American Chemical Society, 1969, https://doi.org/10.1021/ja01054a044.

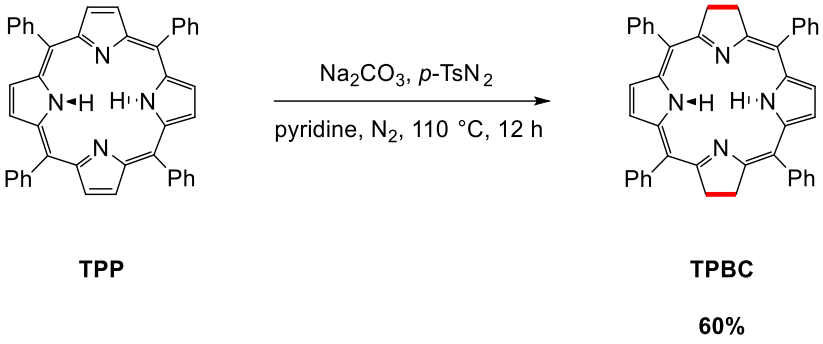

TPP **TPBC**

60%

Fig. 84: Reaction conditions for the reduction of TPP to TPBC.

^{1}H NMR spectra showed the singlet peak at 3.88 ppm corresponding to the 8 protons of the reduced pyrroles. UV-vis spectroscopy didn't show any absorption bands at 650 and 418 nm that correspond to TPC and TPP respectively. Therefore, TPBC could be synthesized in one step in decent yield.

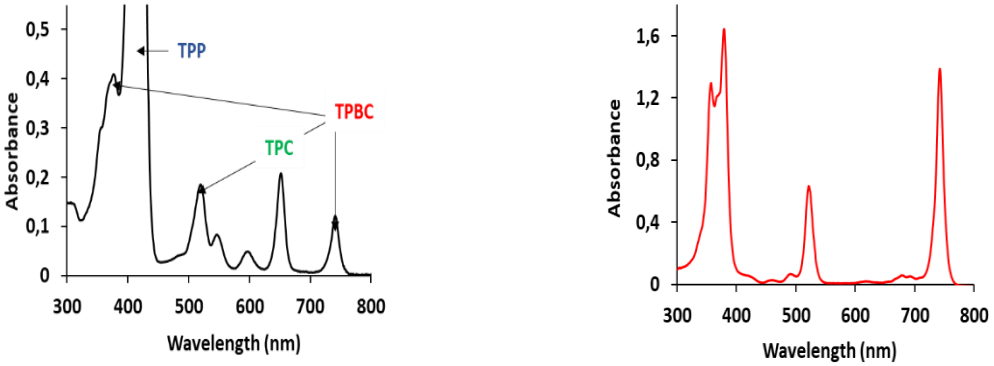

Fig. 85: UV-vis spectroscopy of the obtained mixture after reaction (left) and the purified product (right) after treatment with phosphoric acid.

3.2.2. Stability assessment

Bacteriochlorins are said to be photochemically unstable due to photobleaching. Thus, the photostability of the synthesized TPBC was assessed. A sample of TPBC in benzene was exposed to natural light and another one was stored in the dark. Both samples were kept under air atmosphere. The UV-vis spectra were recorded after 10 weeks (**Fig. 86a**) and were normalized with respect to the 740 nm absorption band. The measurements showed that the sample kept in dark didn't display any changes, as no additional bands appeared. In case of the sample kept under light, the appearance of new bands at 418 and 660 nm proved without doubt that TPBC was partially oxidized to TPP and TPC. The process is photochemical since the sample kept in the dark didn't show any sign of oxidation, even in the presence of oxygen (air atmosphere). In fact, this same sample was kept one year in the dark and didn't show any spectral modifications. Therefore, TPBC is extremely stable as long as it is kept away from light.

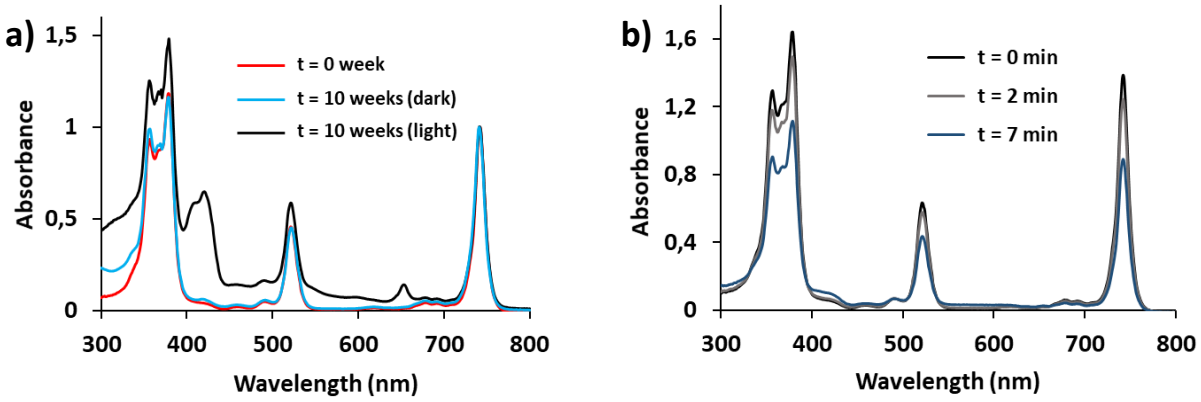

Fig. 86: Photostability of TPBC **a)** under natural light and in dark conditions and **b)** in benzene with a 740 nm light (right) up to 7 min.

Then, a solution of TPBC in benzene was illuminated using a 740 nm light. The process was monitored by UV-vis spectroscopy and showed a slight decrease of all three bands over 7 min of illumination (**Fig. 86b**). A minor increase at 418 nm appeared, probably due to the photooxidation to TPP. No band was observed at 660 nm. The illumination was also performed in chloroform and showed complete photobleaching including partial photooxidation of TPBC to TPP and TPC after 7 min. Hence, the solvent plays a major role in the photostability of TPBC.

3.3. Detection of singlet oxygen using 1,3-diphenylisobenzofuran (DPBF)

As reported in the literature, TPBC has a high quantum yield of singlet oxygen. Therefore, the photosensitizing pathway is mainly type II. 1,3-diphenylisobenzofuran (DPBF) is a common probe for the detection of singlet oxygen. Indeed, in the presence of $^1O_2$, DPBF forms an unstable peroxide that decomposes into 1,2-dibenzoylbenzene (DBB)[292] which turns the solution from green to colorless (**Fig. 87**). To assess its photostability under NIR light, a solution of DPBF in DMSO was subjected to 740 nm light and no alteration was observed after several minutes (**Fig. 88a**).

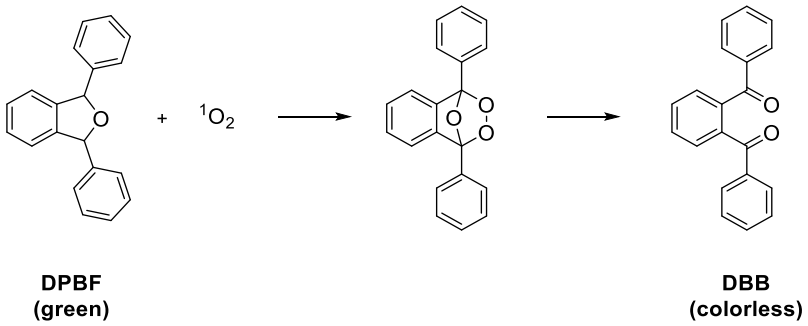

Fig. 87: Reaction of DPBF with singlet oxygen giving DBB.

After assessing the stability of DPBF in DMSO, a solution of TPBC in DMSO was added and the mixture was illuminated at 740 nm. The reaction was monitored using UV-vis spectroscopy (**Fig. 88b**). Firstly, upon addition of TPBC, no modification of the DPBF maximum absorption band at 417 nm was observed. After 1 min of illumination, a drastic decrease in absorbance was noticed, indicating that DPBF was degraded. This observation could be seen by the naked eye, as the solution, initially green, turned colorless. As illumination was extended over longer times, a decrease in TPBC absorption bands was observed due to photobleaching. Nonetheless, the degradation of DPBF was much faster than that of TPBC. The resulting adduct 1,2-dibenzoylbenzene (DBB), from the decomposition of DPBF by singlet oxygen, was detected by mass spectrometry and characterized by ^{1}H NMR with no trace of DPBF. After proving the generation of singlet oxygen in solution, the same experiment was performed in a more

[292] T. Entradas et al., Journal of Photochemistry and Photobbiology, B: Biology, 2020, https://doi.org/10.1016/j.jphotobiol.2020.111787.

realistic model to mimic the real micellar system. Thus, DPBF and TPBC were encapsulated into ferrocene free micelles C_{18}-PEO to provide TPBC-DPBF@C_{18}-PEO micelles (DL_{TPBC} = 0.04%, DL_{DPBF} = 0.2%) (**Fig. 88c**). First, both TPBC and DPBF were able to be encapsulated into C_{18}-PEO micelles individually. Indeed, both hydrophobic molecules were insoluble in water, however, in presence of C_{18}-PEO micelles, UV-vis measurements indicated DPBF and TPBC characteristic absorption bands, proving their encapsulation into the micelles. Loading both molecules together turned out to be successful as both signals were clearly visible by UV-vis spectroscopy, confirming that TPBC-DPBF@C_{18}-PEO micelles were prepared. As the degradation of DPBF was complete after only 60 sec of reaction in DMSO, the photodegradation process inside micelles was monitored every 20 sec up to 240 sec. Since the medium changed, the photostability of DPBF under illumination was once again assessed. DPBF in C_{18}-PEO micelles was stable upon illumination for 4 min (**Fig. 88d**). Hence, TPBC-DPBF@C_{18}-PEO was illuminated under 740 nm light and the photoreaction was monitored by UV-vis spectroscopy every 20 sec (**Fig. 88e**). After only 20 sec of illumination, DPBF completely disappeared by UV-vis and naked eye. Further illumination only showed photodegradation of TPBC. Indeed, the more TPBC was degraded, the more intense the absorption band at 418 nm was, corresponding to TPP (**Fig. 88f**). These results are in accordance with our previous observations in DMSO that only showed TPBC photobleaching from further illumination.

As a conclusion, the degradation of DPBF using TPBC combined with a 740 nm light confirmed the generation of singlet oxygen during the photo-illumination. The kinetics of photodegradation of DPBF into DBB was very rapid in solution in DMSO and in micelles' core. It seemed like no major differences of kinetics were observed between these two experiments as the complete transformation into DBB proceeded only in a few seconds in both cases. However, this demonstrated that the encapsulated TPBC could be photo-activated to release singlet oxygen inside the micelles' core. This proof of concept was important to assess for the next step, which consisted of photodegrading the ferrocene-containing micelles.

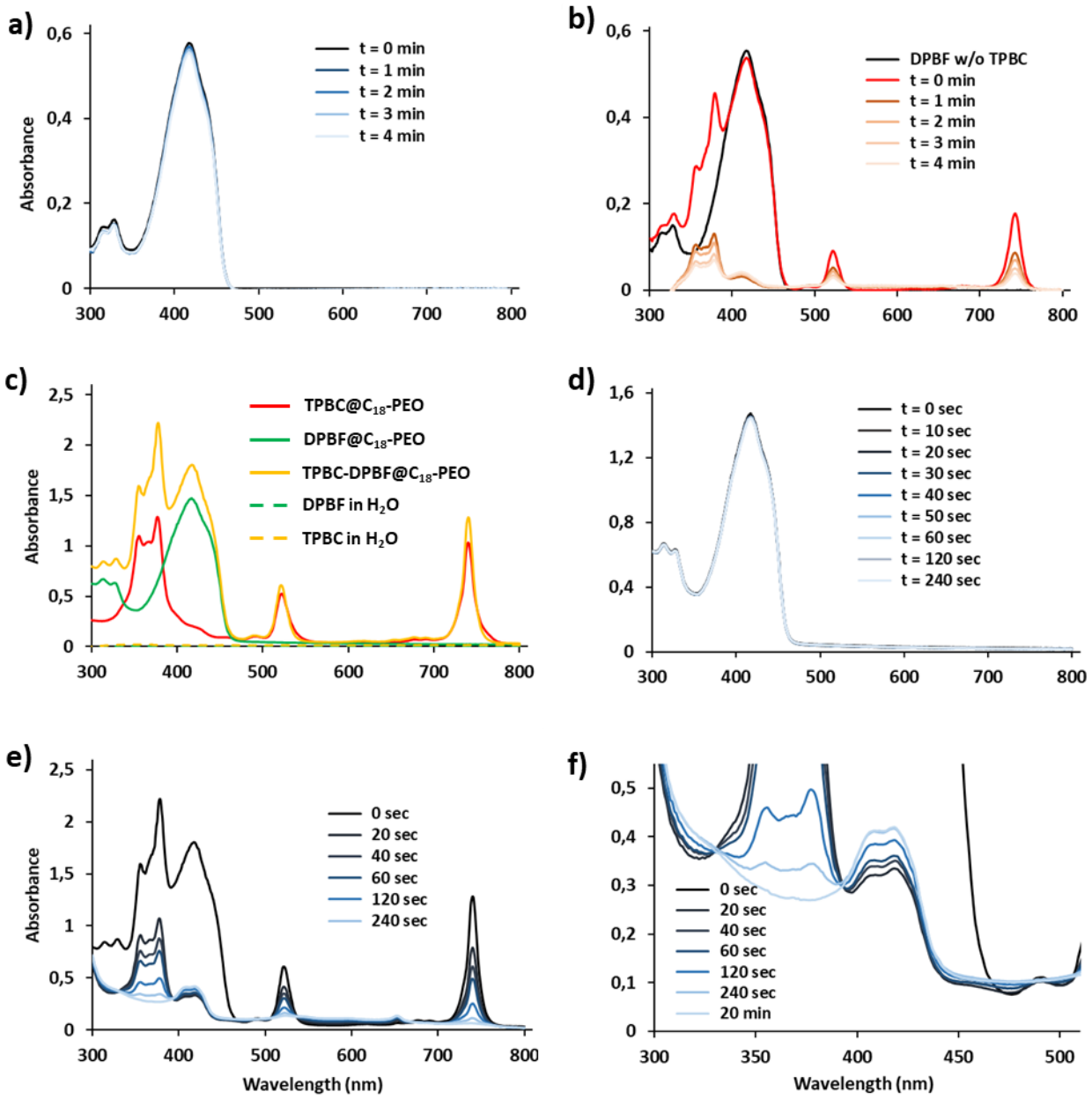

Fig. 88: **a)** Photostability of DPBF in DMSO. **b)** Illumination of a solution of TPBC and DPBF in DMSO. **c)** Individual and co-encapsulation of DPBF and TPBC in C_{18}-PEO micelles. **d)** Photostability of DPBF@C_{18}-PEO. **e)** Illumination of TPBC-DPBF@C_{18}-PEO micelles. **f)** Magnification of **e)** in the 400 nm region, showing the partial photooxidation of TPBC to TPP and TPC.

3.4. Photodegradation of TPBC@C_{18}-Fc-PEO

Ferrocene only absorbs around 442 nm, therefore it cannot be photo-activated in the NIR region. However, it's well known that it is very sensitive to oxidation and especially to reactive oxygen species.[293,294] With this in mind, TPBC was selected as photosensitizer for micelle photodegradation. TPBC shows minimal absorbance in the 400–500 nm region where ferrocene absorbs the most. It is thus possible to monitor both TPBC and ferrocene in the same sample without overlaps of their respective absorption bands (**Fig. 89**). TPBC was loaded into C_{18}-Fc-PEO micelles following the procedure described for NR. First, the photostability of C_{18}-Fc-PEO at 740 nm was assessed. A solution of C_{18}-Fc-PEO in water was illuminated using the 740 nm light. The UV-vis spectra was recorded at certain times until 15 min of light exposure. No modification was observed, except for a slight blue-shift of the absorption band initially at 442 nm (**Fig. 90a**). Moreover, a very low decrease in absorbance was also observed. However, no major change in the UV-vis spectra was observed and the solution remained clear and yellow, confirming that the micelles were photostable under these conditions.

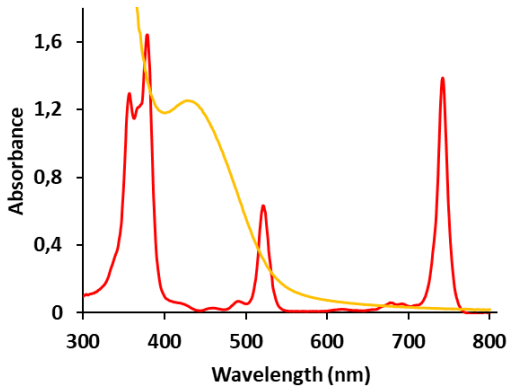

Fig. 89: Absorption spectra of C_{18}-Fc-PEO micelles (orange) and TPBC (red).

We then submitted TPBC@C_{18}-Fc-PEO micelles to 740 nm light. The solution turned from orange-to-pale yellow with the presence of an orange-to-brown precipitate. The observations were very similar to those with the blue light, suggesting that ferric species and photodecomposition of the micelles occurred. The photodegradation was monitored by UV-

[293] Y. Na et al., Journal of Materials Chemistry B, 2020, https://doi.org/10.1039/C9TB02533B.
[294] Y. Xu et al., Carbohydrate Polymers, 2014, https://doi.org/10.1016/j.carbpol.2014.08.003.

vis spectroscopy as depicted in **Fig. 90b**. After 4 min of illumination, TPBC completely disappeared by UV-vis spectroscopy and only a low intensity absorption band of ferrocene remained visible. The complete disappearance of TPBC could be explained by its photobleaching and/or release in water (and subsequent precipitation). The remaining absorbance at 442 nm could be attributed to undegraded ferrocene. Prolonging the illumination over 15 min did not produce any noticeable change compared to the 4 min illumination due to the absence of TPBC. Hence, coupling the 740 nm illumination and TPBC enabled a rapid and efficient photodegradation of the micelles. Indeed, the same kinetics of degradation was observed under these new conditions compared to the use of 460 nm light without photosensitizer. Being able to degrade our micelles utilizing a near infrared lamp is very promising for future potential biological applications.

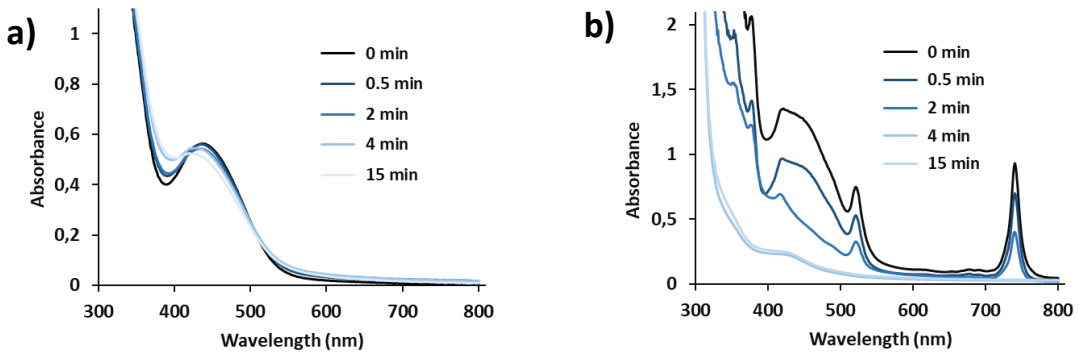

Fig. 90: Illumination of **a)** C_{18}-Fc-PEO and **b)** TPBC@C_{18}-Fc-PEO micelles.

The precipitate was submitted to XPS and compared to the one from the photodegradation using blue light (**Fig. 91**). The sample still presented a lot of carbons, thus overwhelming the peaks of iron in the background, resulting in low intensity and low resolution. However, the analysis of the spectra could still confirm the exact same pattern as for the precipitate of C_{18}-Fc-PEO micelles under blue light. Indeed, both typical binding energies at 711.1 and 724.3 eV corresponding to Fe $2p_{3/2}$ and Fe $2p_{1/2}$ of ferric species were observed. These values confirm that the same ferric species, probably $Fe(OH)_3$, were formed during the photodegradation of TPBC@C_{18}-Fc-PEO micelles under 740 nm light.

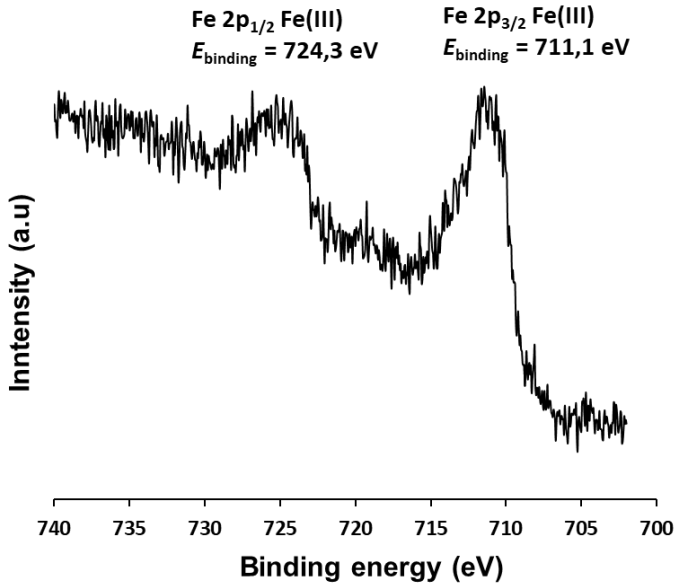

Fig. 91: XPS measurement of the obtained precipitate after illumination of TPBC@C_{18}-FC-PEO micelles.

The photodegradation was performed in presence of DFP and DFO and respectively provided a bright red and orange clear solutions as observed with the decomposition with the blue light. Indeed, the UV-vis spectra could be recorded and provided the same results (**Fig. 92**). For the sample illuminated with DFP, the characteristic absorption band of DFP:Fe^{3+} complex at 460 nm could be observed while the maximum absorption band at 430 nm could be attributed to DFO:Fe^{3+} complex. The matching results between the experiments using blue and red lights highly suggest that the mechanism involved in the photodegradation of C_{18}-Fc-PEO micelles is similar. While the photoexcitation of ferrocene with blue and red lights is different, the following decomposition process seems to be the same which results in the formation of the water-insoluble ferric hydroxide species.

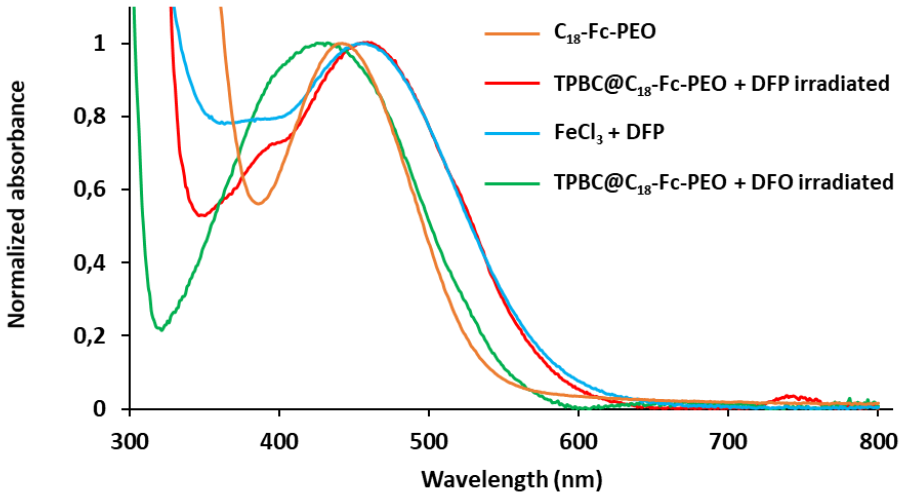

Fig. 92: UV-vis spectroscopy of TPBC@C_{18}-Fc-PEO micelles before illumination (yellow), after illumination at 740 nm in presence of DFP (red) and DFO (green), $FeCl_3$ with DFP (blue).

The presented preliminary data showed that C_{18}-Fc-PEO micelles could be effectively photodegraded in the NIR region by using TPBC as photosensitizer. Indeed, the discoloration of the supernatant and the formation of a precipitate were very similar to the observations made with the blue light. XPS measurements confirmed the presence of the same inorganic ferric species and the kinetics of photodegradation with the red and blue light were similar, resulting in the near complete decomposition of C_{18}-Fc-PEO micelles under 5 min of illumination. This system has yet to be tested *in vitro*.

4. Conclusion

The first part of this chapter was dedicated to the photodegradation of C_{18}-Fc-PEO micelles under blue light (460 nm). The photodecomposition of electron-poor ferrocene derivatives reported by Nesmeyanov and studied by Kutal could be used for the quick release of a hydrophobic cargo as demonstrated with Nile Red. The formation of inorganic ferric oxide/hydroxide species was confirmed by XPS. *In vitro* experiments using MCF-7 cells showed excellent biocompatibility of the micelles. Combining C_{18}-Fc-PEO micelles and the blue illumination, a dose-response effect was observed with an IC_{50} of 49 µM, demonstrating the potent photo-triggered cytotoxicity of our objects. This cytotoxicity could be explained by an

increase in reactive oxygen species leading to more important oxidative stress. The oxidative stress was assumed to be induced by photogenerated inorganic ferric species that could potentially act as Fenton catalysts. Even though the results were very promising, the ultimate goal of these objects is the treatment of solid tumors *in vivo*. The use of short wavelength light (460 nm) is limited to topical treatments due to low tissue penetration. This led us to the development of a different system involving a photosensitizer for an indirect photodegradation of the ferrocene moiety in the NIR region.

Meso-Tetraphenylbacteriochlorin (TPBC) was synthesized in one step from the corresponding porphyrin. The study first demonstrated that TPBC generates singlet oxygen in solution by reaction with DPBF under 740 nm light. Characterization of the oxidized product, DBB, confirmed the mechanism. A proof of concept was performed by encapsulating DPBF and TPBC in ferrocene-free micelles C_{18}-PEO. The illumination of TPBC-DPBF@C_{18}-PEO micelles successfully showed the fast degradation of DPBF, demonstrating the ability of TPBC to generate singlet oxygen inside the micelles. Indeed, the illumination of TPBC@C_{18}-Fc-PEO micelles successfully degraded the micelles. The pale-to-colorless supernatant as well as the precipitate clearly suggested that photodegradation occurred. Monitoring by UV-vis spectroscopy and XPS confirmed the similarities with the illumination using blue light.

In vitro experiments with TPBC@C_{18}-Fc-PEO micelles have yet to be performed to assess their cytotoxicity. According to the similar photodegradation process of C_{18}-Fc-PEO and TPBC@C_{18}-Fc-PEO under blue and red illumination respectively, we expect the red system to induce a similar effect *in vitro*. In addition to that, the encapsulated TPBC might also participate in the treatment by generating in situ ROS to induce direct damage to cells as in conventional PDT treatments. The presented data in this chapter resulted in a patent.[295]

The micelles are intended to treat cancer. Hence, successful *in vitro* experiments would ultimately lead to *in vivo* experiments. The latter would consist of intravenously injecting the micelles and target the tumor by EPR effect. However, previous reports in our group using PEGylated micelles bearing polymerized 10,12-pentacosadiynoyl (PCDA) chains showed low accumulation in tumor-bearing mice by EPR effect.[296] Therefore, it prompted us to improve the

[295] E. Doris et al., European patent, EP23305409 (03/2023).
[296] N. Mackiewicz et al., Small, 2011, https://doi.org/10.1002/smll.201100212.

passive targeting of PEGylated micelles using a simple and non-invasive method named sonoporation.

CHAPTER 3. ENHANCEMENT OF EPR EFFECT BY SONOPORATION

Tumor heterogeneity is the main challenge faced by anticancer therapeutic approaches that rely on the delivery of nanoparticles through passive targeting. In this respect, increasing blood vessel permeability through the combination of microbubbles and ultrasound, known as sonoporation, may be used to improve and standardize the enhanced permeability and retention (EPR) effect. In this chapter, we describe the design and synthesis of PEGylated [^{89}Zr]-complexing micelles encapsulating a fluorescent dye to achieve bi-modal imaging (by positron emission tomography (PET) and optical imaging) in subcutaneous glioblastoma mouse model (U87-MG) allowing real-time tracking of the objects. The micelles were injected in combination with microbubbles and sonoporation was applied to improve the EPR effect.

1. Introduction to EPR effect: an imperfect phenomenon

1.1. Heterogeneity in tumors

Tumors are characterized by an impaired lymphatic drainage and high blood vessel permeability, allowing nanoparticles to extravasate and accumulate within the tissues. The high permeability observed in tumors is the direct consequence of tumor angiogenesis. The discontinuous epithelium and lack of basal membrane in the blood vessels lead to porous vessels. The pores' size can vary from a few hundred nanometers to over a micrometer.[297] Such differences imply variations in the accumulation of the administrated nanoparticles inside the tumor tissue. Moreover, the blood vessels are spatially and structurally disorganized, leading to differences in blood flow in the tumor and impairing the diffusion of the drug. Significant heterogeneity among different types of tumors is observed and the level of permeability can greatly vary. Indeed, it was shown by angiography that hepatocellular carcinoma and renal cell carcinoma have a high vascular density, resulting in a higher permeability, in contrast with pancreatic and prostate cancers.[298]

As the tumor grows, the core becomes less and less vascularized. Consequently, the core of tumors is mostly composed of necrotic and hypoxic cells, and the blood flow is diminished or non-existant. Furthermore, due to the impairment of the lymphatic drainage system, the

[297] R. K. Jain and T. Stylianopoulos, Nature Reviews Clinical Oncology, 2011, https://doig.org/10.1038/nrclinonc.2010.139.
[298] H. Maeda, Advanced Drug Delivery Reviews, 2015, https://doi.org/10.1016/j.addr.2015.01.002.

interstitial fluid pressure is particularly high at the core of the tumor. In fact, the network of lymphatic vessels mainly exists at the surface of the tumor and carries fluids, growth factors and cancer cells. Therefore, the irregular vasculature and high interstitial pressure are the main limitations when using passive targeted nanoparticles for cancer treatment.

The heterogeneity is more noticeable in large tumors. In mouse models, tumors grow rapidly (2–4 weeks) with sizes generally ranging from 3 to 10 mm in diameter.[299] Their fast growth and small size allow them to be rather homogeneous. Consequently, the amount of necrotic and hypoxic cells at the center is limited. Therefore, *in vivo* studies with tumor-bearing mice using EPR effect usually show very good results. Clinical tumors can reach several centimeters in diameter.[300] The much greater scale of clinical tumors compared to preclinical tumors considerably increases the heterogeneity. The larger size of the tumor leads to more necrotic areas and more irregular distribution of blood vessels. Tumors are compressed in a confined space, building up physical pressure that acts as a barrier against the efficient diffusion of nanoparticles.[301] The larger the tumor, the higher the pressure. These differences between murine tumor and human tumors usually explain why the transition between preclinical and clinical studies often fail to succeed.[302,303]

1.2. Influence of the nanoparticle

The heterogeneity of the tumor is inherent and difficult to control. In contrast, the design of the nanoparticle can be tuned precisely to fit the desired application. The nanoparticle's physical features play a crucial role in ensuring an efficient diffusion and accumulation within the tumor tissue. Those features were already described in the "General introduction" section, and mainly include the size and surface charge. Briefly, nanoparticles must be designed in such a way that they can circulate long enough in the blood stream to accumulate in the tumor tissue over time. The first obstacle upon administration is the rapid clearance. Nanoparticles that have a diameter lower than 6 nm are rapidly eliminated by the renal system as opposed

[299] W. Islam et al., Journal of Personalized Medicine, 2022, https://doi.org/10.3390/jpm12121964.
[300] S. Brooman-May et al., American Journal of Roentgenology, 2011, https://doi.org/10.2214/AJR.11.6534.
[301] H. Maeda and M. Khatami, Clinical and Translational Medicine, 2018, https://doi.org/10.1186/s40169-018-0185-6.
[302] Md A. Subhan et al., Journal of Personalized Medicine, 2021, https://doi.org/10.3390/jpm11060571.
[303] M. de Jon and T. Maina, Journal of Nuclear Medicine, 2010, https://doi.org/10.2967/jnumed.109.065706.

to larger nanoparticles that bypass it.[304,305] As the size of pores in tumor blood vessels are estimated to range from 200 to 2000 nm,[306] the ideal size for nanoparticles was determined to be between 10 and 100 nm.[307] The second important feature is the surface charge. Positively charged nanoparticles are known to quickly undergo cellular uptake due to the interaction with the negatively charged cellular membranes. However, cationic nanoparticles easily undergo opsonisation and elimination. Their negatively charged counterparts display lower cellular uptake but tend to be taken up by the reticuloendothelial system in the liver and spleen.[308] Therefore, both cationic and anionic nanoparticles are not tailored for an optimal passive targeting by EPR effect. In contrast, a neutral shell, such as PEO, provides steric hindrance and prevent adsorption of opsonins.[309] As a result, the blood circulation time of neutral nanoparticles is improved and the accumulation by EPR effect is greater than for ionic nanoparticles.

1.3. Sonoporation

The EPR effect is a unique feature of solid tumors that allows the accumulation and retention of nanoparticles. However, in practice, multiple obstacles arise due to the complexity of the tumor microenvironment. Treatments solely based on passive targeting show great results in mice tumors, mostly due to their small sizes and more homogenous tumor microenvironment. The transition to clinical tumors faces issues due to the higher scale and complexity. Cases of late-stage and refractory tumors are associated with poor blood flow due to the coagulation and clot formation, resulting in poor EPR effect and thus, a poor therapeutic effect. Methods to improve the EPR effect were developed and rely mainly on the modulation of the vasculature of the tumor. Indeed, the efficacy of the EPR effect relies on the blood flow. The better the vascularization, the better the accumulation of the nanoparticles in the tumor tissue. One common approach is to administer angiogenesis inhibitors to homogenize the vasculature and reduce the necrotic and hypoxic areas.[310] Another method to improve the vasculature consists

[304] J. Wang and G. Liu, Angewandte Chemie International Edition, 2018, https://doi.org/10.1002/anie.201711705.
[305] G. H. Zhu et al., Trends in Pharmacological Sciences, 2022, https://doi.org/10.1016/j.tips.2022.05.001.
[306] S. K. Hobbs et al., Biological Sciences, 1998, https://doi.org/10.1073/pnas.95.8.4607.
[307] E. A. Sykes et al., ACS Nano, 2014, https://doi.org/10.1021/nn500299p.
[308] H. -X. Wang et al., Nano Today, 2016, https://doi.org/10.1016/j.nantod.2016.04.008.
[309] Q. Yang and S. K. Lai, Wiley Interdisciplinary Reviews: Nanomedicine and Nanobiotechnology, 2015, https://doi.org/10.1002/wnan.1339.
[310] R. T. Tong et al., Cancer Research, 2004, https://doi.org/10.1158/0008-5472..CAAN-04-0074.

of activating receptors responsible for the vasodilation of blood vessels, allowing more blood to flow through the tumor.[311]

Apart from administrating chemical agents to induce a direct modulation of the vasculature of the tumor, activation by external methods such as ultrasound can be used. Three main ultrasound therapies can be named: sonodynamic therapy (SDT), high-intensity focused ultrasound (HIFU), and sonoporation.[312] The latter is based on the local application of ultrasound (1–10 MHz) combined with microbubbles.[313] Microbubbles (1–10 µm diameter) are echo-contrast agents for ultrasound imaging.[314] Their structure is composed of a biocompatible shell usually made of proteins (Albunex®) or lipids (Sonovue®), and a gaseous core (**Fig. 93**). The core of microbubbles is filled with fluorinated gas molecules such as octafluoropropane (Optison™).[315] Air-filled microbubbles are known to be quickly dissolved in the blood stream due to the high solubility of air in blood.[316] Indeed, fluorinated gases are water-insoluble, preventing gas diffusion into blood.

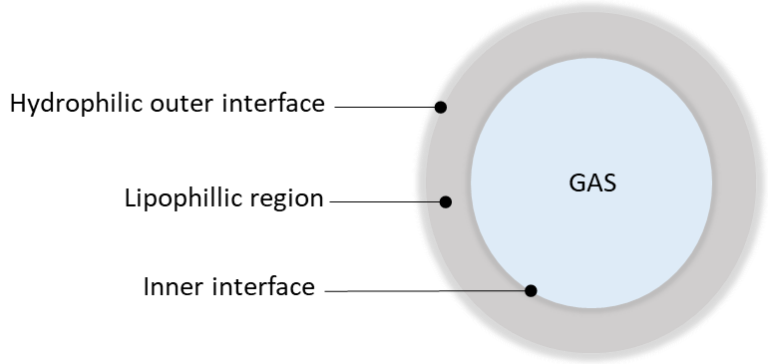

Fig. 93: General structure of a microbubble made of a hydrophilic shell (protein, lipid) and a fluorinated gaseous core.

[311] P. L. N. da Costa et al., Cancer Letters, 2014, https://doi.org/10.1016/j.canlet.2013.12.009.
[312] T. Yamaguchi et al., Cancers, 2021, https://doi.org/10.3390/cancers13246184.
[313] J. -M. Escoffre et al., Current Gene Therapy, 2013, https://doi.org/10.2174/1566523211313010002.
[314] S. Sirsi and M. Borden, Bubble Science, Engineering and Technology, 2009, https://doi.org/10.1179/175889709X446507.
[315] S. Podell et al., Biotechnology and Applied Biochemistry, 2010, https://doi.org/10.1111/j.1470-8744.1999.tb00773.x.
[316] A. Kabalnov et al., Ultrasound in Medicine and Biology, 1998, https://doi.org/10.1016/S0301-5629(98)00033-7.

Sound is a mechanical energy that propagates by alternating high and low-pressure waves through a medium. The high-pressure phase is called compression phase while the low-pressure phase is named rarefaction. Under ultrasound waves, microbubbles oscillate by undergoing successive expansion (rarefaction phase) and contraction (compression phase), leading respectively to the increase and decrease of the microbubble's diameter. This phenomenon is called cavitation. The higher the amplitude of the acoustic pressure, the more amplified are the expansion and contraction phases. If the microbubble is attached or close to a cell, the cavitation can temporary produce openings in the membrane. Indeed, during the rarefaction phase, the expansion of the microbubble can physically push the cell membrane inward, creating a transient opening. In case of compression phase, the contraction motion causes the membrane to be pulled toward the microbubble instead.[317] Under stronger acoustic pressure, the amplitude of the microbubble's oscillation can be high enough to induce intense liquid flows around the microbubble. This effect is called microstreaming and can lead to membrane disruption by exerting shear stresses.[318] When the amplitude of acoustic pressure reaches a maximum threshold, the oscillation motion of the microbubbles is such that the volume expansion can be twice as high as the original volume. The microbubbles suddenly collapse during the compression phase, generating violent shock waves that can transiently enhance the permeability of affected cells.[319] Therefore, the combination of cavitation, microstreaming and shock waves make sonoporation a great non-invasive method to enhance the permeability of vasculature and cell membrane.

1.4. Microbubbles in cancer therapy

The use of sonoporation in cancer therapy is known to enhance the therapeutic efficacy of drugs such as doxorubicin[320,321] and irinotecan.[322] Microbubbles, similar to nanoparticles, can be functionalized with various surface groups. The accumulation of microbubbles to a specific site can be achieved by conjugating targeting groups. For instance, Anderson et al. prepared

[317] M. Postema et al., Ultraschall in der Medizin, 2012, https://doi.org/10.1055/s-0031-1274749.
[318] J. Wu, Progress in Biophysics and Molecular Biology, 2007, https://doi.org/10.1016/j.pbiomolbio.2006.07.016.
[319] B. D. M. Meijering et al., Circulation Research, 2009, https://doi.org/10.1161/CIRCRESAHA.108.183806.
[320] Z. Kovacs et al., Journal of Controlled Release, 2014, https://doi.org/10.1016/j.jconrel.2014.05.033.
[321] C. -Y. Lin et al., Nanomedicine: Nanotechnology, Biology, and Medicine, 2012, https://doi.org/10.1016/j.nano.2011.10.005.
[322] J. -M. Escoffre et al., Molecular Pharmaceutics, 2013, https://doi.org/10.1021/mp400081b.

cRGD-microbubbles with a diameter of 2.5 µm. The cRGD ligand could specifically bind to the overexpressed $\alpha_v\beta_3$ integrin in tumor cells and lead to a better accumulation of the microbubbles *in vivo* by sonoporation.[323] Willmann and coworkers developed VEGFR2-targeted microbubbles that showed to be efficiently accumulated in the tumor tissue under low acoustic pressure.[324]

Beside their use in ultrasound imaging, microbubbles can also be used as carriers. Because of their microsize, microbubbles are mainly suited for intravascular applications. Microbubbles can deliver drugs by encapsulation in the hydrophobic part. Eisenbrey et al. reported the encapsulation of doxorubicin in microbubbles and showed a significant increase in doxorubicin delivery under ultrasound in VX2 liver tumor model in rabbits.[325] Pu et al. prepared LHRHa-targeting microbubbles loaded with paclitaxel. LHRHa is overexpressed in 80% of ovarian cancers,[326] which makes it a target of interest. *In vivo* experiments proved that the intraperitoneally administrated microbubbles could be destroyed under ultrasound and release the active drug leading to tumor apoptosis.[327]

The use of ultrasounds combined with microbubbles proved to be an efficient way of treating cancer. The increased permeability provided by the ultrasounds and microbubbles provide a localized and non-invasive method of treatment. The reported use of sonoporation relies on the use of microbubbles as theranostic objects. Indeed, real-time tracking can be done using ultrasound imaging and the ability of microbubbles to be modified makes them useable as carriers. Most of the reported studies exploit microbubbles with sizes between 1 and 2 µm, which are too large to benefit from the EPR effect. Moreover, the half-life of microbubbles is reported to be around 5 min in blood,[328] which is too short to use them as drug carriers. Finally, their main disadvantage as carriers is their low drug loading.[329] Despite these drawbacks, they proved to be efficient in improving the vasculature of the tumor microenvironment.

[323] C. R. Anderson et al., Investigative Radiology, 2011, https://doi.org/10.1097/RLI.0b013e3182034fed.
[324] J. K. Willmann et al., Radiology, 2008, https://doi.org/10.1148/radiol.2462070536.
[325] J. R. Eisenbrey et al., IEEE Transactions on Biomedical Engineering, 2010, https://doi.org/10.1109/TBME.2009.2030497.
[326] G. Emons et al., Endocrine-Related Cancer, 2003, https://doi.org/10.1677/erc.0.0100291.
[327] C. Pu et al., Molecular Pharmaceutics, 2014, https://doi.org/10.1021/mp400523h.
[328] U. Goncin et al., Science of the Total Environment, 2021, https://doi.org/10.1016/j.scitotenv.2020.141231.
[329] S. Fokong et al., Journal of Controlled Release, 2012, https://doi.org/10.1016/j.jconrel.2012.05.007.

1.5. Objectives

The use of ultrasound-sensitive nanoparticles, known as sonodynamic therapy, is well developed in cancer treatments.[330] However, the use of ultrasound to deliver nanoparticles, and especially micelles, has yet to be explored. Because of the heterogeneity of the tumor microenvironment, the EPR effect can greatly differ between different tumors and even within the same tumor microenvironment. Therefore, the efficacy of treatments solely relying on passive targeting can be inconsistent. In this context, and with our expertise in drug delivery systems using PEGylated micelles, we decided to combine sonoporation and biocompatible micelles to improve the latter's tumor accumulation by EPR effect in a murine model of glioblastoma.

2. Synthesis of PEGylated and complexing polymerized micelles

2.1. PCDA-PEO and PCDA-DFO amphiphiles

Our group has been working on PEGylated (M_w = 2000 g mol^{-1}) micelles bearing a 10,12-pentacosadiynoyl lipophilic chain (PCDA-PEO) for almost 15 years.[331] As introduced in Chapter 1 of the thesis, the PCDA-PEO micelles can be formed by self-assembly of the corresponding amphiphiles to form 10 nm micelles. PCDA-PEO micelles could be used as drug carriers as demonstrated with the encapsulation of the NIR lipophilic carbocyanine dye (DiR) or paclitaxel. Such micelles could be photopolymerized (pPCDA-PEO) to stabilize the self-assembly from being dissociated under high dilution conditions *in vivo*. The uptake of pPCDA-PEO micelles could be assessed and showed retention by EPR effect after several days in mice bearing subcutaneous tumors (human breast cancer MDA-MB-231 cells). However, 24 h post-injection, only 2.7 ± 1.9% of the injected dose remained in the tumor. This relatively low value, although common for similar systems, may indicate that micelles poorly accumulate into the tumor tissue by EPR effect.[332] Thus, we decided to use sonoporation as a non-invasive method to increase the accumulation of pPCDA-PEO micelles in tumor-bearing mice.

[330] G. -Y. Wan et al., Cancer Biology and Medicine, 2016, https://doi.org/10.20892/j.issn.2095-3941.2016.0068.
[331] N. Maciewicz et al., Small, 2011, https://doi.org/10.1002/smll.201100212.
[332] N. Schleich et al., Journal of Controlled Release, 2014, https://doi.org/10.1016/j.jconrel.2014.07.059.

In order to track the micelles in real-time, optical imaging and positron emission tomography (PET) were used. PET is particularly interesting for imaging due its high sensitivity, temporal resolution, penetration depth, and quantitative aspect.[333] For fluorescence imaging, a red emitting dye (DiD) was encapsulated into the hydrophobic core of the micelles. As for PET, radioactive zirconium-89 ([^{89}Zr]) was selected as the radioactive tracer. However, pPCDA-PEO doesn't have strong complexing properties. Therefore, a second amphiphile bearing a desferoxamine (DFO) hydrophilic head was designed for this specific reason. DFO is a common chelator for many metals such as iron(III) and Zr(IV).[334] The strong coordination of DFO to metals comes from the three bidentate hydroxamate groups. The clinically approved molecule is biocompatible, has a low toxicity, decent water solubility, and prolonged circulation time when used as a chelate. DFO is commonly used to chelate Zr(IV) (**Fig. 94**). Indeed, the latter is characterized by a small ionic radius and a high positive charge, thus making oxygen-donor ligands suitable for its chelation.[335] Morevover, the preferred coordination sphere of Zr(IV) is reached with eight ligands. In case of DFO-Zr(IV) complex, the six oxygen atoms from the three hydroxamate bind the metal and two water molecules complete the coordination sphere.[336] For these reasons, DFO was selected as hydrophilic head to complex [^{89}Zr] for PET imaging.

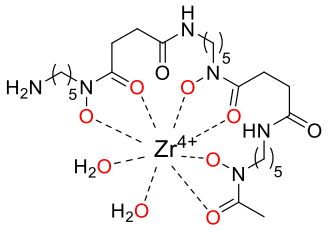

Fig. 94: Coordination sphere of Zr(IV) with DFO and water molecules.

Thus, both PEGylated and complexing amphiphiles could be mixed together to form hybrid micelles. The bi-modal imaging provided real-time information about the location of both the payload (DiD) and the carrier ([^{89}Zr]) in subcutaneous glioblastoma (U87-MG) mouse model.

[333] L. Scarfe et al., Regenerative Medicine, 2017, https://doi.org/10.1038/s41536-017-0029-9.
[334] D. Bellotti and M. Remelli, Molecules, 2021, https://doi.org/10.3390/molecules26113255.
[335] E. W. Price and C. Orvig, Chemical Society Reviews, 2014, https://doi.org/10.1039/C3CS60304K.
[336] M. A. Deri et al., Nuclear Medicine and Biology, 2013, https://doi.org/10.1016/j.nucmedbio.2012.08.004.

2.2. Organic synthesis of amphiphiles

2.2.1. Synthesis of PCDA-PEO

The PCDA-PEO amphiphile was synthesized in three steps (**Fig. 95**). First, commercially available 10,12-pentacosadiynoic acid (PCDA) was reduced by lithium aluminium hydride to provide the corresponding alcohol **33** in good yield (81%). The latter's synthesis was already described in Chapter 1. Compound **33** then underwent an Appel reaction to yield the bromide derivative **43** (59%). Finally, the last step consisted of introducing the PEO chain. The corresponding alkoxide was formed by deprotonation with sodium hydride and reacted with the electrophile **43** by nucleophilic substitution to provide the desired amphiphile **44** (PCDA-PEO) in decent yield (40%).

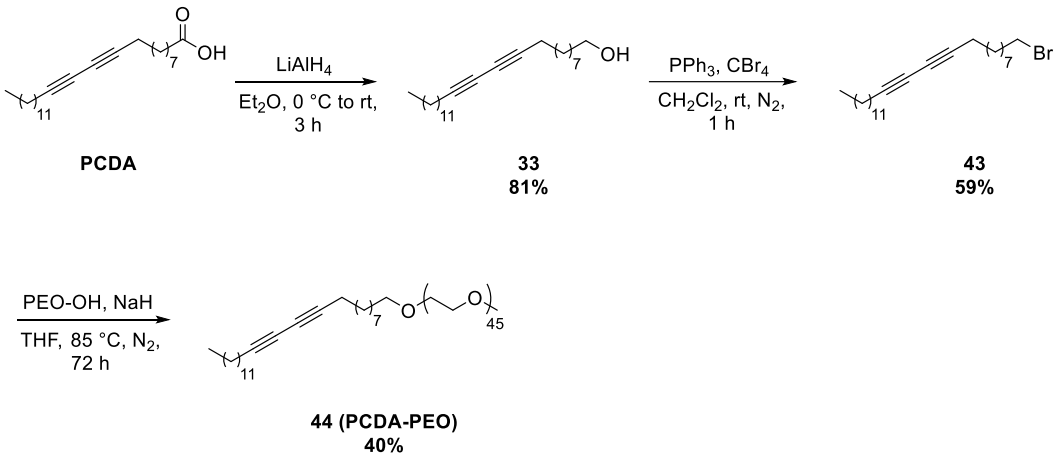

Fig. 95: Synthesis of PCDA-PEO amphiphile starting from 10,12-pentacosadiynoic acid.

2.2.2. Synthesis of PCDA-DFO

The PCDA-DFO amphiphile was synthesized in two easy and quick steps (**Fig. 96**). The first step consisted of activating the carboxyl group of PCDA into the corresponding NHS-ester. This reaction was already described in Chapter 1 (compound **25**). Then, NHS-ester **25** was reacted with the primary amine of desferoxamine mesylate salt (DFO.MsOH) in a PBS/THF mixture at room temperature to provide the desired amphiphile **45** (PCDA-DFO) in high yield (96%).

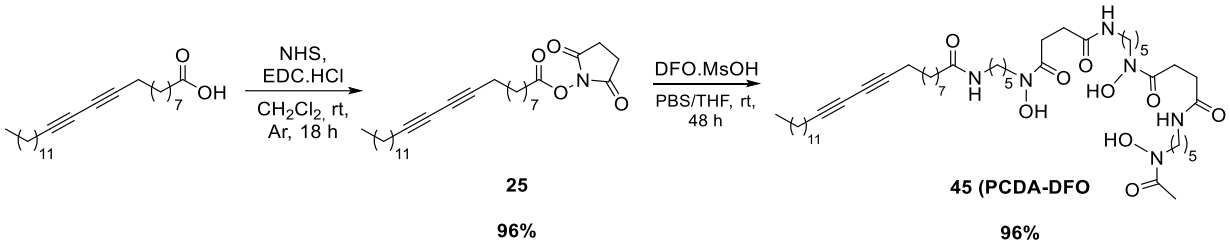

Fig. 96: Synthesis of PCDA-DFO amphiphile starting from 10,12-pentacosadiynoic acid.

2.3. PCDA-DFO micelles

PCDA-PEO amphiphile was already characterized and studied in our group as opposed to PCDA-DFO. The first attempts at micelle formation in water failed with PCDA-DFO as cloudy solutions were obtained. Pure DFO is reported to be slightly soluble in water, hence the use of desferoxamine mesylate salt during the coupling reaction. However, when attached to the PCDA chain, DFO is no longer a salt. Thus, the water solubility decreases which explains the cloudy aspect of the suspensions in water. The reported pK_a values for DFO are between 8 and 10 for the three hydroxamic acids.[337] Thus, to increase the solubility of the polar head and form micelles, the micellization was performed in a basic aqueous solution containing 2% potassium hydroxide (w/w). The deprotonation of the hydroxamic acids into the corresponding hydroxamate anions led to a clear and colorless solution. After sonication and filtration, the prepared colloids were subjected to DLS which confirmed the presence of PCDA-DFO micelles with a hydrodynamic diameter of 12 nm (**Fig. 97**).

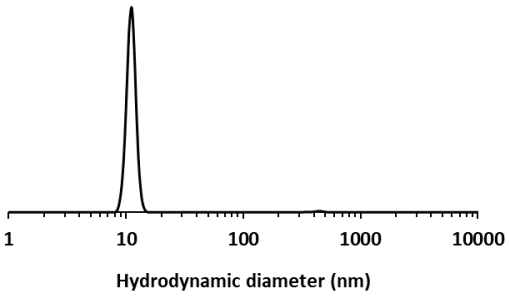

Fig. 97: DLS measurement of a 10 mg mL^{-1} solution of PCDA-DFO micelles

[337] R. Imura et al., Molecules, 2021, https://doi.org/10.3390/molecules26164977.

The micelles were then photopolymerized under UV light (254 nm). The successful photopolymerization was confirmed by the change from colorless to yellow after 3 h of illumination, giving the corresponding polymerized pPCDA-DFO micelles after filtration on a 0.2 µm nylon membrane.

3. Preparation and characterization of DiD@pPCDA-PEO/DFO[^{89}Zr] micelles

3.1. Nanoformulation of pPCDA-PEO/DFO micelles

Because of the high sensitivity of [^{89}Zr] by PET imaging, it was decided to use a ratio of 9:1 for the nanoformulation. We decided to prepare mixed micelles from a 9:1 ratio PCDA-PEO/PCDA-DFO (w/w) based on the high sensitivity of PET imaging and on previous studies by our group.[338] The main component being PCDA-PEO (90%), hybrid micelles should have a behaviour in line with that of pure PCDA-PEO micelles, which are known to be biocompatible and to accumulate in tumor tissues by EPR effect. Thus, a solution of hybrid micelles PCDA-PEO/DFO micelles was prepared by adding 500 µL of an aqueous solution of PCDA-DFO (10 mg mL^{-1}, in 2 wt% KOH) to an aqueous solution of PCDA-PEO (4.5 mL, 10 mg mL^{-1}). Then, the solution was sonicated using the ultrasound probe and filtered on a 0.2 µm nylon syringe filter. The resulting solution was subjected to photopolymerization under 254 nm UV light for 3 h to yield pPCDA-PEO/DFO micelles. DLS analyses of the micelles before and after photopolymerization showed a hydrodynamic diameter of 12 nm (**Fig. 98**).

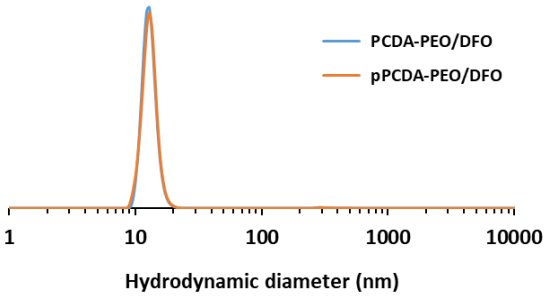

Fig. 98: DLS measurements before (PCDA-PEO/DFO) and after (pPCDA-PEO/DFO) photopolymerization.

[338] A. Doerflinger et al., Chemical Communications, 2018, https://doi.org/10.1039/C8CC00553B.

3.2. Encapsulation of DiD

The encapsulation of the fluorescent dye (DiD) was performed according to our commonly used protocol. 500 µL of a solution of DiD in chloroform (1 mg mL^{-1}) was added to the solution of pPCDA-PEO/DFO micelles (10 mg mL^{-1}, 5 mL). The biphasic solution was sonicated using the ultrasound probe for 10 min at 45% power. The heating from the probe progressively evaporated the organic solvent which led to the slow encapsulation of DiD. Then, filtration on 0.2 µm nylon syringe filter was performed to remove any free DiD that precipitated in water, providing a blue solution of DiD@pPCDA-PEO/DFO micelles. DLS measurements were performed after the encapsulation to ensure the stability of the micelles and displayed an unmodified profile with a hydrodynamic diameter of 12 nm still. The presence of DiD was confirmed by fluorescence (**Fig. 99a**). Then, the micelles were purified through PD-10 desalting column using water to remove the excess of KOH used during the nanoformulation step.

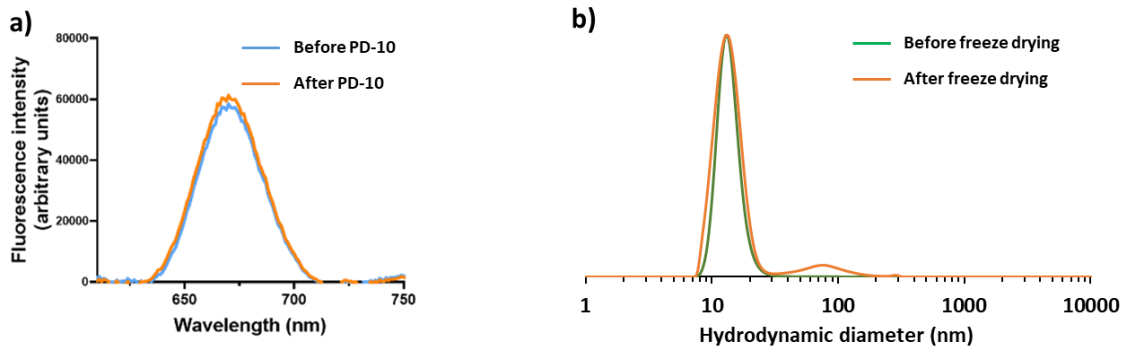

Fig. 99: **a)** Fluorescence spectra before and after purification on PD-10 column. **b)** DLS measurements before and after freeze drying.

Fluorescence spectra after purification through PD-10 remained the same, showing that no leakage of DiD occurred. The sample was freeze dried and resolubilized in water and DLS measurement showed minor changes (**Fig. 99b**). Indeed, a new population around 80 nm was observed, probably due to the presence of a few aggregates after resolubilization. Nonetheless, micelles maintained their size after freeze drying, which prompted us to store them in the solid state before radiolabeling instead of keeping them in the colloidal form.

3.3. *In vitro* cytotoxicity of DiD@pPCDA-PEO/DFO micelles

The cytotoxicity of the DiD@pPCDA-PEO/DFO micelles was determined by MTS assay in U-87 MG and B16F10 cell lines (murine melanoma cell line) (**Fig. 100**). 8 103 cells per well for each cell line in 96-well plate were incubated for 24 h with different concentrations of micelles, ranging from 0.01 to 1 mg mL^{-1}. The control group for this experiment was incubated with phosphate-buffered saline (PBS). To evaluate the impact of toxicity on the tumor cells, staurosporine at a concentration of 1 µM was used as a positive control. Following a 2 h incubation with the MTS reagent at 37 °C, the plate was analyzed using a microplate reader at 490 nm. The control group treated with PBS served as a reference without toxicity. Thus, the cell viability of other conditions was determined by calculating the percentage of surviving cells relative to the control group. Each experiment was repeated six times and no significant impact on cell survival was observed, regardless of micelle concentration. (***: $p < 0.001$). Therefore, we concluded that DiD@pPCDA-PEO/DFO micelles were biocompatible even at high concentrations, which could be attributed to the combined effect of the PEO corona and polymerized micelle's core.

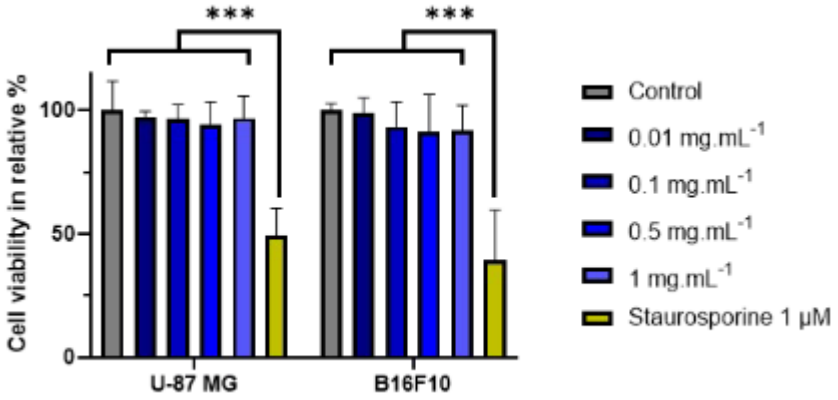

Fig. 100: *In vitro* cytotoxicity of DiD@pPCDA-PEO/DFO micelles determined by MTT assays against U-87 MG and B16F10 cancer cell lines.

3.4. Radiolabelling of DiD@pPCDA-PEO/DFO micelles with [^{89}Zr]

Before radiolabelling, we assessed the ability of PCDA-DFO amphiphiles to complex Zr(IV) under simple conditions. The complexation was performed in refluxing methanol in the presence of excess Zr(IV) acetylacetonate. The reaction was carried out for 18 h and mass spectrometry confirmed the complete complexation of Zr(IV) by PCDA-DFO amphiphiles.

After demonstrating that PCDA-DFO could efficiently chelate Zr(IV), the process was performed using [^{89}Zr] and DiD@pPDCA-PEO/DFO micelles. The radiolabelling was performed on the day of imaging experiments due to the half-life of [^{89}Zr] being 78.3 h.[339] The complexation consisted of mixing a suspension of DiD@pPCDA-PEO/DFO micelles in ultrapure water with a solution of [^{89}Zr] oxalate (237 MBq). The mixture was stirred (500 rpm) for 1 h at 50 °C and was first purified on a PD-10 column using PBS as mobile phase. Then, a second purification was performed by Vivaspin® (5 kDa cutoff) to afford DiD@pPCDA-PEO/DFO[^{89}Zr] micelles in PBS.

The purity of the resulting DiD@pPCDA-PEO/DFO[^{89}Zr] micelles was first confirmed by radio-HPLC as shown on **Fig. 101a**. The purified sample displayed a single sharp peak at 19 min, corresponding to DiD@pPCDA-PEO/DFO[^{89}Zr]. The high purity was further assessed by radio-iTLC, depicting a radiochemical purity over 99% (**Fig. 101b**). Autoradiography of iTLC before purifications showed two signals, which corresponded to the two peaks observed by radio-iTLC. After purifications, only one signal remained. The colocalization of spots from the fluorescence and autoradiography of iTLC proved that the single signal corresponded to DiD@pPCDA-PEO/DFO[^{89}Zr] micelles (**Fig. 101c**). Thus, we managed to prepare polymerized and PEGylated micelles with [^{89}Zr] at the surface and DiD in the core.

[339] E. Garcia-Torano et al., Applied Radiation and Isotopes, 2018, https://doi.org/10.1016/j.apradiso.2017.10.033.

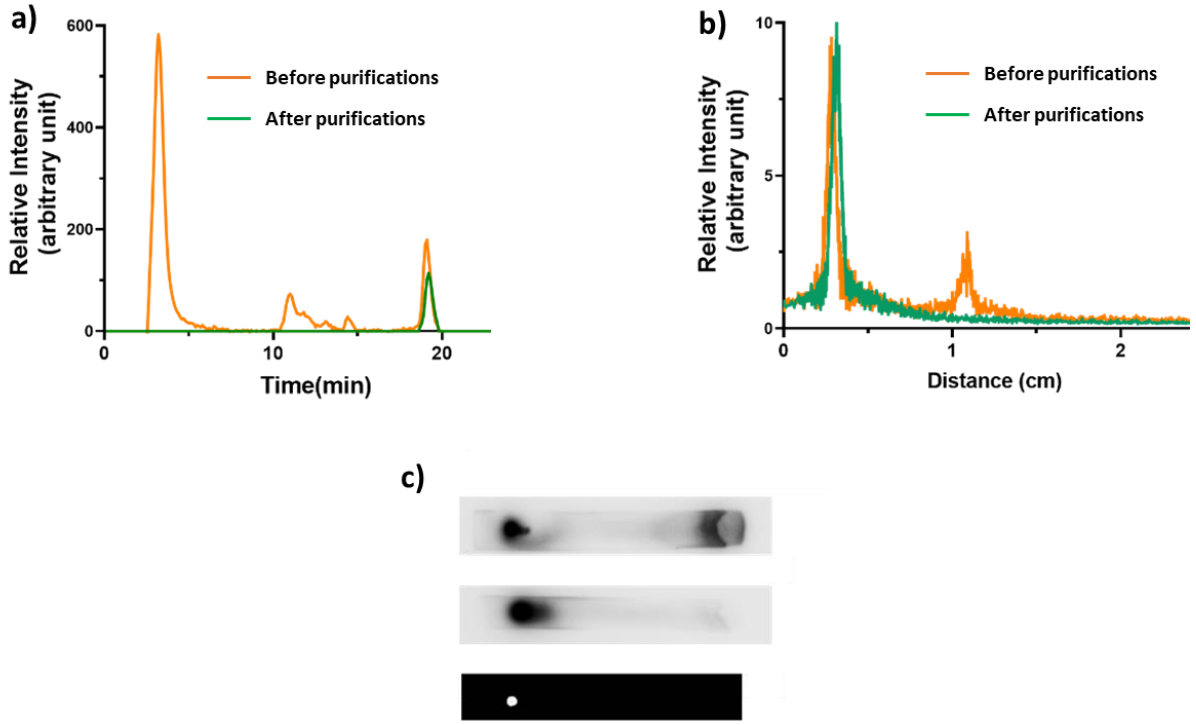

Fig. 101: **a)** Radio-HPLC chromatogram of radiolabelled DiD@pPCDA-PEO/DFO[^{89}Zr] micelles before and after purifications. **b)** Radio-iTLC of the same batch before and after purifications. **c)** Dots autoradiography before (top) and after (middle) purification. Fluorescence of the purified sample (bottom) on iTLC-SG using acetonitrile/citric acid (1:9 *v/v*) as eluent.

3.5. Stability assessment

The radiolabelling stability of the DiD@pPCDA-PEO/DFO[^{89}Zr] micelles was evaluated in different biological relevant media (**Fig. 102**). The radiolabelled micelles were incubated at 37 °C in PBS, mouse plasma and mouse serum for 48 h. The samples were analyzed by radio-iTLC and the corresponding chromatograms were recorded at 24 and 48 h. These results show that [^{89}Zr] remained chelated to DFO even in presence of proteins and enzymes, demonstrating the strong coordination of DFO to [^{89}Zr] and thus, the high stability of the complex.

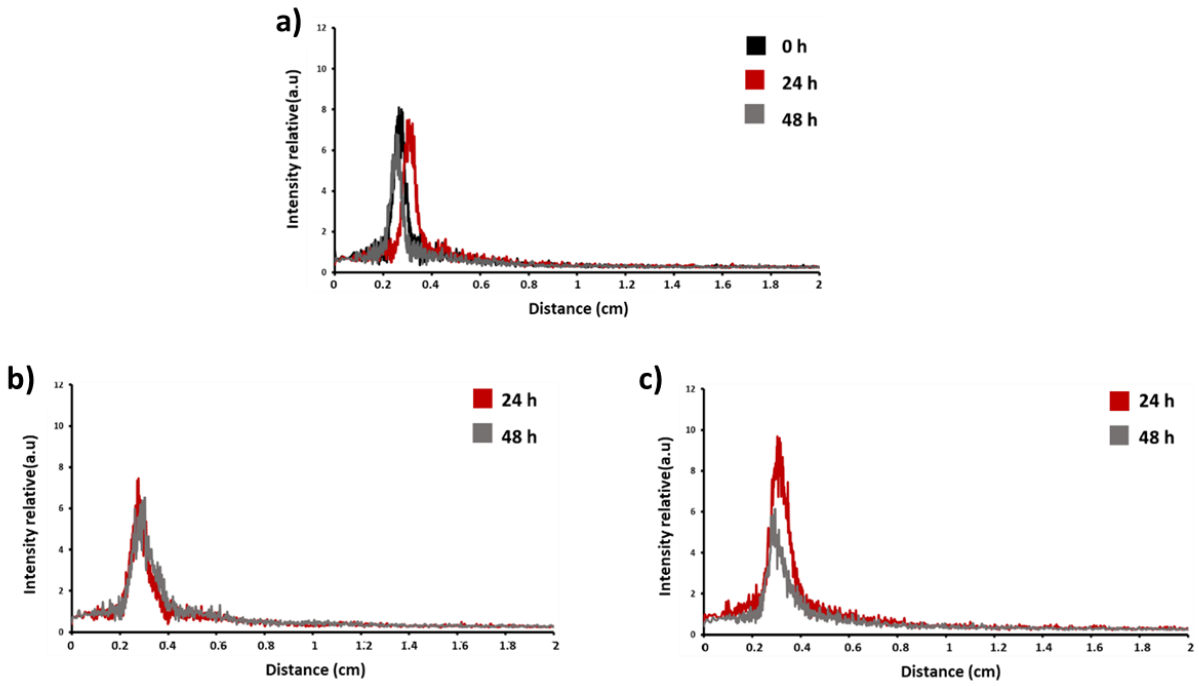

Fig. 102: Incubation of DiD@pPCDA-PEO/DFO[^{89}Zr] micelles in **a)** PBS, **b)** mouse plasma and **c)** mouse serum at 37 °C.

4. Animal experiments

The experiments presented in this section were performed by Dr Estelle Porret at the Orsay Hospital (CEA/DRF/Joliot/SHFJ/BioMaps), under the supervision of Dr Charles Truillet.

4.1. Tumor model

12 mice (n = 6 with sonoporation, n = 6 without sonoporation) were anesthetized and received a subcutaneous injection of 5.0 × 10^6 U-87 MG cells suspended in 100 µL of PBS in both right and left flanks for heterotopic establishment of tumors. The tumors were allowed to grow for three weeks before the beginning of the experiments. At the end of the experiments, mice were euthanized by cervical dislocation under isoflurane and tumors were collected and stored in 2-methylbutan frozen in liquid nitrogen. The glioblastoma U-87 MG cell line was selected for its high vascularization which is crucial for evaluating sonoporation efficacy.[340]

[340] J. -L. Li et al., Cancer Research, 2011, https://doi.org/10.1158/0008-5472.CAN-11-1704.

4.2. Experimental setup

The sonoporation procedure was performed under isoflurane anesthesia and followed a protocole similar to that described a previous study.[322] The setup consists of an ultrasound transducer connected to a programmable generator, all mounted on a holder to ensure a 3 cm distance between the tumor and the transducer. An acoustic window (5 mm circular opening) made of polymethylpentene membrane (trademark TPX®) is placed in front of the transducer to improve the transmission of ultrasounds to the tumor. The transducer is immersed into deionized and degassed water and an acoustic gel is added between the holder and the animal skin to ensure proper ultrasound transmission. Then, DiD@pPCDA-PEO/DFO[^{89}Zr] micelles with or without microbubbles (50 µL, SonoVue®) were intravenously administrated in the tail vein. For the 6 mice that were subjected to sonoporation (ultrasound + microbubbles), the ultrasound was applied to only one of the two tumors (one on each flank). The tumor in direct contact with the ultrasound transducer is called the enestic tumor while the opposite tumor is named anenestic tumor (**Fig. 103**). The ultrasonic waves were applied by pulse repetition frequency of 10 kHz for 2 min. After treatment, the mice could be imaged by PET and optical imaging at different times.

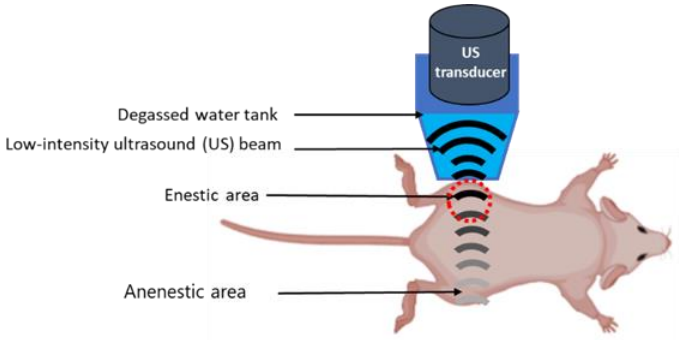

Fig. 103: Experimental setup used for sonoporation.

4.3. Biodistribution study

The biodistribution of DiD@pPCDA-PEO/DFO[^{89}Zr] micelles was evaluated in 12 mice bearing subcutaneous U-87 MG tumors, with half of them treated by sonoporation in combination with micelles, while the other half constituted the negative control without ultrasound. The presence of DiD and [^{89}Zr] allowed us to precisely track the micelles' location *in vivo* by optical and PET

imaging and thus, evaluate the delivery and biodistribution of DiD@pPCDA-PEO/DFO[^{89}Zr] micelles. The injection of micelles without or with microbubbles was performed simultaneously when the tumor reached around 200 mm^3. After applying the ultrasounds for 2 min, static PET acquisitions were performed at 4 h, 24 h, 48 h, 72 h and 7 days post injection. Whole-body images at maximum concentration accumulation time (48 h) are shown in **Fig. 104**. Both mice treated without (**Fig. 104a**) and with sonoporation (**Fig. 104b**) showed accumulation of micelles in the tumor (indicated by orange arrows). These images also showed accumulation in the liver, which is commonly observed with nanoparticles. Indeed, *ex vivo* analyses (**Fig. 104c**) obtained one week post injection proved that the micelles mainly accumulated in the liver and spleen, suggesting that elimination takes place mainly by the hepato-biliary pathway.

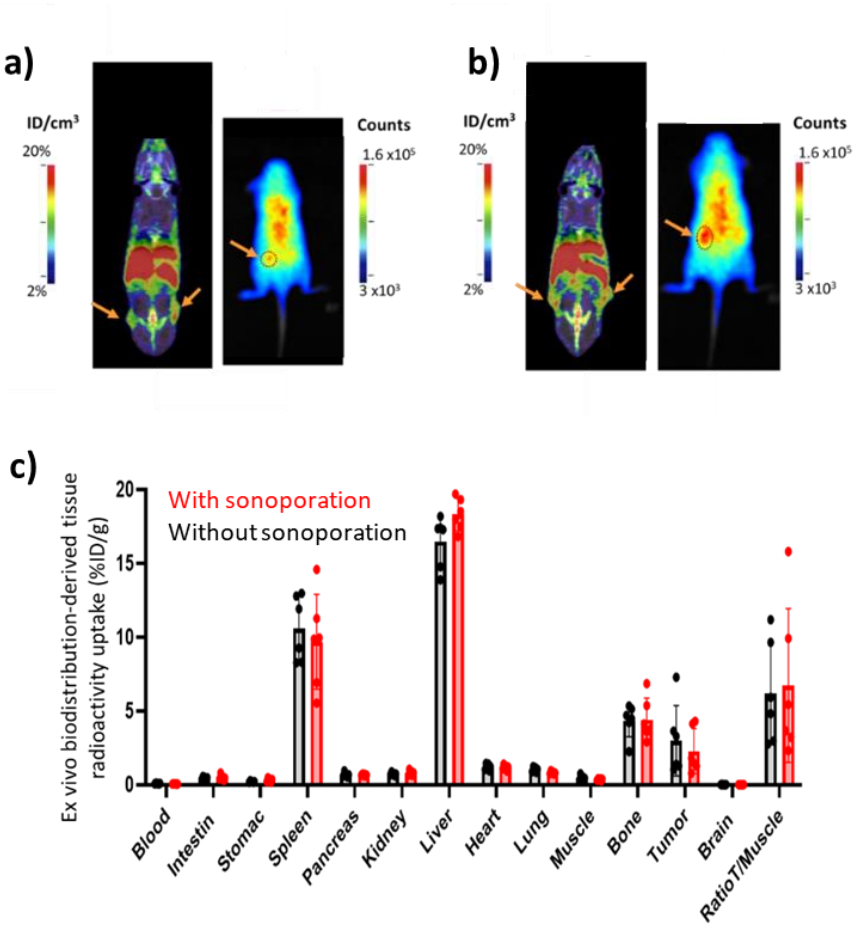

Fig. 104: *In vivo* biodistribution of DiD@pPCDA-PEO/DFO[^{89}Zr] micelles in subcutaneous U-87 MG tumor model. PET and optical images at 48 h post injection **a)** without and **b)** with sonoporation. The orange arrows indicate the tumors and the red circle shows the enestic tumor. **c)** *Ex vivo* biodistribution of DiD@pPCDA-PEO/DFO[^{89}Zr] micelles in the main organs in mice without sonoporation.

The accumulation of DiD@pPCDA-PEO/DFO[^{89}Zr] micelles in the main organs without sonoporation was quantified with respect to activity deposited in tissues using volume-of-interest analysis on PET images (**Fig. 105a**). The early activity detected in the bladder from 1 to 4 h post injection suggests that some of the micelles are quickly eliminated by urine. However, the lack of activity after 4 h in the bladder and the high radioactivity in the liver indicate that micelles are indeed mainly eliminated by the hepato-biliary pathway, as shown by the ex vivo analyses.

The accumulation of the micelles in the tumor reached a maximum value of 3 %ID cm^{-3} after 48 h post injection and decreased to 2.3 %ID cm^{-3} after five days. Therefore, most of the accumulated micelles were retained in the tumor. A similar accumulation can be observed in bones, which is a common feature with [^{89}Zr] complexes.[341] Almost no signal was detected in the brain or muscle at any time point, as expected.

The comparison of micelles' accumulation over time, with and without sonoporation is reported in **Fig. 105b**. The tumor solely treated with micelles and both enestic and anestetic tumors treated with sonoporation showed similar accumulation profiles. Maximum accumulation was observed 48 h post injection and reached around 3 %ID cm^{-3} for the two first cases and 3.5 %ID cm^{-3} for the latter. Although no significant changes were seen in terms of efficacy of accumulation, a more homogenous delivery of micelles into the enestic tumor was observed. Indeed, the standard deviation was significantly lower than for the two others, demonstrating the more homogenous delivery of micelles into the tumor.

[341] D. S. Abou et al., Nuclear Medicine and Biology, 2011, https://doi.org/10.1016/j.nucmedbio.2010.12.011.

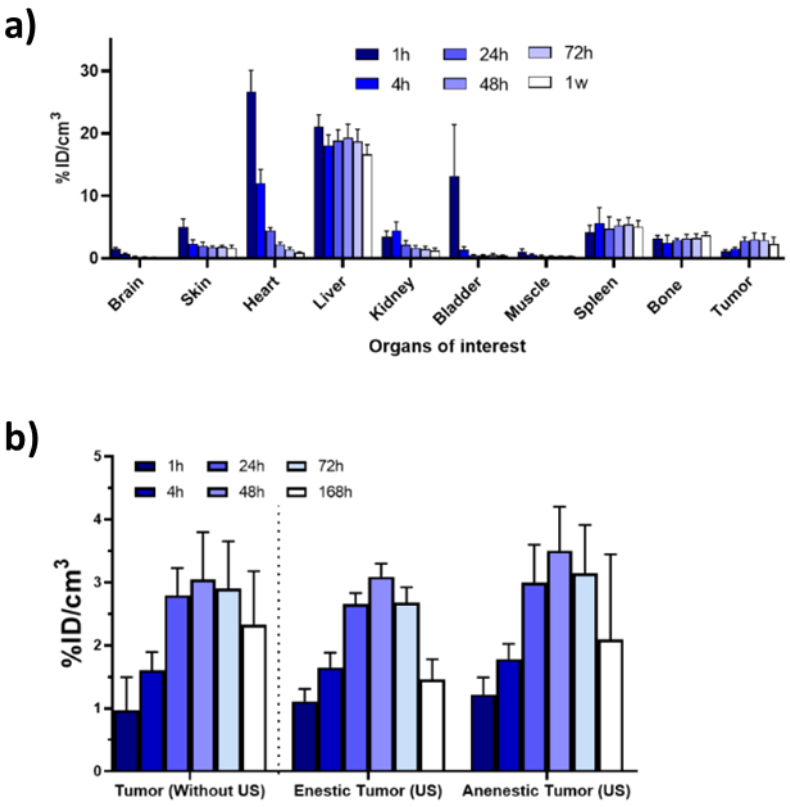

Fig. 105: **a)** Biodistribution derived from PET imaging of DiD@pPCDA-PEO/DFO[^{89}Zr] micelles over time into the main organs without sonoporation. **b)** Quantitative DiD@pPCDA-PEO/DFO[^{89}Zr] micelles accumulated into the tumors with and without sonoporation (enestic and anenestic).

4.4. Pharmacokinetic study

On the basis of PET quantification, modelling of blood kinetics was performed using the blood pool volume-of-interest analysis. Thus, blood time activity curves were obtained and the *in vivo* kinetics of DiD@pPCDA-PEO/DFO[^{89}Zr] micelles could be determined. When intravenously injecting a drug, a first distribution phase occurs, called α-phase, consisting of the very rapid spreading of the drug from the central compartment (blood circulation) to the body tissue, resulting in quick decrease of the drug's plasma concentration (steep slope). When the drug distribution equilibrium is reached, a second phase takes place, called β-phase, and is characterized by a slow decrease of the drug's plasma concentration mainly attributed to the drug's elimination. Both α- and β-phases are characterized by a half-life value that describes the drug's kinetic of elimination during these two phases. **Fig. 106a** shows that for DiD@pPCDA-PEO/DFO[^{89}Zr] micelles without sonoporation have a faster α-phase but slower

β-phase ($t_{1/2}(\alpha)$ = 136 ± 33 min; $t_{1/2}(\beta)$ = 40.6 ± 11.8 h) than with sonoporation ($t_{1/2}(\alpha)$ = 128 ± 39 min; $t_{1/2}(\beta)$ = 30.8 ± 5.9 h). No significant difference was observed and it can therefore be considered that sonoporation has no effect on the *in vivo* kinetics of elimination of DiD@pPCDA-PEO/DFO[^{89}Zr] micelles.

Concerning the tumors activity curves (**Fig. 106b**), all three cases (control, enestic and anenestic tumors with sonoporation) showed very similar profiles. Indeed, the area under curve, expressed in %ID cm^{-3} h, is 475.5 ± 79.7 for the control tumor, 462.8 ± 76.8 for the anenestic tumor and 384.7 ± 20.4 for the enestic tumor. Again, these results showed that sonoporation didn't improve the accumulation efficiency of DiD@pPCDA-PEO/DFO[^{89}Zr] micelles but the lower standard deviation for the enestic tumor indicates a more homogenous distribution of micelles.

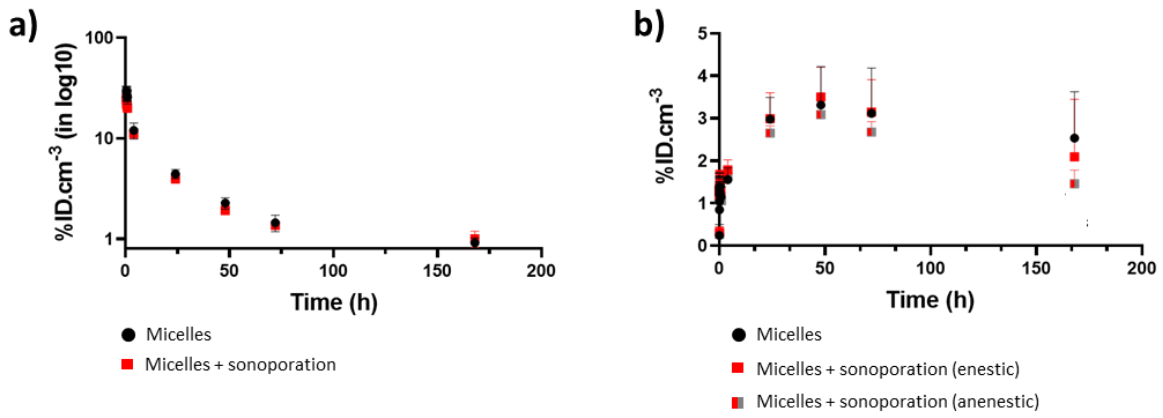

Fig. 106: *In vivo* kinetic of DiD@pPCDA-PEO/DFO[^{89}Zr] micelles. Micelles without (black) and with sonoporation (red for enestic and red/grey for anenestic tumors). **a)** Blood activity curves and **b)** Tumors activity curves.

4.5. Ex vivo characterization of sonoporation on DiD@pPCDA-PEO/DFO[^{89}Zr] micelles delivery

Tumors were harvested 72 h or 7 days post injection. Post-mortem distribution of DiD@pPCDA-PEO/DFO[^{89}Zr] micelles was assessed by autoradiography, fluorescence and histological analysis using hematoxylin-eosin staining of tissue sections (**Fig. 107**).

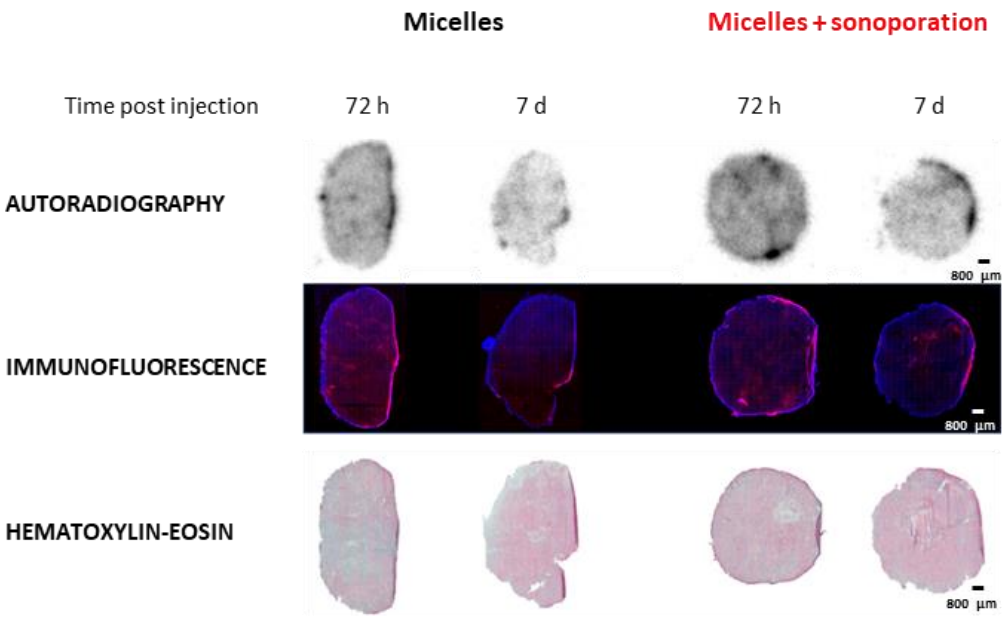

Fig. 107: Histological analyses of adjacent slices from tumors without (left) and with (right) sonoporation, collected 72 h and 7 days post injection of DiD@pPCDA-PEO/DFO[^{89}Zr] micelles.

DiD@pPCDA-PEO/DFO[^{89}Zr] micelles could be visualized by autoradiography and immunofluorescence thanks to [^{89}Zr] and DiD respectively. The colocalization between autoradiography (dark spots) and immunofluorescence (bright pink/red) confirmed the delivery of DiD@pPCDA-PEO/DFO[^{89}Zr] micelles in the whole tumor volume. Tumor sections stained with hematoxylin-eosin showed a few necrotic sites (white areas). No significant differences between the tumors treated with and without sonoporation could be noticed. In agreement with the *in vivo* experiments, the detected intensities in autoradiography and immunofluorescence were lower in the tumor sections after 7 days post injection compared to 72 h due to a slow washout. However, DiD@pPCDA-PEO/DFO[^{89}Zr] micelles could be clearly detected even after 7 days of treatment, confirming their strong *in vivo* stability (**Fig. 108**).

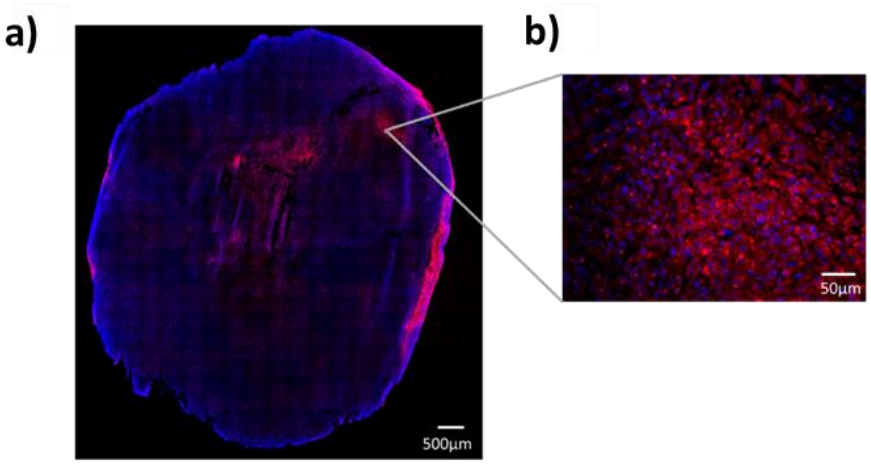

Fig. 108: **a)** Immunofluoresence of a slice of an enestic tumor 7 days post injection of DiD@pPCDA-PEO/DFO[^{89}Zr] micelles. **b)** Magnification of an area. Blue and red dots correspond to cell nucleus and micelles (DiD).

5. Conclusion

Hybrid pPCDA-PEO/DFO micelles were prepared by self-assembly in aqueous phase of a mixture of two photopolymerizable amphiphiles PCDA-PEO and PCDA-DFO in a 9:1 ratio (w/w). The micelles were characterized by DLS, showing a size of 12 nm. The fluorescent dye DiD was succesfully encapsulated within the micelles without disturbing the assembly as demonstrated by DLS and fluorescence measurements. The resulting DiD@pPCDA-PEO/DFO micelles were tested *in vitro* and their cytotoxicity was determined by MTT assays against U-87 MG and B16F10 cancer cell lines. The micelles displayed high biocompatibility as cell viability remained constant from 0.01 to 1 mg mL^{-1}.

DiD@pPCDA-PEO/DFO micelles were then radiolabelled with [^{89}Zr] and purified to obtain DiD@pPCDA-PEO/DFO[^{89}Zr] micelles. *In vivo* experiments showed that the micelles were mainly taken up by the liver and spleen, suggesting that the hepato-biliary system was the main elimination pathway. Despite the fact that sonoporation didn't improve the accumulation efficiency of the micelles, it significantly increased the homogeneity of delivery, as demonstrated by the biodistribution and pharmacokinetics studies.

Finally, ex vivo characterization of tumor sections showed that DiD@pPCDA-PEO/DFO[^{89}Zr] micelles were distributed throughout the tumor, underlining the good diffusion capacity of the objects. However, no noticeable differences could be observed with and without sonoporation,

in agreement with the other studies. Therefore, sonoporation, in this case, could be used as a strategy to homogenize the delivery of micelles for therapeutic applications. The presented data were recently published.[342] Studies with an active molecule such as doxorubicin would be the next stage of this study to assess the efficacy of the sonoporation in cancer treatments

[342] E. Porret et al., Nanoscale, 2023, http://doi.org/10.1039/d3nr01539d.

GENERAL CONCLUSION

In this work, different micelles were developed for cancer treatment, thanks to their targeted delivery by EPR effect. An original PEGylated micelle containing a photo-activable ferrocene unit to simultaneously induce cytotoxicity and release a hydrophobic payload was synthesized and tested *in vitro*. In parallel, a more conventional hybrid micelle could be combined with sonoporation to improve the EPR effect.

The first part of the work focused on the preparation and characterization of photo-activable PEGylated ferrocene-based micelles. The amphiphile C_{18}-Fc-PEO could be synthesized in a few steps starting from 1,1'-ferrocenedicarboxylic acid. Self-assembly in aqueous medium provided a colloidal solution of micelles that could be detected by DLS, showing a hydrodynamic diameter of 10 nm. C_{18}-Fc-PEO micelles readily underwent photodecomposition by photo-excitation of the ferrocene unit when illuminated in the d-d forbidden transition band at 442 nm. The photodegradation process was partially studied and showed that micelles could efficiently decompose to inorganic water-insoluble ferric species. The dissociation of the iron atom and the Cp rings was confirmed by UV-vis spectroscopy and XPS measurements. This unique feature could be exploited to phototrigger drug delivery as demonstrated with Nile Red as cargo model. *In vitro* experiments using MCF-7 breast cancer cells showed efficient cellular uptake of C_{18}-Fc-PEO micelles loaded with NR. Cytotoxicity assays of C_{18}-Fc-PEO micelles were performed and displayed a dose-response effect from 2 to 200 µM. The observed toxicity could be triggered on-demand by light and was attributed to an increase of reactive oxygen species leading to cell death by oxidative damage.

The photodegradation process of C_{18}-Fc-PEO micelles was adapted to *in vivo* applications by combining the NIR-photosensitizer *meso*-Tetraphenylbacteriochlorin and a light source emitting at 740 nm. The indirect photodegradation of the micelles was based on possible charge and electron transfer between the encapsulated photosensitizer and ferrocene unit. Another mechanism by photoactivation of oxygen with help of TPBC could generate singlet oxygen and subsequently oxidize ferrocene to ferricenium. Although the mechanism wasn't studied nor reported in the literature for this specific case, the very efficient photodecomposition of the TPBC@C_{18}-Fc-PEO micelles under 740 nm light showed a photodecomposition process similar to that of C_{18}-Fc-PEO micelles under blue light. Indeed, the use of Fe^{3+} chelators (DFP and DFO) produced the same complexes during the photodegradation of C_{18}-Fc-PEO micelles with both the blue and red light under their

respective conditions. XPS measurements confirmed the formation of the same ferric species as with the blue light. Therefore, it's highly plausible that both mechanisms with the blue and red conditions follow the same process with, however, a different photo-activation step of the ferrocene unit. Ultimately, the next stages of the study would be *in vitro* and then *in vivo* experiments. The latter would consist of intravenously administrating TPBC@C_{18}-Fc-PEO micelles into tumor-bearing mice. By mean of prolonged circulation, the micelles would accumulate in the tumor tissue over time by the EPR effect. However, while this effect is reported to allow nanoparticles to mainly target the tumor, many obstacles are met due to the tumor microenvironment, greatly reducing the treatment efficacy.

Another part of the work focused on the improvement of the passive targeting of micelles by EPR effect using sonoporation. To track micelles efficiently, a dual imaging strategy was implemented, by combining PET and optical imaging. Micelles were tracked in real-time thanks to the encapsulation of the red emitting dye DiD and the complexation of [^{89}Zr] at the surface of the micelles. The bi-modal imaging allowed to accurately locate the micelles and their payload in mice bearing glioblastoma U-87 MG tumors. The combination of ultrasound and microbubbles greatly improved the homogeneity of the accumulation of DiD@pPCDA-PEO/DFO[^{89}Zr] micelles. Retention of the micelles in tumors 7 days post injection was observed, assessing their great *in vivo* stability.

In the future, it may be interesting to combine near-infrared photo-activable ferrocene-based micelles and sonoporation. The latter would lead to a better distribution of the micelles in the whole tumor and potentially increase the therapeutic efficiency.

Résumé en français

La nanomédicine pour la thérapie anticancéreuse est un domaine innovant combinant nanovecteurs (ou nanoparticules) et molécules actives. La nanomédicine a été développée dans le but de contourner les contraintes de la médicine conventionnelle, à savoir les effets secondaires induits par la non spécificité des médicaments et à leur propriétés physico-chimiques non adaptées vis-à-vis de l'environnement biologique. Réduire les effets secondaires est un enjeu majeur en thérapie anticancéreuse due à l'utilisation de molécules ayant une forte activité biologique. Les nanomédicaments (i.e combinaison d'un nanovecteur et d'une molécule active) permettent aux molécules actives telles que le paclitaxel d'être incorporées en surface ou au cœur du nanovecteur, fournissant une meilleure protection contre l'environnement. Le nanovecteur peut être modifié en surface et fournir des propriétés spécifiques tels que le ciblage de cellules cancéreuses et la délivrance de molécules actives. La nanomédicine permet donc, par opposition à la médecine conventionnelle, de protéger la molécule active et l'amener à la cible. Par conséquent, la spécificité du médicament est grandement améliorée et les effets secondaires sont ainsi réduits. Dans le cadre de la thèse, les micelles sont utilisées en tant que nanovecteurs. Deux projets ont pu être réalisés, le premier étant la préparation de micelles photo-activables pouvant induire une cytotoxicité contrôlée par illumination. Le second projet met en avant l'amélioration de la diffusion passive de micelles au sein de tumeurs greffées sur souris par sonoporation.

Le premier projet est divisé en deux chapitres, l'un montre la synthèse organique des amphiphiles photo-activables ainsi que leur auto-assemblage en micelles, et le deuxième chapitre étudie leur étude physico-chimique, à savoir leur capacité à être photodégradée et à générer une cytotoxicité contrôlée. Le premier chapitre montre les différentes voies de synthèse entreprises pour parvenir aux molécules finales. Une première approche consiste à faire des acylations de Friedel-Crafts successives du ferrocène non substitué. De nombreuses difficultés ont été rencontrées, notamment l'incompatibilité des conditions d'acylation avec le substrat, et n'a pas permis d'obtenir la molécule finale. La seconde voie proposée utilise une méthode d'acylation plus douce mais des problèmes de réactivités ont empêchés la synthèse des molécules finales. Finalement, une troisième et dernière approche, plus directe, consiste à

commencer par l'acide 1,1'-ferrocenedicarboxylique. Par simples réactions d'activations et substitutions, les molécules finales ont pu être synthétisées. Leur auto-assemblage en micelles dans un milieu aqueux a pu être ensuite caractérisé par diverses techniques telles que la diffusion dynamique de la lumière ou par tensiométrie. Après avoir confirmé la formation de micelles, les études photochimiques ont été réalisées en solution, puis in vitro. Sous illumination bleue, les micelles ont pu être photodégradées en 5 min. Cette observation a pu être vérifiée en encapsulant une molécule fluorescente, le Nile Red, au cœur des micelles. Il a été montré qu'une diminution de l'absorbance liée au Nile Red était directement due à la photodégradation des micelles pendant l'illumination. Ces études montrent que les micelles peuvent efficacement encapsuler et relarguer une molécule hydrophobe par illumination. Des études in vitro ont ensuite été réalisées pour mettre en avant l'effet cytotoxique des objets sous illumination. Les cellules cancéreuses MCF-7 ont été incubées avec différentes concentrations en micelles, allant de 2 µM à 200 µM. Avant illumination, aucune diminution significative de la survie cellulaire est observée. Après 10 min d'irradiation, une diminution de cette dernière est observée, qui montre un effet dose-réponse liée à la concentration en micelles. Cette expérience in vitro montre que les micelles sont biocompatibles même à forte concentration et peuvent induire une cytotoxicité sous illumination seulement.

Le but final de ce projet étant de tester sur souris, l'utilisation d'une illumination bleue n'est pas adaptée due à une faible pénétration de la lumière dans les tissue. Pour transférer le système du vitro en vivo, l'utilisation d'une lampe proche infrarouge est plus adaptée. Pour induire la photodégradation des micelles, la lampe proche IR n'est pas compatible avec le motif ferrocène, c'est pourquoi le système a été légèrement modifié. L'utilisation d'une molécule relai absorbant dans le proche infrarouge, appelé photosensibilisateur, a pu être encapsulée au sein des micelles. Cette molécule, un dérivé de bactériochlorine, a la capacité d'absorber la lumière à 740 nm et générer de l'oxygène singulet. Une preuve de concept a été réalisée en solution et a montré la photodégradation de micelles contenant la bactériochlorine en seulement 5 min. La prochaine étape est de tester ce nouveau système in vitro pour comparer ses effets cytotoxiques et si les résultats sont prometteurs, expérimenter in vivo.

Le troisième et dernier chapitre traite du deuxième projet sur l'utilisation de la sonoporation pour améliorer l'accumulation passive de micelles au sein de tumeurs solides. Les micelles utilisées sont constituées de deux amphiphiles différents photopolymérisables.

L'un comporte une chaine hydrophile complexante (DFO) du zirconium-89 pour l'imagerie TEP et l'autre une chaine hydrophile PEG pour les propriétés de biocompatibilité. Ces micelles ont pu d'abord être synthétisées et auto-assemblées. La formulation des micelles a été réalisée d'abord par auto-assemblage dans un milieu aqueux puis photopolymerisation sous UV. Puis, l'encapsulation d'une molécule fluorescente, le DiD, a été réalisée. Cette encapsulation nous permet de suivre le contenu des micelles par fluorescence in vivo. Avant incorporation du radiotraceur zirconium-89, une étude in vitro de biocompatibilité a été réalisée. Les résultats montrent que les micelles sont biocompatibles même à hautes concentrations (400 µM). Finalement, la dernière étape de formulation a pu être réalisée pour incorporer le zirconium-89 à la surface des micelles. La haute stabilité de complexation a pu être faite dans divers milieux biologiques et l'étude a montré la forte stabilité du complexe DFO-Zr. Après la formulation des micelles photopolymerisées, fluorescentes et radioactives, les expériences in vivo ont pu être réalisées. Une première étude par imagerie TEP et fluorescence ont montré que les souris traitées par sonoporation ne suggèrent pas une meilleure accumulation des micelles au sein des tumeurs. Une étude de biodistribution a été faite et a montré que les micelles sont principalement éliminées par le foie et la rate. Une étude comparative entre les tumeurs traitées avec et sans sonoporation n'a révélé aucune différence par rapport à l'accumulation des micelles, en accord avec les imageries TEP. Cependant, les souris traitées par sonoporation ont montré une distribution plus homogène au sein des tumeurs en contact direct des ultrasons.

En conclusion, ce projet met en avant l'utilisation de la sonoporation pour induire une distribution des micelles plus homogène au sein d'un même type de tumeur mais ne permet pas une meilleure accumulation.

Binding statement

I declare that the thesis was written independently and that I took part and contributed to all presented results in the thesis. All sources and literature were cited properly. The present thesis has not been used for another or similar type of higher education qualification. Herein, I declare respecting the Dean's Meassure No. 22/2017 from Charles University for the submission of the thesis (Art.11 of OD 22/2017)

MSc. Stéphane Hoang

Prof. Martin Hruby

Dr Edmond Gravel

List of outputs during the thesis

Publications / patent:

Accepted paper: Estelle Porret, Stéphane Hoang, Caroline Denis, Eric Doris, Martin Hruby, Anthony Novell, Edmond Gravel and Charles Truillet, "Sonoporation-assisted micelles delivery in subcutaneous glioma-bearing mice evaluated by PET/fluorescence bi-modal imaging", *Nanoscale*, 2023, https://doi.org/10.1039/D3NR01539D.

Accepted patent: Eric Doris, Edmond Gravel, Stéphane Hoang, Martin Hruby, Guillaume Pinna, Micelles in cancer therapy, European Patent, EP23305409 (03/2023).

Submitted paper: Stéphane Hoang, Marie Vandamme, Guillaume Pinna, Frédéric Miserque, Petr Stephanek, Eric Doris, Martin Hruby and Edmond Gravel, "Photo-triggered cytotoxicity of ferrocene-based micelles – a non-conventional approach to phototherapy.

Attended conferences:

73. ZJAZD CHEMIKOV 6 – 10 September 2021 Vysoké Tatry, Horný Smokovec

Abstract: Nanomedecine consists of designing nanosystems for diagnosis, monitoring and treating diseases such as cancer. These so-called nanosystems can have specific features such as active or passive targeting (EPR effect), encapsulation of active drugs, controlled delivery of the cargo, stealth properties and more. Herein, ferrocene-based micelles loaded with gold nanoparticles are used as drug carrier. Polyethyleneglycol as hydrophilic chain provides biocompatibility and stealth properties. Upon illumination at the gold nanoparticles' surface plasmon resonance (SPR) frequency, hyperthermia is triggered, leading to the generation of reactive oxygen species (ROS) near the micelles as well as thermal ablation. Furthermore, Iron (II) is easily oxidizable especially in presence of ROS, also known as the Fenton reaction, to produce iron (III) which is a highly active Fenton catalyst. The presented nanosystem is based on the hyperthermia effect which has three major consequences: thermal ablation (apoptosis), generation of ROS leading to the oxidation of ferrocene and thus degradation of the micelles allowing a controlled delivery, and the immune restoration in the tumor environment. Therefore, we expect this nanoassembly to display a potent therapeutic effect and perhaps lead to new possibilities regarding the use of ferrocene as a multi-purpose linker.

Financial support from the Czech Science Foundation (grant # 21-01090S) and from Ministry of Education, Youth and Sports of the Czech Republic (grant # LM2018133) is gratefully acknowledged. This work was supported by the Joint PhD Programme of Université Paris-Saclay as part of the « Investissements d'Avenir » program [grant number ANR-11-IDEX-003].

Semaine d'Etude de Chimie Organique 60 (SECO60), 21 – 26 May 2023 Arêches-Beaufort, France

Abstract: Nanomedicine uses unique size-related properties of nanospecies such as liposomes, quantum dots, micelles etc. for the diagnosis and therapy of various diseases. The concentration of free iron is strictly regulated inside cells. An abnormal additional amount of iron leads to oxidative stress which can cause irreversible damage of the cells. Indeed, excessive iron accumulation leads to overproduction of lipid peroxides and subsequently to cell death[1]. Previously, our group developed photoactivable micelles using nitrobenzyl groups to trigger cytotoxicity upon illumination at 365 nm[2]. Herein, our work aims at developing micelles that can transport and release iron on demand, causing oxidative stress in cancer cells after illumination. To this end, we selected ferrocene as an iron source and light-activable linker for the synthesis of micelle-forming amphiphiles. The stearyl and poly(ethylene oxide)(PEG) chains, acting as the lipophilic and hydrophilic blocks, respectively, are both linked to the ferrocene moiety *via* amide bonds. This enables easy photodegradation[3] of the correponding micelles and release of iron upon illumination under 460 nm light. Hydrophobic cargo may be encapsulated into such micelles and its release can be synchronized with micelle photodegradation as we demonstrated using Nile Red as a model substrate. The micelles were tested *in vitro* on MCF-7 cell cultures and showed efficient light-triggered cytotoxicity.

Financial support from the Czech Science Foundation (grant # 21-01090S) and from Ministry of Education, Youth and Sports of the Czech Republic (grant # LM2018133) is gratefully acknowledged. This work was supported by the Joint PhD Programme of Université Paris-Saclay as part of the « Investissements d'Avenir » program [grant number ANR-11-IDEX-003].

References

[1]Y. Wang and M. Tang, *Environmental Pollution*, **2019**, 112937.
[2]P. Anilkumar, E. Gravel, I. Theodorou, K. Gombert, B. Thézé, F. Ducongé and E. Doris, *Advanced Functional Material*, **2014**, 24, 5246-5252.
[3]Y. Yamaguchi, W. Ding, C. T. Sanderson, M. L. Borden, M. J. Morgan and C. Kutal, *Coordination Chemistry Reviews*, **2007**, 251, 515-524.

TABLE OF FIGURES

EXPERIMENTAL SECTION

General procedures

Synthesis and characterization

Unless otherwise specified, all chemicals were purchased from Sigma-Aldrich and used without further purification. Flash chromatography was carried out on Kieselgel 60 (230–240 mesh, Merck).

^{1}H NMR and ^{13}C NMR spectra were recorded using a Bruker Avance DPX 400 spectrometer at 400 and 100 MHz respectively. Chemical shifts (δ) are given in ppm relative to the NMR solvent residual peak. Chemical shifts were reported in parts per million (ppm) downfield from residual solvent peaks and coupling constants were reported in Hertz (Hz). Splitting patterns were designated as singlet (s), doublet (d) and triplet (t). Splitting patterns that could not be interpreted or easily visualized were designated as multiplet (m). Spectra were analyzed using MestRenova software.

FT-IR spectra were recorded using a Spectrum 2 FT-IR (PerkinElmer). Wavenumbers were given in cm^{-1} at their maximum intensity.

Electrospray mass spectra were obtained on a ESI-Quadripole from Waters Mass Spectrometer or from Thermo Scientific LCQ Fleet Ion Trap LC/MS.

Size exclusion chromatography (SEC) analyses were performed on a setup equipped with PLgel 5 µm 100 Å and DeltaGel Mixed-B columns, RI detector, and chloroform as the mobile phase with a flow rate of 1 mL min^{-1}. The molecular weights (M_n, M_w) and dispersity ($Đ$) values were based on methoxy poly(ethylene) oxide 2000.

Illumination

All samples were illuminated in a quartz cuvette (4 mL volume, 1 cm path length) and UV spectra were measured at various times depending on the experiment, using either the 460 (A160WE Tuna Blue) or 740 nm (PR160L) nm light source. Samples were illuminated at 8 cm away from the light source with an irradiance of 55 $mW.cm^{-2}$ for A160WE Tuna Blue. About PR160L-740, no data was available from the provider thus no irradiance could be provided. In case of A160WE Tuna Blue, the irradiance at 8 cm was calculated using experimental data from the provider at 5 cm with an irradiance of 140 $mW.cm^{-2}$ and equation **(Eq. I)**, with $I_2 = 140$

mW.cm^{-2}, $d_2 = 5$ cm and $d_1 = 8$ cm. For both lights, experiments were done at maximum power output (~40 W according to provider). All light sources were purchased from Kessil (https://kessil.com/products/science_main.php). Varian Cary® 50 UV-Vis spectrophotometer was used to perform all measurements.

$$\frac{I_1}{I_2} = \frac{d_2^2}{d_1^2} \qquad \textbf{(Eq. I)}$$

Encapsulation of hydrophobic molecules

The percentage of encapsulation efficiency (*EE*) and drug loading capacity (*DL*) were calculated according to the following equations:

$$EE = \frac{m_{exp}}{m_i} \times 100 \qquad \textbf{(Eq. II)}$$

$$DL = \frac{m_{exp}}{m_{tot}} \times 100 \qquad \textbf{(Eq. III)}$$

With m_{exp} the weight of entrapped molecule, m_i the initial weight of molecule added and m_{tot} the total weight of the sample that is equal to the sum of the weight of the micelles and the initial weight of molecule added.

Micelles size analysis by dynamic light scattering (DLS)

Hydrodynamic diameters D_h were recorded using Malvern Zetasizer Nano ZS at 25 °C (He-Ne laser 633 nm). Samples were prepared at the given concentration by dispersing the solid amphiphiles in 1 mL of milliQ water. Sonication by ultrasound bath or ultrasound probe followed by filtration on 0.20 µm nylon membrane afforded a colloidal suspension of micelles that was used for DLS measurements.

CHAPTER 1

1

Synthesis of 10,12-pentacosadiynoyl chloride (1)

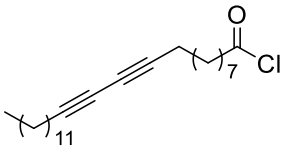

To a solution of 10,12-pentacosadiynoic acid (200 mg, 0.53 mmol, 1.0 equiv.) in anhydrous CH_2Cl_2 (3 mL) was added dropwise oxalyl chloride (95 µL, 1.12 mmol, 2.1 equiv.) under argon and stirring for 18 h at room temperature. A red solid was formed during the reaction and was removed by filtration on cotton. The filtrate was then evaporated to afford the desired product **1** (92%) as a colorless oil.

^{1}H NMR (400 MHz, $CDCl_3$) δ (ppm): 2.88 (t, 2H, J = 7.2 Hz), 2.24 (t, 4H, J = 6.8 Hz), 1.70 (m, 2H), 1.74 (m, 4H), 1.42–1.19 (m, 26H), 0.88 (t, 3H, J = 6.8 Hz).

2

Synthesis of 10,12-pentacosadiynoylferrocene (2)

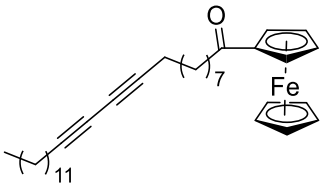

To a solution of 10,12-pentacosadiynoic acid (412 mg, 1.10 mmol, 1.1 equiv.) and TFAA (153 µL, 1.10 mmol, 1.1 equiv.) in anhydrous CH_2Cl_2 (5 mL) was added ferrocene (186 mg, 1.0 mmol, 1.0 equiv.) and TfOH (97 µL, 1.1 mmol, 1.1 equiv.) at once under argon and stirring during 3 h. Water (15 mL) was then added and the mixture was extracted multiple times with CH_2Cl_2. The combined organic phases were dried over $MgSO_4$, filtered and evaporated. The crude product was purified on silica gel (95:5, Cy/AcOEt) to afford the desired product **2** (46%) as an orange-to-red solid.

^{1}H NMR (400 MHz, $CDCl_3$) δ (ppm): 4.78 (m, 2H), 4.49 (m, 2H), 4.19 (s, 5H), 2.69 (t, 2H, J = 7.6 Hz), 2.39 (m, 2H), 2.22 (m, 2H), 1.70 (m, 2H), 1.56 (m, 2H), 1.49–1.18 (m, 28H), 0.88 (t, 3H, J = 6.4 Hz).

3

Synthesis of stearoylchloride (3)

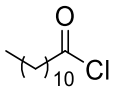

To a solution of stearic acid (200 mg, 1.0 mmol, 1.0 equiv.) in anhydrous CH_2Cl_2 (2 mL) was added oxalyl chloride (129 µL, 1.50 mmol, 1.5 equiv.) under argon and the mixture was stirred for 6 h at room temperature. The mixture was concentrated under vacuum to afford the desired product **3** (93%) as a color less oil.

^{1}H NMR (400 MHz, $CDCl_3$) δ (ppm): 2.88 (t, 2H, J = 7.2 Hz), 1.71 (m, 2H), 1.41–1.17 (m, 16H), 0.88 (t, 3H, J = 6.8 Hz).

Synthesis of lauroylferrocene (4) and 1,1′-bislauroylferrocene (5)

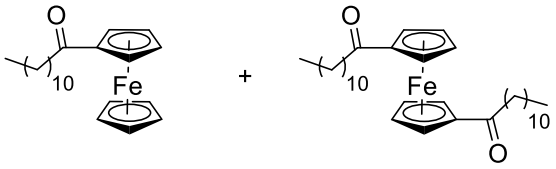

To a suspension of $AlCl_3$ (167 mg, 1.25 mmol, 1.5 equiv.) in anhydrous CH_2Cl_2 (1 mL) was added a solution of **3** (200 mg, 0.92 mmol, 1.1 equiv.) in anhydrous CH_2Cl_2 (1 mL) under argon and the mixture was stirred at room temperature. After 30 min of stirring, a solution of ferrocene (155 mg, 0.83 mmol, 1.0 equiv.) in anhydrous CH_2Cl_2 (1 mL) was added and the reaction was stirred for 20 h. Water (5 mL) was added and the reaction was further stirred for 5 min. The mixture was extracted multiple times with CH_2Cl_2. The combined organic phases were dried over $MgSO_4$, filtered and concentrated. The crude product was purified on silica gel (Cy/AcOEt 90:10) to afford both **4** (22%) and **5** (52%) as red solids.

4: 1H NMR (400 MHz, $CDCl_3$) δ (ppm): 4.78 (m, 2H), 4.48 (m, 2H), 4.19 (s, 5H), 2.69 (t, 2H, J = 7.2 Hz), 1.70 (m, 2H), 1.44–1.08 (m, 16H), 0.88 (t, 3H, J = 6.8 Hz).

5: ^{1}H NMR (400 MHz, $CDCl_3$) δ (ppm): 4.76 (m, 4H), 4.47 (m, 4H), 2.64 (m, 4H), 1.68 (m, 4H), 1.42–1.02 (m, 32H), 0.88 (m, 6H)

6

Synthesis of α-methoxy-ω-*tert*-Butyl ester PEO2000 (6)

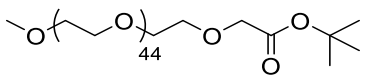

NaH (30 mg, 1.24 mmol, 5.0 equiv.) was added to a solution of PEO2000-OH (500 mg, 0.25 mmol, 1.0 equiv.) in anhydrous DMF (5 mL) under argon at 50 °C with stirring for 1 h. Then, the reaction mixture was cooled down to room temperature and *tert*-butylbromoacetate (92 µL, 0.62 mmol, 2.5 equiv.) was added. The reaction mixture was stirred at room temperature for 48 h. As the reaction was slow, additional *tert*-butylbromoacetate (92 µL, 0.62 mmol, 2.5 equiv.) and NaH (15 mg, 0.62 mmol, 2.5 equiv.) were added. The reaction mixture was stirred at 80 °C for 24 h. The reaction mixture was cooled down to room temperature and MeOH (2 mL) was added. The mixture was stirred for an additional 10 min and then evaporated under vacuum. The crude product was solubilized in CH_2Cl_2 and the white solid (NaBr salt) was removed by cotton filtration. The filtrate was concentrated under vacuum once more. The resulting crude product was purified on silica gel (90:10 CH_2Cl_2/MeOH) to afford the desired product **6** (61%) as a white solid.

^{1}H NMR (400 MHz, $CDCl_3$) δ (ppm): 4.56 (s, 1H), 4.26 (s, 1H), 3.85–3.51 (m, 180H), 3.37 (s, 3H), 1.47 (s, 9H).

Synthesis of α-methoxy-ω-carboxy PEO2000 (7)

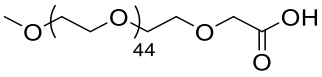

To a solution of **6** (325 mg, 0.15 mmol, 1.0 equiv.) in CH_2Cl_2 (5 mL) was added TFA (3 mL) and the mixture was stirred for 24 h at room temperature. The solvent was evaporated under vacuum and the crude product was solubilized in CH_2Cl_2 and concentrated again. This step was repeated 4 times with CH_2Cl_2 and finally carried out once more with acetone to afford the desired product **7** (quantitative).

^{1}H NMR (400 MHz, $CDCl_3$) δ (ppm): 4.15 (s, 2H), 3.84–3.43 (m, 180H), 3.37 (s, 3H).

8

Synthesis of 2,5-dioxopyrrolidin-1-yl carboxylferrocene (8)

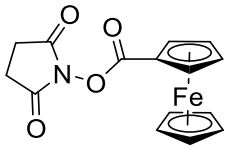

Ferrocenecarboxylic acid (464 mg, 2.02 mmol, 1.0 equiv.), NHS (279 mg, 2.42 mmol, 1.2 equiv.) and EDC.HCl (464 mg, 2.42 mmol, 1.2 equiv.) were dissolved in anhydrous CH_2Cl_2 (15 mL) under argon and the mixture was stirred for 6 h at room temperature. The organic phase was washed with water, dried over $MgSO_4$, filtered and concentrated under vacuum to afford **8** (99%) as an orange solid.

^{1}H NMR (400 MHz, $CDCl_3$) δ (ppm): 4.94 (m, 2H), 4.57 (m, 2H), 4.39 (s, 5H), 2.88 (m, 4H).

Synthesis of *N*-propylcarbamoylferrocene (9)

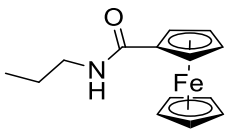

n-Propylamine (21 µL, 0.26 mmol, 1.5 equiv.) was added to a solution of **8** (40 mg, 0.17 mmol, 1.0 equiv.) in anhydrous CH_2Cl_2 (1.5 mL) under argon and the mixture was stirred for 18 h at room temperature. The organic phase was washed with water, dried over $MgSO_4$, filtered and concentrated under vacuum to provide molecule **8** (52%).

^{1}H NMR (400 MHz, $CDCl_3$) δ (ppm): 5.74 (s, 1H), 4.66 (m, 2H), 4.33 (m, 2H), 4.19 (s, 5H), 3.35 (m, 2H), 1.62 (m, 2H), 0.99 (t, 3H, J = 7.6 Hz).

10

Synthesis of 1-(10,12-pentacosadiynoyl)-1′-(2,5-dioxopyrrolidin-1-yl carboxyl)ferrocene (10)

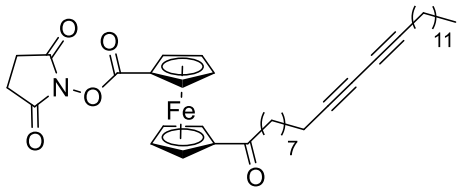

To a solution of 10,12-pentacosadiynoic acid (353 mg, 0.94 mmol, 1.1 equiv.) and TFAA (131 µL, 0.94 mmol, 1.1 equiv.) in anhydrous CH_2Cl_2 (2 mL) was added **8** (280 mg, 0.86 mmol, 1.0 equiv.) and TfOH (83 µL, 0.94 mmol, 1.1 equiv.) under argon and the mixture was stirred at room temperature. After 16 h of stirring, the organic phase was washed with water, dried over $MgSO_4$, filtered and concentrated under vacuum. The crude product was purified on silica gel (Cy/AcOEt 70:30, then a second purification using 98:2 CH_2Cl_2/acetone) to afford molecule **10** (2%).

^{1}H NMR (400 MHz, $CDCl_3$) δ (ppm): 4.99 (m, 2H), 4.91 (m, 2H), 4.71 (m, 2H), 4.57 (m, 2H), 2.91 (m, 4H), 2.70 (t, 2H, J = 7.2 Hz), 2.32 (m, 4H), 1.68 (m, 2H), 1.53 (m, 2H), 1.47–1.16 (m, 26H), 0.88 (t, 3H, J = 6.4 Hz).

Synthesis of succinylferrocene (11)

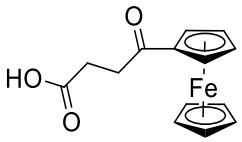

To a solution of succinic anhydride (1.10 g, 11.02 mmol, 2.1 equiv.) and $AlCl_3$ (1.47 g, 11.02 mmol, 2.1 equiv.) in anhydrous CH_2Cl_2 (35 mL) was added ferrocene (1.0 g, 5.38 mmol, 1.0 equiv.) under argon and the mixture was stirred at 0 °C. The orange precipitate was filtered and washed using CH_2Cl_2 to afford molecule **11**. The filtrate was concentrated under vacuum and the crude product was purified on silica gel (100% acetone) to afford **11** as well (total yield = 80%).

^{1}H NMR (400 MHz, acetone-d_6) δ (ppm): 10.61 (s, 1H), 4.84 (m, 2H), 4.54 (m, 2H), 4.29 (s, 5H), 3.10 (t, 2H, J = 6.4 Hz), 2.65 (t, 2H, J = 6.4 Hz).

12a

Synthesis of α-methoxy-ω-tosyl PEO2000 (12a)

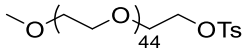

To a solution of methoxypoly(ethylene glycol) 2000 (mPEO2000) (2.0 g, 1.0 mmol, 1.0 equiv.) and tosyl chloride (419 mg, 2.2 mmol, 2.2 equiv.) in CH_2Cl_2 (20 mL) was added Et_3N (350 µL, 2.5 mmol, 2.5 equiv.) and the mixture was stirred for 48 h at room temperature. The solvent was evaporated under vacuum and the crude product was purified on silica gel (90:10 CH_2Cl_2/MeOH) to afford the tosylated polymer **12a** (78%) as a white-yellowish solid.

^{1}H NMR (400 MHz, $CDCl_3$) δ (ppm): 7.81 (d, 2H, *J* = 8.0 Hz), 7.36 (d, 2H, *J* = 8.0 Hz), 4.17 (m, 2H), 3.85–3.46 (m, 178H), 3.39 (s, 3H), 2.47 (s, 3H).

12b

Synthesis of α-methoxy-ω-tosyl PEO750 (12b)

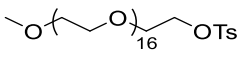

To a solution of methoxypoly(ethylene glycol) 750 (PEO750) (1.0 g, 1.36 mmol, 1.0 equiv.) and tosyl chloride (570 mg, 2.99 mmol, 2.2 equiv.) in CH_2Cl_2 (10 mL) was added Et_3N (475 µL, 3.40 mmol, 2.5 equiv.) and the mixture was stirred at room temperature. The organic phase was washed with water, dried over $MgSO_4$, filtered and concentrated under vacuum. The crude product was purified on silica gel (95:5 CH_2Cl_2/MeOH) to afford the tosylated polymer **12b** (48%) as a yellowish oil.

^{1}H NMR (400 MHz, $CDCl_3$) δ (ppm): 7.79 (d, 2H, J = 8.4 Hz) 7.33 (d, 2H), 4.15 (t, 2H, J = 8.0 Hz), 3.84–3.42 (m, 66H), 3.37 (s, 3H), 2.44 (s, 3H).

13a

Synthesis of α-methoxy-ω-azido PEO2000 (13)

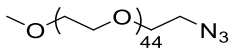

To a solution of **12a** (715 mg, 0.33 mmol, 1.0 equiv.) in anhydrous DMF (5 mL) was added NaN_3 (64 mg, 0.99 mmol, 3.0 equiv.) under argon and the mixture was stirred at 80 °C for 48 h. The reaction mixture was cooled down to room temperature and acetone (5 mL) was added. The precipitate was filtered on cotton and washed with acetone. The solvent was evaporated under vacuum and the residue was solubilized in CH_2Cl_2. The organic phase was washed with water, dried over $MgSO_4$, filtered and evaporated under vacuum to afford the desired product **13a** (89%) as a white solid.

^{1}H NMR (400 MHz, $CDCl_3$) δ (ppm): 3.84–3.44 (m, 178H), 3.38 (m, 2H), 3.37 (s, 3H)

.

13b

Synthesis of α-methoxy-ω-azido PEO750 (13b)

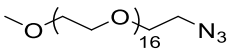

To a solution of **12b** (156 mg, 0.18 mmol, 1.0 equiv.) in anhydrous DMF (1 mL) was added NaN_3 (34 mg, 0.53 mmol, 3.0 equiv.) under argon and the mixture was stirred at 80 °C for 22 h. The reaction mixture was cooled down to room temperature and acetone (1 mL) was added. The precipitate was filtered on cotton and washed with acetone before evaporation under vacuum. The crude product was solubilized in CH_2Cl_2 and the organic phase was washed with water, dried over $MgSO_4$, filtered and evaporated under vacuum to afford the desired product **13b** (91%) as a white oil.

^{1}H NMR (400 MHz, $CDCl_3$) δ (ppm): 3.84–3.44 (m, 66H), 3.38 (m, 2H), 3.37 (s, 3H)

14a

Synthesis of α-methoxy-ω-amino PEO2000 (14a)

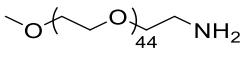

Staudinger reduction of **13a**:

To a solution of **13a** (428 mg, 0.21 mmol, 1.0 equiv.) in THF (4 mL) was added PPh_3 (110 mg, 0.42 mmol, 2.0 equiv.) and the mixture was stirred for 2 h at room temperature. Then, water (1 mL) was added and the reaction was stirred for an additional 24 h. 1 M HCl (3 mL) was added and the reaction was stirred for 30 min after which CH_2Cl_2 (10 mL) was added. The organic phase was washed with water, dried over $MgSO_4$, filtered and evaporated under vacuum. The crude product was purified on silica gel (CH_2Cl_2/MeOH 90:10, then 80:20 and finally 100% MeOH to elute the primary amine) to afford the desired amine **14a** (20%) as a white solid.

Amination of **12a**:

12a (4.634 g, 2.14 mmol, 1.0 equiv.) was added to an aqueous solution of 38% ammoniac (100 mL) and the mixture was stirred vigorously at room temperature for 48 h. CH_2Cl_2 (100 mL) was added and the organic phase was washed with water, dried over $MgSO_4$, filtered and evaporated under vacuum to afford **14a** (64%) as a white solid.

^{1}H NMR (400 MHz, $CDCl_3$) δ (ppm): 3.83–3.41 (m, 178H), 3.36 (s, 3H), 2.88 (t, 2H, J = 5.4 Hz)

14b

Synthesis of α-methoxy-ω-amino PEO750 (14b)

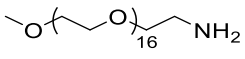

A Schlenk flask containing a mixture of **13b** (118 mg, 0.15 mmol) and Pd/C (35 mg) in MeOH (8 mL) was vacuumed to remove air and filled with argon. This process was done at least 10 times. Then, argon was replaced with dihydrogen and the procedure was proceeded 10 times again. In the end, the atmosphere was saturated in dihydrogen and the reaction mixture was allowed to stir for 24 h at room temperature. The catalyst was filtered over celite and washed thoroughly with MeOH. The filtrate was concentrated under vacuum to afford the desired product **14b** (89%) as a white oil.

^{1}H NMR (400 MHz, $CDCl_3$) δ (ppm): 3.84–3.44 (m, 66H), 3.38 (s, 3H), 2.86 (t, 2H, J = 5.2 Hz).

15

Synthesis of 2,5-dioxopyrrolidin-1-yl succinylferrocene (15)

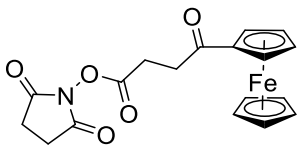

A solution of **11** (615 mg, 2.15 mmol, 1.0 equiv.), NHS (297 mg, 2.58 mmol, 1.2 equiv.) and EDC.HCl (495 mg, 2.58 mmol, 1.2 equiv.) in anhydride CH_2Cl_2 (15 mL) was stirred under argon at room temperature for 72 h. Water (15 mL) was added and the organic phase was collected, dried over $MgSO_4$, filtered and concentrated under vacuum to afford the desired molecule **15** (85%) as an orange solid.

^{1}H NMR (400 MHz, $CDCl_3$) δ (ppm): 4.82 (m, 2H), 4.52 (m, 2H), 4.23 (s, 5H), 3.17 (t, 2H, *J* = 7.6 Hz), 3.04 (t, 2H, *J* = 7.6 Hz), 2.85 (m, 4H).

16a

Synthesis of α-methoxy-ω-amino PEO2000 succinylferrocene (16a)

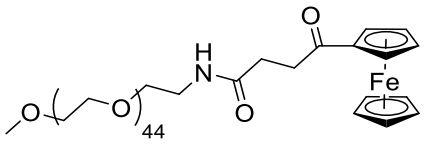

A solution of **15** (34 mg, 0.09 mmol, 1.0 equiv.), **14a** (216 mg, 0.11 mmol, 1.2 equiv.) and DMAP (23 mg, 0.19 mmol, 2.1 equiv.) in anhydrous DMF (6 mL) was stirred under argon at 90 °C for 48 h. The reaction mixture was cooled down and the solvent was evaporated under vacuum. The crude mixture was purified on silica gel (CH_2Cl_2/MeOH 90:10) to afford the desired product **16a** (24%) as an orange solid.

^{1}H NMR (400 MHz, $CDCl_3$) δ (ppm): 6.51 (s, 1H), 4.82 (m, 2H), 4.52 (m, 2H), 4.25 (s, 5H), 3.85–3.46 (m, 180), 3.40 (s, 3H), 3.13 (t, 2H, J = 6.8 Hz), 2.59 (t, 2H, J = 7.2 Hz)

16b

Synthesis of α-methoxy-ω-amino PEO750 succinylferrocene (16b)

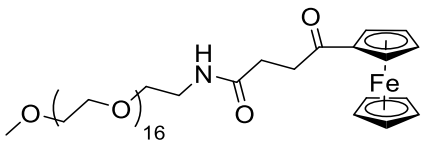

A solution of **15** (466 mg, 0.63 mmol, 1.1 equiv.), **14b** (221 mg, 0.58 mmol, 1.0 equiv.) and Et_3N (162 µL, 1.16 mmol, 2.0 equiv.) in CH_2Cl_2 (5 mL) was stirred under argon at room temperature for 17 h. The organic phase was washed with water (5 mL), dried over $MgSO_4$, filtered and evaporated under vacuum. The crude product was purified on silica gel (CH_2Cl_2/MeOH 95:5) to afford the desired product **16b** (36%) as an orange oil.

^{1}H NMR (400 MHz, $CDCl_3$) δ(ppm): 6.48 (s, 1H), 4.80 (m, 2H), 4.50 (m, 2H), 4.23 (s, 5H), 3.85–3.43 (m, 68H), 3.38 (s, 3H), 3.11 (t, 2H, *J* = 6.8 Hz), 2.57 (t, 2H, *J* = 6.8 Hz).

17

Synthesis of 4-oxo-4-(propylamino)butanoylferrocene (17)

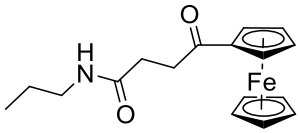

To a solution of **15** (397 mg, 1.04 mmol, 1.0 equiv.) in CH_2Cl_2 (10 mL) was added *n*-propylamine (855 µL, 10.4 mmol, 10.0 equiv.) under argon and the mixture was stirred at room temperature for 20 h. The organic phase was washed with water (10 mL), dried over $MgSO_4$, filtered and evaporated under vacuum to afford the desired molecule **17** (96%) as an orange solid.

^{1}H NMR (400 MHz, $CDCl_3$) δ (ppm): 5.90 (s, 1H), 4.80 (m, 2H), 4.51 (m, 2H), 4.22 (s, 5H), 3.22 (m, 2H), 3.12 (m, 2H), 2.55 (m, 2H), 1.53 (m, 2H), 0.93 (t, 3H, J = 7.2 Hz).

18

Synthesis of 1-(4-oxo-4-(propylamino)butanoyl)-1′-succinylferrocene (18)

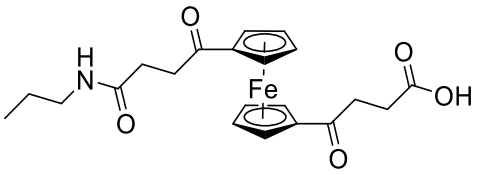

To a suspension of $AlCl_3$ (570 mg, 4.28 mmol, 8.0 equiv.) in anhydrous CH_2Cl_2 (10 mL) was added succinic anhydride (428 mg, 4.28 mmol, 8.0 equiv.) under argon and vigorous stirring at room temperature. 5 min after, a solution of **17** (175 mg, 0.54 mmol, 1.0 equiv.) in anhydrous CH_2Cl_2 (5 mL) was added to the reaction mixture at 0 °C. After addition, the reaction mixture was allowed to cool down to room temperature and was stirred for 36 h. Water (10 mL) was added and the reaction was vigorously stirred for 5 min after which the organic phase was washed with water, dried over $MgSO_4$, filtered and concentrated under vacuum. The crude product was purified on silica gel (CH_2Cl_2/MeOH 90:10) to afford molecule **18** (61%) as an orange solid.

^{1}H NMR (400 MHz, $CDCl_3$) δ (ppm): 10.73 (s, 1H), 7.14 (s, 1H), 4.92 (m, 4H), 4.66 (m, 4H), 3.17 (m, 2H), 3.03 (m, 4H), 2.64 (m, 2H), 2.49 (t, 2H, J = 6.4 Hz), 1.52 (m, 2H), 0.91 (t, 3H, J = 7.2 Hz).

19

Synthesis of 4-((2-((tert-butoxycarbonyl)-azaneyl)ethyl)amino)-4-oxobutanoylferrocene (19)

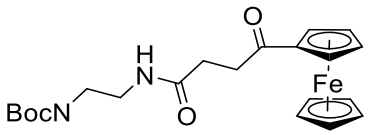

A solution of **15** (250 mg, 0.65 mmol, 1.0 equiv.) and *N*-Boc-ethylenediamine (312 mg, 1.95 mmol, 3.0 equiv.) in anhydrous CH_2Cl_2 (3 mL) was stirred under argon at room temperature for 16 h. The organic phase was washed with water (3 mL), dried over $MgSO_4$, filtered and concentrated under vacuum. The crude product was purified on silica gel (100% AcOEt) to afford the desired compound **19** (50%) as an orange solid.

^{1}H NMR (400 MHz, $CDCl_3$) δ (ppm): 6.31 (s, 1H), 5.00 (s, 1H), 4.81 (m, 2H), 4.51 (m, 2H), 4.23 (s, 5H), 3.37 (m, 2H), 3.29 (m, 2H), 3.13 (t, 2H, J = 6.4 Hz), 2.55 (t, 2H, J = 6.4 Hz), 1.45 (s, 9H).

20

Synthesis of 4-((2-hydroxyethyl)amino)-4-oxobutanoylferrocene (20)

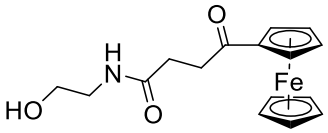

To a solution of ethanolamine (900 µL, 14.98 mmol, 20.0 equiv.) in anhydrous CH_2Cl_2 (2 mL) was added dropwise a solution of **15** (287 mg, 0.75 mmol, 1.0 equiv.) in anhydrous CH_2Cl_2 (10 mL) under argon and vigorous stirring at room temperature. After the addition, the reaction was stirred for 17 h. Water (10 mL) and CH_2Cl_2 (8 mL) were added and the reaction was stirred for an additional 5 min. The organic phase was washed with water, dried over $MgSO_4$, filtered and evaporated under vacuum to afford the desired product **20** (85%) as an orange solid.

^{1}H NMR (400 MHz, $CDCl_3$) δ (ppm): 6.37 (s, 1H), 4.80 (m, 2H), 4.52 (m, 2H), 4.23 (s, 5H), 3.74 (t, 2H, J = 5.2 Hz), 3.43 (m, 2H), 3.15 (t, 2H, J = 6.4 Hz), 2.57 (t, 2H, J = 6.4 Hz).

21

Synthesis of 4-(2-(3-carboxypropanamido)ethoxy)-4-oxobutanoylferrocene (21)

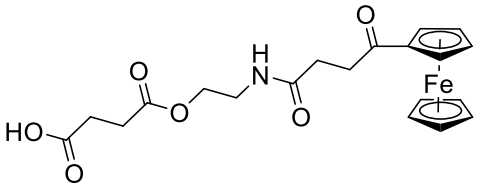

To a suspension of $AlCl_3$ (305 mg, 2.29 mmol, 4.0 equiv.) in anhydrous CH_2Cl_2 (5 mL) was added succinic anhydride (120 mg, 1.20 mmol, 2.1 equiv.) under argon and vigorous stirring at room temperature. 5 min after, a solution of **20** (188 mg, 0.57 mmol, 1.0 equiv.) in anhydrous CH_2Cl_2 (5 mL) was added dropwise to the reaction mixture at 0 °C. After addition, the reaction mixture was allowed to cool down to room temperature and was stirred for 19 h. Water (10 mL) was added and the reaction was vigorously stirred for 5 min after which the organic phase was collected, dried over $MgSO_4$, filtered and concentrated under vacuum. The crude product was purified on silica gel (CH_2Cl_2/MeOH 90:10 + 1% Et_3N) to afford molecule **21** (51%) as an orange triethylammonium salt.

^{1}H NMR (400 MHz, $CDCl_3$) δ (ppm): 7.75 (s, 1H), 4.82 (m, 2H), 4.52 (m, 2H), 4.29 (s, 5H), 4.15 (t, 2H, J = 5.6 Hz), 3.48 (q, 2H), 3.09 (t, 2H, J = 6.4 Hz), 2.51 (t, 2H, J = 6.4 Hz).

22

Synthesis of 4-oxo-4-((2-(tosyloxy)ethyl)amino)butanoylferrocene (22)

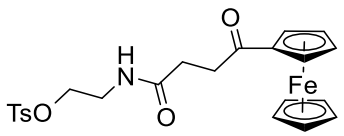

A solution of **20** (1.500 g, 4.56 mmol, 1.0 equiv.), TsCl (1.732 g, 9.12 mmol, 2.0 equiv.), DMAP (279 mg, 2.28 mmol, 0.5 equiv.) and Et_3N (1.3 mL, 9.12 mmol, 2.0 equiv.) in CH_2Cl_2 (40 mL) was stirred under argon at room temperature for 72 h. The organic phase was washed with water (40 mL), dried over $MgSO_4$, filtered and concentrated under vacuum. The crude product was purified on silica gel (Cy/AcOEt 50:50) to afford the desired product **22** (43%) as an orange solid.

^{1}H NMR (400 MHz, $CDCl_3$) δ (ppm): 7.81 (d, 2H, *J* = 8.0 Hz), 7.31 (d, 2H, *J* = 8.0 Hz), 5.26 (s, 1H), 4.82 (m, 2H), 4.54 (m, 2H), 4.26 (s, 5H), 4.21 (t, 2H, *J* = 5.6 Hz), 3.25 (m, 2H), 3.10 (t, 2H, *J* = 5.6 Hz), 2.61 (m, 2H), 2.43 (s, 3H).

23

Synthesis of 1-(4-oxo-4-((2-(tosyloxy)ethyl)amino)butanoyl)-1'-succinylferrocene (23)

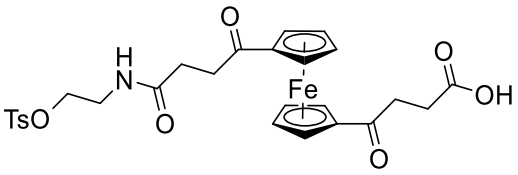

To a suspension of $AlCl_3$ (340 mg, 2.55 mmol, 8.0 equiv.) in anhydrous CH_2Cl_2 (3 mL) was added succinic anhydride (255 mg, 2.55 mmol, 8.0 equiv.) under argon and vigorous stirring at room temperature. 5 min after, a solution of **22** (154 mg, 0.32 mmol, 1.0 equiv.) in anhydrous CH_2Cl_2 (4 mL) was added dropwise to the reaction mixture at 0 °C. After addition, the reaction mixture was allowed to cool down to room temperature and was stirred for 24 h. Water (10 mL) was added and the reaction was vigorously stirred for 5 min after which the organic phase was collected, dried over $MgSO_4$, filtered and concentrated under vacuum. The crude product was purified on silica gel (CH_2Cl_2/MeOH 90:10 then 80:20) to afford molecule **23** (51%) as an orange solid.

^{1}H NMR (400 MHz, acetone-d_6) δ (ppm): 10.70 (s, 1H), 7.80 (d, 2H, J = 8.0 Hz), 7.41 (d, 2H, J = 8.0 Hz), 4.94 (m, 4H), 4.65 (m, 4H), 4.15 (t, 2H, J = 5.6 Hz), 3.07 (m, 4H), 2.66 (m, 2H), 2.43 (s, 3H).

24

Synthesis of 1-(4-oxo-4-((2-(tosyloxy)ethyl)amino)butanoyl)-1′- (4-((2,5-dioxopyrrolidin-1-yl)oxy))-4-oxobutanoylferrocene (24)

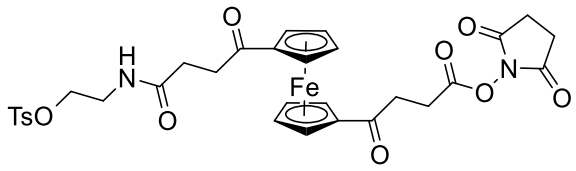

A solution of **23** (556 mg, 0.95 mmol, 1.0 equiv.), NHS (274 mg, 1.43 mmol, 1.5 equiv.) and EDC.HCl (165 mg, 1.43 mmol, 1.5 equiv.) in anhydrous CH_2Cl_2 (15 mL) was stirred under argon at room temperature for 19 h. The organic phase was washed with water (15 mL), dried over $MgSO_4$, filtered and concentrated under vacuum to afford the desired molecule **24** (36%) as an orange solid.

^{1}H NMR (400 MHz, $CDCl_3$) δ (ppm): 7.76 (d, 2H, *J* = 8.0 Hz), 7.31 (d, 2H, *J* = 8.0 Hz), 5.50 (s, 1H), 4.19 (t, 2H, *J* = 5.2 Hz), 3.26 (m, 2H), 3.11 (m, 2H), 3.00 (m, 6H), 2.83 (m, 4H), 2.75 (m, 2H), 2.64 (m, 2H), 2.42 (s, 3H).

25

Synthesis of 2,5-dioxopyrrolidin-1-yl pentacosa-10,12-diynoate (25)

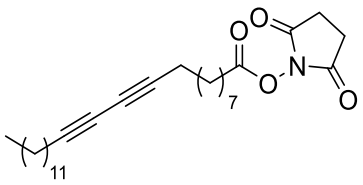

A solution of 10,12-pentacosadiynoic acid (1.0 g, 2.67 mmol, 1.0 equiv.), NHS (350 mg, 3.04 mmol, 1.1 equiv.) and EDC.HCl (600 mg, 3.13 mmol, 1.2 equiv.) in anhydrous CH_2Cl_2 (25 mL) under argon was stirred at room temperature for 18 h. The organic phase was washed with water (20 mL), dried over $MgSO_4$, filtered and concentrated under vacuum to afford **25** (96%) as a white solid.

^{1}H NMR (400 MHz, $CDCl_3$) δ (ppm): 2.84 (m, 4H), 2.60 (t, 2H, J = 7.6 Hz), 2.24 (t, 4H, J = 6.8 Hz), 1.74 (m, 2H), 1.45 (m, 4H), 1.45–1.15 (m, 26), 0.88 (t, 3H, J = 6.4 Hz).

26

Synthesis of *N*-(2-aminoethyl)pentacosa-10,12-diynamide (26)

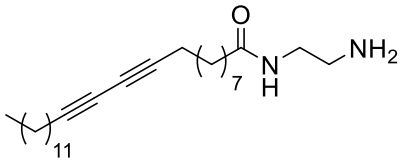

To a solution of ethylenediamine (1.34 mL, 20.10 mmol, 19.0 equiv.) in anhydrous CH_2Cl_2 (3 mL) was added dropwise a solution of **25** (500 mg, 1.06 mmol, 1.0 equiv.) in anhydrous CH_2Cl_2 (5 mL) under argon and vigorous stirring at room temperature. After addition, the reaction was stirred for 17 h. Water (20 mL) and CH_2Cl_2 (15 mL) were added to the stirred mixture and the organic phase was collected, dried over $MgSO_4$, filtered and concentrated under vacuum to afford the compound **26** (72%) as a white solid.

^{1}H NMR (400 MHz, $CDCl_3$) δ (ppm): 5.88 (s, 1H), 3.31 (m, 2H), 2.83 (t, 2H, J = 6.0 Hz), 2.22 (m, 6H), 1.62 (m, 2H), 1.50 (m, 4H), 1.42–1.08 (m, 26H), 0.88 (t, 3H, J = 6.8 Hz).

27

Synthesis of 1-(4-oxo-4-((2-(tosyloxy)ethyl)amino)butanoyl)-1′-(4-oxo-4-((2-(pentacosa-10,12-diynamido)ethyl)amino)butanoyl)ferrocene (27)

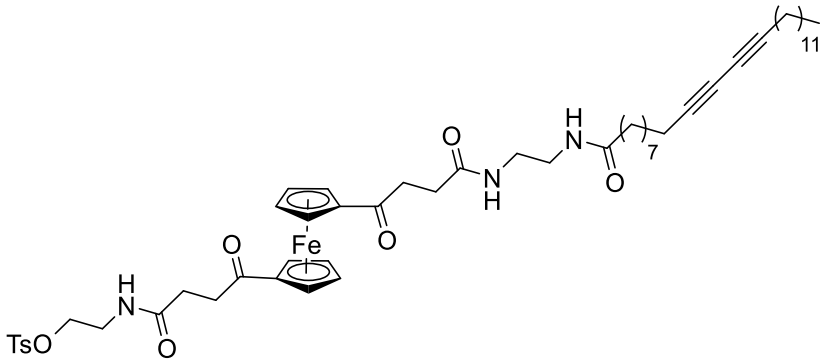

A solution of **24** (230 mg, 0.34 mmol, 1.0 equiv.), **26** (227 mg, 0.54 mmol, 1.6 equiv.) and Et_3N (300 µL, 2.15 mmol, 6.3 equiv.) in anhydrous DMF (4 mL) was stirred under argon at 90 °C for 48 h. The reaction was cooled down to room temperature and CH_2Cl_2 (50 mL) and water (50 mL) were added. After mixing and decantation, the organic phase was collected, dried over $MgSO_4$, filtered and evaporated under vacuum. The crude product was purified on silica gel (Cy/AcOEt 90:10) to afford compound **27** (37%) as an orange solid.

^{1}H NMR (400 MHz, $CDCl_3$) δ (ppm): 7.79 (d, 2H, *J* = 8.0 Hz), 7.31 (d, 2H, *J* = 8.0 Hz), 6.57 (s, 1H), 6.45 (s, 1H), 6.20 (s, 1H), 4.87 (m, 4H), 4.59 (m, 4H), 4.21 (m, 2H), 3.27 (m, 2H), 3.02 (m, 4H), 2.71–2.54 (m, 6H), 2.46 (t, 2H, *J* = 6.8 Hz), 2.42 (s, 3H), 2.27–2.12 (m, 6H), 1.60 (m, 2H), 1.50 (m, 4H), 1.43–1.10 (m, 26H), 0.88 (t, 3H, *J* = 6.4 Hz).

28

Synthesis of *N*-(2-hydroxyethyl)carbamoylferrocene

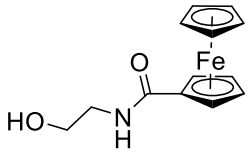

To a solution of ethanolamine (2.40 mL, 39.75 mmol, 20.0 equiv.) in anhydrous CH_2Cl_2 (2 mL) was added dropwise a solution of **8** (650 mg, 1.99 mmol, 1.0 equiv.) under argon and vigorous stirring at room temperature. After addition, the reaction was stirred for 48 h. CH_2Cl_2 (10 mL) and water (10 mL) were added, after mixing and decantation, the organic phase was collected, dried over $MgSO_4$, filtered and evaporated under vacuum. The crude product was purified on silica gel (CH_2Cl_2/MeOH 90:10) to afford the desired product **28** (60%) as an orange solid.

^{1}H NMR (400 MHz, $CDCl_3$) δ (ppm): 6.22 (s, 1H), 4.68 (m, 2H), 4.36 (m, 2H), 4.21 (s, 5H), 3.81 (m, 2H), 3.56 (m, 2H).

29

Synthesis of *N*-(2-ethyl 4-methylbenzenesulfonate)carbamoylferrocene (29)

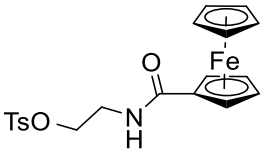

A solution of **28** (327 mg, 1.20 mmol, 1.0 equiv.), TsCl (683 mg, 3.59 mmol, 3.0 equiv.) and Et_3N (500 µL, 3.59 mmol, 3.0 equiv.) in anhydrous CH_2Cl_2 (10 mL) was stirred under argon for 48 h at room temperature. The organic phase was washed with water (10 mL), dried over $MgSO_4$, filtered and evaporated under vacuum. The crude product was purified on silica gel (100% CH_2Cl_2) to afford the desired compound **29** (26%) as an orange solid.

^{1}H NMR (400 MHz, $CDCl_3$) δ (ppm): 7.89 (d, 2H, *J* = 8.0 Hz), 7.34 (d, 2H, *J* = 8.0 Hz), 4.77 (m, 2H), 4.48 (m, 2H), 4.19 (m, 7H), 3.78 (t, 2H, *J* = 7.2 Hz), 2.43 (s, 3H).

30

Synthesis of 1-(*N*-(2-ethyl 4-methylbenzenesulfonate)carbamoyl)-1′-succinylferrocene (30)

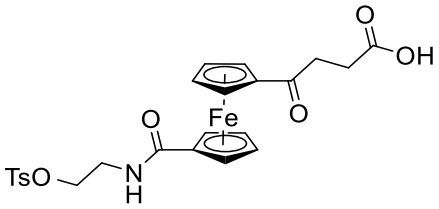

To a suspension of $AlCl_3$ (164 mg, 1.29 mmol, 4.0 equiv.) in anhydrous CH_2Cl_2 (2 mL) was added succinic anhydride (129 mg, 1.29 mmol, 4.0 equiv.) under argon and vigorous stirring at room temperature. 5 min after, a solution of **29** (131 mg, 0.31 mmol, 1.0 equiv.) in anhydrous CH_2Cl_2 (4 mL) was added dropwise to the reaction mixture at 0 °C. After addition, the reaction mixture was allowed to cool down to room temperature and was stirred for 24 h. Water (10 mL) was added and the reaction was vigorously stirred for 5 min after which the organic phase was collected, dried over $MgSO_4$, filtered and concentrated under vacuum. The crude product was purified on silica gel (CH_2Cl_2/MeOH 90:10) to afford molecule **30** (89%) as an orange solid.

^{1}H NMR (400 MHz, $CDCl_3$) δ (ppm): 7.87 (d, 2H, *J* = 8.0 Hz), 7.35 (d, 2H, *J* = 8.0 Hz), 4.80 (m, 4H), 4.51 (m, 4H), 4.14 (t, 2H, *J* = 6.8 Hz) 3.73 (t, 2H, *J* = 6.8 Hz), 3.08 (m, 2H), 2.75 (m, 2H), 2.44 (s, 3H).

31

Synthesis of 1-(*N*-(2-ethyl 4-methylbenzenesulfonate)carbamoyl)-1'-(4-((2,5-dioxopyrrolidin-1-yl)oxy)-4-oxobutanoyl)ferrocene (31)

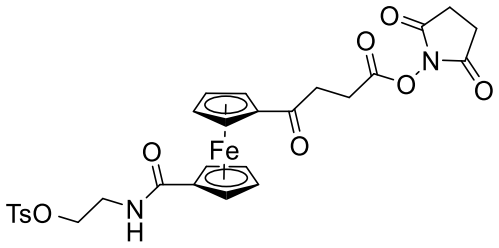

A solution of **30** (55 mg, 0.10 mmol, 1.0 equiv.), NHS (18 mg, 0.16 mmol, 1.5 equiv.) and EDC.HCl (31 mg, 0.16 mmol, 1.5 equiv.) in anhydrous CH_2Cl_2 (2 mL) was stirred under argon at room temperature for 5 h. Water (10 mL) and CH_2Cl_2 (8 mL) were added and, after mixing and decantation, the organic phase was collected, dried over $MgSO_4$, filtered and concentrated under vacuum to afford the desired compound **31** (89%) as an orange solid.

^{1}H NMR (400 MHz, $CDCl_3$) δ (ppm): 7.85 (d, 2H, *J* = 8.0 Hz), 7.35 (d, 2H, *J* = 8.0 Hz), 4.78 (m, 4H), 4.50 (m, 4H), 4.11 (t, 2H, *J* = 6.8 Hz) 3.74 (t, 2H, *J* = 6.8 Hz), 3.14 (t, 2H, *J* = 6.8 Hz), 3.01 (t, 2H, *J* = 6.8 Hz), 2.86 (m, 4H), 2.44 (s, 3H).

32

Synthesis of 1-(*N*-(2-ethyl 4-methylbenzenesulfonate)carbamoyl)-1′-(α-methoxy-ω-amino PEO2000)-oxobutanoylferrocene (32)

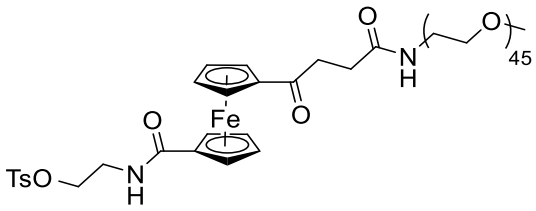

A solution of **31** (55 mg, 0.09 mmol, 1.0 equiv.) and **14a** (247 mg, 0.12 mmol, 1.4 equiv.) in anhydrous CH_2Cl_2 (2 mL) was stirred under argon at room temperature for 17 h. The solvent was evaporated under vacuum and the crude product was purified on silica gel (CH_2Cl_2/MeOH 90:10) to afford the desired product **32** (26%) as an orange solid.

^{1}H NMR (400 MHz, $CDCl_3$) δ (ppm): 7.86 (d, 2H, *J* = 8.0 Hz), 7.34 (d, 2H, *J* = 8.0 Hz), 6.37 (s, 1H), 4.81 (m, 4H), 4.51 (m, 4H), 4.15 (t, 2H, *J* = 6.8 Hz), 3.86–3.44 (m, 182H), 3.38 (s, 3H), 3.07 (t, 2H, *J* = 6.8 Hz), 2.55 (t, 2H, *J* = 6.8 Hz), 2.43 (s, 3H).

33

Synthesis of 10,12-pentacosadiyn-1-ol (33)

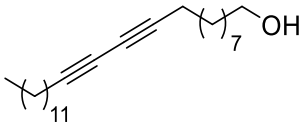

To a solution of 10,12-pentacosadiynoic acid (1.0 g, 2.67 mmol, 1.0 equiv.) in anhydrous Et_2O (44 mL) was added in small portion $LiAlH_4$ (200 mg, 5.27 mmol, 2.0 equiv.) under vigorous stirring at 0 °C. 5 min after addition of $LiAlH_4$, the reaction was stirred at room temperature for 1.5 h. Then, successive additions of water (200 µL), 15% NaOH (200 µL) and water (600 µL) again under vigorous stirring at 0 °C quenched the remaining $LiAlH_4$. The precipitate was filtered over celite and washed thoroughly with Et_2O. 1M HCl was added to the filtrate and the biphasic mixture was stirred for 1 min. The organic phase was collected, dried over $MgSO_4$, filtered and concentrated under vacuum to afford the desired product **33** (81%) as a white solid.

^{1}H NMR (400 MHz, $CDCl_3$) δ (ppm): 3.63 (m, 2H), 2.24 (t, 4H, J = 6.8 Hz), 1.53 (m, 6H), 1.43–1.16 (m, 28H), 0.88 (t, 3H, J = 6.4 Hz).

34

Synthesis of 1,1′-bis(2,5-dioxopyrrolidin-1-yl carboxyl)ferrocene (34)

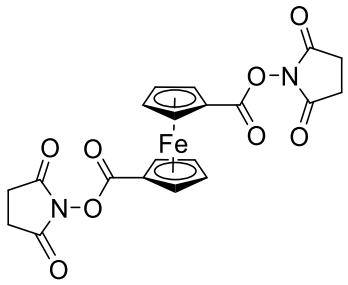

To a suspension of 1,1′-ferrocenedicarboxylic acid (100 mg, 0.36 mmol, 1.0 equiv.) in ACN (5 mL) was added Et_3N (200 µL, 1.43 mmol, 4.0 equiv.) under stirring at room temperature. After 5 min, *N,N*-disuccinimidyl carbonate (200 mg, 0.78 mmol, 2.2 equiv.) was added to the solution. The reaction was stirred for 6 h. Water (10 mL) was added and the reaction was stirred for an additional 5 min. A precipitate formed and was filtered, washed with water, ACN then *n*-hexane. The resulting solid was dried in the oven at 100 °C for at least 30 min to afford the desired product **34** (70%) as an orange solid.

^{1}H NMR (400 MHz, DMSO-d_6) δ (ppm): 5.16 (m, 4H), 4.92 (m, 4H), 2.88 (m, 8H).

^{13}C NMR (100 MHz, DMSO-d_6) δ (ppm): 170.5, 165.8, 75.7, 72.5, 66.2, 25.5.

FT-IR (cm^{-1}): 1761, 1726, 1072.

35

Synthesis of 1-(*N*-(2-(pentacosa-10,12-diynamido)ethyl)carbamoyl)-1′-(2,5-dioxopyrrolidin-1-yl carboxyl)ferrocene (35)

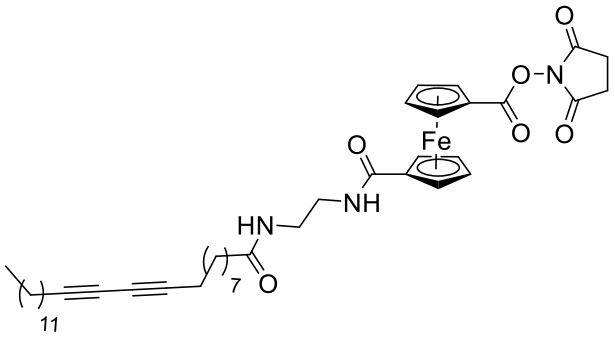

To a solution of **34** (150 mg, 0.32 mmol, 1.0 equiv.) in anhydrous DMF (3 mL) was added dropwise a solution of **26** (134 mg, 0.32 mmol, 1.0 equiv.) in anhydrous DMF (2 mL) under argon and vigorous stirring at room temperature. After addition, the reaction was stirred for 72 h. The solvent was evaporated under vacuum and the residue was solubilized in CH_2Cl_2 (15 mL). The organic phase was washed with water (15 mL), dried over $MgSO_4$, filtered and concentrated under vacuum. The crude product was purified on silica gel (100% AcOEt) to afford the desired compound **35** (13%) as an orange solid.

^{1}H NMR (400 MHz, $CDCl_3$) δ (ppm): 7.05 (s, 1H), 6.29 (s, 1H), 4.90 (m, 2H), 4.81 (m, 2H), 4.67 (m, 2H), 4.50 (m, 2H), 3.41 (m, 4H), 2.96 (m, 4H), 2.24 (m, 4H), 2.16 (t, 2H, *J* = 7.6 Hz), 1.60 (m, 2H), 1.49 (m, 4H), 1.42–1.14 (m, 26H), 0.88 (t, 3H, *J* = 6.4 Hz).

36

Synthesis of 1-(*N*-(2-(tricosa-10,12-diynamido)ethyl)carbamoyl)-1′-(α-methoxy-ω-amino PEO2000) ferrocene (36)

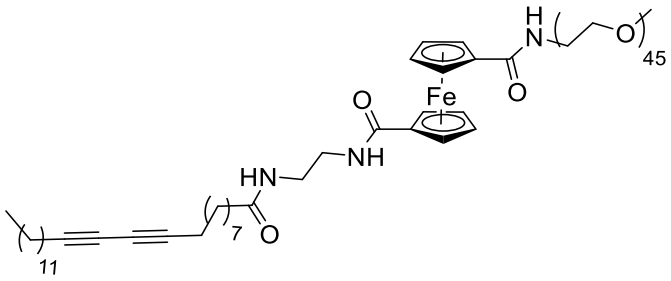

A solution of **35** (30 mg, 0.04 mmol, 1.0 equiv.), **14a** (157 mg, 0.08 mmol, 2.0 equiv.) and Et_3N (100 µL, 0.72 mmol, 18.0 equiv.) in anhydrous CH_2Cl_2 (4 mL) was stirred under argon at room temperature for 17 h. The solvent was evaporated under vacuum and the crude product was purified on silica gel (CH_2Cl_2/MeOH 90:10) to afford the compound **36** (69%) as an orange solid.

^{1}H NMR (400 MHz, $CDCl_3$) δ(ppm): 7.55 (s, 1H), 6.93 (s, 1H), 4.55 (m, 4H), 4.41 (m, 4H), 3.84–3.42 (m, 184H), 3.38 (s, 3H), 2.22 (m, 6H), 1.63 (m, 2H), 1.48 (m, 4H), 1.40–1.12 (m, 26H), 0.88 (t, 3H, J = 6.8 Hz).

Synthesis of 10,12-pentacosadiynoyl-α-methoxy-ω-amino PEO2000 (37)

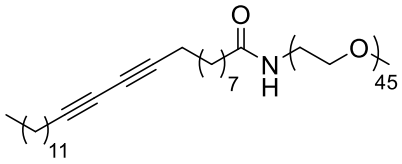

A solution of **25** (100 mg, 0.21 mmol, 1.0 equiv.) and **14a** (507 mg, 0.25 mmol, 1.2 equiv.) in anhydrous CH_2Cl_2 (4 mL) was stirred under argon at room temperature for 16 h. The solvent was evaporated under vacuum and the crude product was purified on silica gel (CH_2Cl_2/MeOH 90:10) to afford the desired product **37** (43%) as a white solid.

^{1}H NMR (400 MHz, $CDCl_3$) δ (ppm): 6.07 (m, 1H), 3.85–3.41 (m, 180H), 3.38 (s, 3H), 2.23 (t, 4H, *J* = 6.8 Hz), 2.16 (t, 2H, *J* = 6.8 Hz), 1.61 (m, 2H), 1.50 (m, 4H), 1.44–1.17 (m, 26H), 0.88 (t, 3H, *J* = 6.8 Hz).

38

Synthesis of 1-stearoyl-1′-(2,5-dioxopyrrolidin-1-yl carboxyl)ferrocene (38)

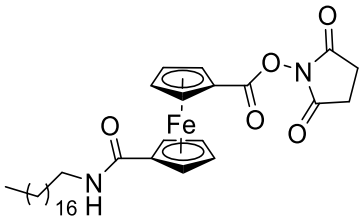

A solution of **34** (166 mg, 0.37 mmol, 1.0 equiv.) and Et_3N (250 µL, 1.79 mmol, 4.8 equiv.) in anhydrous $HCCl_3$ (30 mL) under argon and stirring was heated to 40 °C. After 10 min, *n*-octadecylamine (99 mg, 0.37 mmol, 1.0 equiv.) was added in one portion and the reaction was stirred vigorously for 19 h. The solvent was evaporated under vacuum and the crude product was purified on silica gel (Cy/AcOEt 60:40) to afford the desired product **38** (56%) as a yellow solid.

^{1}H NMR (400 MHz, $CDCl_3$) δ(ppm): 6.60 (s, 1H), 4.88 (m, 2H), 4.83 (m, 2H), 4.67 (m, 2H), 4.47 (m, 2H), 3.31 (m, 2H), 2.95 (m, 4H), 1.52 (m, 2H), 1.40–1.19 (m, 30H), 0.88 (t, 3H, J = 6.8 Hz).

^{13}C NMR (100 MHz, $CDCl_3$) δ(ppm): 169.5, 169.8, 166.3, 78.4, 73.5, 72.2, 71.4, 70.7, 70.3, 64.9, 39.3, 31.3, 29.2, 29.0, 26.5, 25.2, 22.2, 13.6.

FT-IR (cm^{-1}): 2918, 2850, 1770, 1741, 1076.

39

Synthesis of 1-stearoyl-1′-(α-methoxy-ω-amino PEO2000) ferrocene (39)

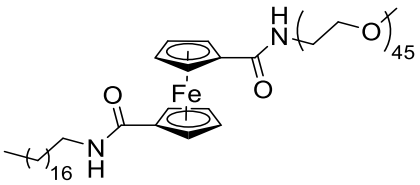

A solution of **38** (50 mg, 0.08 mmol, 1.0 equiv.), **14a** (321 mg, 0.16 mmol, 2.0 equiv.) and Et_3N (100 µL, 0.72 mmol, 9.0 equiv.) in anhydrous CH_2Cl_2 (3 mL) was stirred under argon at room temperature for 18 h. The solvent was evaporated under vacuum and the crude product was purified on silica gel (CH_2Cl_2/MeOH 90:10) to afford compound **39** (78%) as an orange solid.

^{1}H NMR (400 MHz, $CDCl_3$) δ (ppm): 7.10 (s, 1H), 7.03 (s, 1H), 4.57 (m, 2H), 4.52 (m, 2H), 4.36 (m, 2H), 4.35 (m, 2H), 3.84–3.51 (m, 180H), 3.37 (m, 5H), 1.64 (m, 2H), 1.48–1.18 (m, 30H), 0.88 (t, 3H, J = 6.8 Hz).

^{13}C NMR (100 MHz, $CDCl_3$) δ (ppm): 72.1, 71.3, 71.0, 70.8, 59.2, 40.1, 32.0, 30.0, 29.8, 22.9, 14.2.

FT-IR (cm^{-1}): 2883, 1101, 962, 841.

HR-MS (ESI-TOF) calcd for $C_{121}H_{230}FeN_2O_{47}$+2Na $[M+Na]^{2+}$ 1282.7415, found 1282.7410.

SEC ($HCCl_3$): M_n = 2345, M_w = 2415, $Đ$ = 1.03

40

Synthesis of 2,5-dioxopyrrolidin-1-yl heptadecanoate (40)

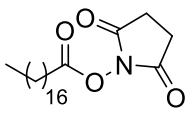

A solution of stearic acid (1.0 g, 3.51 mmol, 1.0 equiv.), NHS (606 mg, 5.27 mmol, 1.5 equiv.) and EDC.HCl (1.01 g, 5.27 mmol, 1.5 equiv.) in anhydrous 3:1 THF/CH_2Cl_2 (20 mL) was stirred under argon at room temperature for 18 h. The solvent was evaporated under vacuum and the crude product was solubilized in CH_2Cl_2 (20 mL). Water (20 mL) was added and, after mixing and decantation, the organic phase was collected, dried over $MgSO_4$, filtered and concentrated under vacuum to afford the desired product **40** (78%) as a white solid.

^{1}H NMR (400 MHz, $CDCl_3$) δ (ppm): 2.83 (m, 4H), 2.60 (t, 2H, J = 7.2 Hz), 1.74 (m, 2H), 1.40 (m, 2H), 1.36–1.21 (m, 26H), 0.88 (t, 3H, J = 6.8 Hz).

^{13}C NMR (100 MHz, $CDCl_3$) δ (ppm): 169.3, 168.8, 32.1, 31.1, 29.8, 29.7, 29.5, 29.2, 28.9, 25.7, 24.7, 22.8.

FT-IR (cm^{-1}): 2918, 2848, 1785, 1724, 1070.

41

Synthesis of stearoyl-α-methoxy-ω-amino PEO 2000 (41)

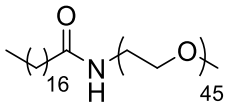

A solution of **40** (50 mg, 0.13 mmol, 1.0 equiv.), **14a** (383 mg, 0.19 mmol, 1.5 equiv.) and Et_3N (100 µL, 0.72 mmol, 5.5 equiv.) in anhydrous CH_2Cl_2 (3 mL) was stirred under argon at room temperature for 17 h. The solvent was evaporated under vacuum and the crude product was purified on silica gel (CH_2Cl_2/MeOH 90:10) to afford the compound **41** (61%) as a white solid.

^{1}H NMR (400 MHz, $CDCl_3$) δ (ppm): 6.18 (s, 1H), 3.81–3.45 (m, 180H), 3.37 (s, 3H), 2.16 (t, 2H, J = 7.6 Hz), 1.61 (m, 2H), 1.34–1.20 (m, 28H), 0.88 (t, 3H, J = 6.8 Hz).

^{13}C NMR (100 MHz, $CDCl_3$) δ (ppm): 171.9, 71.4, 70.0, 69.6, 69.4, 58.5, 38.7, 36.1, 31.4, 29.2, 29.0, 28.9, 28.8, 24.9, 22.2, 13.6.

FT-IR (cm^{-1}): 2885, 1639, 1554, 1101.

ESI-MS calcd for $C_{109}H_{219}NO_{46}$ $[M]^{2+}$ 1139.9421, found 1140.1431.

SEC ($HCCl_3$): M_n = 2265, M_w = 2337, $Đ$ = 1.03

CHAPTER 2

Synthesis of *meso*-Tetraphenylbacteriochlorin (42)

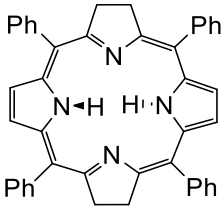

A solution of *meso*-Tetraphenylporphyrin (1.16 mmol, 100 mg, 1.0 equiv.), anhydrous Na_2CO_3 (3.96 mmol, 420 mg, 24.0 equiv.) and tosyl hydrazide (1.63 mmol, 304 mg, 10.0 equiv.) in anhydrous pyridine (7.5 mL) was stirred and heated at 100 °C for 12 h under nitrogen. The mixture was allowed to cool down to room temperature. Benzene (100 mL) and water (50 mL) were added. The organic phase was washed in the following order with 3N HCl, H_3PO_4 85%, saturated $NaHCO_3$ and water. All washes were done 5 times per reagent except for HCl which was performed once. 50 mL was used each time. The organic layer was dried over $MgSO_4$, filtered and concentrated under vacuum. TPBC was obtained as a purple solid (66% yield). The UV-vis spectrum is in accordance with the litterature, showing no presence of TPP or tetraphenylchlorin (TPC).

^{1}H NMR (400 MHz, $CDCl_3$) δ (ppm): 7.82 (m, 4H), 7.70 (m, 8H), 7.51 (m, 12H), 3.87 (s, 8H).

Encapsulation of NR, TPBC and DPBF in C_{18}-Fc-PEO and C_{18}-PEO micelles

The values of molar extinction coefficient ε (M^{-1} cm^{-1}) were taken from the literature: ε(NR) = 28900,[343] ε(TPBC) = 120000,[291]291 ε(DPBF) = 18000[344]

Preparation of NR@C18-Fc-PEO and NR@C18-PEO. Micelles solutions were prepared in order to obtain a concentration of 4 mM in 2 mL. The quantities were as follow: C_{18}-Fc-PEO (20 mg) and C_{18}-PEO (18 mg). Respectively, 400 µL and 360 µL of a NR solution (1 mg mL^{-1}) in chloroform (1 mL) were introduced in the micelle solution. The mixture was sonicated using an ultrasound sonicator probe (power 40%, 10 min, pulse) allowing NR to be gradually encapsulated by evaporation of chloroform via heating of the probe. The resulting solution was filtered on 0.45 µm nylon filter to eliminate any unloaded NR in solution.

NR@C18-Fc-PEO (EE = 19%, DL = 0.3%) and NR@C_{18}-PEO (EE = 7%, DL = 0.1%).

Preparation of DPBF@C18-PEO and TPBC@C18-PEO. To a solution of C_{18}-Fc-PEO (10 mg mL^{-1}) in water (1 mL) was added a solution of TPBC or DPBF (12.5 µL, 1 mg mL^{-1}) in chloroform (1 mL). The mixture was sonicated using an ultrasound sonicator probe (power 40%, 10 min, pulse) allowing TPBC or DPBF to be gradually encapsulated by evaporation of chloroform via heating of the probe. The resulting colloidal solution was filtered on 0.45 µm nylon filter to eliminate any unloaded TPBC or DPBF in solution.

DPBF@C_{18}-PEO (EE = 70%, DL = 0.09%) and TPBC@C_{18}-PEO (EE = 30%, DL = 0.04%).

Preparation of TPBC@C18-Fc-PEO. To a solution of C18-Fc-PEO (10 mg mL^{-1}) in water (1 mL) was added a solution of TPBC (25 µL, 1 mg mL^{-1}) in chloroform (1 mL). The mixture was sonicated using an ultrasound sonicator probe (power 40%, 10 min, pulse) allowing TPBC to be gradually encapsulated by evaporation of chloroform via heating of the probe. The resulting

[343] M. Hornum et al., Photochemical and Photobiological Sciences **2020**, 19, 1382–1391. https://doi.org/10.1039/d0pp00076k.
[344] A. Ogunsipe et al., Journal of. Molecular Structure, **2003**, 650, 131–140. https://doi.org/10.1016/S0022-2860(03)00155-8.

TPBC@C_{18}-Fc-PEO colloidal solution was filtered on 0.45 µm nylon filter to eliminate any unloaded TPBC in solution.

TPBC@C_{18}-Fc-PEO (EE = 19%, DL = 0.05%).

Preparation of TPBC-DPBF@C18-PEO. To a solution of C_{18}-Fc-PEO (10 mg mL^{-1}) in water (1 mL) was added a solution of TPBC (12.5 µL, 1 mg mL^{-1}) in chloroform (1 mL). The mixture was sonicated using an ultrasound sonicator probe (power 40%, 10 min, pulse) allowing TPBC to be gradually encapsulated by evaporation of chloroform via heating of the probe. The resulting TPBC@C_{18}-Fc-PEO colloidal solution was filtered on 0.45 µm nylon filter to eliminate any unloaded TPBC in solution. To this solution was then added a solution of DPBF (50 µL, 1 mg mL^{-1}) in chloroform (1 mL). The resulting mixture was sonicated in the same conditions as previously. After filtration on a 0.45 µm nylon filter, TPBC-DPBF@C_{18}-PEO micelles were obtained.

TPBC-DPBF@C_{18}-PEO (EE_{TPBC} = 30%, DL_{TPBC} = 0.04%, EE_{DPBF} = 44%, DL_{DPBF} = 0.2%).

Cell culture

MCF-7 (human breast adenocarcinoma cell line) cells were routinely maintained in DMEM (Sigma) supplemented with 10% (*v/v*) Fetal Bovine Serum (PAA), Sodium Pyruvate 1 mM (Sigma), Penicllin (100 U mL^{-1}, Sigma) and Streptomycin (100 µg mL^{-1}, Sigma). For all cell-based experiments, MCF-7 cells suspended in culture medium were seeded at a final density of 1500 cells per well (100µL per well) into the wells of an optical black-walled, clear bottom 96-well culture microplate (Costar, #3904), pre-coated with rat tail collagen (Sigma).

Cell proliferation/Survival assay

24 h post-seeding in 96-well plates, cells were treated with C_{18}-PEO or C_{18}-Fc-PEO micelles (or vehicle) at the indicated final concentrations. Cells were then incubated for 1 h at 37 °C, before replacing culture supernatants with 100 µL of fresh medium. Cells destined to be illuminated were immediately exposed to blue light (460 nm, Kessil, Tuna Blue Led Lamp #A160WE) for 10 min, while non-illuminated cells were maintained at room temperature and protected from

light. Cells were then returned to the incubator. 72 h post micelle treatment, cells were fixed with 4% (*w/v*) formaldehyde solution (36% formaldehyde, Sigma, #47608-1L-F) diluted in PBS with Ca^{2+} and Mg^{2+} (Sigma, #D8662) and containing Hoechst 33342 (2 µg mL^{-1} final, Sigma, #B2261). The plates were then sealed with aluminium adhesive foils (Corning®, #6569) and incubated overnight at 4 °C. Supernatants were then replaced with 200 µL of PBS with Ca^{2+} and Mg^{2+} and wells were imaged using a high-content screening epifluorescence microscope (Operetta, PerkinElmer). The culture wells were acquired with nine fields per well at a 10× magnification in the blue fluorescence channel (λ_{ex} = 380 ± 20 nm; λ_{em} = 445 ± 35 nm). For image quantification, an automated segmentation and quantification algorithm was developed using Harmony 3.0 software (PerkinElmer). Briefly, the algorithm segments the nuclear Regions of Interest (ROI) based on Hoechst fluorescence, and then quantifies the number of cells per field and per well. Results are normalized to untreated wells and expressed as mean ± standard deviation per condition.

CellRox assay

72 h post seeding in 96-well plates, cells were treated with C_{18}-PEO or C_{18}-Fc-PEO micelles (or vehicle) to a final concentration of 100 µM. Cells were incubated for 1 h at 37 °C, before replacing the culture supernatants with 100 µL of fresh medium. Cells destined to be illuminated were immediately exposed to blue light (460 nm, Kessil, Tuna Blue Led Lamp #A160WE) for 10 min, while non-illuminated cells were maintained at room temperature and protected from light. Immediately after light exposure, culture wells were treated with CellROX reagent diluted in complete culture medium (final CellROX concentration: 5 µM). The cells were then incubated for 8 h at 37 °C. 30 min before the end of the incubation, all wells were treated with Hoechst 33342 (2 µg mL^{-1}, Sigma), and control wells were treated with hydrogen peroxide (H_2O_2, Sigma, #95321) at a final concentration of 1 mM. 8 h after CellROX treatment, the supernatants from the wells were replaced with 200 µL of ice-cold PBS with Ca^{2+} and Mg^{2+}. Culture plates were immediately imaged using a high-content screening epifluorescence microscope (Operetta, PerkinElmer). Nine fields were acquired per well at 10× magnification, each field acquired in the blue (λ_{ex} = 380 ± 20 nm; λ_{em} = 445 ± 35 nm) and far-red (λ_{ex} = 630 ± 10 nm; λ_{em} = 705 ± 55 nm) fluorescence channels for Hoechst and CellROX imaging, respectively. For image quantification, an automated segmentation and quantification

algorithm was developed using Harmony 3.0 (PerkinElmer). Briefly, the algorithm was designed to segment nuclear ROIs based on Hoechst fluorescence. An artificial cytoplasm was then extended around the nuclei, within which the integrated cytoplasmic CellROX signal was quantified cell by cell. The results were expressed as average cytoplasmic fluorescence intensities (arbitrary units) per well. All results were normalized to untreated (vehicle) wells and expressed as mean ± standard deviation per condition.

Internalization assay

72 h post-seeding in 96-well plates, MCF7 cells were treated with C_{18}-PEO or C_{18}-Fc-PEO micelles (loaded or not with Nile Red) at the indicated final concentrations, and cells were incubated for 1 h at 37 °C. Supernatants were then removed and cells fixed with 4% (*w*/*v*) formaldehyde diluted in PBS with Ca^{2+} and Mg^{2+}, and containing 2 µg mL^{-1} of Hoechst 33342. After 20 min, the fixation solution was replaced with 200 µL of PBS with Ca^{2+} and Mg^{2+}. For cellular fluorescence quantification, the culture plates were imaged using a high-content screening epifluorescence microscope (Operetta, PerkinElmer). The culture wells were acquired with nine fields per well at a 10× magnification in the blue (λ_{ex} = 380 ± 20 nm; λ_{em} = 445 ± 35 nm) and red (λ_{ex} = 535 ± 15 nm; λ_{em} = 595 ± 35 nm) fluorescence channels for Hoechst and Nile Red, respectively. The images were quantified using an automated segmentation algorithm developed in Harmony 3.0 software (PerkinElmer). Briefly, the algorithm was designed to segment nuclear ROIs based on Hoechst fluorescence. An artificial cytoplasm was then extended around the nuclei, within which the average cytoplasmic Nile Red signal was quantified cell by cell. The results are expressed as mean fluorescence intensities (arbitrary units) measured in two replicates per condition (> 1000 cells measured). Illustrative images were obtained using confocal laser microscopy (SP8, Leica) at 20× magnification. Images were acquired in the blue fluorescence channel for Hoechst (λ_{ex} = 472 nm) and in the red fluorescence channel for Nile Red (λ_{ex} = 560 nm). Human breast cancer cell line (MCF-7) was used for all *in vitro* experiments. Cells were cultured in medium with Dulbecco's modified Eagle's medium (DMEM), fetal bovine serum (FBS) 10% (*v*/*v*), Pen-Strep 1% (*v*/*v*) and sodium pyruvate (1 mM). Before treatment with micelles, cells were washed with warm PBS, trypsinized and centrifuged at 200 ×*g* for 2 min. The supernatant was removed, cells were resuspended in fresh medium and filtered with a cell strainer (40 µm) to remove cell aggregates. One hundred

microliters of cell suspension were seeded with automation into the wells of a 96-well plate (final: 1500 cells/well). 24 h after incubation, cells were treated with either C_{18}-PEO or C_{18}-Fc-PEO micelles. 50 µL of OptiMEM were layered on top of the culture wells (final [micelles] = 2–200 µM). The plates were incubated (37 °C, 5% CO_2) for 1 h. Supernatant was removed first partly by aspiration using Biotek ELX405. The remaining supernatant was removed by centrifuging the plate upside down on top of a paper towel (70 ×*g*, 10 sec). Then, 100 µL of fresh culture medium were immediately added manually to the wells. When necessary, the plates were illuminated 10 min with the A160WE TB light positioned 8 cm away from the bottom of the wells. Cells were then incubated (37 °C, 5% CO_2) for 72 h. Then, cells were fixed and stained by addition of 50 µL PFA (4% [*w*/*v*] final) and Hoechst 33342 (final: 2 µg mL^{-1}). Plates were incubated overnight at 4 °C, then the supernatant was removed by aspiration and replaced by 100 µL PBS. Plates were acquired on the Operetta device. All experiments were done in triplicate.

CHAPTER 3

43

Synthesis of 1-bromopentacosa-10,12-diyne (43)

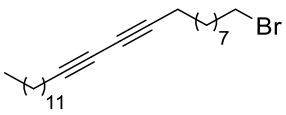

To a solution of **33** (427 mg, 1.01 mmol, 1.0 equiv.) and triphenylphosphine (397 mg, 1.52 mmol, 1.5 equiv.) in anhydrous CH_2Cl_2 (3 mL), was added carbon tetrabromide (497 mg, 1.52 mmol, 1.5 equiv.) under nitrogen. The brown mixture was stirred for 1 h, then cold water (10 mL) was added. The organic phase was washed with water (3 × 20 mL). The combined organic layers were dried over $MgSO_4$, filtered and concentrated under vacuum. The brown crude product was purified on silica gel using 100% CH_2Cl_2 to afford **43** (300 mg, 59%) as a yellowish waxy solid.

^{1}H NMR (400 MHz, $CDCl_3$) δ (ppm): 3.39 (t, 2H, J = 6.9 Hz), 2.23 (t, 4H, J = 6.9 Hz), 1.89–1.78 (m, 2H), 1.56–1.45 (m, 4H), 1.45–1.17 (m, 28H), 0.87 (t, 3H, J = 6.9 Hz).

^{13}C NMR (100 MHz, $CDCl_3$) δ (ppm): 77.6, 77.4, 65.3, 65.1, 34.0, 32.8, 31.9, 29.6, 29.4, 29.3, 29.2, 29.1, 28.9, 28.8, 28.7, 28.6, 28.3, 28.2, 28.1, 22.7, 19.2, 14.1.

44

Synthesis of 10,12-pentacosadiynoyl-α-methoxy-ω-hydroxy PEO2000 (44)

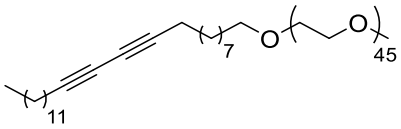

Under nitrogen, polyethylene glycol monomethyl ether (M_w = 2 000 g mol^{-1}), 250 mg, 0.13 mmol, 1.0 equiv.) in anhydrous acetonitrile (10 mL) was added to a suspension of sodium hydride (6 mg, 0.26 mmol, 2.0 equiv.) in anhydrous acetonitrile (2 mL). The mixture was refluxed for 30 min and allowed to cool down to room temperature. Compound **43** (211 mg, 0.52 mmol, 4.0 equiv.) in tetrahydrofurane (2 mL) was slowly added and the reaction was stirred at room temperature for 96 h. After concentration under vacuum, purification on silica gel (CH_2Cl_2/methanol 95:5) afforded the desired product as a yellow solid (265 mg, 90%).

^{1}H NMR (400 MHz, $CDCl_3$) δ (ppm): 3.80–3.45 (m, 180H), 3.33 (s, 3H), 2.19 (t, 4H, J = 7.0 Hz), 1.57–1.45 (m, 6H), 1.37–1.17 (m, 28H), 0.83 (t, 3H, J = 7.0 Hz).

^{13}C NMR (100 MHz, $CDCl_3$) δ (ppm): 77.4, 77.3, 72.5, 71.9, 70.7–77.2, 70.3, 70.0, 65.3, 65.2, 61.6, 58.9, 31.8, 29.6, 29.5, 29.4, 29.3, 29.2, 29.1, 29.0, 28.8, 28.7, 28.3, 26.0, 22.6, 19.1, 14.0.

45

Synthesis of 10,12-pentacosadiynoyl-deferoxamine (45)

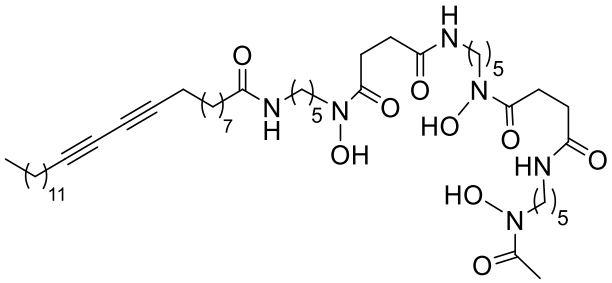

To a solution of desferoxamine mesylate salt (0.131 g, 0.20 mmol, 1.0 equiv.) in phosphate-buffered saline 0.1 M (4 mL, pH 7.4) was added a solution of **25** (0.100 g, 0.24 mmol, 1.2 equiv.) in tetrahydrofuran (4 mL). The mixture was stirred at room temperature under nitrogen during 48 h. The solvent was removed under vacuum until dryness. Water (30 mL) was then added and the mixture was cooled in an ice bath. The suspension was then filtered and successively washed with cold water (60 mL), cold saturated sodium carbonate solution (60 mL), cold water (60 mL), cold acetone (20 mL) and cold diethyl ether (60 mL) to afford **45** (106 mg, 52%) as a white solid.

ESI-MS calculated for $C_{50}H_{88}N_6O_9$ $[M]^+$ 916.7, found 916.3.

Materials

Citric acid monohydrate ($C_6H_6O_7,H_2O$ ≥ 99%), phosphate buffered saline (PBS) tablets, buffer formalin 10%, were purchased from Sigma-Aldrich (France). Sodium carbonate (Na_2CO_3) was purchased from VWR (France). Zirconium-89 [^{89}Zr]Zr-oxalic acid was obtained from PerkinElmer (Netherlands). H_2O Optimal LC/MS and 2-Methylbutan were purchased from Fisher chemical (Thermo Fisher Scientific, France) and Honeywell (France). Trifluroacetic acid, ethanol, acetonitrile were obtained from Carlo Erba (France). Isoflurane was purchased from Baxter (France). PD-10 desalting columns and instant thin-layer chromatography on glass microfiber chromatography paper impregnated with silica gel were purchased from GE Healthcare (France). Vivaspin® ultrafiltration tubes (5 kDa) were obtained from Sartorius (France). Prolong Diamond Antifade Mountain with DAPI was purchased from Invitrogen (Thermo Fisher Scientific, France) and optimum cutting temperature from Cell Path (United Kingdoms). Dulbecco's phosphate buffered saline (10 mM), Trypsin-EDTA, antibiotic-antimycotic, fetal bovine serum and cell culture medium (Dulbecco's Modified Eagle's medium) were purchased from Gibco (Thermo Fisher Scientific, France). Microbubbles (SonoVue®, 1.5×10^8 µB mL^{-1}) were purchased from Bracco (Milan, Italy). Ultrapure water (resistivity > 18 MΩ cm) was obtained using a Milli-Q system (Millipore, France) and used for all immunohistological buffers.

Micelle radiolabeling with zirconium-89

On the day of imaging experiments, a suspension of DiD@pPCDA-PEO/DFO micelles (8.96 mg, 3 mg mL^{-1} in H_2O Optimal LC/MS) was adjusted at pH 7.2 by adding 0.01 M HCl (5 µL). The oxalic acid of the ^{89}Zr solution (320 µL, 237 MBq) was neutralized with 2 M Na_2CO_3 (192 µL) before addition to the DiD@pPCDA-PEO/DFO suspension. The mixture was stirred for 1 h at 50 °C and 500 rpm to complete the reaction. DiD@pPCDA-PEO/DFO[^{89}Zr] was purified through PD-10 column using phosphate buffered saline (PBS) as mobile phase and concentrated by Vivaspin® ultrafiltration tubes (5 kDa cutoff).

Stability of DiD@pPCDA-PEO/DFO[^{89}Zr] micelles in mouse plasma and serum

The stability study was designed so that the ratio between the volume of serum (or plasma) and the volume of DiD@pPCDA-PEO/DFO[^{89}Zr] micelles was higher than the theoretical

0.25:0.075 ratio of *in vivo* experiments (described in section 1.8). For each 30 µL of radiolabeled micelles (1 mg, 17 MBq), 120 µL of either PBS, mouse plasma or mouse serum was added. Samples were analyzed by thin-layer chromatography (TLC) right after mixing (0 h), after 24 h and 48 h of incubation at 37 °C and 500 rpm.

Characterization of DiD@pPCDA-PEO/DFO[^{89}Zr] micelles

The radiochemical yield and purity were determined using instant thin-layer chromatography on glass microfiber chromatography paper impregnated with silica gel (iTLC-SG) as stationary phase and citric acid solution (20 mM , pH adjusted to 4.9–5.1 with 2 M Na_2CO_3) with 10% of acetonitrile as mobile phase. The elution was followed by radio-TLC detection (Mini-Scan TLC Imaging Scanner, Eckert & Ziegler, Berlin, Germany) and by exposition to a storage phosphor screen (VWR) in an exposure cassette (Molecular Dynamics) for 20 min at room temperature (RT) before developing the screen with Storm 860 Molecular Imager (50 µm resolution).

High performance liquid chromatography (HPLC) allowed measuring the complexation of [^{89}Zr] by the DA-DFO and therefore determining the radiopurity of the final DiD@pPCDA-PEO/DFO radiolabeled micelles. HPLC was performed on a Dionex system (ThermoFisher Scientific, France) with a P680HPLC pump, an oven column compartment (TCC-100 at 30 °C), a UV-vis (UVD170U UV/VIS) and a scintillation detector (Packard, Canberra, Austria) detector. A reversible phases Jupiter C4 column (150 mm × 4.60 mm, 5 µm, 300 Å, 16 496 Phenomenex) was used to separate the different diacetylene amphiphiles (PEO and DFO) according to an established protocol.[14] Briefly, 20 µL of sample at 20 µCi was injected into the column and a linear-gradient elution was carried out with a solution of (A) Milli-Q water/trifluroacetic acid (TFA) 99.9:0.1 *v/v* and (B) acetonitrile (MeCN)/TFA 99.9:0.1 *v/v*, at a flow rate of 1 mL min^{-1}. The elution was programmed as: 1% of solvent B during 5 min to elute the reactive, then a gradient from 1% to 90% in 13 min followed by 90% of solvent B during 4 min to elute the fragment and the micelles and finally 1% of B during 7 min to wash the column. Eluted species were detected via UV and radioactivity detection.

Cell culture

Human U87-MG cells derived from human astrocyte glioblastoma grade III, were purchased from ATCC (HTB-14). Cells were cultured in a humidified incubator (Sanyo, Japan) at 37 °C in

an atmosphere containing 5% of CO_2 in DMEM (Dulbecco's Modified Eagle's medium) supplemented with 10% of heat-inactivated FBS (fetal bovine serum), 1% antibiotic-antimycotic (streptomycine, amphotericin B, penicillin). Mycoplasma absence was confirmed using MycoAlert™ kit (Lonza, USA).

Animal experiments

Animal experiments were conducted in agreement with the European Directive 2010/63/EU on the protection of laboratory animals (French law transposition: Decree No. 2013-118). They were performed at the imaging facility CEA-SHFJ with protocols approved by the Ethical Committee of CETEA-CEA DSV IdF (authorization D91–471-105). In total, 16 five-week-old female athymic NMRI nude mice were purchased from Janvier laboratories (Le Genet sur Isle, France, Mus musculus, NMRI-FOXN1 Nu/Nu). Mice were housed, four per cage, with food and water *ad libitum* in an enriched environment (polycarbonate cottages and wooden stocks), in a room with controlled temperature (22 °C) and humidity (40%), and were maintained under specific pathogen-free conditions.

Subcutaneous tumor model

Mice anesthetized with isoflurane (4% in O_2 for induction and 2% in O_2 for maintenance) received a subcutaneous injection of 5.0×10^6 U87 cells suspended in 100 µL of PBS in both right and left flanks for heterotopic establishment of tumors. Animal weight and tumor growth were monitored three times a week. The tumors were allowed to grow for three weeks before the beginning of the experiments. At the end of the experiments, mice were euthanized by cervical dislocation under isoflurane (5 %). Tumors were removed, immersed in 2-methylbutan and frozen in liquid nitrogen.

Sonoporation using US

Animal experiments were performed under Isoflurane anesthesia (4 % for induction and 2 % for maintenance) in a mixture of air/O_2 8:2. The US procedure was similar to the protocol in our previous study. [50]

Briefly, US were delivered using a transducer (active diameter 5 mm, focal depth 3 cm, Imasonic, Voray sur l'Ognon, France) connected to a programmable generator (Image Guided Therapy,

Pessac, France). The transducer was mounted on a 3D-printed support and coupled to the mouse skin using a latex balloon filled with deionized and degassed water and coupling gel. A 50 µL bolus of SonoVue® was intravenously administered in the tail vein. The US opening covered a circular region centered on the subcutaneous tumor (5 mm in diameter) and allowed deep penetration (up to 2 cm). Ultrasonic waves were transmitted at 1.0 MHz during 2 min with a duty cycle of 40 %. The transmitted *in situ* peak negative pressure in the mouse brain was estimated to be 400 kPa at 1.0 MHz.

Sonoporation protocol was performed on mice bearing U87MG subcutaneous tumors. Each mouse carried two tumors, one in each flank. The US procedure was applied in only one tumor flank (the enestic tumor). The other tumor was used as a negative control (without US) within the same mouse (the anenestic tumor).

PET acquisition and image reconstruction

PET acquisitions were performed using the Inveon microPET-CT (Siemens Medical Solutions, Knoxville, TN, USA). The spatial resolution of the PET scanner is ~ 1.5 mm (FWHM). After the PET scan, a 6 min 80 kV/500 µA CT scan was performed for attenuation correction. PET images were reconstructed using a 3D OSEM iterative algorithm (4 iterations, 16 subsets, voxel size = 0.4 mm × 0.4 mm × 0.8 mm). Normalization, dead time correction, random subtraction, CT-based attenuation and scatter corrections were applied.

Longitudinal PET evaluation of DiD@pPCDA-PEO/DFO[^{89}Zr] micelle tumor delivery with and without US

Image protocol

Three weeks after tumor implantation, a total of 14 mice were randomized into 2 groups that received intravenous injection of µB (Sonovue, 50 µL) and DiD@pPCDA-PEO/DFO[^{89}Zr] micelles (150 µL, 10 mg mL^{-1}, 4.18 ± 0.21 µCi) with or without US (n = 7 for each both group). Dynamic PET scans of 60 min performed under the camera (framing: 3 × 30 s, 5 × 60 s; 5 × 120 s, 3 × 180 s, 3 × 240 s, 4 × 300 s, 1 × 240 s) were acquired immediately after injection of DiD@pPCDA-PEO/DFO[^{89}Zr] micelles into the tail vein. Then, a 20 min PET acquisition was performed 4 h, 24 h, 48 h, 72 h and 7 days after the injection. For one mouse per group, optical imaging was acquired prior to injection, 24 h, 48 h, 72 h and 7 days after the injection. One mouse per group

was sacrificed by cervical dislocation under isoflurane (5%) 72 h post-injection. The tumor directly in contact with the transducer was removed, immersed in 2-methylbutan, frozen in liquid nitrogen and stored at −80 °C until histological analysis (auto-radiography, immunofluorescence, and hematoxylin-eosin staining).

Image analysis

Imaging analyses were performed with the PMOD software (Version 3.9, Switzerland). All the images and extracted data were corrected according to the half-life of ^{89}Zr ($t_{½}$ = 3.3 days).

The accumulation of DiD@pPCDA-PEO/DFO[^{89}Zr] micelles in the different organs of interest (brain, skin, heart, liver, kidneys, bladder, muscle, spleen and bone) were measured by positioning a VOI of 8.0 mm^3 on the middle of the organ.

The accumulation of DiD@pPCDA-PEO/DFO[^{89}Zr] micelles in the tumor was measured by drawing the iso-contour of the tumor at 48 h, which corresponds to the maximal tumor accumulation time. Then the same VOI was used for other time points.

The activities were expressed using the following formula:

$$\%ID.cm^{-3} = \frac{\text{activity (kBq)/cm}^3\text{ of tissue}}{\text{injected activity (kBq)}} \times 100 \qquad \textbf{(Eq. IV)}$$

After the last acquisition, mice were sacrificed by cervical dislocation under isoflurane (5%). The tumor directly in contact with the transducer was removed, immersed in 2-methylbutan and frozen in liquid nitrogen. The main organs (brain, heart, liver, left kidney, the tumor that was not directly in contact with the transducer, muscle, spleen, and bone) were collected and weighed. The radioactivity in these tissues were counted in a gamma counter (Cobra II 576 autogamma, Packard). Tissue uptake was expressed as % of injected activity/g of tissue.

The correlation between the DiD@pPCDA-PEO/DFO[^{89}Zr] micelle accumulation value determined from images and gamma counter was assessed through Pearson's correlation coefficient.

Blood pharmacokinetics

Blood activity concentrations were determined from the blood pool activity issued from PET image VOI. The radioligand blood half-life contributions were interpolated with a tri-

exponentials model from blood time-activity curves from each individual mouse using the PMOD kinetic modeling tool (v4.2). The areas under the curve (AUC) were compared between the group without US and the group with US.

Histological analysis

Tissue section process

Serial tumor sections (14 µm thick) were cut at −20 °C with a cryostat (Leica CM3050 S, Leica biosystems) and adhered on SuperFrost Ultra Plus TM slides (FisherScientific). Slides were stored at −80 °C until histological analysis (hematoxylin-eosin, autoradiography, and immunofluorescence).

Autoradiography

Tumor slides were exposed to a storage phosphor screen (VWR) in an exposure cassette (Molecular Dynamics) for 24 h at 4 °C. The screen was developed with Storm 860 Molecular Imager at 50 µm resolution. Images were analyzed using ImageJ software (v1.53i).

Immunofluorescence staining

Frozen tumor slides were fixed in neutral buffer formalin 10% for 15 min at RT, then washed three times with PBS buffer. Slides were mounted using Prolong Diamond Antifade Mountain with DAPI. Fluorescence microscopy was performed on Axio Observer 5 microscope (Zeiss, Germany) at 20× and 40× magnifications. Image post-processing was performed with the ZEN software (v2.6, Zeiss).

Hematoxylin-eosin staining

Tumor slides were fixed in neutral buffer formalin 10% for 30 min then washed with distilled water. Standard hematoxylin and eosin (H&E) staining was performed using Harris hematoxylin and Eosin Y alcoholic (Sigma-Aldrich). Transmitted light images of stained tumor sections were acquired with the Axio Observer 5 microscope (Zeiss, Germany) at 20× magnification. Image post-processing was performed with the ZEN software (v2.6, Zeiss).

Statistical analysis

All data are presented as mean ± standard deviation. The statistical analyses were performed using GraphPad Prism software (Graph Pad software Inc., San Diego, USA). Comparisons of uptakes in different organs of interest issued from PET data with US and without US over time were performed via Mann Whitney U rank test. Statistical changes at the 95% confidence level ($P < 0.05$) were qualified as significant.

université PARIS-SACLAY

ÉCOLE DOCTORALE
Sciences Chimiques : Molécules, Matériaux, Instrumentation et Biosystèmes (2MIB)

Titre : Micelles PEGylées pour le diagnostic et la thérapie de tumeurs solides.

Mots clés : micelles, ferrocène, photolyse, vectorisation, nanoparticule, oxygène singulet

Résumé : La nanomédecine est un domaine émergent répondant aux contraites rencontrées par la médecine conventionnelle. L'utilisation d'objets nanométriques permet de réduire les effets secondaires par un traitement ciblé, spécifique et à dose réduite. Parmis ces nanoparticles, les micelles sont largement exploitées du fait de leur petite taille et forte modularité. Ainsi, leur application s'étend à deux nombreux domaines dont la cancérologie. En effet, leurs tailles permettent de pleinement bénéficier des caractéristiques du microenvironnement tumoral qui ont pour conséquence une accumulation et rétention accrues des micelles dans les tissues tumoraux. Ainsi, l'utilisation de micelles en tant que nanovecteurs permet une approche théranostique pour le traitement anticancéreux.

Dans ce cadre, les travaux présentés se divisent en deux parties distinctes. La première présente la synthèse et formulation de micelles PEGyléess photodégradables capable de générer à la fois de la cytotoxicité et de délivrer une molécule hydrophobe au niveau intracellulaire. La deuxième partie porte sur l'amélioration de l'effet EPR par sonoporation, une méthode considérée non-invasive. Les résultats sur modèles murins ont pu démontrer l'effet positif de la méthode en augmentant grandement l'homogénéité au niveau de la distribution des micelles au sein des tumeurs.

université PARIS-SACLAY
ÉCOLE DOCTORALE
Sciences Chimiques: Molécules, Matériaux, Instrumentation et Biosystèmes (2MIB)

Název: PEGylované micely pro diagnostiku a terapii solidních nádorů.

Klíčová slova: micely, ferrocen, fotolýza, vektorizace, nanočástice, singletový kyslík

Abstrakt: Nanomedicína je nově vznikající obor, který řeší problémy, jimž čelí konvenční medicína. Použití nanometrických objektů umožňuje snížit vedlejší účinky prostřednictvím cílené, specifické léčby při snížených dávkách. Mezi těmito nanočásticemi jsou díky své malé velikosti a vysoké modularitě hojně využívány micely. Díky tomu se jejich použití rozšiřuje do mnoha oblastí, včetně onkologie. Jejich velikost jim totiž umožňuje plně využít vlastností nádorového mikroprostředí, což vede ke zvýšené akumulaci a retenci micel v nádorové tkáni. Použití micel jako nanovektorů tak nabízí teranostický přístup k léčbě rakoviny. V této souvislosti je zde prezentovaná práce rozdělena do dvou samostatných částí. První představuje syntézu a formulaci fotodegradovatelných PEGylovaných micel, které jsou schopny generovat cytotoxicitu a zároveň dodávat hydrofobní molekulu intracelulárně. Druhá část se zaměřuje na zesílení EPR efektu pomocí sonoporace, což je metoda považovaná za neinvazivní. Výsledky na myších modelech prokázaly pozitivní účinek této metody tím, že výrazně zlepšila homogenitu distribuce micel v nádorech.

Title : PEGylated micelles for diagnostic and therapy against solid tumors.

Keywords : micelles, ferrocene, photolysis, vectorization, nanoparticle, singlet oxygen

Abstract : Nanomedicine is an emerging field that addresses the challenges faced by conventional medicine. The use of nanometric objects makes it possible to reduce side effects through targeted, specific treatment at reduced doses. Among these nanoparticles, micelles are widely exploited thanks to their small size and high modularity. As a result, their application extends to many fields, including oncology. Indeed, their size enables them to take full advantage of the characteristics of the tumor microenvironment, resulting in increased accumulation and retention of micelles in tumor tissue. Thus, the use of micelles as nanovectors offers a theranostic approach to cancer therapy. In this context, the work presented here is divided into two distinct parts. The first presents the synthesis and formulation of photodegradable PEGylated micelles capable of both generating cytotoxicity and delivering a hydrophobic molecule intracellularly. The second part focuses on the enhancement of the EPR effect by sonoporation, a method considered to be non-invasive. Results on murine models demonstrated the positive effect of this method by greatly improving the homogeneity of micelles distribution within the tumors.